University of New Mexico
UNM Digital Repository

Chemistry ETDs | Electronic Theses and Dissertations

7-2-2011

Spectroscopic and electronic structure studies of bis-metallodithiolenes

Regina Mtei

Follow this and additional works at: https://digitalrepository.unm.edu/chem_etds

Recommended Citation
Mtei, Regina. "Spectroscopic and electronic structure studies of bis-metallodithiolenes." (2011). https://digitalrepository.unm.edu/chem_etds/15

This Dissertation is brought to you for free and open access by the Electronic Theses and Dissertations at UNM Digital Repository. It has been accepted for inclusion in Chemistry ETDs by an authorized administrator of UNM Digital Repository. For more information, please contact disc@unm.edu.

Regina Peter Mtei
Candidate

Chemistry and Chemical Biology
Department

This dissertation is approved, and it is acceptable in quality and form for publication:

Approved by the Dissertation Committee:

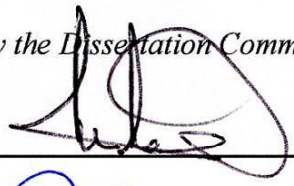

, Chairperson

SPECTROSCOPIC AND ELECTRONIC STRUCTURE STUDIES OF BIS-METALLODITHIOLENES

BY

REGINA PETER MTEI

B.Sc (Horns)., University of Dar Es Salaam, 2002
M.Sc., Chemistry, University of Botswana, 2004

DISSERTATION

Submitted in Partial Fulfillment of the
Requirements for the Degree of

Doctor of Philosophy
Chemistry

The University of New Mexico
Albuquerque, New Mexico

May, 2011

To my dad **Peter** and mam the late **Thea**

My sisters and brothers

Acknowledgments

I am very grateful to the almighty God for giving me strength and be able to accomplish this work. First I would like to thank my advisor Prof. Martin L. Kirk for his guidance, patience and support he offered throughout this work.

Special thanks to my family; my dad, my sisters and brothers; Mr & Mrs. P. Kavuyimbo, Alphonce, Rose, Charles, Monica, Restituta, Alfred, and Benedicta for their molar and spiritual support all the time when I was far away from home. Without them my studies and life in general could be so difficult.

I would like to thank our collaborators Prof. H. Sugimoto from Osaka university for provision of bis-dithiolene compounds, Prof. P. Basu for provision of bis-dithione Mo(IV) compounds and Prof. R. Hille for provision of dimethylsulfoxide reductase enzyme. I would like to extend my appreciation to former and current Professor Kirk group members; Dr. Sushilla Z. Knottenbelt, Dr. Abebe, Antonio William, Meita Fulton, Dr. Jing Yang, Joseph Sempombe, Diana Habel-Rodriguez, Domnic Kersi, Chao Dong and Benjamin Stein for their discussion, assistance and encouragement. Without forgetting everyone who in one way or another has contributed in my studies and my safely stay here at USA.

I am very grateful to the Department of Chemistry and Chemical Biology for their financial support and this opportunity to pursue my Ph.D studies in chemistry at University of New Mexico.

SPECTROSCOPIC AND ELECTRONIC STRUCTURE STUDIES OF BIS-METALLODITHIOLENES

BY

REGINA PETER MTEI

ABSTRACT OF DISSERTATION

Submitted in Partial Fulfillment of the
Requirements for the Degree of

Doctor of Philosophy
Chemistry

The University of New Mexico
Albuquerque, New Mexico

May, 2011

SPECTROSCOPIC AND ELECTRONIC STRUCTURE STUDIES OF BIS-METALLODITHIOLENES

BY

REGINA PETER MTEI

B.Sc (Horns)., University of Dar Es Salaam, 2002

M.Sc., Chemistry, University of Botswana, 2004

Ph.D., Chemistry, University of New Mexico, 2011

Abstract

Dimethylsulfoxide reductase (DMSOR) enzyme family members catalyze oxygen atom transfer to or from organic or inorganic substrate and play important roles in the global cycles of sulfur and nitrogen, as well as the detoxification of arsenite. This enzyme has recently been subject of investigation due to its catalytic nature of oxygen atom transfer. This work reports on the electronic structure and reactivity properties of dimethylsulfoxide reductase enzyme studied using spectroscopic and computational methods. The spectroscopic methods included electronic absorption (EA), electron paramagnetic resonance (EPR), magnetic circular dichroism (MCD) and resonance Raman rRaman). Here, we report full characterization of the DMSOR and DMSOR model compounds, MoO/S/Se(L^{COOMe})$_2$, MoO(L^{H}/L^{O})$_2$, MoS/Se(L^{Ph})$_2$, MoO($L_2^{ipro/meth}$),

$MoO(SPh)_2(L^{ipro})$, $MoO(bdt)_2$ and $WO/S(L^{Ph})_2^-$ and the nature of their charge transfer transitions. The model compounds were studied in the (IV), (V) oxidation states. The electron withdrawing nature of LCOOMe, L_2ipro/meth, LPh ligands have indicated the presence of a low energy intraligand charge transfer transition. Ligand field, metal to ligand charge transfer, ligand to metal charge transfer and intraligand charge transfer bands for these model compounds have been successfully assigned using both electronic absorption and rRaman spectroscopies for Mo(IV) compounds. EA and MCD spectroscopic methods enabled the assignment of Mo(V) compounds. The density functional theory calculations have supported our assignments. EPR spectroscopy revealed a rhombic g-tensor and axial A-tensors for Mo(V) compounds indicative of low symmetry coordination and a d_{xy} redox orbital. Spin density calculations revealed that electron transfer is through unbent side of ene-dithiolene ligands for regeneration of Mo(VI) resting state in the catalytic cycle. In particular, for DMSO reductase enzyme, the electronic structure of a *des*oxo Mo(V) intermediate has been probed by EPR, electronic absorption and MCD spectroscopies. The EPR spectra revealed a rhombic g-tensor that indicated a low symmetry coordination for this intermediate. For the first time a rhombic ^{95,97}Mo A-tensor has been determined, that indicated a d_{z^2} redox orbital admixed with $d_{xy}/_{dx^2-y^2}$ type orbitals. In general, these methods have indicated that the geometry of Mo(V) intermediate is distorted trigonal prismatic.

TABLE OF CONTENTS

List of Figures

List of Tables

CHAPTER 1

Introduction to Dimethysulfoxide Reductase Enzyme Family and Spectroscopic Methods

1.1 Molybdenum Containing Enzyme

Molybdenum is the only second row transition metal that is required for the growth of animals, plants and microorganisms as an essential trace element. The metal is associated with a diverse range of redox active enzymes or group of proteins that differ in structure and function that catalyzes key reactions in the metabolism of nitrogen, sulfur, and carbon compounds.[1-3] Molybdenum containing enzymes can be classified into two groups (i) bacteria nitrogenase enzyme (Molybdenum containing nitrogenase) and (ii) pyranopterin molybdenum enzyme.[1] All pyranopterin molybdenum enzymes share a common feature which is the presence of one or two pyranopterin rings that coordinates to the molybdenum at the active site (Figure 1.1). The pyranopterin ene-1,2-dithiolenes have been reported to play an important role in modulating molybdenum reduction potential and also in facilitating electron transfer pathway to regenerate the molybdenum active site resting state.[1,4]

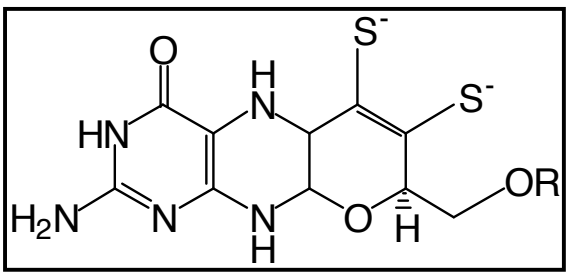

Figure 1.1: The structure of pyranopterin dithiolene.

Most pyranopterin molybdenum enzymes catalyze a range of reactions that involve two-electron redox chemistry coupled to the transfer of an oxygen atom to or from organic or inorganic substrates. Based on sequence homology, active-site structure and function, pyranopterin molybdenum enzymes have been classified into three distinct families such as xanthine oxidase, sulfite oxidase, and DMSO reductase (DMSOR) (Figure 1.2).[1] However, during catalysis all pyranopterin molybdenum enzymes cycled between Mo(IV) and (VI) oxidation states.

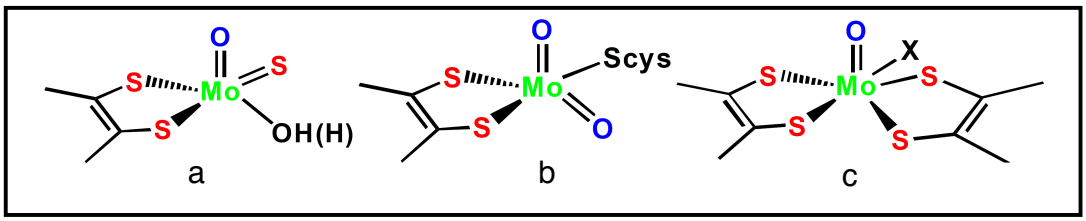

Figure 1.2: Pyranopterin molybdenum enzymes (a). xanthine oxidase, (b). sulfite oxidase, and (c). dimethylsulfoxide reductase enzymes.

1.2 Dimethylsulfoxide Reductase Family

Dimethylsulfoxide reductase family enzymes possess molybdenum and tungsten metal centers, and are isolated from lower organisms such as bacteria and archaea. Based on their similarities in sequence homology all members have been grouped in the same family. Members of this family are DMSO reductase,[5] trimethylamine N-oxide (TMAO) reductase, arsenite oxidase,[6,7] nitrate reductase,[8] formate dehydrogenase,[9] and biotin sulfoxide reductase. This enzyme family is diverse in both structure and function, and all members have

two equivalents of the pterin cofactor bound to the metal as a unique characteristic. All DMSO reductase family members catalyze the oxygen atom transfer to or from the substrate except formate dehydrogenase which facilitate cleavage of a substrate C-H bond.[10]

1.2.1 Dimethylsulfoxide Reductase

Dimethylsulfoxide reductase enzyme is isolated from variety of bacteria such as *Rhodobacter capsulatus, Rhodobacter sphaeroides and Escherichia coli*. It catalyzes the reduction of dimethylsulfoxide (DMSO) to dimethylsulfide (DMS) (Equation 1.1), where as the former is a chemical compound found in seawater from methylated sulfur compounds which are the byproducts of marine phytoplanktons.[11] However the later is a biogenic sulfur gas produced by reduction of DMSO to DMS by bacteria in the sea and then released to the atmosphere where it plays important role in atmospheric sulfur cycle and climate regulation (cloud formation).[11-13] An alternative substrate for the enzyme is trimethylamine N-oxide (TMAO) which is faster than DMSO as observed in the kinetic study.[14]

$$DMSO + 2H^+ + 2e^- \rightarrow DMS + H_2O \qquad \text{..... (1.1)}$$

Several crystal structures of the oxidized [5,15,16] and reduced [17] forms of DMSO reductase enzyme have been reported previously, but there was a debate whether the crystal structure active site is penta-, hexa-, or hepta- coordinated to the molybdenum center. Therefore, in 2000 Schindelin and coworkers reported a

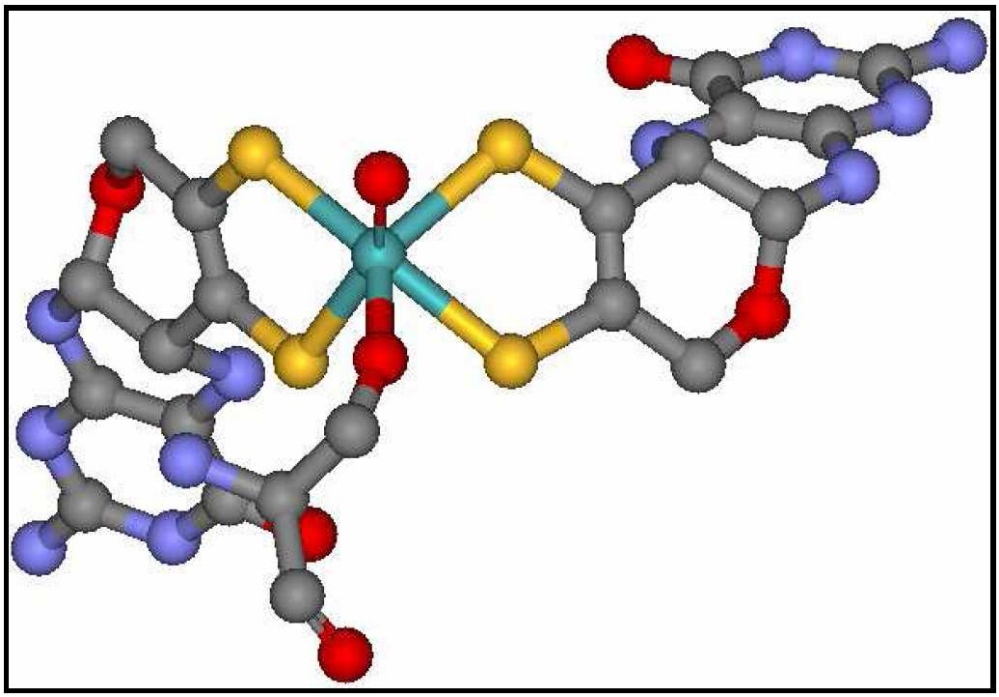

Figure 1.3: The crystal structure of oxidized dimethylsulfoxide reductase enzyme.

high resolution crystal structure of DMSO reductase enzyme. The structure of oxidized form of DMSO reductase enzyme was determined at 1.3Á resolution with a distorted trigonal prismatic geometry.[18] The active site is hexa-coordinated with four sulfurs from the two pyranopterin rings attached to the molybdenum, an oxo ligand and side chain amino acid serine 147 (Figure 1.3). The reduced form of DMSO reductase has a square pyramidal geometry with four sulfurs attached to the molybdenum and oxygen of serine, but lack a terminal oxo ligand. This coordination was confirmed by resonance Raman data which shows enhancement of the Mo-S stretch, Mo-Oserine and not Mo-oxo stretch.[19-22] In addition to molybdenum cofactor no other prosthetic groups have been reported

in DMSO reductase enzyme from *R. capsulatus* or *R. sphaeroides* hence making it possible for this enzyme to be studied intensively using spectroscopic techniques.

In the catalytic cycle DMSO reductase cycles between Mo(IV), Mo(V) and Mo(VI). Starting with Mo(IV) which is the resting stage the introduction of the substrate leads to the formation of a strong Mo-OS$(CH_3)_2$ bond which cause a weakening of substrate oxygen sulfur (O-S$(CH_3)_2$) bond. Therefore Mo(IV) is oxidized to Mo(VI) through a product bound intermediate with release of DMS. Mo(VI) is reduced back to Mo(IV) via Mo(V) intermediate by two sequential coupled proton (H^+) electron transfers (Scheme 1.1).[14,21] Mo(V) intermediate possesses two pyranopterin dithiolenes attached to the molybdenum center, oxygen of serine and an hydroxyl group. The presence of a hydroxide was confirmed by electronic paramagnetic resonance (EPR) [14,19,23] and chapter four in this work covers proton hyperfine tensor of Mo(V) intermediate. However, no crystal structure of the Mo(V) intermediate has been reported todate.

Several spectroscopic studies have been done on the oxidized, Mo(V) intermediate and the reduced DMSO reductase enzyme but so far the nature and geometry of the Mo(V) intermediate SOMO is not known. The molybdenum hyperfine parameters which is important in determining the nature of the redox orbital has not been reported. Therefore chapter 4 in this work explains in detail the nature of the redox orbital and determined the spin Hamiltonian parameters

obtained by spectral simulation and computationally in order to gain insight in the electronic structure of the Mo(V) intermediate.

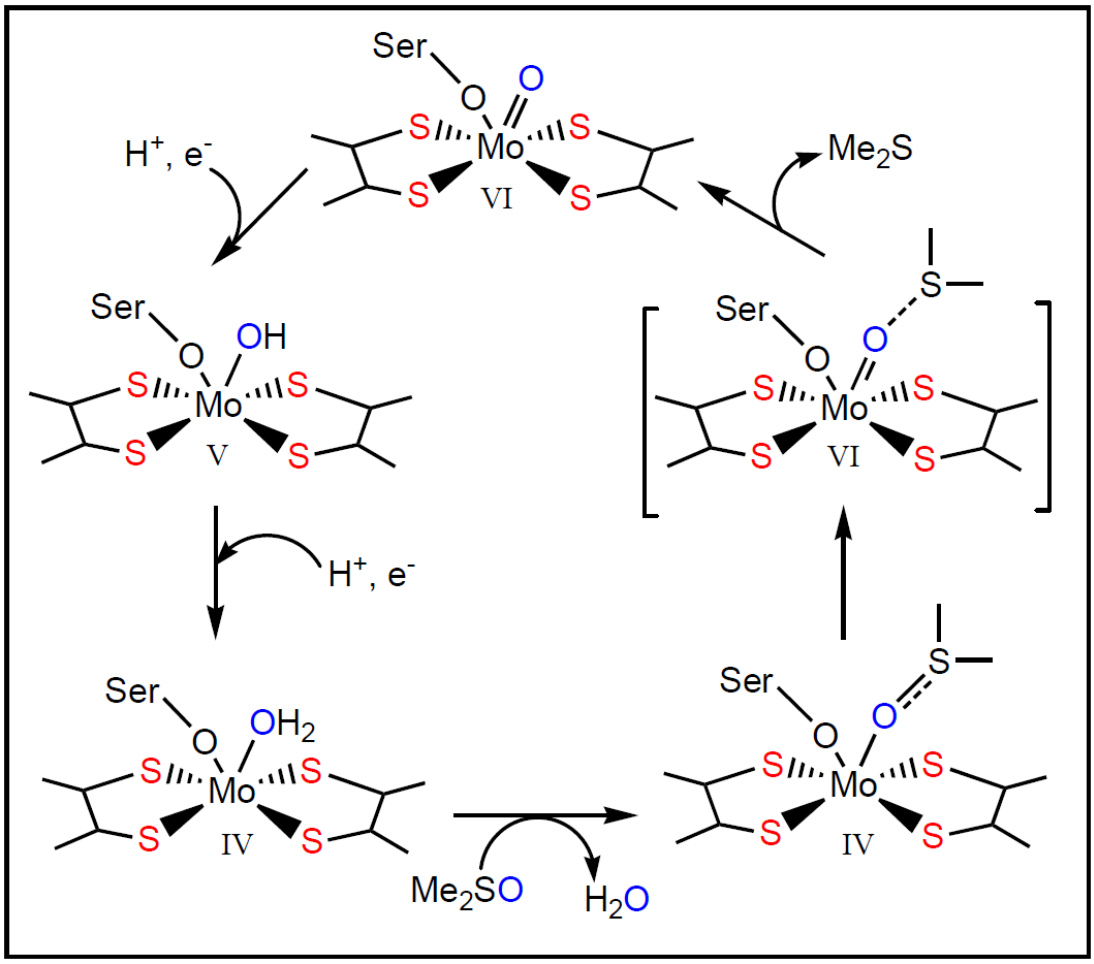

Scheme 1.1: Proposed catalytic mechanism for DMSO reductase enzyme.

1.2.2 Nitrate Reductase

Nitrate reductase is a bacterial based enzyme like other members of the DMSOR family. Based on their cell location, metabolic pathway and the active site, these enzymes are classified into membrane bound respiratory nitrate reductase (Nar), cytoplasmic assimilatory nitrate reductase (Nas) and the periplasmic dissimilatory

nitrate reductase (Nap).[24] The crystal structures for dissimilatory nitrate reductase [8,25,26] and respiratory nitrate reductase [27,28] have been reported with very distinct active sites suggesting that they evolved from the same pyranopterin molybdenum enzymes. The discussion below will cover only the membrane bound respiratory nitrate reductase isolated from *Escherichia coli* bacterial that catalyze the reduction of nitrate to nitrite (Equation 1.2), and plays an important role in nitrogen dissimilation for respiration.[2,28,29]

$$NO_3^- + 2H^+ + 2e^- \rightarrow NO_2^- + H_2O \qquad E^0 = +420 \text{ mV} \qquad \ldots\ldots\ldots\ldots (1.2)$$

This enzyme is a heterotrimeric consist of a catalytic subunit that is pyranopterin molybdenum (NarG), an electron transfer subunit that is four iron-sulfur clusters (NarH) and a membrane anchor subunit heme (NarI). The catalytic subunit active site is composed of four sulfur atoms from the two pyranopterin rings connected to the molybdenum, an oxo ligand and a monodentate interaction from carboxylate oxygen of aspartate (Asp 222)[28] in its oxidized form (Figure 1.4). Membrane bound respiratory nitrate reductase (NarG) is the first DMSOR family member to have aspartate coordinated to the molybdenum.[27,28] However Bertero and coworkers reported for the first time the presence of an open ring system "bicyclic dihydropterin structure" in the membrane bound nitrate reductase enzyme instead of the typical tricyclic pyranopterin structure observed in all DMSOR family members.[27] This enzyme is able to bind the active site in both forms as ring opening and closure participate in the proton handling for nitrate reduction. Therefore due to significance of ring opening and ring closure in

chapter 2.4 we have utilized model compounds having a square pyramidal geometry and open ring system to probe the role of conjugated ene-1,2-dithiolene in the electronic structure of the membrane bound nitrate reductase.

During catalysis nitrate reductase cycles between Mo(IV), Mo(V) and Mo(VI) oxidation states. The Mo(V) intermediate has hydroxyl bound to the molybdenum, as evident from the EPR studies.[30] In addition to the molybdenum cofactor in the catalytic unit, Bertero and coworkers reported the presence of the iron-sulfur cluster (FS0) between the Mo and the first iron-sulfur (FS1) (in the electron transfer subunit). The iron-sulfur (F50) proposed to have a direct role in the electron transfer mechanism as observed in the site directed mutagenesis study where substitution of histidine 50 (His-50) with cystein (Cys) amino acid perturbs the hydrogen bonding networking and therefore lead to loss in enzyme activity.[31] The presence of iron-sulfur clusters in the enzyme complicates characterizations of molybdenum active site using spectroscopic techniques. Therefore spectroscopic studies of small molecule model complexes for reduced Mo(IV) and Mo(V) have been covered in Chapter 2 and 3 providing insight into the detailed electronic structure of the 1,2-dithiolenes ligands which mimic the bicyclic dihydropterin structure that governs the electron transfer in the catalysis.

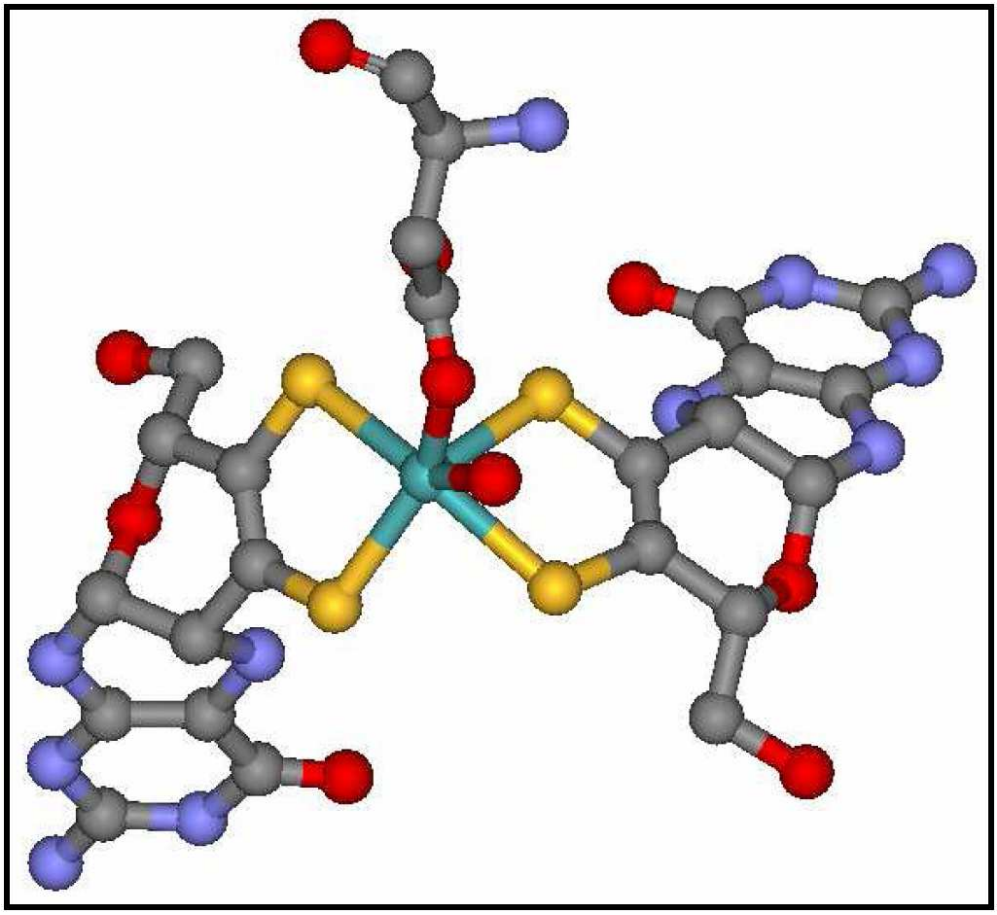

Figure 1.4: The crystal structure of oxidized nitrate reductase enzyme active site.

1.2.3 Arsenite Oxidase

Arsenite oxidase is a periplasmic enzyme isolated from *Alcaligenes faecalis* bacteria. The enzyme catalyzes the oxidation of arsenite to arsenate using azurine or cytochrome c as its ultimate electron acceptor (Equation 1.3).[32] In the environment, both arsenite and arsenate (the two water soluble forms of arsenic) are toxic to cells. However arsenite is more toxic due to its high affinity for thiols.

$$As(OH)_3 + H_2O \rightarrow As(OH)_2O_2^- + 3H + 2e^- \quad \ldots\ldots\ldots\ldots\ldots\ldots \quad (1.3)$$

From X-ray crystallographic [6] and EXAFS [7] data, the active site of arsenite oxidase is similar to other members of DMSO reductase family except that it lacks an enzyme derived amino acid which coordinates to the molybdenum. In the reduced form, the active site contains two pyranopterin dithiolenes attached to the molybdenum and an oxo group located at apical position to form a five coordinate square pyramid geometry (Fig 1.5). The molybdenum atom is displaced approximately 0.8 A˚ from the mean plane defined by the four sulfur ligands. Further more EXAFS data showed an extra Mo-O bond in the oxidized form which is consistent with a dioxo Mo(VI) species[7]. In addition to the molybdenum active site, the enzyme has [3Fe-4S] and [2Fe-2S] clusters as other prosthetic groups involved in the catalysis. Crystallographic characterization of the active site is consistent with resonance Raman study,[33] where a Mo-oxo stretch was observed in the Raman spectrum of the oxidized but not in the reduced form of the enzyme.

During catalysis arsenite oxidase cycles between the Mo(IV) and (VI) oxidation states but no Mo(V) intermediate has been detected in this enzyme. This is of interest as the Mo(V) state is believed to be an obligatory catalytic intermediate in the electron transfer regeneration in other pyranopterin molybdenum enzymes (Scheme 1.2). The instability of the Mo(V) intermediate, was observed in EPR [32] and protein film voltammetric studies,[33] suggests a highly cooperative two-electron transfer between the Mo(IV) and Mo(VI) oxidation states.

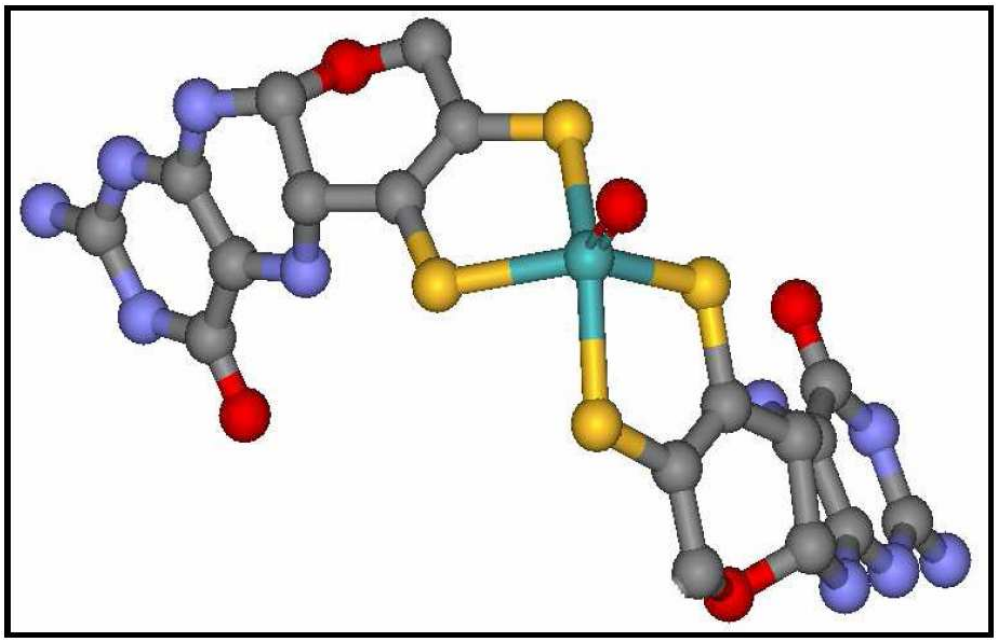

Figure 1.5: The crystal structure of reduced arsenite oxidase enzyme.

The presence of [3Fe-4S] and [2Fe-2S] Iron-sulfur clusters in arsenite oxidase complicates spectroscopic analysis of the enzyme. This is clearly evident in the EPR and electronic absorption spectra of this enzyme. Therefore in chapters 2 and 3 we have utilized small molecules analogues that possess square pyramid geometry as the enzyme in order to probe electronic structure. This has been accomplished using EPR, MCD, rRaman and electronic absorption spectroscopies.

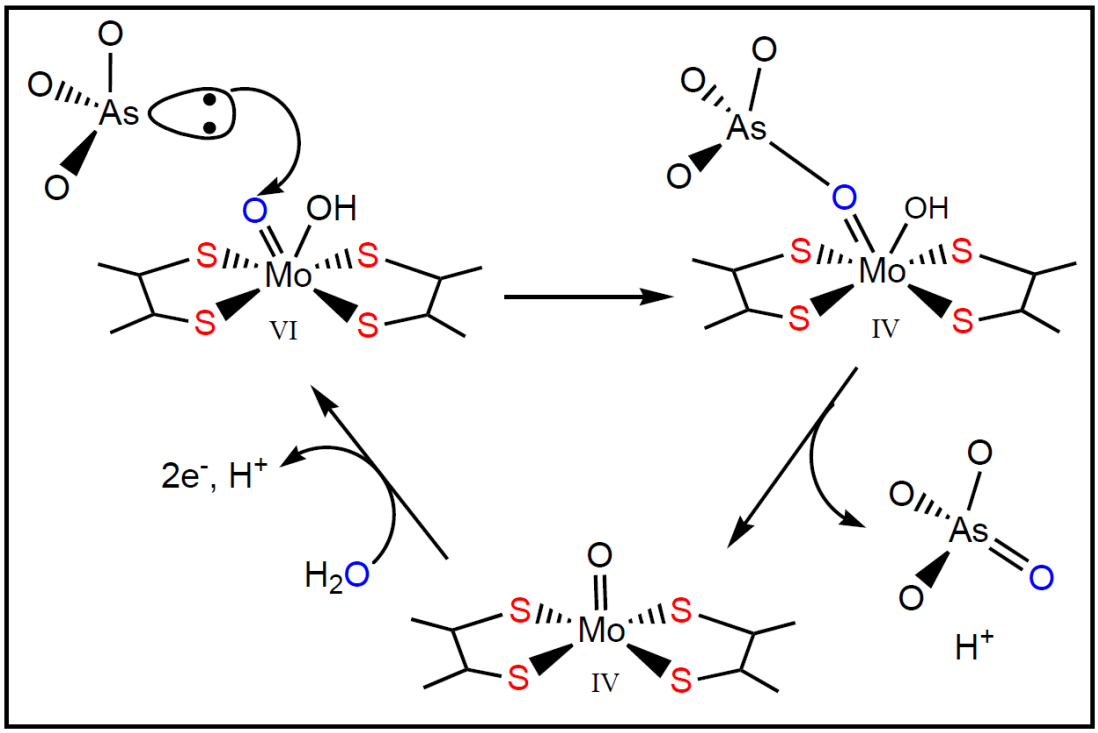

Scheme 1.2: Proposed catalytic mechanism for arsenite oxidase enzyme.

1.2.4 Formate Dehydrogenase

To date, there are three classes of formate dehydrogenase that have been characterized by X-ray crystallography. Formate dehydrogenase H (Fdh-H) is a component of the anaerobic formate hydrogen lyase complex of *Escherichia coli*,[9,34,35] the membrane bound formate dehydrogenase N (Fdh-N) is a component of *E. coli* nitrate respiratory which is involved in the proton motive force generation by redox loop[36] and tungsten-containing formate dehydrogenase (W-Fdh) from *Desulfovibrio gigas*.[9,37-39] Formate dehydrogenase is a unique enzyme, as it catalyzes the oxidation of formate to carbon dioxide (Equation 1.4) by facilitating cleavage of a substrate C-H bond. This leads to the formation of a C=O bond from a C-OH bond. The reaction is unlike any other

DMSOR family enzyme, since these catalyze the oxygen transfer to or from organic/inorganic substrates.[1]

$$HCOO^- \rightarrow CO_2 + H^+ + 2e^- \qquad E^0 = -420 \text{ mV} \qquad \text{..... (1.4)}$$

In the oxidized forms, all three classes of the formate dehydrogenase enzyme catalytic subunit possess an active site with a distorted trigonal prismatic geometry (Fig 1.6) and contain five iron-sulfur (4Fe-4S) clusters. The Mo ion in the Fdh-H and Fdh-N active sites is coordinated by two pyranopterin dithiolenes, a hydroxyl ligand, and a selenocysteine (Se-Cys) donor.[35,36] The W-Fhd active site contains a tungsten ion coordinated by four sulfur donors from two pyranopterin dithiolenes, a thiol ligand and a Se-Cys side donor.[38] The presence of a hydroxyl ligand in the active site of Fdh-H and Fdh-N is supported by EXAFS data [34] which failed to detect any oxo group in different oxidation states.

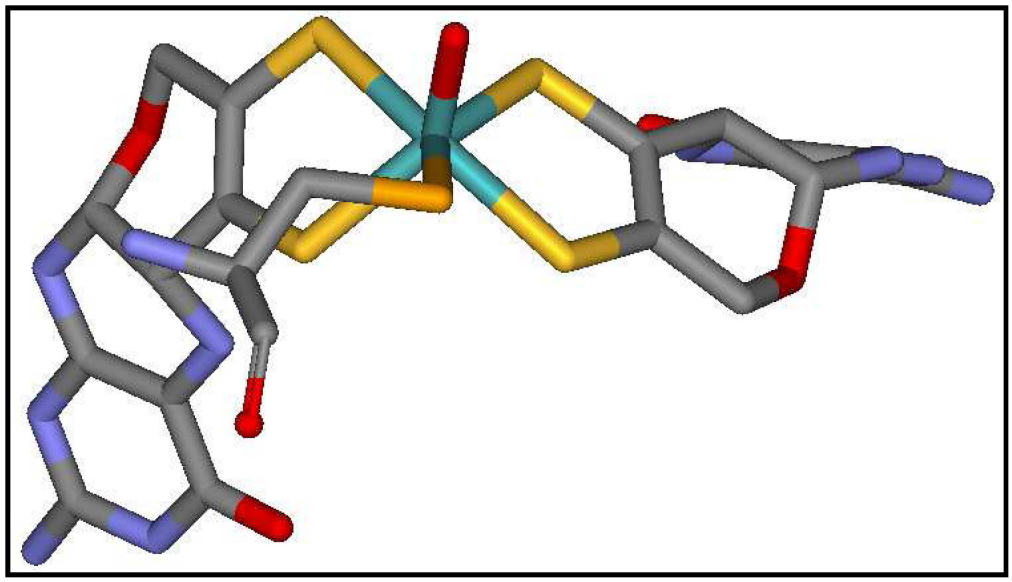

Figure 1.6: The crystal structure of oxidized formate dehydrogenase enzyme.

In the reduced enzyme form, only the crystal structure of *E. coli* Fdh-H has been reported so far.[35,40] The active site of this enzyme has a square pyramidal geometry with four sulfurs from the two pyranopterin dithiolenes attached to the Mo ion in the equatorial plane, and an axial Se donor of Se-Cys.[35] Additionally EPR studies on Mo(V) form of formate dehydrogenase isolated from *Desulfovibrio desulfuricans* ATCC 27774 revealed an apical SH ligand after CO_2 release.[41]

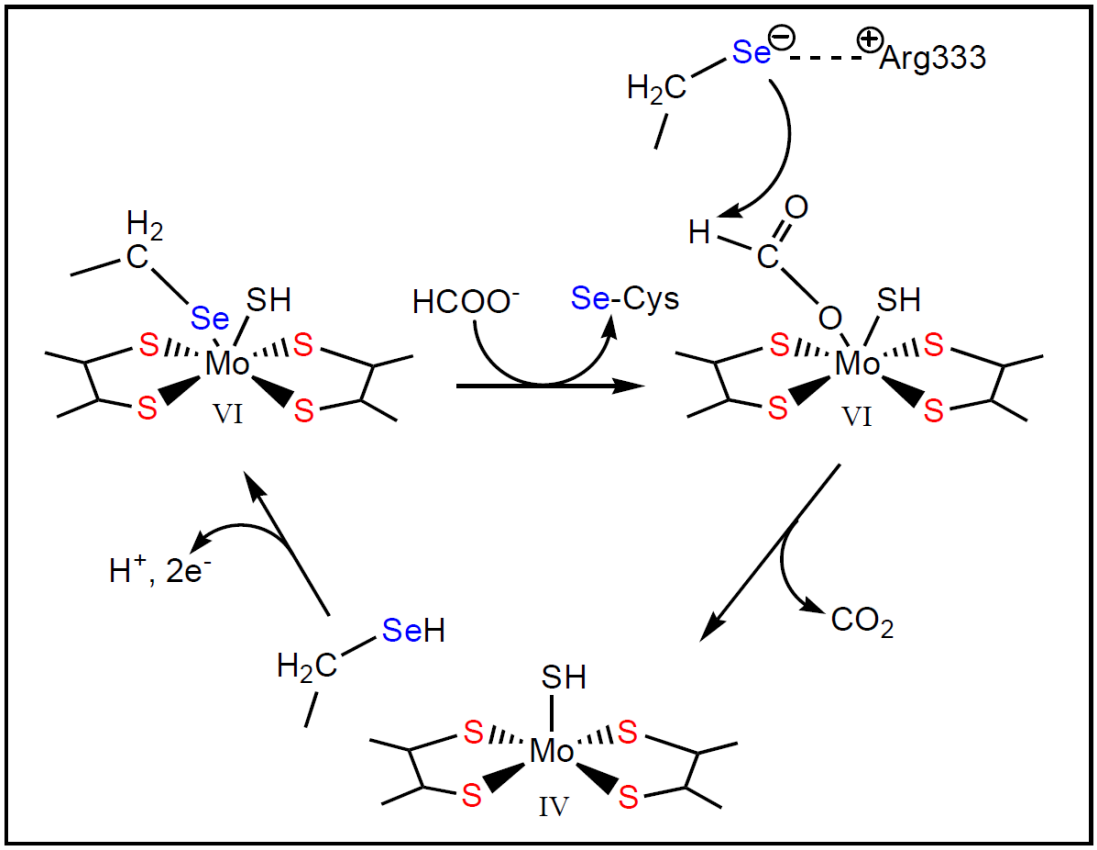

Scheme 1.3: Proposed catalytic mechanism for formate dehydrogenase enzyme based on the reanalyzed crystal structure of *E. coli* Fdh.

Furthermore during catalysis, formate dehydrogenase enzymes cycles between the +4 and +6 oxidation states as shown in Scheme 1.3.[40,42] Spectroscopic studies on Mo and W containing model compounds that possess oxo/ selenido/ sulfido donors at the apical position are covered in Chapter 2 of this work, where we explain the nature of the Fdh enzyme active site in its reduced form during the course of catalysis.

1.3 Spectroscopic Methods

X-ray absorption and EXAFS studies have been utilized to study the active site of DMSO reductase enzyme family, in which several crystal structures have been reported in the reduced and oxidized forms. The electronic structure characterization of this enzyme family have been performed using electronic absorption, resonance Raman, magnetic circular dichroism (MCD), and electron paramagnetic resonance (EPR) spectroscopies. These spectroscopic techniques are more effective if the active site does not possess other cofactors apart from the active site, otherwise the presence of other cofactors complicates spectroscopic characterization of the active site. Model compounds with active site similar to a reduced enzyme form have been intensively spectroscopically characterized, where rRaman combined with electronic absorption probe the nature of excited states. EPR spectroscopy have been utilized to probe the ground state properties for DMSO reductase Mo(V) intermediate and Mo(V) models for arsenite oxidase and formate dehydrogenase enzymes paramagnetic centers while electronic absorption combined with MCD spectroscopies have probe the nature of excited states. Additionally, variable temperature MCD spectroscopy is a higher resolution technique in understanding the excited state electronic structure of Mo(V) compounds. These spectroscopic techniques have been described below.

1.3.1 Electronic Absorption Spectroscopy

This is a usefully technique in studying the electronic energy levels and bonding characteristics of metal center in metalloenzyme and synthetic compounds. In the electronic absorption the amount of incident light transmitted depends on the concentration of the sample and the pathlength, as explained by Beer's law (Equation 1.5) where A is the absorbance, ε is the molar extinction coefficient, c is the sample molar concentration and l is the pathlength (cm).

$$A = \varepsilon c l \qquad \text{..... (1.5)}$$

The square of the transition moment integral (**P**) is proportional to intensity of light absorption I associated with an electronic transition from ground state (ψ_g) to the excited state (ψ_e) (Equation 1.6) where R is an operator representing the interaction of the electromagnetic radiation with the molecule.

$$I \propto |\langle \psi_e | R | \psi_g \rangle|^2 = P^2 \qquad \text{..... (1.6)}$$

The molar extinction coefficient describes the absorption intensity but alternatively the intensity can be defined in terms of an oscillator strength (f), which is a dimensionless quantity that describes the probability of photon absorption. Experimental oscillator strengths can be calculated by Equation 1.7, where $\varepsilon(\bar{\nu})$ is the molar extinction coefficient ($M^{-1}cm^{-1}$), $\int \varepsilon(\bar{\nu}) d\bar{\nu}$ is the integral of the area under the band of a given transition.[43,44]

$$f = 4.32 \times 10^{-9} \int \varepsilon(\bar{\nu}) d\bar{\nu} \qquad \text{..... (1.7)}$$

Any transition induced by electromagnetic radiation will involve a contribution from the electric and magnetic dipole components of the incident radiation. With the exception of a very weak transition where only the electric dipole mechanism dominates, the magnetic dipole intensity has less contribution in the electronic transition compared to electric dipole intensity which contributes ~10^4 times than magnetic dipole intensity.

Selection rules in the electronic absorption spectroscopy are based on the transition moment integral and determine whether the transition is allowed of forbidden. First, when the spin and orbital electronic wavefunction are treated separately, the transition moment integral is written as (Equation 1.8) where Φg and $\theta_{g,s}$ represent the orbital and spin component of the ground state wavefunction.

$$P = \left\langle \Phi_e \middle| r \middle| \Phi_g \right\rangle \left\langle \theta_{e,s} \middle| \theta_{g,s} \right\rangle \qquad \text{..... (1.8)}$$

The spin quantum numbers of the ground $\theta_{g,s}$ and excited state $\theta_{e,s}$ must be equal ($\Delta S = 0$) for a spin allowed transition. In the second integral a change in parity must accompany a transition. This rule state that the transition moment will be non-zero only if the direct product of the irreducible representation of ground state $\left(\Phi_g\right)$ and excited state $\left(\Phi_e\right)$ with the irreducible representation of the electric dipole operator, r, contains the totally symmetrical representation

(Equation 1.9) where, x and ⊂ symbols represent the direct product and "contains".

$$\Gamma(\Phi_g) \times \Gamma(r) \times \Gamma(\Phi_e) \subset A_1(g) \quad \text{..... (1.9)}$$

For centrosymmetric molecules, allowed transitions occur with change in parity (g (gerade) → u (ungerade)). This means g → g and u → u transitions are forbidden. As a result, only weak transitions are observed for g → g (ligand field) transition. The ligand field transition can appear as the result of relaxation of Laporte selection rule which is contributed by two factors. First, a slight change in geometry must occur that removes the inversion, or a complex can undergo an asymmetric vibration which destroys the inversion center.

In the transition metal complexes several band/transitions may be observed in the electronic absorption spectral and these include ligand field and charge transfer transitions. Figure 1.7 shows the charge transfer transition in an octahedral complex. Charge transfer transitions that involve the transfer of electron from an orbital with predominantly ligand character to the excited state orbital with predominantly metal character is known as ligand to metal charge transfer (LMCT) transition. However if the transfer of electron is from the ground state with predominantly metal character to an excited state with predominantly ligand character are known as metal to ligand charge transfer (MLCT) transitions. However if the promotion of an electron is from a ground state with predominantly metal character to an excited state with predominantly ligand

character, this transition is known as a metal to ligand charge transfer (MLCT) transitions.

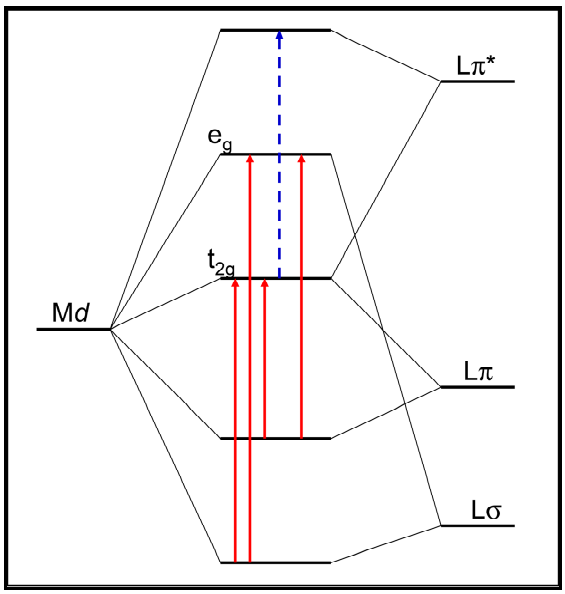

Figure 1.7: Schematic diagram showing the ligand to metal charge transfer (LMCT) transition (——) and metal to ligand charge transfer (MLCT) transition (– – – –) in the octahedral complex.

Additionally, if a transition involves the promotion of an electron from an orbital with predominantly ligand character to an excited state that also possesses predominantly ligand characters, the transition is known as a ligand to ligand charge transfer (intraligand/LLCT), and can be very intense.[43,45,46]

1.3.2 Magnetic Circular Dichroism Spectroscopy

The MCD technique probes the electronic and magnetic properties of transition metal centers in small molecules and metalloenzyme active sites. This technique is quite sensitive and is used in conjunction with electronic absorption, and rRaman spectroscopies in probing excited state electronic structure or with EPR for probing ground state electronic structure. Magnetic ground state information is obtained by monitoring the temperature and magnetic field dependence of discrete bands and utilizing applied magnetic fields up to 7T and typically temperatures between 1.5–300 K (this is a variable temperature variable field experiment and is not covered in this work). This study covers the excited state characterization of metallodithiolene compounds and DMSOR by utilizing the variable temperature MCD technique in either 0 or a 7 T applied magnetic field.[43,47]

In the MCD experiment we measure the differential absorption of left and right circular polarized light ($\Delta A = A_{LCP} - A_{RCP}$) as a function of wavelength with the application of magnetic field parallel to the propagation direction of the incident light. For a system with ground state (A) and excited state (*J*), where both possess angular momentum (J) with J=1/2, the application of a magnetic field splits the A and *J* (with J-values) states into $M_j = \pm 1/2$ sublevels. The magnitude of the splitting is governed by Zeeman operator, where for J=1/2 the splitting is $g_i \beta H$.

$$\frac{\Delta\varepsilon}{E} = \gamma\beta H\left[A_1\left(-\frac{\partial f(E)}{\partial E}\right) + \left(B_0 + \frac{C_0}{kT}\right)f(E)\right] \quad \text{..... (1.10)}$$

Where $\Delta\varepsilon$ is the differential molar absorptivity for LCP and RCP light, γ is a collection of constant terms, β is the Bohr magneton, H is the applied magnetic field, $f(E)$ is a band shape function, and $\partial f(E)/\partial E$ is a derivative of the band function. The MCD dispersion has three contributions, $-A_1(\partial f/\partial E)$, $B_0 f$, and $C_0 f/kT$ which correspond to A-, B- and C-terms. All transition must obey the MCD selection rules which are $\Delta M_L = \pm 1$, and $\Delta M_s = \pm 0$.

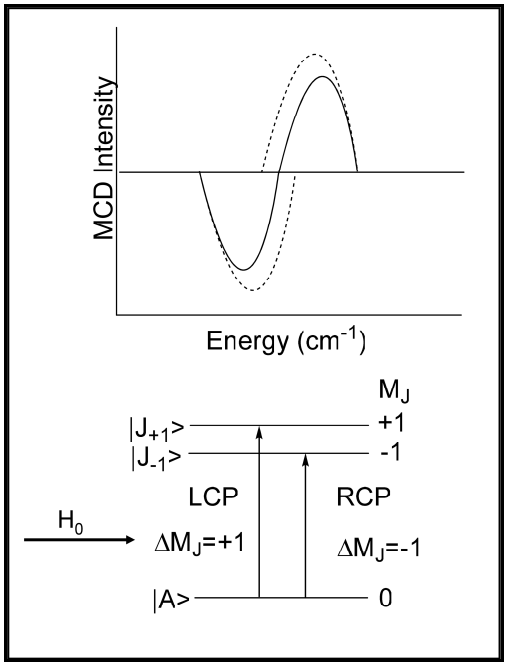

Figure 1.8: The origin of MCD A -terms.

A terms, are temperature independent but field dependent bands and they arise from transitions that originate from non-degenerate ground states to a

degenerate exited states. A-terms have a derivative shaped MCD dispersion with a crossover point at the band maximum (Figure 1.8).[43]

B terms, are temperature independent, field dependent bands that arise from either a transition from a non-degenerate ground state (|A>) to an excited state (|J>) mixed with intermediate excited state (K) or the ground state which is mixed with intermediate state (K) to a non-degenerate excited state (|J>) (Figure 1.9). The electric dipole moment for the transition and the extent of spin-orbit mixing determine the magnitude of this band.[43,48]

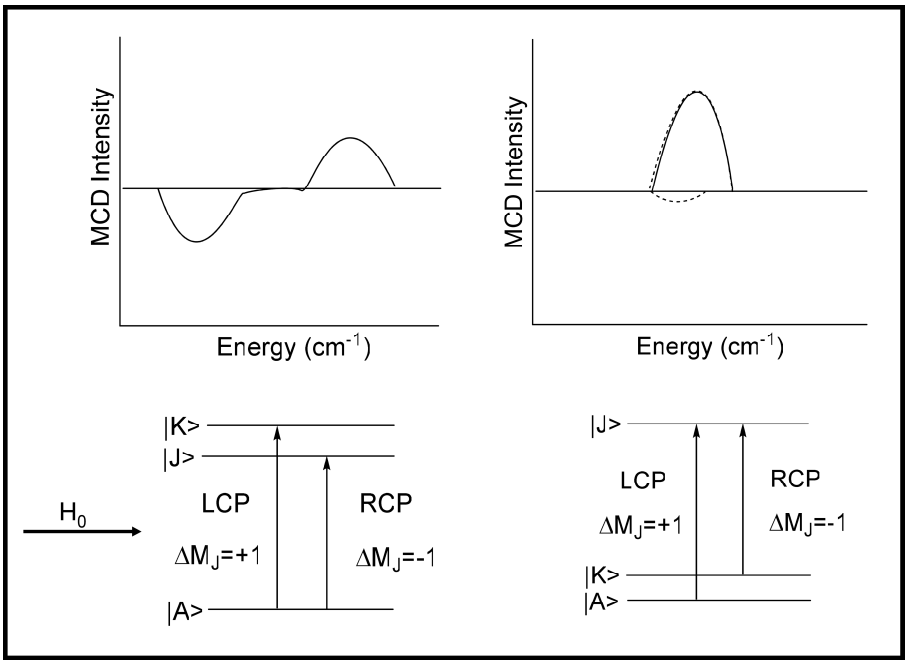

Figure 1.9: The origin of MCD B-terms.

C terms arise in transitions involving Zeeman split degenerate ground states to a non-degenerate excited state where the ground state population is governed by

the Boltzman distribution. These are temperature and field dependent bands with intensities that increase with a decrease in temperature.[49,43] The intensity of MCD C-terms have an inverse temperature (1/T) dependence. Thus, a derivative shaped MCD band is observed at high temperature since the transition occurs from nearly equally populated Zeeman split levels in the ground state to an excited state. However an absorptive band shape is observed at low temperature since there is an unequal population in Zeeman split, as illustrated in Figure 1.10.[49,48] C terms bands are commonly observed in the MCD spectra of molybdenum and tungsten compounds and enzymes. Pseudo A-terms derived from C-terms are temperature dependent and are commonly observed in the MCD spectra of molybdenum model compounds and enzymes.[49,43]

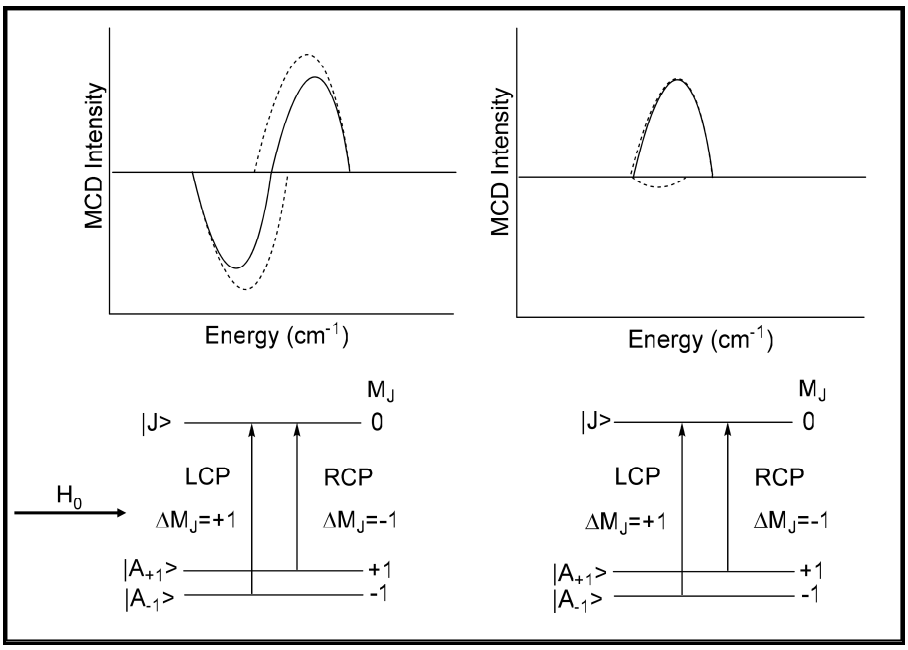

Figure 1.10: The origin of MCD C-terms.

1.3.3 Electron Paramagnetic Spectroscopy

EPR is a powerful technique that provides information on the electronic and geometric structure of transition metal ions by characterizing the interaction of the metal center spin with the applied magnetic field. EPR parameters (hyperfine tensors and g-tensors) are sensitive to the coordination environment of the metal center.[44,43]

In the EPR experiment, the spin interacts with applied magnetic field. This interaction can be expressed in quantum mechanical terms by the Hamiltonian (Equation 1.11) where g is the free electron value, β is the Bohr magneton, S is the total spin and H is the applied magnetic field.

$$\mathrm{H}_z = g\beta S \bullet H \quad \text{..... (1.11)}$$

For a Mo(V) (d^1) S = ½ system, the electron is allowed to have m_s ±½ values. The introduction of magnetic field (H), lead to stabilization (m_s = -1/2) and destabilization of (m_s = +1/2), while the magnitude of the splitting depends on the intensity of the magnetic field. For an EPR transition (ΔE) to occur, the frequency of the oscillating microwave field (ν) should meet the resonance condition (Figure 1.11).

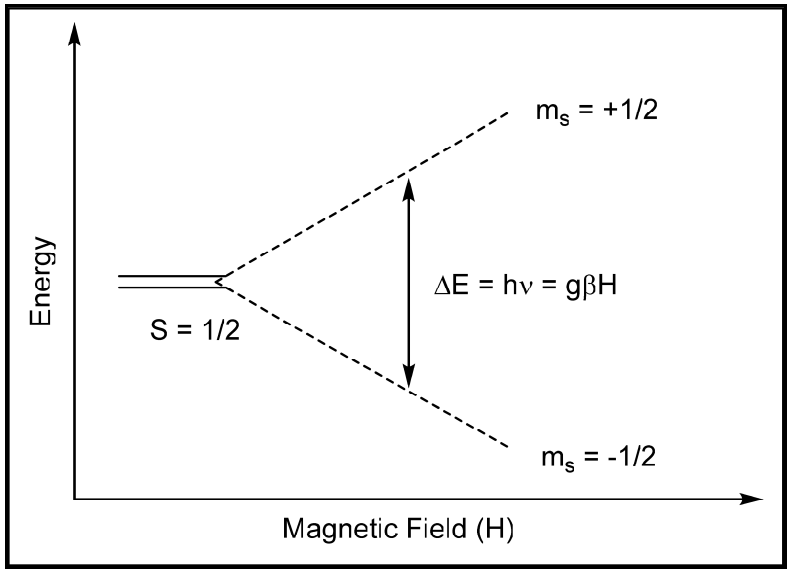

Figure 1.11: EPR splitting diagram for S = ½ system.

The EPR experiment is operated at a fixed frequency. Most spectrometers operate at 9.5 GHz (X band), with a field strength of 3,400 gauss. However 3 GHz (S band) can be used to enhance the resolution of the unresolved hyperfine structure where as 35 GHz (Q band) and higher frequencies may be use to increase the resolution associated with g anisotropy. An EPR spectrum is obtained when the energy ($h\nu = g\beta H$) of the microwave quantum matches the energy separation between the two spin orientations. The absorbed microwave radiation obeys the selection rule ($\Delta M_s = \pm 1$).[44,43,50,51] Three types of EPR spectra can be obtained experimentally i). isotropic spectra (gx = gy = gz), for cubic systems ii). axial spectra ($g_x = g_y < g_z$ or gx = gy > gz), for C_{3v} and higher systems and iii). rhombic spectra (gx = gy = gz) for low symmetry. Knowing $h\nu$, β and H, the g value of a metal center can be determined. The deviation of the g-

tensor from the free electron value can be attributed to ligand field effects, spin orbital coupling, charge transfer, and metal ligand covalency. [43,51,52,53]

The hyperfine interaction is found when an unpaired electron of a metal center interacts with a magnetic nucleus with $I \neq 0$. Therefore a line observed in the EPR spectrum will split according $(2I + 1)$, where I is the nuclear spin. Application of an applied magnetic field lead to transitions that are magnetic dipole allowed and obey the $\Delta M_s = \pm 1$, $\Delta M_I = 0$ selection rules. As an example, for a Mo center with spin S = ½, and nuclear spin I = 5/2, we observe six hyperfine lines (Figure 1.12).

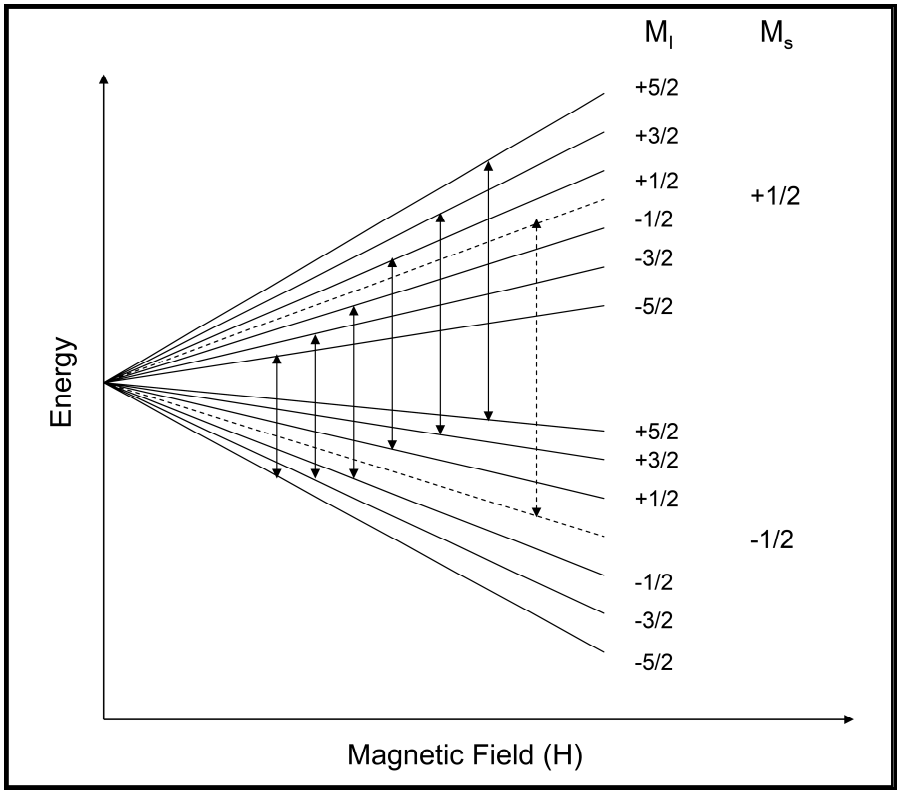

Figure 1.12: Hyperfine splitting energy levels for molybdenum d^1 system with spin S = ½ (M_s = ½ state) interacting with nucleus spin I = 5/2. The broken line shows the level before nuclear interaction and the solid line the level after nuclear interaction. All allowed transition obeys $\Delta M_s = \pm 1$ and $\Delta M_I = 0$ selection rules.

The hyperfine coupling parameter, A, has contributions from isotropic (Fermi contact) and anisotropic (spin and orbital dipolar) interactions. The fermi contact interaction arises from direct symmetry mixing of s orbital character into the ground state wavefunction or indirectly by spin polarization of a core s orbital. The dipolar term arises from the interaction of nuclear moment with i). the spin of the electron and ii). the orbital angular momentum of the electron. The spin dipolar term depends on the nature of the spin bearing orbital, and as observed in Table 1-1 and it is traceless. Strong interaction between the metal unpaired electron and its nuclear spin is observed in free ion, but metal ligand covalency tends to delocalize the unpaired electron into the ligands therefore reducing the hyperfine interaction between the unpaired electron and the nucleus.[44,43,50,51]

Table 1-1: Anisotropy hyperfine contributions due to the dipolar interaction of a nucleus with a single d electron with incorporation of Euler angle.[43,44,53]

Orbital	x	y	z
z^2	4	4	-2
x^2-y^2	-2	-2	4
yz	4	-2	-2
xz	-2	4	-2
xy	-2	-2	4

1.3.4 Raman Spectroscopy

Raman is very usefully technique for probing the structure of metal complexes or metal centers in biology and for obtaining key excited state information. In the Raman experiment a laser beams with a specific wavelength excites the sample molecule. Part of the incident energy, which is equal to the vibrational quantum (ν_k) is retained by the vibrating molecule, and the scattered photon appears with lower frequency ($\nu_0 - \nu_k$) and energy $\{h(\nu_0-\nu_k)\}$ as this represent an inelastic collision (Figure 1.13) and known as Stoke shift (Raman).[43,44,54] Alternatively, when a molecule possesses an energy equal to the vibrational quantum (ν_k) before excitation therefore, the scattered photon appears with higher frequency ($\nu_0 + \nu_K$) and energy $\{h(\nu_0+\nu_K)\}$, this phenomenon is known as Anti-Stoke shift.

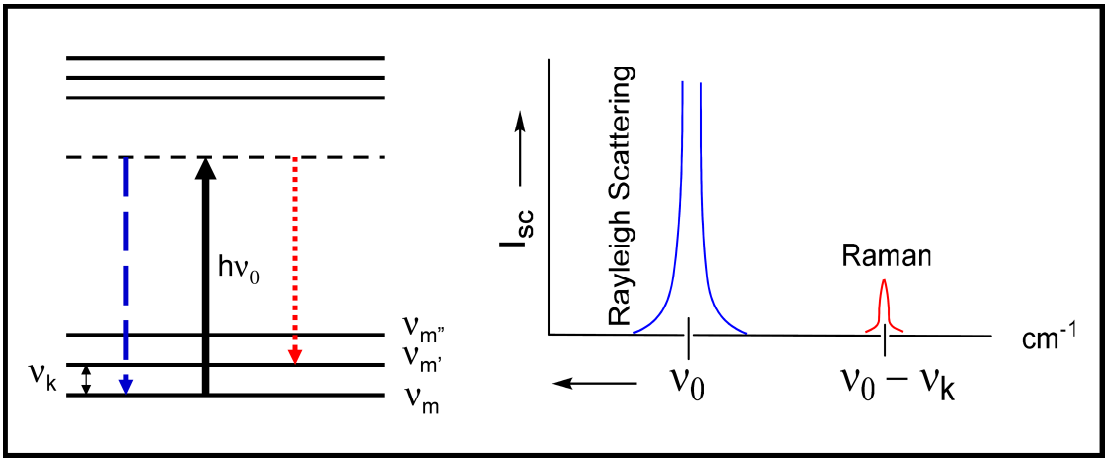

Figure 1.13: Schematic diagram showing (left) excitation of molecule from ground state (ν_m) to an excited state, which lead to (— — -) Rayleigh scattering (ν_0) and (········) stokes scattering (ν_0-ν_k), (right) scattered photon produces an intense Rayleigh peak and a weak Raman peak displaced from Rayleigh by ν_k.

The Raman intensity is proportional to the sample concentration (Equation 1.12) where ν_{sc} is the frequency of scattered radiation, E_0 is the laser intensity, and c is the volume concentration of scattering molecules.

$$I_{sc} \propto \nu_{sc}^4 E_0 c \quad \text{..} \quad (1.12)$$

Not all transitions between vibrational levels are allowed. Allowed transitions are determined by the symmetry of the molecule. A change in molecular polarizability as the result of vibrations is required for Raman scattering to occur. This occurs when a laser beam (E) of frequency (ν_0) (which is higher than the vibrational frequency (ν_k)) strikes a sample. The molecules become polarized and form an induced electrical dipole moment (**P**), which oscillates at the frequency (ν_0) of the

incoming laser beam. The scattered intensity is proportional to the square of the induced dipole moment (**P**). Therefore the strength of the laser beam (E) and degree of electronic polarization determine the magnitude of induced dipole moment (P) according to Equation (1.13).

$$P = \alpha E \qquad \text{..... (1.13)}$$

Here α is the polarizability of the molecule which closely related to the structure and bonding properties of the molecules. The intensity of a Raman vibration is given by Equation (1.14).[43,44,54,]

$$I_R \propto P^2 = (\alpha E)^2 \qquad \text{..... (1.14)}$$

Resonance Raman Spectroscopy

In resonance Raman spectroscopy, the laser excitation frequency determines the intensity of Raman scattering. The laser wavelength is very important in resonance Raman experiments as it increases the sensitivity and the selectivity of the technique. When the laser line is tuned to the vicinity of an allowed transition (on resonance), the intensity of the some of the Raman bands can increase up to 10^6 fold. Here, Raman bands gain intensity only when the molecular vibrations are couple to an electronic transition (Figure 1.14).

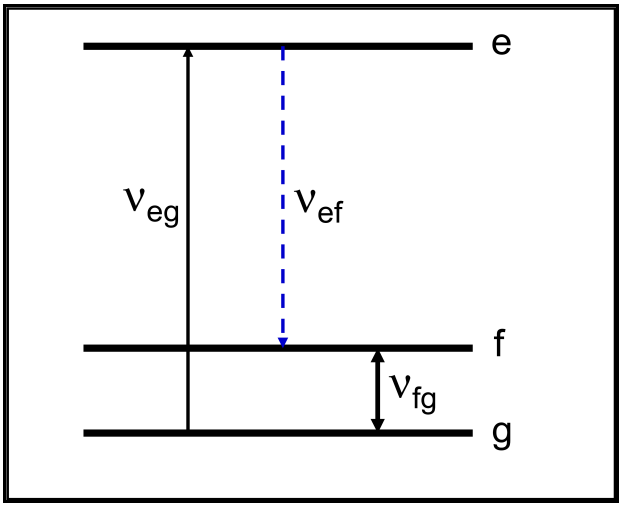

Figure 1.14: Resonance Raman bands intensity increases when the frequency of the exciting laser line is equal or close to the frequency of an allowed electronic absorption (ν_{eg}).

In Raman experiment a change in molecular polarizability as the result of vibrations is required for Raman scattering to occur. The polarizability can be expressed as the sum of contributions from the wave functions of all the excited state with the use of second order perturbation theory. The result is the Kramers-Heisenberg dispersion equation 1.15.

$$\alpha_{\rho\sigma} = \frac{1}{h}\sum_{e}\frac{\langle f|\mu_\rho|e\rangle\langle e|\mu_\sigma|g\rangle}{\nu_{eg}-\nu_0+i\Gamma_e}+\frac{\langle f|\mu_\sigma|e\rangle\langle e|\mu_\rho|g\rangle}{\nu_{ef}-\nu_0+i\Gamma_e} \qquad \text{..... (1.15)}$$

Where subscripts ρ and σ are Cartesian directions of the dipole moment operator μ and α is the polarization tensor element, while g, e and f are wave functions of the ground, excited and final states, respectively. In the

denominators ν_{eg} and ν_{ef} are frequencies of g → e and e → f transitions, ν_0 is the laser frequency, and Γ_e is the damping constant, which correspond to the half band width of the excited state. When the frequency of the exciting laser line (ν_0) approaches the frequency of the electronic transition ν_{eg} in the denominator of the first term, polarizability of the molecule increases and consequently resonance enhancement of a Raman band occurs.[43,44,54,]

CHAPTER 2

Electronic Structure of Bis-dithiolene Molybdenum and Tungsten (IV) Compounds

2.1 Introduction

Molybdenum enzymes of the DMSOR family and tungsten containing enzymes possess two pyranopterin dithiolenes coordinated to the Mo ion in the active site.[14,35,37,55] Several model compounds with metal-ligand multiple bonds have been synthesized to mimic the molybdenum and tungsten containing enzymes.[56,57] The importance of studying the coordination chemistry and electronic structure of compounds with Mo≡O, Mo≡S, and Mo≡Se bonds has increased recently as the results of the structural characterization of some pyranopterin molybdenum enzymes.[1] The xanthine oxidase and sulfite oxidase families have a Mo≡O unit in their +4, +5, or +6 oxidation states, however for the DMSO reductase from *R. capsulatus* and *R. sphaeroides*, the Mo≡O unit is only present in the +6 oxidation state. In the DMSO reductase family the Mo≡O unit is always coordinated by two pyranopterin–ene–1,2–dithiolate ligands.[2,16] This is supported by crystal structures of DMSO reductase,[5,18] arsenite oxidase,[6,7] formate dehydrogenase,[34,35,40] nitrate reductase,[8] and biotin sulfoxide enzymes showing two pyranopterin dithiolenes attached to the molybdenum or tungsten center. In addition to the Mo≡O unit in the DMSOR reductase enzymes, a Mo≡S unit has been reported in a reduced form of formate dehydrogenase that also possesses two pyranopterin dithiolenes attached to the molybdenum or tungsten ions.[38,40]

Although a large number of compounds possessing molybdenum with apical oxo ligand have been synthesized and spectroscopically characterized,[4,5] very few studies have been conducted on the electronic structure of molybdenum complexes possessing terminal sulfido or selenido ligands due to difficulties in synthesizing Mo≡Se/S compounds.[58,59] Only the $[WO/S/Se(S_2C_2Ph_2)_2]^{2-}$ series,[60] the $[MoO/S/Se(Adm)_2]^{-1}$ series,[61,62] the *trans*–$Mo(O/S/Se)_2(P–P)_2$ complex (P–P is either 1,2–bis(diphenylphosphino)ethylene or its ethane derivative) series,[63] and $MoO/S/Se(N(R)Ar)_3$ ($R = C(CD_3)_2CH_3$, $Ar = 3,5–C_6H_3Me_2$)[64] compounds with apical O/S/Se donors and the same supporting ligands have been synthesized and crystallographic characterized. Very few spectroscopic studies detailing the electronic structure as a function of the Mo≡E unit have been performed.[60,63] However, *trans*–$Mo(O/S/Se)_2(P–P)_2$ and $MoO/S/Se(N(R)Ar)_3$ complexes do not possess sulfur supporting ligands attached to the molybdenum ion possessing electron withdrawing or donating group that would allow for a study of the substituents effects on the reactivities and electronic structure of the complexes.

Recently, a series of square pyramidal Mo≡(O/S/Se) complexes that possess an identical supporting ligand, $[Mo^{IV}(O/S/Se)(L^H)_2]^{2–}$ ($L^H = L^{C4H8}$ = cyclohexene–1,2–dithiolate),[57,65-67] $[MoO/S/Se(L^{Ph})_2]^{2-}$ ($L^{Ph} = L^{S2C2Ph2}$ = 1,2–diphenyl–1,2–dithiolate),[57] and $[MoO/S/Se(L^{COOMe})_2]^{2-}$ (L^{COOMe} = 1,2–dicarbomethoxyethylene–1,2–dithiolate)[57] have been synthesized and crystallographically characterized. These complexes have made possible detailed investigations regarding the effects of the Mo≡E unit and ene-1,2-dithiolene on the spectroscopy and

reactivity of these complexes. In addition, the usefulness of these model compounds is due to the fact that they possess a square pyramidal geometry as found in the active site of reduced (Mo(IV)) formate dehydrogenase, nitrate reductase and arsenite oxidase enzymes. Therefore, we expect that spectroscopic and computation studies on these models will enhance our understanding of electronic structure contributions to reactivity in the enzymes.

In this chapter we have employed electronic absorption spectroscopy, resonance Raman spectroscopy, and DFT calculations in order to understand the effects of the O/S/Se terminal chalcogen and ene-1,2-dithiolene substituents on electronic structure and the nature of low energy ligand-field and charge transfer transitions in $[MoO(L^{H})_2]^{2-}$, $[MoO(L^{O})_2]^{2-}$, $[MoS/Se(L^{Ph})_2]^{2-}$, $MoO/S/Se(L^{COOMe})_2]^{2-}$, and their tungsten derivatives $[WO/S(L^{Ph})_2]^{2-}$. Similarities between these compounds and enzymes will allow for the development of detailed reactivity and electronic structure models for the formate dehydrogenase, nitrate reductase and arsenite oxidase enzymes.

2.2 Statement of the Problem

Arsenite oxidase, formate dehydrogenase and nitrate reductase enzymes all possess the same square pyramidal geometry as the model compounds under study. However the presences of iron-sulfur clusters in the enzymes make them difficult to probe spectroscopically. The synthesis and spectroscopic studies of model compounds with the same geometry as the reduced Mo(IV) active site will

provide considerable new information that will assist our understanding of the reactivities and electronic structure of the enzyme active sites. In these model compounds the effect of the apical chalcogen, the nature of the low energy ligand field and charge transfer transitions, and the effect of ene-1,2-dithiolene ligands on electronic structure are unknown.

2.3 Hypotheses

i. The strong interaction of multiply bonded O/S/Se apical ligands with molybdenum in bis-dithiolene Mo(IV) compounds has a pronounced effect on the electronic structure of the complexes.

ii. The electron withdrawing nature of L^{COOMe}, L^{Ph}, L^{ipro} and L^{meth} dithiolenes stabilizes Mo(IV) centers, while L^{H} and L^{O} ligands destabilize the Mo(IV) center.

iii. Low energy intraligand charge transfer transitions are anticipated for $Mo(O/S/Se)L^{COOMe}$, $Mo(S/Se)L^{Ph}$ and $MoOCl(L_2^{ipro/meth})$ compounds and low energy ligand field transitions are anticipated for $MoOL^{H}/L^{O}$ compounds due to the electron withdrawing or donating nature of ene-dithiolene substituted ligands, respectively.

2.4 Materials and Methods

All procedures were carried out under anaerobic conditions. Dry acetonitrile was obtained from Sigma-Aldrich and stored under molecular sieves in a glove box and used for electronic absorption measurements. $(Et_4N)_2[Mo^{IV}O(S_2C_2(COOMe)_2)_2]$ is abbreviated as $[MoO(L^{COOMe})_2]^{2-}$,

$(Et_4N)_2[Mo^{IV}S(S_2C_2(COOMe)_2)_2]$ is abbreviated as $[MoS(L^{COOMe})_2]^{2-}$, $(Et_4N)_2[Mo^{IV}Se(S_2C_2(COOMe)_2)_2]$ is abbreviated as $[MoSe(L^{COOMe})_2]^{2-}$, $(Et_4N)_2[Mo^{IV}S(S_2C_2Ph_2)_2]$ is abbreviated as $[MoS(L^{Ph})_2]^{2-}$, $(Et_4N)_2[Mo^{IV}Se(S_2C_2Ph_2)_2]$ is abbreviated as $[MoSe(L^{Ph})_2]^{2-}$, $(Et_4N)_2[W^{IV}O(S_2C_2Ph_2)_2]$ is abbreviated as $[WO(L^{Ph})_2]^{2-}$, $(Et_4N)_2[Mo^{IV}S(S_2C_2Ph_2)_2]$ is abbreviated as $[WS(L^{Ph})_2]^{2-}$, $(Ph_4P)_2[MoO(C_6H_8)_2]$ abbreviated as $[MoO(L^{H})_2]^{2-}$, $(Ph_4P)_2[MoO(C_5OH_6)_2]$ abbreviated as $[MoO(L^{O})_2]^{2-}$ and $(Ph_4P)_2[WO(C_6H_8)_2]$ abbreviated as $[WO(L^{H})_2]^{2-}$ were prepared and provided to us by Prof. Sugimoto from Osaka University. Whereas $[MoOCl(S_2C_{10}N_2H_{18})_2](PF_6)$ is abbreviated as $(MoOCl(L_2^{ipro}))$, $[MoOCl(S_2C_6N_2H_{10})_2](PF_6)$ is abbreviated as $(MoOCl(L_2^{meth}))$, and $[MoO(S_2C_{10}N_2H_{18})(S_2C_{12}H_{10})]$ abbreviated as $(MoO(L^{ipro})(SPh)_2)$ were synthesized and provided to us by Prof. P. Basu from Duquesne University. The following abbreviations will be used representing dithiolene throughout this chapter: L^{H} = cyclohexene-1,2-dithiolate, L^{O} = 2,3-dihydro-2H-pyran-4,5-dithiolate, L^{COOMe} = 1,2-dicarbomethoxyethylene-1,2-dithiolate, L^{Ph} = 1,2-diphenyl-1,2-dithiolate, L^{ipro} = 1,4-diisopropyl piperazine-2,3-dithione, L^{meth} = 1,4-dimethyl piperazine-2,3-dithione and L^{SPh} = benzenethiolate, respectively.

Electronic Absorption Spectroscopy

Room temperature electronic absorption spectra were collected under anaerobic conditions in an air sensitive 1cm cuvette using a Hitachi U-3501 UV-vis spectrophotometer, scanning a 180-3000 nm wavelength range. The spectral bands were resolved using the Grams/AI (7.02) software package.

Resonance Raman Spectroscopy

Solid-state resonance Raman (rR) data were collected using a Coherent Innova Ar^+ ion laser (453-528.7 nm) and a Coherent Innova 300C Kr^+ ion laser (406.7-676.4 nm) as photon sources. Solid state resonance Raman (rR) spectra and associated rR excitation profiles were collected using a system comprised of an PI/Acton SpectraPro SP-2556 500 mm focal length imaging spectrograph with a triple grating turret and a PI/Acton Spec-10:100B back-illuminated 1340 x 100 pixel digital CCD spectroscopy system with a cryogenically cooled camera head. Low laser powers below ~100 mW were used to prevent any photo- or thermal degradation of the sample. Solid samples were prepared as fine-grounded powders dispersed in $NaCl/Na_2SO_4$ with Na_2SO_4 as an internal standard. Resonance Raman excitation profiles were collected using Kr^+ laser lines at 407, 568 and 647nm and Ar^+ laser lines at 458, 488 and 514 nm for all Mo / W (IV) bis-dithiolene samples. All rR peaks were normalized with respected to the 992 cm^{-1} Na_2SO_4 peak.

Computational details

Density Functional Theory calculations were performed using the Gaussian 03W program. Model compound calculations were accomplished using a hybrid B3LYP functional with a 6-31G* basis set for carbon, oxygen and sulfur and the effective core potential basis sets LANL2DZ and LANL2 were used for molybdenum and tungsten. Model compound geometry optimizations were performed in spin-restricted mode (B3LYP). The lowest-energy excited states for

the model compounds were computed using time-dependent density functional theory (TD-DFT) as implemented in the Gaussian 03W program.

2.5 1,2–Dicarbomethoxyethylene–1,2–dithiolate (L^{COOMe}) Molybdenum Compounds

Compounds and X-ray crystallographic data for the $[MoO/S/Se(L^{COOMe})_2]^{2-}$ series of compounds have been provided by Prof. Sugimoto, and they possess the same basic geometry as the active sites of reduced arsenite oxidase, formate dehydrogenase and nitrate reductase enzymes. The $[MoO/S/Se(L^{COOMe})_2]^{2-}$ compounds (Figure 2.1) have a square pyramid geometry with two dithiolenes (L^{COOMe}) in the equatorial position attached to the molybdenum center and O/S/Se ligands at the apical position. The molybdenum atom is displaced above the basal plane by 0.71 Å [68] for $[MoO(L^{COOMe})_2]^{2-}$, by 0.80 Å for $[MoS(L^{COOMe})_2]^{2-}$ and by 0.79 Å for $[MoSe(L^{COOMe})_2]^{2-}$,[57] and these values are close to the 0.80 Å displacement observed in the active site of reduced arsenite oxidase.[6] Also the model compound crystal structures have equatorial Mo-S bonds that average as 2.38, 2.37 and 2.36 Å for the $[MoO/S/Se(L^{COOMe})_2]^{2-}$ compounds, and this is similar to the 2.37 and 2.30 Å Mo-S bond distances reported for the active sites of arsenite oxidase[7] and formate dehydrogenase[35] respectively. Although the presence of the L^{COOMe} ligands lowers the overall symmetry of these complexes to C_1, the complexes maintain effective C_{2V} symmetry for the first coordination sphere.

Several spectroscopic studies have been performed on mono-oxo dithiolenes but considerably fewer studies have been directed toward the electronic structure of molybdenum complexes possessing terminal sulfido or selenido coordination. Therefore, this section details the effects of the apical chalcogen ligands and the equatorial 1,2-ene dithiolene (L^{COOMe}) ligands on the nature of charge transfer transitions in order to develop an understanding of arsenite oxidase and nitrate reductase electronic structure in their reduced forms. This is accomplished by employing a combined spectroscopic approach coupled with detailed bonding calculations.

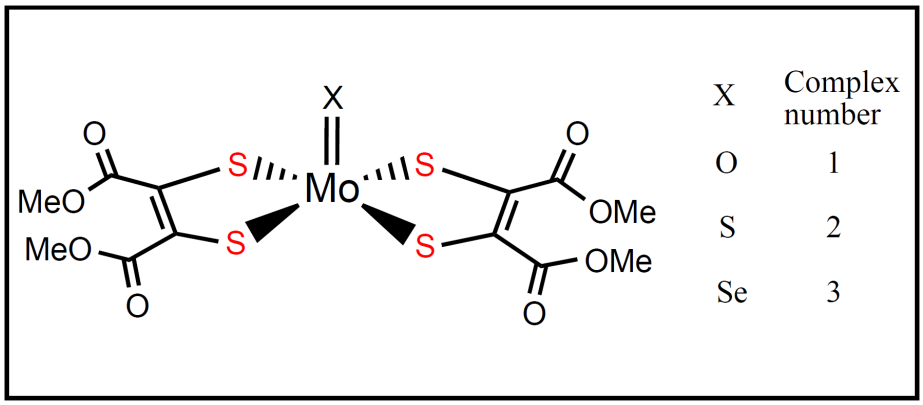

Figure 2.1: Structure of $[MoX(L^{COOMe})_2]^{2-}$ complexes.

2.5.1 Results and Analysis

2.5.1.1 The Effect of Apical Chalcogens on the Spectral Shift in the Low Energy Charge Transfer Region

Formate dehydrogenase and arsenite oxidase enzymes have been the center of this study due to the presence of apical oxygen, sulfido or selenido ligands in their Mo(IV) reduced form. Therefore, a series of $[MoO(L^{COOMe})_2]^{2-}$, $[MoS(L^{COOMe})_2]^{2-}$ and $[MoSe(L^{COOMe})_2]^{2-}$ compounds have been synthesized to mimic the active sites of these enzymes. Room temperature electronic absorption spectra overlays for the $[MoO/S/Se(L^{COOMe})_2]^{2-}$ series in the 8000 cm^{-1} to 37,000 cm^{-1} energy region are displayed in Figure 2.2. Each spectrum shows similar features but differs in the energy position of the observed bands. In all three compounds the spectra can be divided into three parts; a weak band region below 16,000 cm^{-1}, a well resolved region between 16,000 and 29,000 cm^{-1} and a region of high intensity transitions with extinction coefficients over 10,000 $M^{-1}cm^{-1}$ at energies above 29,000 cm^{-1}. A summary of the energies of the observed bands are provided in Table 2-1.

The low energy bands have very low intensity with extinction coefficients below 200 $M^{-1}cm^{-1}$ and their peak maxima are observed at 13,220 cm^{-1} for $[MoO(L^{COOMe})_2]^{2-}$, 14,330 cm^{-1} for $[MoS(L^{COOMe})_2]^{2-}$ and at 13,750 cm^{-1} for $[MoSe(L^{COOMe})_2]^{2-}$. No clear trend on band energies is observed with regard to the O/S/Se apical ligands. This suggests no contribution to these transitions

from the apical ligands and that the low energy excited states may possess considerable L^{COOMe} ligand character.

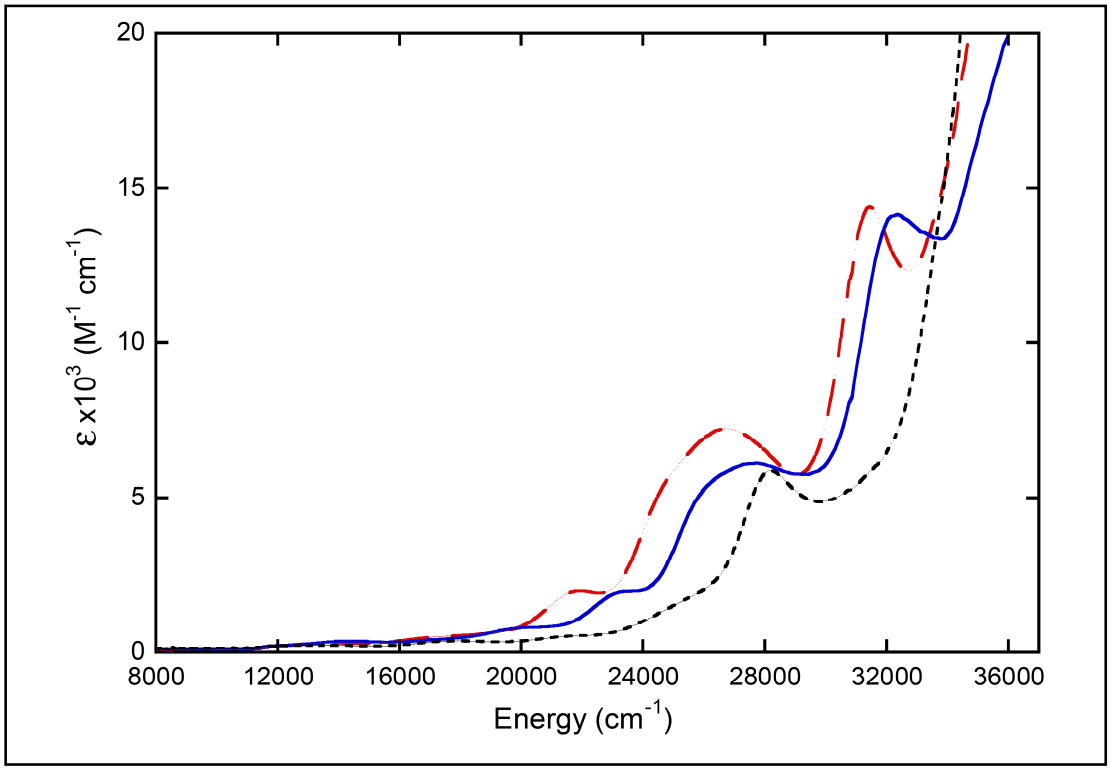

Figure 2.2: Room temperature electronic absorption spectra of $[MoO(L^{COOMe})_2]^{2-}$ (– – –), $[MoS(L^{COOMe})_2]^{2-}$ (– · –) and $[MoSe(L^{COOMe})_2]^{2-}$ (——) showing a progressive decrease in energy as the function of terminal chalcogen ligands.

The second region of the spectra displays a clear bands shift to lower energy with O > S > Se. Below the 29,000 cm^{-1} energy region, three well resolved peaks are observed for each compound with extinction coefficients below 8000 $M^{-1}cm^{-1}$. An intense peak in this region occurs at 28,200 cm^{-1} (~6000 $M^{-1}cm^{-1}$) for $[MoO(L^{COOMe})_2]^{2-}$, at 27,700 cm^{-1} ($\varepsilon \approx 6100$ $M^{-1}cm^{-1}$) for $[MoS(L^{COOMe})_2]^{2-}$ and at

26,700 cm^{-1} ($\varepsilon \approx 7300\ M^{-1}cm^{-1}$) for $[MoSe(L^{COOMe})_2]^{2-}$. The observed energy shift between 500-1500 cm^{-1} is slightly higher than what was reported for $[Mo(XAd)(dmdt)_2]^-$ compounds (X= O, S, Se) (500-1000 cm^{-1}). The observed decrease in transition energy is due to electronegativity effects and the valence ionization energy of the apical chalcogen ligands according to O > S > Se. The apical ligands (O, S, Se) have three p-orbitals that can interact with the five molybdenum d-orbitals. The oxygen p-orbital interacts strongly with Mo d_{z^2} and $d_{xz/yz}$ orbitals through a sigma (σ) and two pi (π) bonds due to its strongly electronegative nature which decreases according to O>S>Se. The stronger σ and π apical ligand interactions with the metal d-orbitals lead to a destabilization of the metal d-orbitals as shown in Figure 2.3. These results are supported by the length of the Mo≡E (E=O/S/Se) bond in the model compound crystal structures and in computational modeling of their structures which show Mo≡O bond lengths of 1.686 Å (*1.709* Å), Mo≡S at 2.150 Å (*2.160* Å) and Mo≡Se at 2.290 Å (*2.298* Å) [57] confirming a strong Mo-oxygen interaction and a weaker Mo-selenium bonding interaction.

Table 2-1: Summary of the Gaussian resolved electronic absorption band maxima (cm^{-1}) for the $[MoO/S/Se(L^{COOMe})_2]^{2-}$ complexes

Band	$MoO(LCOOMe)_2$	$MoS(LCOOMe)_2$	$MoSe(LCOOMe)_2$
1	12 260	12 800	12850
2	14 058	14 560	14520
3	17 690	17 260	17150
4	21 900	20 250	19860
5	24 764	23 430	21880
6	28 200	25 920	24980
7	29 990	27 620	27110
8	31 690	29 600	29330
9	33 700	32 340	31540
10	35 220	33 810	33440
11	37 090	35 000	35370

Higher energy charge transfer transitions are expected for oxygen ligation and this result in a larger observed d-orbital splitting which decreases progressively with sulfur and selenium ligation. In terms of valence ionization energies, selenium has larger radial distribution function which correlates with an electron that is easier to remove from the valence shell when compared to O or S. The highly electronegative terminal oxygen possesses a high valence ionization energy which correlates with an electron that is harder to remove from the valence shell. The higher energy regions of the spectra do not display as clear a trend in the band energies as the middle region, and this indicates the absence of an appreciable apical ligand contribution. However the higher intensity of these bands indicates that they do possess considerable charge transfer character.

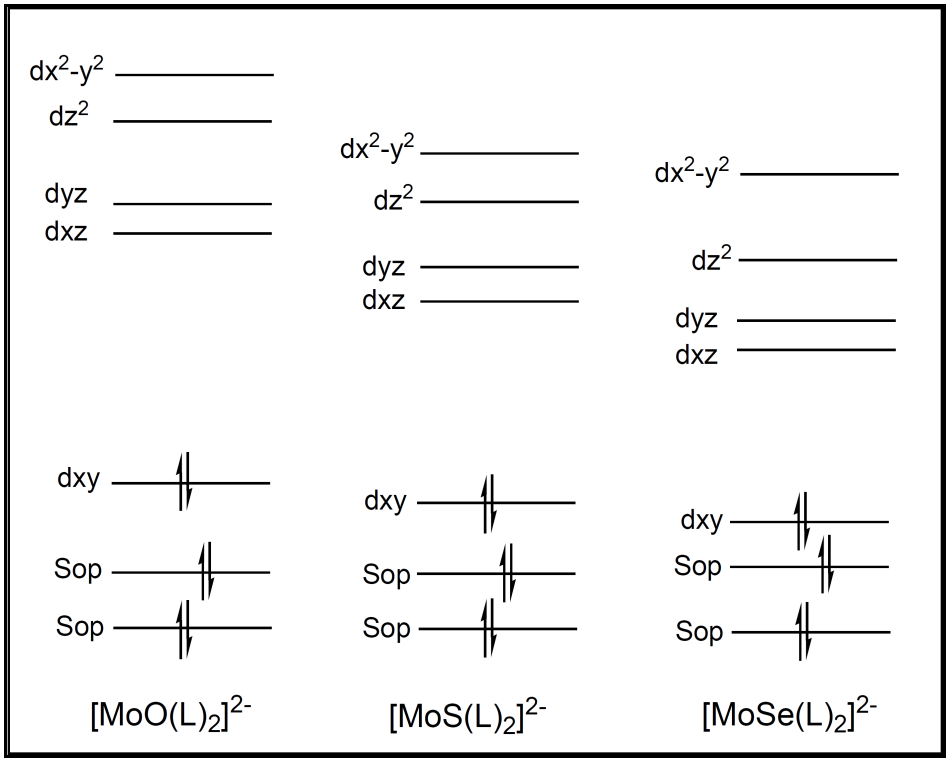

Figure 2.3: Molecular orbital diagrams showing the metal-ligand multiple bonding effects on orbital splitting in MoO(L), MoS(L) and MoSe(L) compounds.

2.5.1.2 Molecular Orbital Description and the Effect of Ene-1,2-dithiolene L^{COOMe} Ligand

A typical metal-ligand multiple bond results in a splitting pattern similar to what is observed in Figure 2.3,[56,69,70] but the presence of the L^{COOMe} ligand in the model compounds under study also has a significant effect on the splitting pattern. Figure 2.4 shows the molecular orbital energy diagram obtained from a fully optimized geometry calculation for the $[MoO/S/Se(L^{COOMe})_2]^{2-}$ complexes.

Bonding calculations were performed on fully optimized geometries of the $[MoO/S/Se(L^{COOMe})_2]^{2-}$ complexes and analyzed using the AOMix program. The results show that the Mo-d_{xy} redox orbital is the HOMO orbital with ~80% Mo character. This observation is similar across the series and the HOMO does not possesses apical ligand character. The LUMO orbital for the $[MoO(L^{COOMe})_2]^{2-}$ compound contains 80% dithiolene orbital character with C=Cπ^* (L^{COOMe} ligand) character, however in the $[MoS(L^{COOMe})_2]^{2-}$ compound, the LUMO possesses 22% Mo-d_{yz}, 14% apical Sπ^* and 57% L^{COOMe} ligand character whereas in $[MoSe(L^{COOMe})_2]^{2-}$ complex the same orbital contains 26% Mo-d_{yz}, 14% apical Seπ^* and 51% L^{COOMe} ligand character. This result shows that for $[MoO(L^{COOMe})_2]^{-}$ the LUMO orbital possesses dominant dithiolene ligand character while an admixture of Mo-d_{yz}, L^{COOMe} ligand and an apical Sπ^*/Seπ^* ligands character is present in $[MoS(L^{COOMe})_2]^{2-}$ and $[MoSe(L^{COOMe})_2]^{2-}$ compounds. The percentage composition of Mo-d_{yz} and apical Sπ^*/Seπ^* character contained in the LUMO orbital decreases according to Se > S > O. The L^{COOMe} ligand character in the LUMO+1 is 82%, 81% and 77% for $[MoO(L^{COOMe})_2]^{2-}$, $[MoS(L^{COOMe})_2]^{2-}$ and $[MoSe(L^{COOMe})_2]^{2-}$ respectively. Figure 2.5 displays the frontier molecular orbital contour plots for $[MoO/S/Se(L^{COOMe})_2]^{2-}$ complexes showing the ligand and metal based orbital characters. The presence of L^{COOMe} ligand character in the LUMO and LUMO+1 orbitals is due to the electron withdrawing nature of the L^{COOMe} ligand, which acts as an electron acceptor. In addition, the rRaman data in Figure 2.7 shows strong υ(C-C & C-O),

υ(C=C) and υ(C=O) stretches with excitation into low energy bands that supports the presence of L^{COOMe} ligand character in the LUMO and LUMO+1 orbitals.

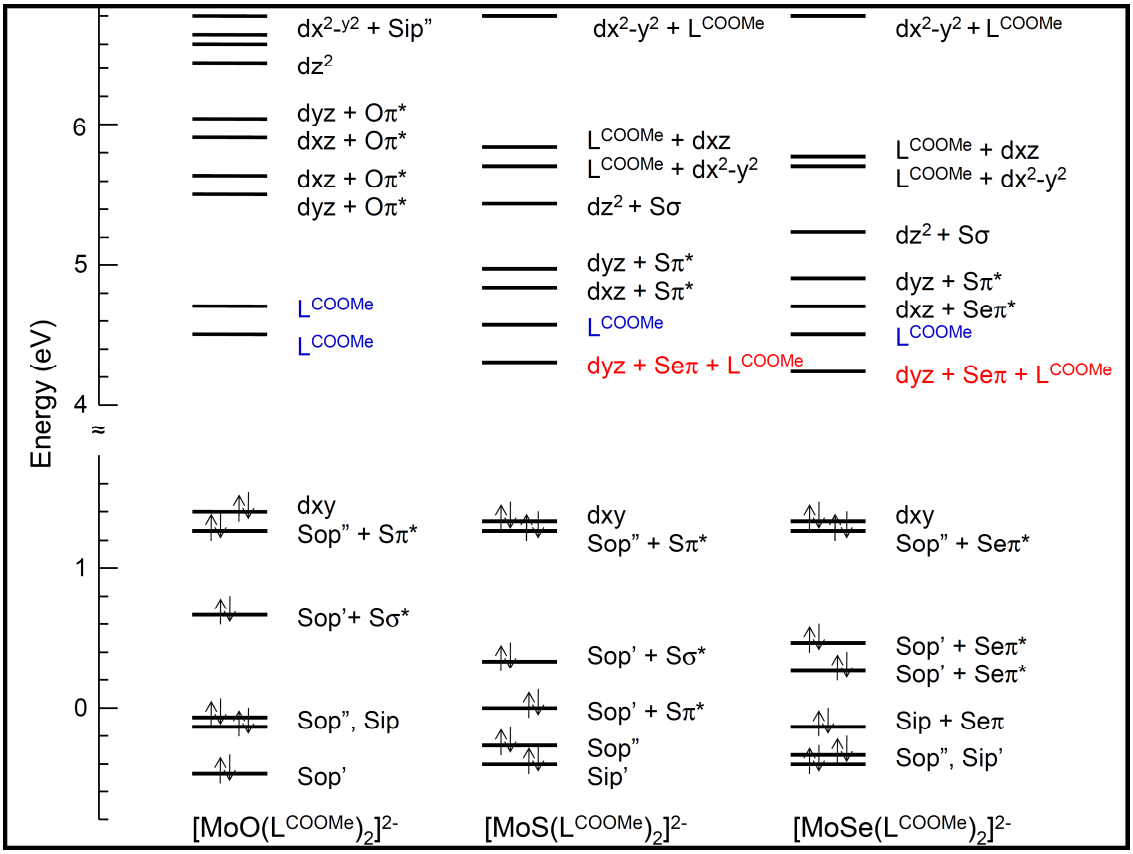

Figure 2.4: Molecular orbital energy description resulting from DFT calculation showing the effect of L^{COOMe} ligand in the $[MoO/S/Se(L^{COOMe})_2]^{2-}$ compounds.

The LUMO+2 and LUMO+3 orbitals possess Mo-d_{xz} and Mo-d_{yz} orbital character with apical E (E = Oπ*/Sπ*/Seπ*) ligand character. The presence of Mo-d_{xz}/d_{yz} character has been confirmed using rRaman excitation profiles which show a strong enhancement of υ(Mo≡O), υ(Mo≡S) and υ(Mo≡Se) stretches when pumping into these higher energy bands. In summary, these results suggest the

possibility of low-energy MLCT transitions in [MoO/S/Se(L^{COOMe})$_2$]$^{2-}$ compounds that results from low-energy acceptor orbitals with significant dithiolene ligand character that reside in between the highest occupied Mo-d_{xy} orbital and other unoccupied Mo(IV) d-orbitals.

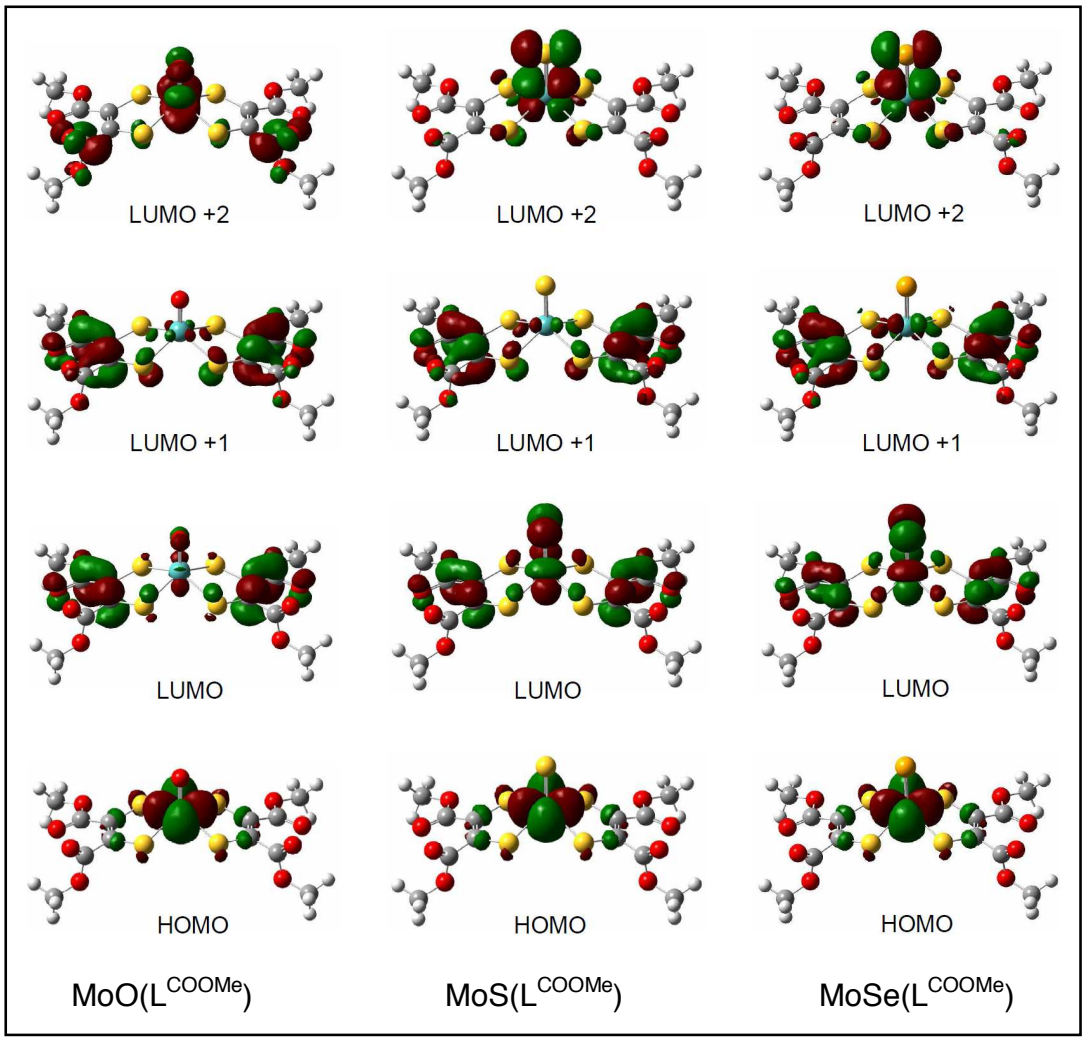

Figure 2.5: Frontier molecular orbital contour plots resulting from DFT calculations that show the relative metal and ligand character in these orbitals for the [MoO/S/Se(L^{COOMe})$_2$]$^{2-}$ complexes.

2.5.1.3 The Low Energy MLCT, Intraligand Charge Transfer, Ligand Field and Band Assignments

Time dependent density functional theory (TD-DFT) and frequency calculations have been performed on fully optimized geometries and combined with resonance Raman (rR) and electronic absorption spectroscopies in order to study the nature of charge transfer transition and to make proper band assignments. Room temperature Gaussian resolved electronic absorption spectra for $[MoO(L^{COOMe})_2]^{2-}$, $[MoS(L^{COOMe})_2]^{2-}$ and $[MoSe(L^{COOMe})_2]^{2-}$ compounds are displayed in Figure 2.6. Gaussian resolved spectra for these compounds show that there are 11-12 bands that occur in the 12,000 – 37,000 cm^{-1} spectral region.

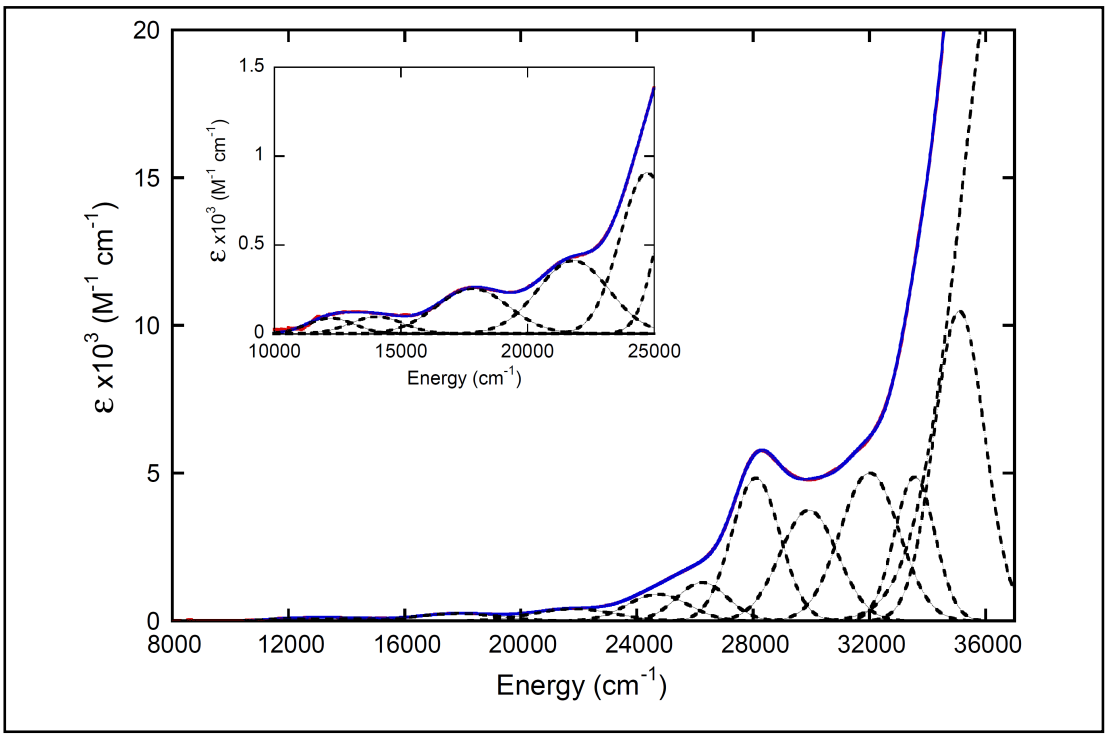

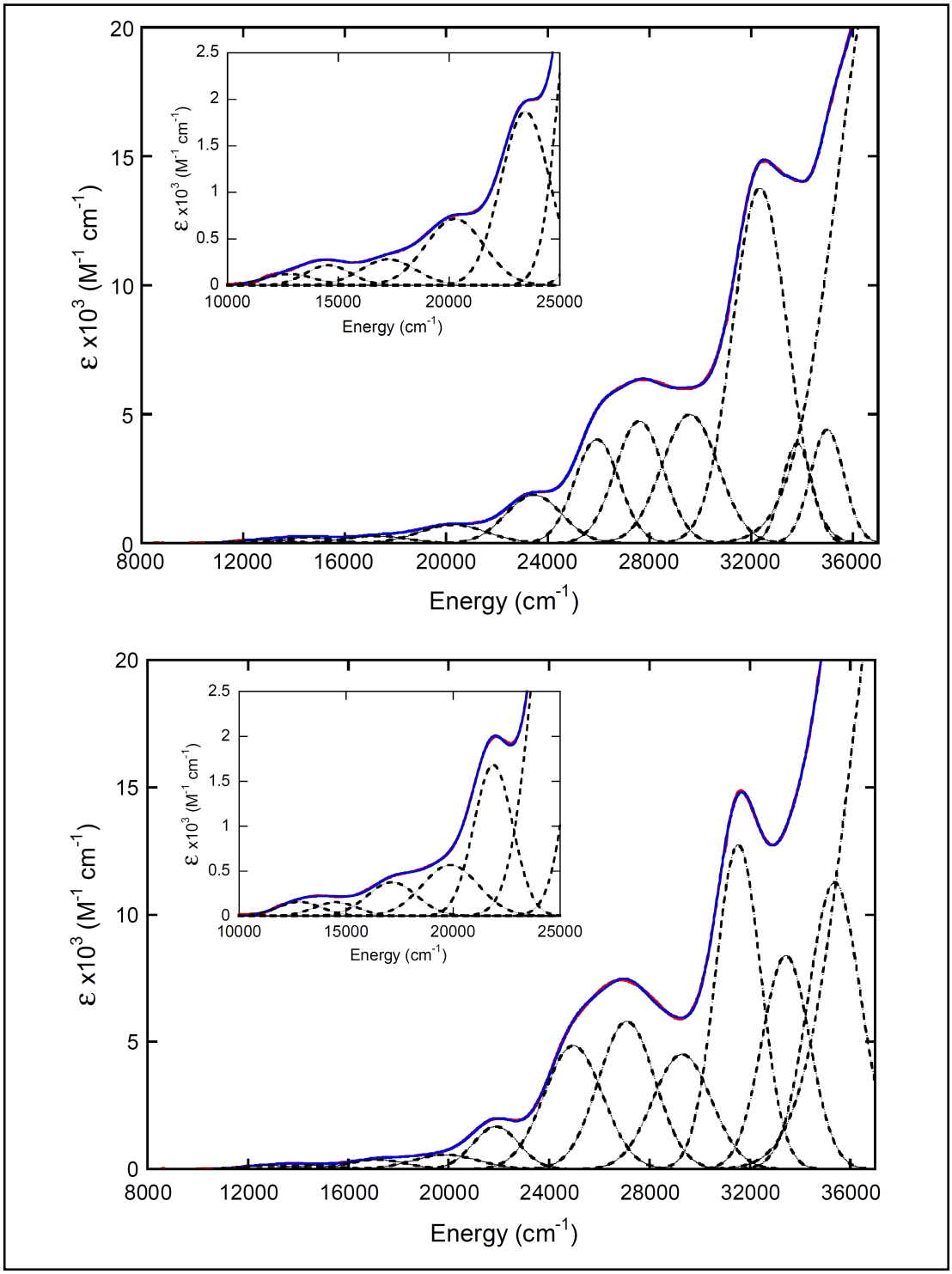

Figure 2.6: Gaussian resolved room temperature electronic absorption spectra for $[MoO(L^{COOMe})_2]^{2-}$, $[MoS(L^{COOMe})_2]^{2-}$ and $[MoSe(L^{COOMe})_2]^{2-}$ compounds. The insert is the expansion of the low energy spectral region.

The low energy spectral region below 16,000 cm^{-1} in $[MoO/S/Se(L^{COOMe})_2]^{2-}$ compounds possesses two bands with very low intensity (~200 M^{-1} cm^{-1}) that lack a progressive energy shift as observed in the higher energy region (insert Figure 1.6).

Band 1 and 2: Band 1 is assigned as the HOMO → LUMO transition and Band 2 as the HOMO → LUMO+1 transition. These transitions possess Mo-d_{xy} character in the HOMO and L^{COOMe} ligand character in both the LUMO and LUMO+1 orbitals for the $[MoO(L^{COOMe})_2]^{2-}$ compound. These are low energy metal to ligand charge transfer transitions (LMCT) and their assignments are supported by the nature of the rR excitation profiles which show enhancement of υ(C-O + C-C), υ(C=C) and υ(C=O) stretches, but no resonance enhancement of υ(Mo-$S_{dithiolene}$) or υ(Mo≡O) (Figure 2.7). Bonding calculation results show that the HOMO orbital (Mo-d_{xy}) does not possess oxo character, which is confirmed by rRaman data that reveal the absence of a υ(Mo≡O) stretch. This indicates a minimal admixture of Mo-d_{xz} and d_{yz} with Oπ^* character in the LUMO and LUMO+1 ligand-based orbitals. The presence of low energy metal to ligand charge transfer (MLCT) indicates a possible electron transfer pathway in enzymes that possess electron deficient dithiolenes since the LUMO and LUMO+1 orbitals possess dominant ligand character and occur at low energy.

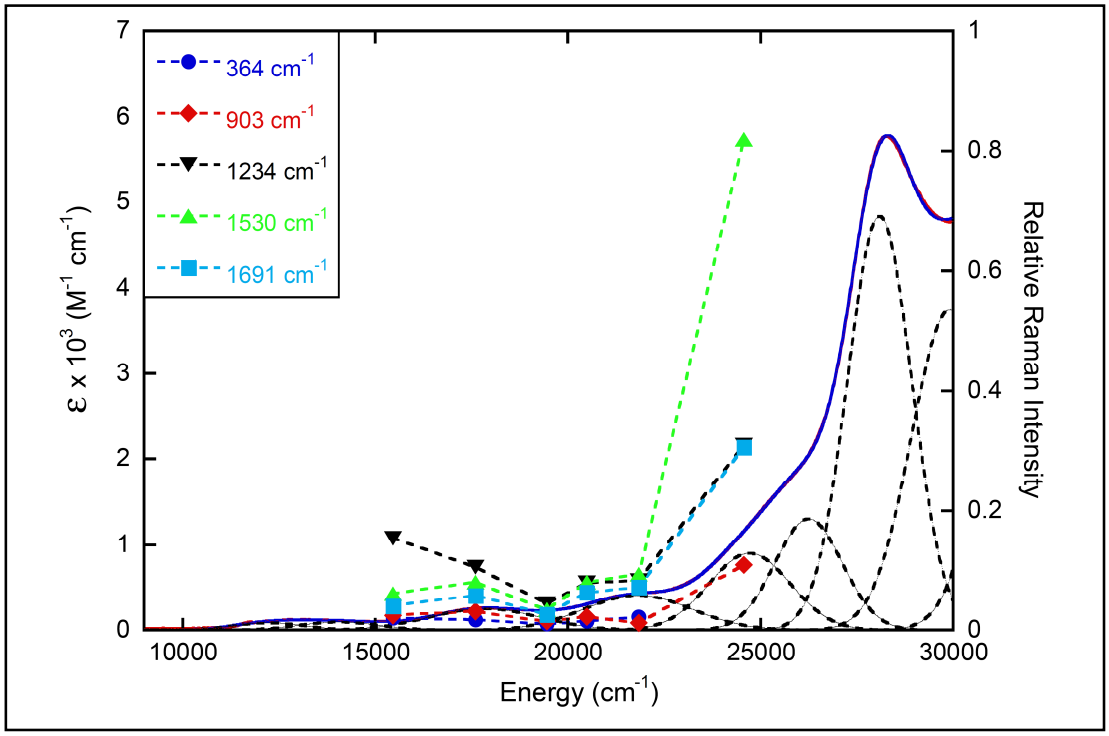

Figure 2.7: Resonance Raman excitation profiles for $[MoO(L^{COOMe})_2]^{2-}$ showing $\upsilon(Mo\text{-}S_{dithiolene})$ at 364 cm^{-1}, $\upsilon(Mo{\equiv}O)$ at 903 cm^{-1}, $\upsilon(C\text{-}C + C\text{-}O)$ at 1234 cm^{-1}, $\upsilon(C{=}C)$ at 1530 cm^{-1} and $\upsilon(C{=}O)$ stretch at 1691 cm^{-1}.

Band 3 and 4: These bands are assigned as the HOMO-1→LUMO and HOMO-1→LUMO+1 transitions respectively. The HOMO-1 possesses sulfur out of plane ($S_{op"}$) orbital character and is non bonding with respect to the metal ion, while the LUMO and LUMO+1 have L^{COOMe} ligand character. Therefore, we expect enhancement of $\upsilon(C\text{-}O + C\text{-}C)$, $\upsilon(C{=}C)$ and $\upsilon(C{=}O)$ vibrations, and not the $\upsilon(Mo\text{-}S_{dithiolene})$ stretch. The resonance Raman excitation profile shown in Figure 2.7 indicates enhancement of $\upsilon(C\text{-}O + C\text{-}C)$, $\upsilon(C{=}C)$ and $\upsilon(C{=}O)$ stretches and adds additional support to our assignment. These two transitions are intraligand in

nature with charge transfer from the dithiolene sulfurs to the carbon backbone of the ligand. The nature of the intraligand charge transfer is apparent in the electron density difference map (EDDM) constructed for the HOMO-1→LUMO and HOMO-1→LUMO+1 transitions (Figure 2.8). The effect of electron withdrawing L^{COOMe} dithiolene substituents is evident in the intraligand charge transfer bands in $[MoO(L^{COOMe})_2]^{2-}$ complexes.

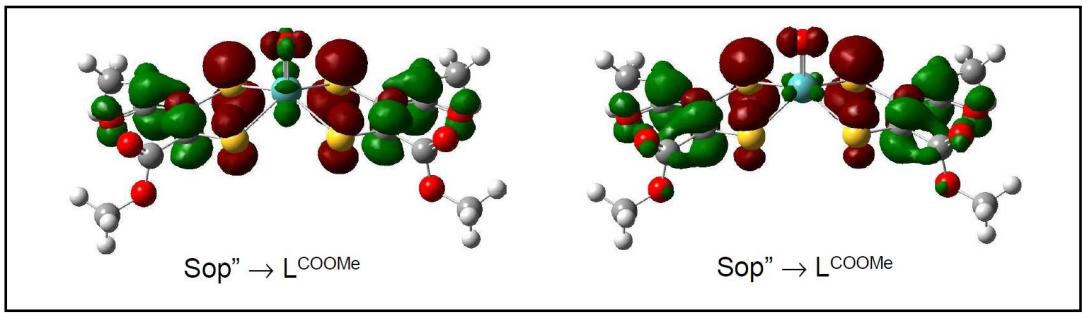

Figure 2.8: Electron density difference maps (EDDMs) showing the nature of the intraligand charge transfer for bands 3 and 4, where red indicates electron density loss, and green indicates an electron density gain in the transition.

Band 5 and 6: A combination of HOMO-2 → LUMO and HOMO-1 → LUMO+2 transitions are assigned for band 5 whereas band 6 is assigned as arising from a HOMO-2 → LUMO+3 excitation. Both HOMO-1 and HOMO-2 possess sulfur out of plane (S_{op}) character with C=Cπ^* character, and are non bonding with respect to the metal. The LUMO has L^{COOMe} ligand character while the LUMO+2 and LUMO+3 have Mo-d_{xz}, $d_{yz,}$, and Oπ^* character. The intensity increase observed in the electronic absorption spectrum indicates a mixture of intraligand charge transfer and ligand to metal charge transfer (LMCT) transitions which are

supported by rRaman data that shows strong resonance enhancement of total symmetric υ(Mo=O), υ(C-O + C-C), υ(C=C) and υ(C=O) stretches. The nature of the intraligand and LMCT transitions are clearly apparent in the electron density difference maps (EDDM) constructed for the HOMO-2→LUMO and HOMO-1→LUMO+2 transitions (Figure 2.9).

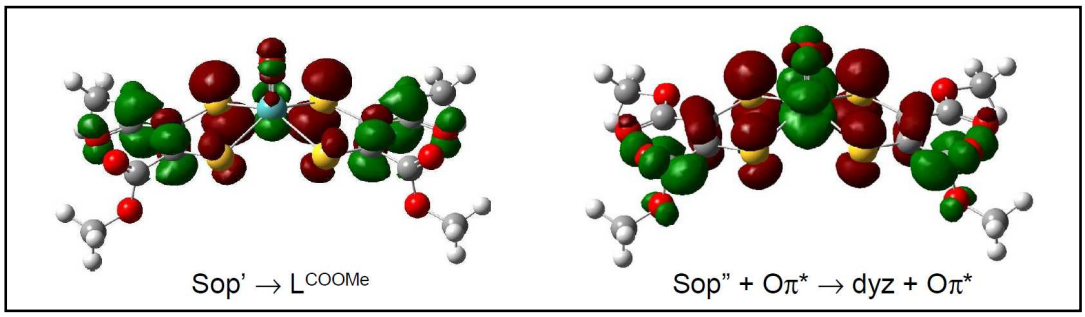

Figure 2.9: Electron density difference map (EDDMs) showing the nature of ligand to metal charge transfer (LMCT) for band 5, where red indicates electron density loss, and green indicates an electron density gain in the transition.

The lack of resonance Raman excitation laser lines at higher energy complicates the higher energy charge transfer assignments. Therefore, tentative band assignments have been made for bands 7, 8, 9, 10 and 11 based on calculated oscillator strengths obtained from excited state time dependent DFT calculations. Figure 2.10 displays a TD-DFT bar diagram showing oscillator strengths at their respective energy for $[MoO(L^{COOMe})_2]^{2-}$.

Band 7: Band 7 is assigned as the HOMO-2 → LUMO+2 transition with an 0.0177 oscillator strength. The HOMO-2 orbital contains symmetric $S_{op'}$ ligand

character while the d_{yz} with Oπ* character is present in the LUMO+2 orbital. The intensity of this band is consistent with the LMCT transition assignment.

Band 8: A combination of one-electron promotions from HOMO-4 → LUMO+1 and HOMO-3 → LUMO comprise Band 8, which possesses a 0.2138 oscillator strength. These one electron promotions involve highly stabilized sulfur in plane ($S_{ip'}$) character in the HOMO-4 and asymmetric $S_{op"}$ character in the HOMO-3 orbital, while the L^{COOMe} ligand character is present in both the LUMO and LUMO+1 orbitals.

Band 9 and 10: These are higher energy bands assigned as HOMO-6 → LUMO+1 and HOMO-5 → LUMO+1 transitions, with asymmetric $S_{ip"}$ character in the HOMO-6 and symmetric S_{op} character in the HOMO-5 orbital, while the LUMO+1 orbital contains L^{COOMe} ligand character. Band 9 has an oscillator strength of 0.0097 while band 10 has an oscillator strength of 0.1441. Since bands 8, 9 and 10 involve the same acceptor orbital (LUMO+1), band 9 can borrow its intensity from bands 8 and 10. The intensities of these bands are in good agreement with the calculated oscillator strengths, and this support their assignment as LMCT transitions.

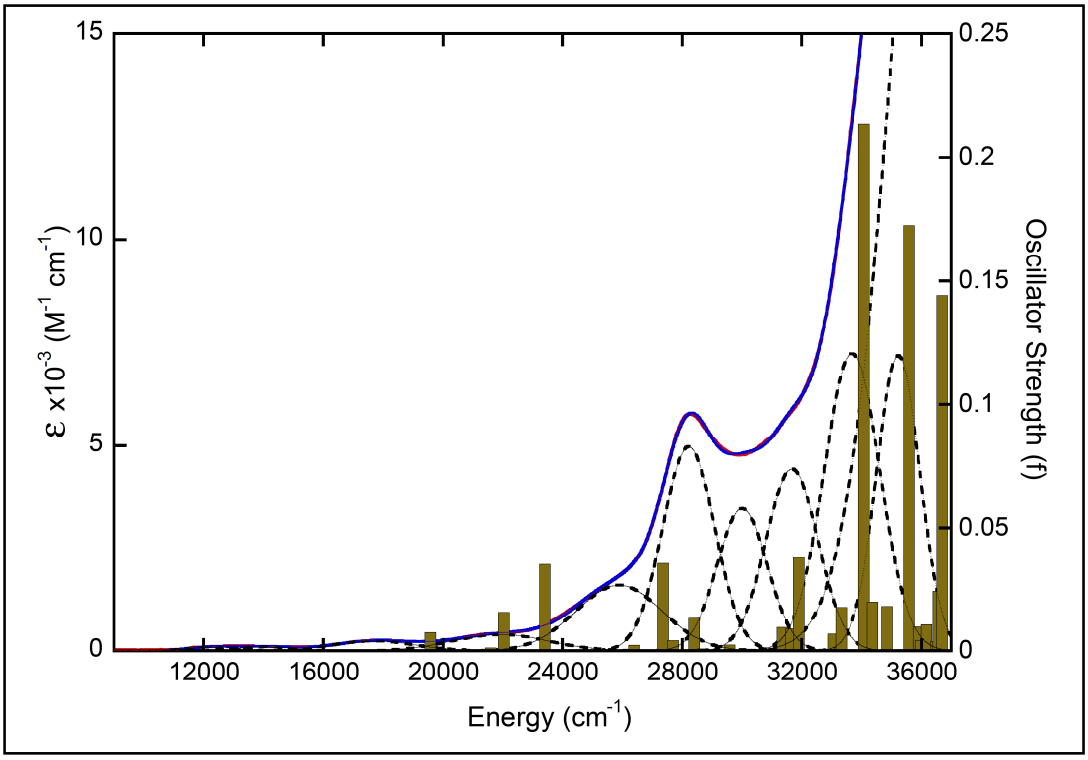

Figure 2.10: TD-DFT bar diagram for $[MoO(L^{COOMe})_2]^{2-}$ showing transition states oscillator strength (f) at their respective energy.

The $[MoS(L^{COOMe})_2]^{2-}$ and $[MoSe(L^{COOMe})_2]^{2-}$ compounds have similar electronic structures and due to this, their band assignments will be discussed together.

Band 1 and 2: These are ligand field transitions and are assigned as HOMO → LUMO for band 1 and HOMO → LUMO+2 for band 2. The HOMO contains Mo-dxy character while the LUMO possesses Mo-d_{yz} + Sπ*/Seπ* + L^{COOMe} ligand character. Mo-d_{xz} + Sπ*/Seπ* character is present in the LUMO+2 orbital. This assignment is strongly supported by the nature of the rRaman excitation profiles that show enhancement of υ(Mo≡S/Se), υ(C-C + C-O) and υ(C=C) stretches and not the υ(Mo-$S_{dithiolene}$) stretch (Figure 2.11). Similarity in the ligand field

strengths for apical sulfido and selenido donors in $[MoS(L^{COOMe})_2]^{2-}$ and $[MoSe(L^{COOMe})_2]^{2-}$ compounds is evidently in the small energy splitting observed for bands 1 and 2 coupled with their similar band energies. Therefore, the low intensity present in the electronic absorption spectrum for bands 1 and 2 indicates a ligand field transition.

Band 3 and 4: Band 3 is the first LMCT band with some intraligand charge transfer character and is assigned as the HOMO-1 → LUMO transition. Asymmetric $S_{op"}$ + $S\pi^*/Se\pi^*$ character is present in the HOMO-1 while the LUMO orbital possesses Mo-d_{yz} + $S\pi^*/Se\pi^*$ + L^{COOMe} character. However, a combination of HOMO → LUMO+1 and HOMO-1 → LUMO+2 transitions are assigned for band 4 which contains Mo-d_{xy} character in the HOMO and asymmetrical $S_{op"}$ + $S/Se\pi^*$ characters in HOMO-1 whereas LUMO possesses d_{xz} + $S/Se\pi^*$ characters and L^{COOMe} ligand character is present in LUMO+1 orbital. These transitions are manifested in the electron density difference map (EDDM) constructed in Figure 2.12. Additionally, this assignment is supported by rRaman excitation profiles which show enhancement of both υ(Mo-$S_{dithiolene}$), υ(C-C + C-O) and υ(C=C) modes in the $[MoSe(L^{COOMe})_2]^{2-}$ compound. Interestingly, the υ(Mo≡Se) vibrational enhancement become strong with excitation under band 3 and the enhancement increases as one pumps into band 4. This likely result from a higher contribution of the HOMO-1 → LUMO+2 transition in band 4 compared to the HOMO → LUMO+1 transition.

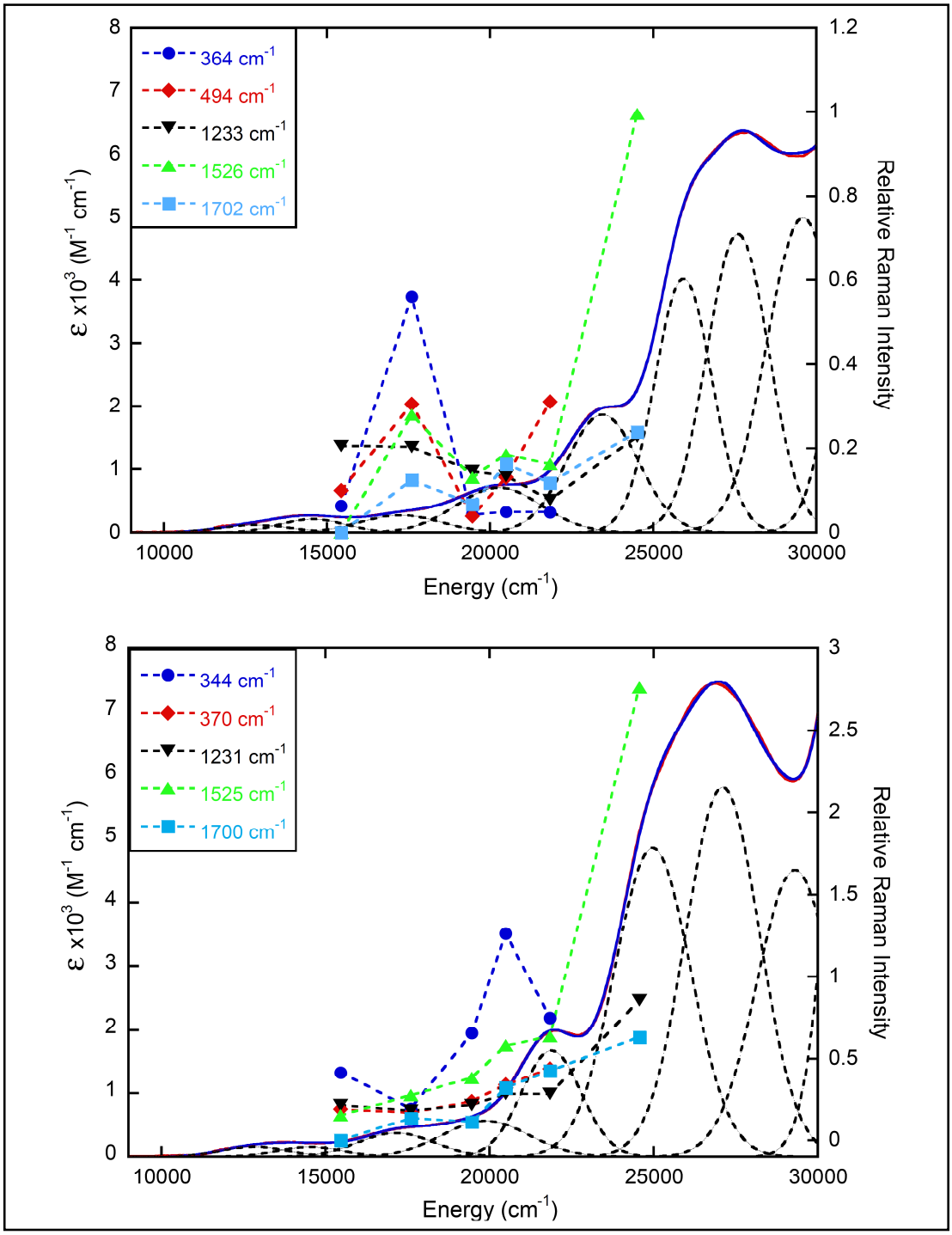

Figure 2.11: Resonance Raman excitation profiles spectra for $[MoO/S/Se(L^{COOMe})_2]^{2-}$ compounds. Top: $[MoS(L^{COOMe})_2]^{2-}$ Shows υ(Mo-$S_{dithiolene}$) at 364 cm^{-1}, υ(Mo≡S) at 494 cm^{-1}, υ(C-C + C-O) at 1233 cm^{-1}, υ(C=C) at 1526

cm^{-1} and υ(C=O) stretch at 1702 cm^{-1}. Bottom: $[MoSe(L^{COOMe})_2]^{2-}$ shows υ(Mo-$S_{dithiolene}$ + Mo≡Se) at 370 cm^{-1}, υ(Mo≡Se + Mo-$S_{dithiolene}$) at 344 cm^{-1}, υ(C-C + C-O) at 1231 cm^{-1}, υ(C=C) at 1525 cm^{-1} and υ(C=O) stretch at 1700 cm^{-1}.

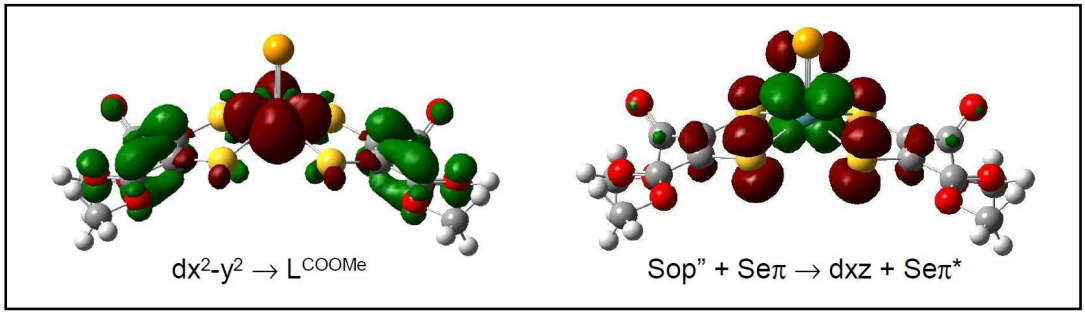

Figure 2.12: Electron density difference map (EDDMs) showing the nature of metal to ligand charge transfer (MLCT) and ligand to metal charge transfer (LMCT) for band 4, where green indicates electron density gain, and red indicates electron density loss in transition.

Band 5: Band 5 is assigned as combination of one-electron promotions from HOMO-1 → LUMO+1 and HOMO-1 → LUMO+3 transitions. Since HOMO-1 possesses asymmetric $S_{op"}$ + Sπ*/Seπ* character, LUMO+1 has L^{COOMe} ligand character, and LUMO+3 has Mo-d_{yz} + Sπ*/Seπ* character, we anticipate a strong enhancement of C=C, C=O and Mo≡S/Se vibrations, and this is what is observed in the rRaman excitation profile in Figure 2.11 confirming the assignment. The EDDMs for the two transitions that principally contribute to this band in $[MoS(L^{COOMe})_2]^{2-}$ and $[MoSe(L^{COOMe})_2]^{2-}$ are given in Figure 2.13. In addition the observed progressive shift of this band to higher energies is due to apical ligand

E → Mo charge transfer character present in these transitions as the result of increasing electronegativity and an increase in valence ionization energy of apical E donor.

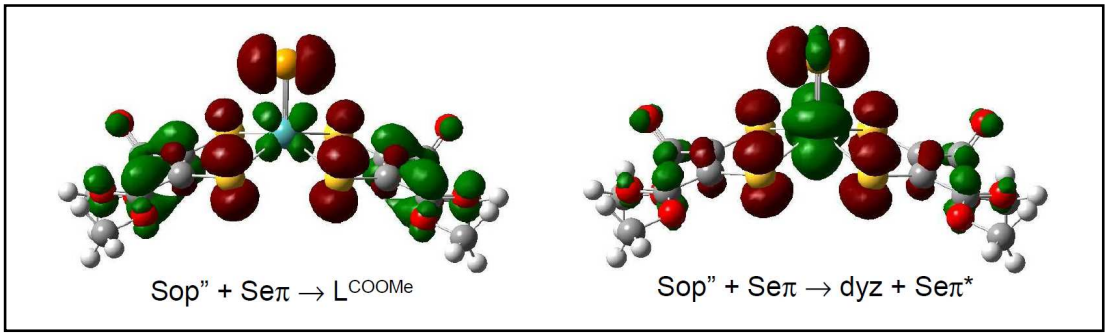

Figure 2.13: Electron density difference map (EDDMs) showing the nature of intraligand charge transfer and ligand to metal charge transfer (LMCT) for band 5, where green indicates electron density gain, and red indicates electron density loss in transition.

Band 6 and 7: Bands 6 and 7 are assigned as HOMO-3 → LUMO and HOMO-3 → LUMO+2 transitions respectively. These transitions involve one-electron promotions from the HOMO-3 orbital with symmetric $S_{op'}$ + Seπ ligand character to the LUMO orbital that possesses d_{yz} + Seπ* + L^{COOMe} character, and d_{xz} + Seπ* character present in LUMO+2 orbital. This assignment is supported by rRaman data (Figure 2.13) that shows a very strong enhancement of υ(C-C + C-O), υ(C=C) and υ(C=O) stretches.

Bands 8, 9, 10 and 11 have been tentatively assigned based on bonding calculations, ground and excited state DFT calculations, and calculated oscillator strengths obtained from time dependent DFT calculations. Thus, states with higher oscillator strength are assigned for intense peaks in the electronic absorption spectrum. Figure 2.14 shows a TD-DFT bar diagram showing the transition state oscillator strengths at their respectively energies.

Band 8 and 9: Band 8 is assigned as the HOMO-2 → LUMO+1 transition that possesses symmetric Sop' + Seπ* character in the HOMO-2 and L^{COOMe} ligand character in the LUMO+1 orbital. Band 9 is assigned as a HOMO-5 → LUMO transition that involves asymmetric $S_{op"}$ ligand character in the HOMO-5 and d_{yz} + Seπ* + L^{COOMe} character in the LUMO orbital. The strong intensity (~15,000 M^{-1} cm^{-1}) of band 9 results from the combination of LMCT and intraligand charge transfer and is supported by a strong calculated oscillator strength (f ~0.1490) in Figure 2.14.

Band 10 and 11: Band 10 is assigned as a combination of HOMO-5 → LUMO+1, LUMO+2 and HOMO-6 → LUMO+1 transitions, while band 11 is assigned as the HOMO-5 → LUMO+1 transition. These transitions possess asymmetric $S_{op"}$ character in the HOMO-5 and symmetric $S_{ip'}$ character in the highly stabilized HOMO-6 orbital, while L^{COOMe} and d_{xz} + Seπ* character is present in the LUMO+1 and LUMO+2 orbitals respectively. The intensities of these bands are consistent

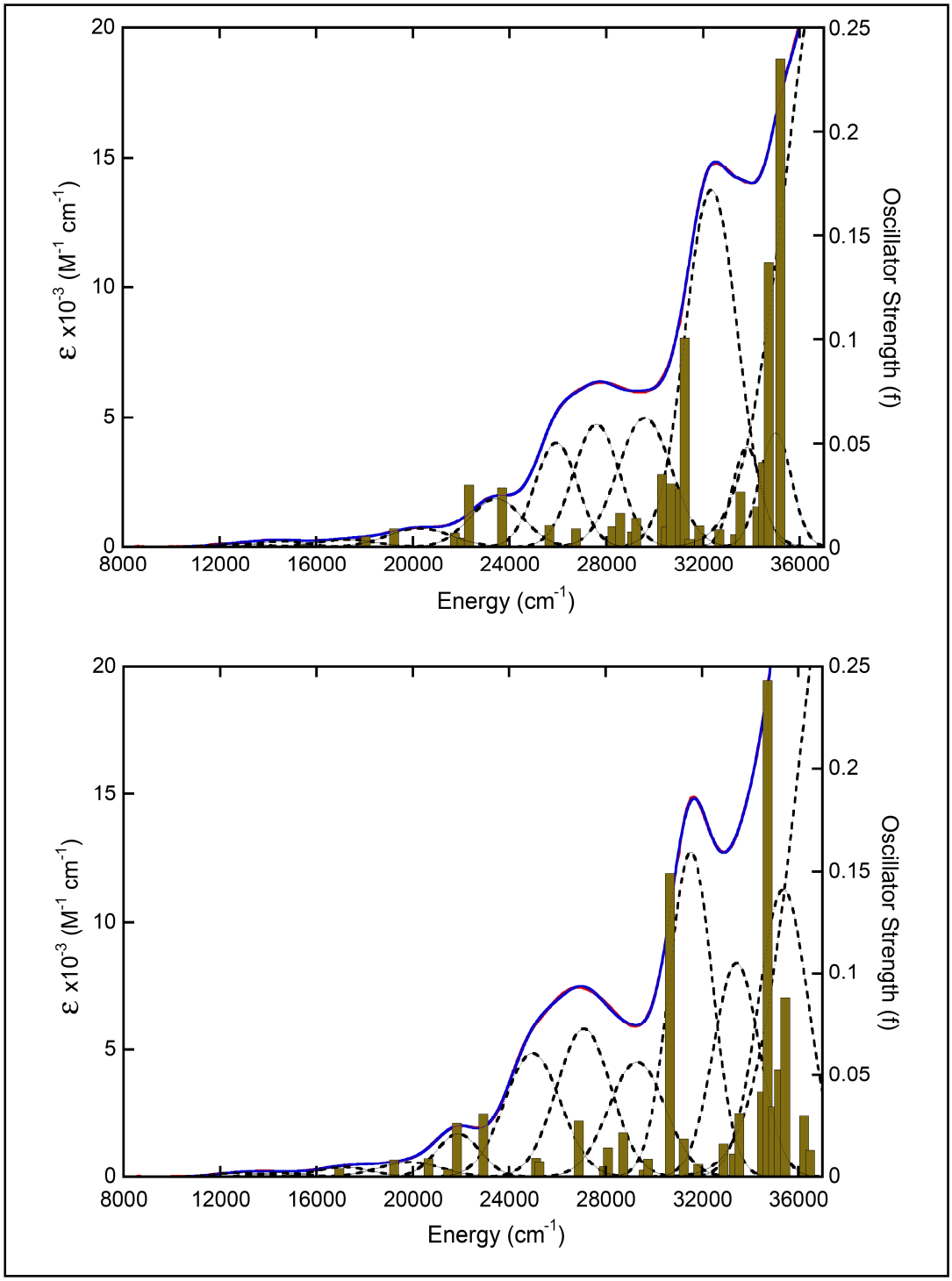

Figure 2.14: TD-DFT bar diagram showing transition states oscillator strength (f) at their respective energy for $[MoS(L^{COOMe})_2]^{2-}$ (top) and $[MoSe(L^{COOMe})_2]^{2-}$ (bottom) compounds.

with the assignment as a combination of intraligand charge transfer and LMCT transitions.

2.5.2 Discussion

2.5.2.1 The Effect of Apical Chalcogens in the Electronic Structure

$[MoO/S/Se(L^{COOMe})_2]^{2-}$ model compounds have a square pyramidal geometry with a mono-O/S/Se apical ligand similar to that observed in the active sites of arsenite oxidase and formate dehydrogenase enzymes in their reduced form. The effects of apical chalcogen character on $MoO/S/SeL^{COOMe}$ compounds have been investigated using electronic absorption spectroscopy and detailed bonding calculations. The electronic absorption spectra for $[MoO/S/Se(L^{COOMe})_2]^{2-}$ compounds show a progressive shift to low energy according to O > S > Se for the apical ligands due to their relative electronegativity nature and their valence ionization energies. The same trend was reported for trans-$Mo(Q)_2(PH_3)_4$ (Q = O, S, Se, Te),[63,70] and des-oxo Mo(XAd)dmt (X=O/S/Se) series of compounds.[62] The des-oxo Mo(XAd)dmt (X=O/S/Se) series show an ~1000 cm^{-1} spectral energy shift which is less than the ~1500 cm^{-1} shift observed in our system (mono-oxo compounds). This is due to the fact that the O/S/Se as apical ligands have three p-orbitals available to interact with molybdenum, the pz strongly destabilize Mo-d_{z^2} through s σ–bond, Mo-d_{xz} and d_{yz} are less destabilized via π–bonding with the p_x and p_y orbitals of the apical ligand (Figure 2.15). The Mo-$d_{x^2-y^2}$ is destabilized through σ interactions with the four equatorial sulfur ligands.

These interactions result in a large destabilization of $d_{x^2-y^2}$ orbital followed by d_{z^2} and $d_{xy,yz}$ orbitals at lower energy. However, for the des-oxo Mo(XAd)dmt compounds, only the p_z-orbital from the apical ligand interact strongly through σ bonding with the Mo-d_{z^2} orbital, and the four equatorial dithiolene sulfurs destabilize the Mo-$d_{x^2-y^2}$ orbital through σ bonding. This results to a larger splitting gap between occupied d_{xy} orbital and unoccupied d_{xz}, d_{yz}, d_{z^2}, $d_{x^2-y^2}$ orbitals, according to O>S>Se. The same trend is observed in the electronic absorption spectra overlay (Figure 2.2) for the $[MoO/S/Se(L^{COOMe})_2]^{2-}$ series which shows a progressive energy shift.

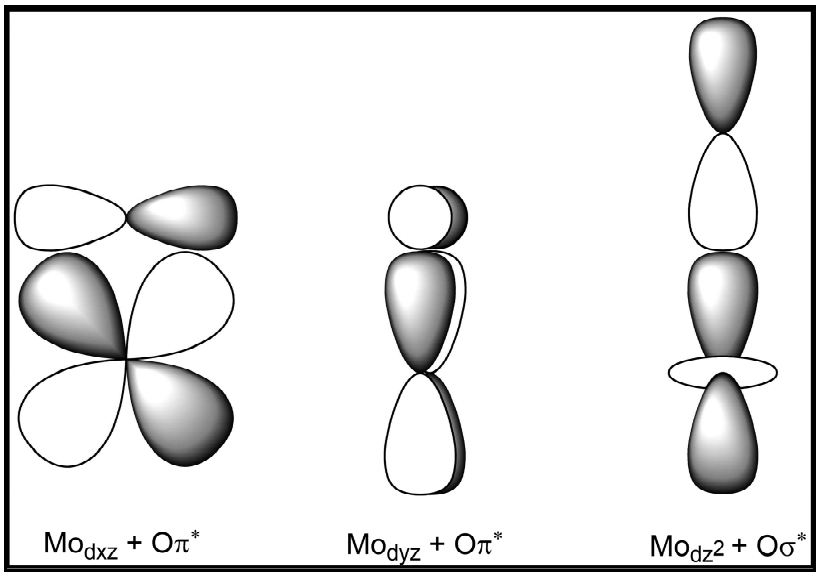

Figure 2.15: Schematic representation showing π^* and σ^*-interaction between Mo-d_{xz}, d_{yz}, and d_{z^2} orbitals with p_x, p_y and p_z orbitals from the apical O/S/Se atoms. This leads to a strong destabilization of d_{z^2} followed by the $d_{xz/yz}$ orbitals.

The LUMO orbital of all three compounds shows an admixture of metal and apical ligand character (Note: the apical ligand contribution in the LUMO is 2.8, 11.8 and 13.6% for O, S and Se) which decreases according to Se > S > O series (Figure 2.5). This result is consistent with the apical ligand valence ionization energy for these $[MoO/S/Se(L^{COOMe})_2]^{2-}$ compounds, where selenium can easily donate electron density to the metal as the result of its low valence ionization energy and vice versa for oxygen. Therefore, low energy charge transfer transitions are favored in compounds with Mo≡Se bonds and higher energy transitions for compounds with an Mo≡O bond as we have observed in the electronic absorption spectra (Figure 2.2).

The formate dehydrogenase enzyme active site has a square pyramidal geometry with an apical S/Se atom in its reduced form, similar to the $[MoO/S/Se(L^{COOMe})_2]^{2-}$ compounds in this study. In addition, this enzyme contains iron sulfur clusters which participate in electron transfer, but their presence prevents optical spectroscopic studies of the Mo site.[35,7] Thus, based on the spectroscopic and computational results we have proposed that the presence of an apical S/Se in the enzyme active site to have a smaller destabilization effect on the metal dπ-orbitals compared to apical oxo ligation, as we have observed in the $[MoO/S/Se(L^{COOMe})_2]^{2-}$ compounds. This favors low energy MLCT processes may be operative in enzymes that possess terminal sulfide and selenido ligation.

2.5.2.2 The Effect of Ene-1,2-dithiolene L^{COOMe} Ligand in the Molecular Orbital Description and Electron Transfer

The effects of an electron withdrawing substituent in the L^{COOMe}) ligand present in $[MoO/S/Se(L^{COOMe})_2]^{2-}$ compounds has been investigated using electronic absorption and resonance Raman spectroscopies, and detailed bonding calculations. Geometry optimization results from all three compounds lead to the construction of the molecular orbital diagram in Figure 2.4 that show the presence of L^{COOMe} ligand character in the LUMO and LUMO+1 orbitals. The presence of ligand character is also evidently in resonance Raman excitation profile (Figures 2.7 and 2.11) that show strong enhancement of υ(C-C + C-O), υ(C=C) and υ(C=O) stretches between 15,000 – 25,000 cm^{-1} for the $MoO/S/SeL^{COOMe}$ series. This indicates the presence of L^{COOMe} ligand character in the low energy CT excited states. A similar behavior was observed in $Tp^*MoO(S_2BMOQO)$[71] where the LUMO and LUMO+1 orbitals possess quinoxalline ligand character instead of metal character. Thus, the observed result is due to the strong electron withdrawing nature of L^{COOMe} ligand that destabilizes L^{COOMe} ligand orbitals and allows the ligand to possess some electron acceptor character.

Cyclic voltammetry results reported by Sugimoto and coworker show reversible redox couples at -0.03, -0.12 and -0.12 V for the $[MoO/S/Se(L^{COOMe})_2]^{2-}$ series. These potentials are less negative compared to averaged potentials of -0.45 and

-0.73 V for $[MoO/S/Se(L^{Ph})_2]^{2-}$ and $[MoO/S/Se(L^{H})_2]^{2-}$ compounds.[57,66] The less negative potentials observed in $[MoO/S/Se(L^{COOMe})_2]^{2-}$ compounds imply difficulty in oxidizing molybdenum center. This phenomenon is supported with our DFT calculation results on $[MoO/S/Se(L^{COOMe})_2]^{2-}$ that show the Mo-d_{xy} orbital is more stabilized and occurs at 1.41, 1.38 and 1.36 eV while Mo-$d_{xz/dyz}$ orbitals are more destabilized and occur at 5.55, 4.80 and 4.69 eV respectively. The Mo-d_{xy} redox orbital in $[MoO/S/Se(L^{COOMe})_2]^{2-}$ compounds is very stabilized when compared to the 2.55 eV observed in $[MoO(L^{H})_2]^{2-}$ for the d_{xy} orbital. However, this stabilization energy is within the range (1.43 and 1.48 eV) observed for $[MoS/Se(L^{Ph})_2]^{2-}$ compounds.[57] The stabilization of the redox orbital (d_{xy}) in $[MoO/S/Se(L^{COOMe})_2]^{2-}$ and $[MoS/Se(L^{Ph})_2]^{2-}$ compounds series can be due to the electron withdrawing nature of the COOMe substituent on the dithiolene or to strong resonance effects of a Ph substituent. Therefore electrochemistry, spectroscopy, and DFT calculations support our hypothesis that COOMe substituents on dithiolene ligands in $[MoO/S/Se(L^{COOMe})_2]^{2-}$ compounds stabilize Mo(IV) centers, disfavor metal oxidation, and lead to low energy MLCT transitions.

2.6 1,2–Diphenyl ene-1,2-dithiolates (L^{Ph}) Molybdenum Compounds

Spectroscopic studies of $[MoX(L^{Ph})_2]^{2-}$ (where X=S/Se) model compounds with the same geometry as reduced arsenite oxidase and formate dehydrogenase enzymes will be useful in the development of active site electronic structure descriptions for these enzymes. Figure 2.16 depicts the $[MoX(L^{Ph})_2]^{2-}$ structure with a square pyramidal geometry and two coordinated dithiolene (L^{Ph}) ligands in the equatorial position and a terminal S/Se chalcogen at the apical position bound to the molybdenum center. The crystal structure of $[MoS(L^{Ph})_2]^{2-}$ and $[MoSe(L^{Ph})_2]^{2-}$ shows average Mo-$S_{dithiolene}$ bond distances of 2.36 and 2.35 Å,[57] that is similar to the 2.37 and 2.30 Å Mo-$S_{dithiolene}$ bond distances observed in the crystal structure of reduced arsenite oxidase [7] and formate dehydrogenase.[35] The model compounds in this study possess L^{Ph} ligands that lower their symmetry to C_1. When one have considers only the first coordination sphere, these compounds possess C_{2v} symmetry.

Synthetic and X-ray crystallographic studies on $[MoS(L^{Ph})_2]^{2-}$ and $[MoSe(L^{Ph})_2]^{2-}$ compounds have been performed by Prof. Sugimoto and coworkers, and samples were provided to us for spectroscopic study. Very few spectroscopic studies have been performed on Mo complexes that possess terminal sulfido or selenido coordination. As a result, very little is known about their electronic structure compared to mono-oxo dithiolene compounds. One of the goals of this study is to probe these models spectroscopically in order to gain insight into formate dehydrogenase and arsenite oxidase electronic structure. Therefore,

this section details the effect of the apical chalcogen ligands and the equatorial 1,2-ene dithiolene (L^{Ph}) ligands on the nature of their charge transfer transitions. When the spectroscopic studies are coupled with detailed bonding calculations, this allows for an increased understanding of arsenite oxidase and nitrate reductase electronic structure in their reduced forms.

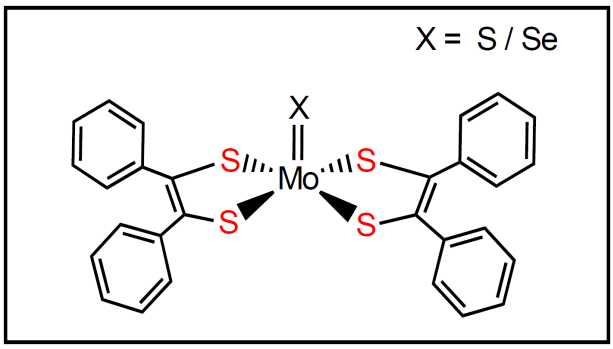

Figure 2.16: Structure of $[MoX(L^{Ph})_2]^{2-}$ complexes.

2.6.1 Results and Analysis

2.6.1.1 The Electronegative Effect of Terminal Ligands on the Electronic Spectra

Room temperature electronic absorption spectra for $[MoS(L^{Ph})_2]^{2-}$ and $[MoSe(L^{Ph})_2]^{2-}$ are depicted in Figure 2.17. The electronic absorption spectra for these two compounds are remarkably similar in the low energy region and differ only slightly at higher energies. Visual inspection of the data indicates a total number of seven bands in each compound between 9,000 and 37,000 cm^{-1}. We can discuss these spectra in two regions; a low energy region below 20,000cm^{-1} and the higher energy region above 20,000cm^{-1}. Bands in the low energy region

occur at 14,370 and 18,570 cm^{-1} for $[MoSe(L^{Ph})_2]^{2-}$ while in $[MoS(L^{Ph})_2]^{2-}$ they occur at 14,250 and 18200 cm^{-1}. These bands do not show a progressive shift to low energy according to S > Se, indicative of the absence of apical ligand character in these transitions.

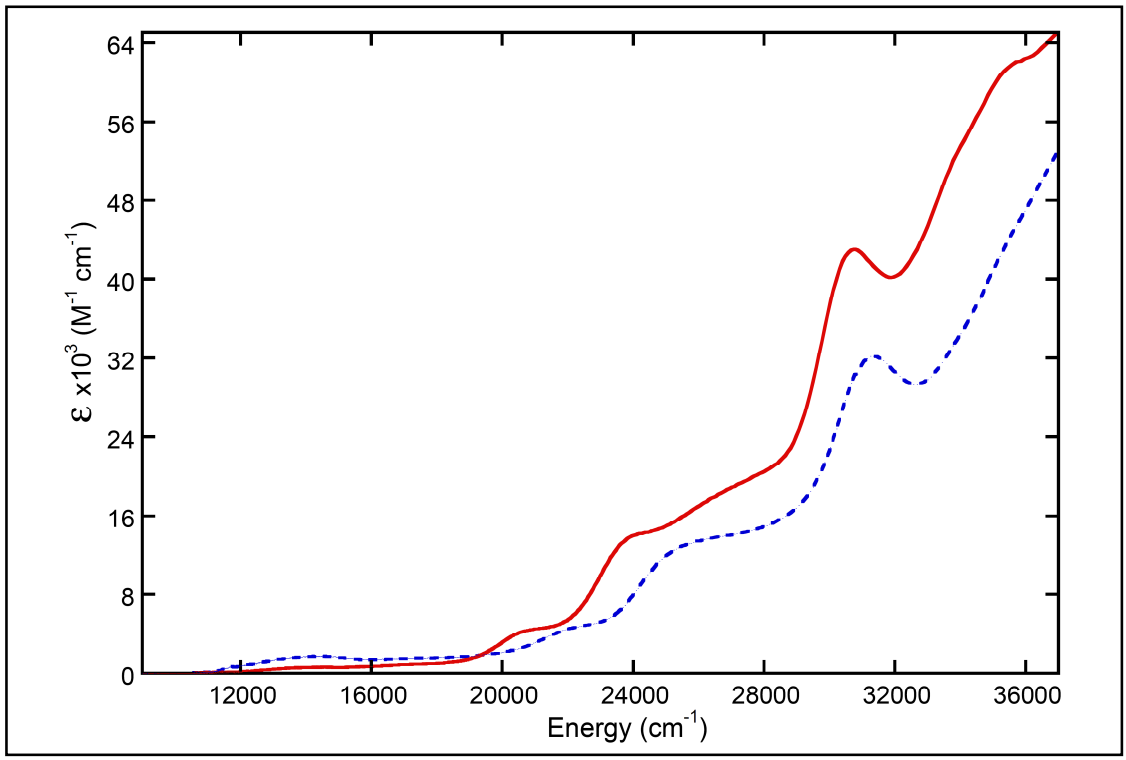

Figure 2.17: Room temperature electronic absorption spectra for $[MoS(L^{Ph})_2]^{2-}$ (– – –) and $[MoSe(L^{Ph})_2]^{2-}$ (——).

In contrast, the higher energy bands show a progressive energy shift of ~1500 cm^{-1} in going from an apical sulfido to selenide due to the differences in apical ligand electronegativity and valence ionization energy. The strong Mo≡S interaction is supported by crystal structure data that shows a Mo≡S bond length

of 2.1592 Å compared with 2.2915 Å for the Mo≡Se bond.[57] Both sulfur and selenium interact through a σ and two π bonding interactions with molybdenum that lead to a destabilization of the d_{z^2}, d_{xz}, and d_{yz} orbitals. The $d_{x^2-y^2}$ orbital is destabilized due to the four equatorial dithiolene sulfur ligands through σ bonding interactions with molybdenum (Figure 2.3). The level of interaction differs based on the electronegativity and valence ionization energy of apical chalcogen. Sulfur has smaller atomic radius than selenium and possesses a higher electronegativity compared to selenium. This favors a stronger interaction with molybdenum which leads to a greater d-orbital destabilization of the d_{xz}, and d_{yz} orbitals and consequently a larger t_{2g} splitting. This leads to higher energy dithiolene →Mo charge transfer bands for $[MoS(L^{Ph})_2]^{2-}$ compared with $[MoSe(L^{Ph})_2]^{2-}$ (Figure 2.17). Table 2-2 summarizes these charge transfer bands for $[MoS(L^{Ph})_2]^{2-}$ and $[MoSe(L^{Ph})_2]^{2-}$. Selenium has a lower valence ionization energy compared to sulfur, and can therefore more easily donate electron density to Mo and this results in lower energy charge transfer bands.

Table 2-2: Summary of electronic absorption maxima for $[MoS/Se(L^{Ph})_2]^{2-}$ compounds.

Band	$MoSe(L^{Ph})_2$	$MoS(L^{Ph})_2$
1	14 370	14 250
2	18 570	18 200
3	21 340	22 700
4	24 600	27 030
5	30 750	31 360
6	40 400	36 100

2.6.1.2 The Effect of the L^{Ph} Ligand on the Electronic Structure of $[MoS(L^{Ph})_2]^{2-}$ and $[MoSe(L^{Ph})_2]^{2-}$ Compounds

Electronic structure calculations and resonance Raman spectroscopy has been utilized to determine the effect of the 1,2-diphenyl ligand on the electronic structure of $[MoS(L^{Ph})_2]^{2-}$ and $[MoSe(L^{Ph})_2]^{2-}$. Figure 2.18 displays the relevant valence molecular orbitals for the $[MoS/Se(L^{Ph})_2]^{2-}$ compounds. It is interesting to note that the computational results show that the LUMO - LUMO+5 and LUMO+7 orbitals contain mostly L^{Ph} ligand character for $[MoS(L^{Ph})_2]^{2-}$. However, for $[MoSe(L^{Ph})_2]^{2-}$ dominant L^{Ph} ligand character is observed in the LUMO - LUMO+6, and LUMO+8 orbitals (Table 2.6.2). The presence of L^{Ph} ligand character in these unoccupied orbitals is supported by low energy metal to ligand and intraligand charge transfer bands. This is also evident in the results of bonding calculations and confirmed by rR experiments that show strong resonance enhancement of υ(C-C), υ(C=C) and υ(Ph) symmetric stretches in the low energy region (Figure 2.20). This behavior is similar to what has been observed in the $[MoO/S/Se(L^{COOMe})_2]^{2-}$ series of compounds (Section 2.6), where acceptor orbitals with ligand character lie in between the Mo-d_{xy} redox orbital and the higher energy unoccupied Mo d-orbitals. The presence of acceptor orbitals with ligand character is the result of a resonance effect within the L^{Ph} ligand which destabilizes ligand orbitals and allows them to possess electron acceptor character. This electronic structure description supports the presence of low

energy metal to ligand or ligand to ligand (intraligand) charge transfer transitions in these compounds.

Table 2-3: Molybdenum and L^{Ph} ligand percentage compositions for LUMO to LUMO+8 molecular orbitals.

Wave Function	Fragment	$MoS(L^{Ph})_2$	$MoSe(L^{Ph})_2$
LUMO	Mo	8.00	5.74
	L^{Ph}	83.41	84.12
LUMO+1	Mo	4.15	9.17
	L^{Ph}	86.90	80.32
LUMO+2	Mo	2.95	6.22
	L^{Ph}	88.67	74.95
LUMO+3	Mo	1.36	2.04
	L^{Ph}	96.67	94.97
LUMO+4	Mo	20.61	11.94
	L^{Ph}	66.77	79.16
LUMO+5	Mo	3.42	6.31
	L^{Ph}	93.60	88.71
LUMO+6	Mo	28.92	0.78
	L^{Ph}	45.84	87.00
LUMO+7	Mo	3.42	30.52
	L^{Ph}	91.53	48.95
LUMO+8	Mo	25.70	21.28
	L^{Ph}	46.06	65.76

The phenyl substituents can π-delocalize into the C=C orbitals of the dithiolene which increases ligand stability. Thus, the ligand develops some π-acceptor character that results in decrease in S donor ability leading to a stabilization of the Mo(IV) oxidation state over Mo(V) for these compounds. This result has a large implication for catalysis in the enzymes, since enhanced dithiolene delocalization can lead to redox potentials that stabilize the Mo(IV) state.

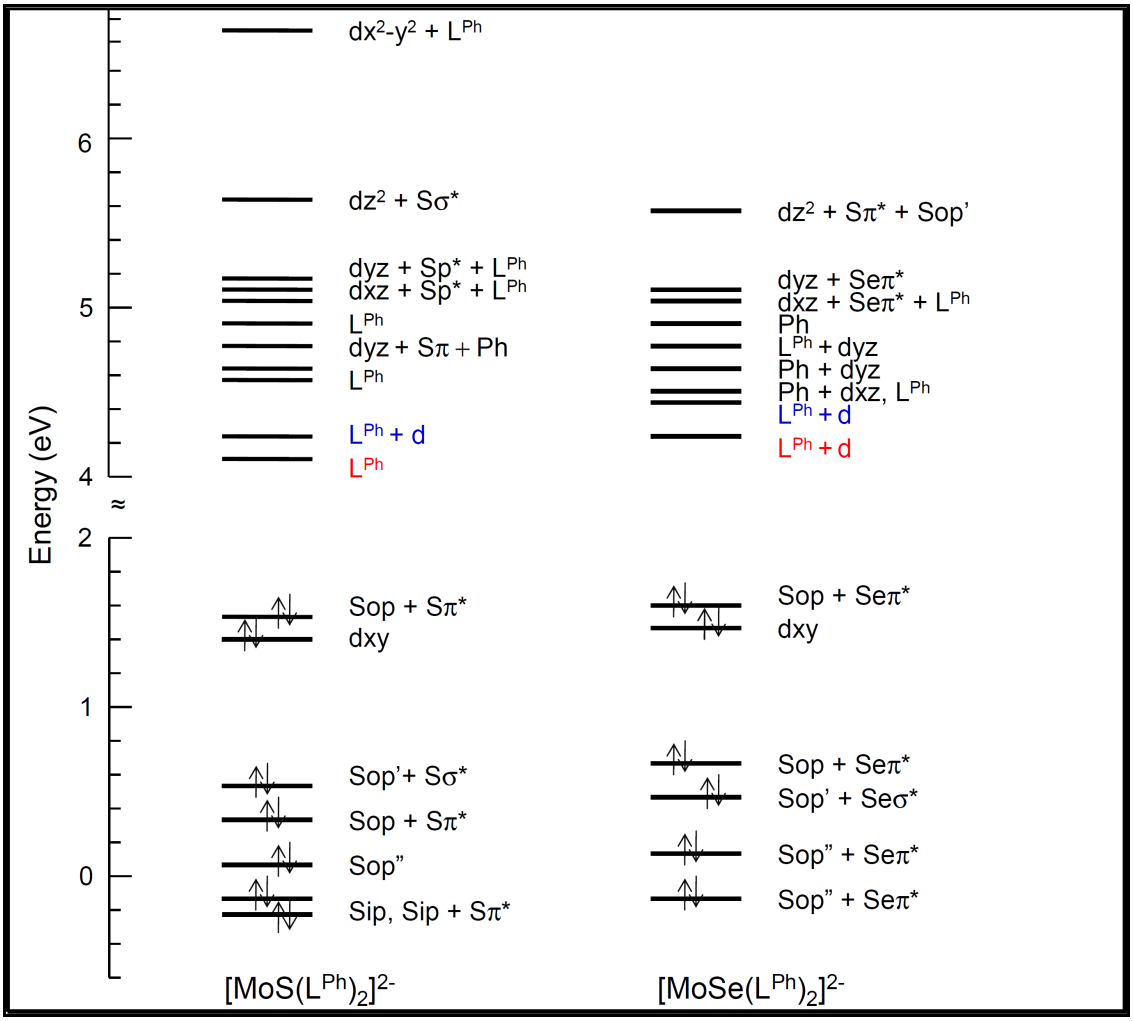

Figure 2.18: Molecular orbital energy diagram for $[MoS(L^{Ph})_2]^{2-}$ and $[MoSe(L^{Ph})_2]^{2-}$ compounds.

2.6.1.3 Band Assignments and the Nature of Low Energy MLCT, Intraligand CT and Ligand Field Transitions

Band assignments have been made with the help of ground state and excited state TD-DFT calculations, and electronic absorption and resonance Raman spectroscopies. TD-DFT calculations have been performed on geometry

optimized structures with atoms in the first coordination sphere fixed at the crystal structure geometry for $[MoOS(L^{Ph})_2]^{2-}$ and $[MoSe(L^{Ph})_2]^{2-}$ compounds.

Band 1: Band 1 is assigned as the HOMO-1 → LUMO transition in both $[MoS(L^{Ph})_2]^{2-}$ and $[MoSe(L^{Ph})_2]^{2-}$. The HOMO-1 orbital possesses Mo-d_{xy} character while the LUMO possesses C=C antibonding and phenyl ring character that is localized on one side of dithiolene. This transition is shown in the electron density different map (EDDM) in Figure 2.19. The weak intensity of this band is consistent with a weak calculated oscillator strength (f = 0.0048 and 0.0196) for this transition in both $[MoSe(L^{Ph})_2]^{2-}$ and $[MoS(L^{Ph})_2]^{2-}$.

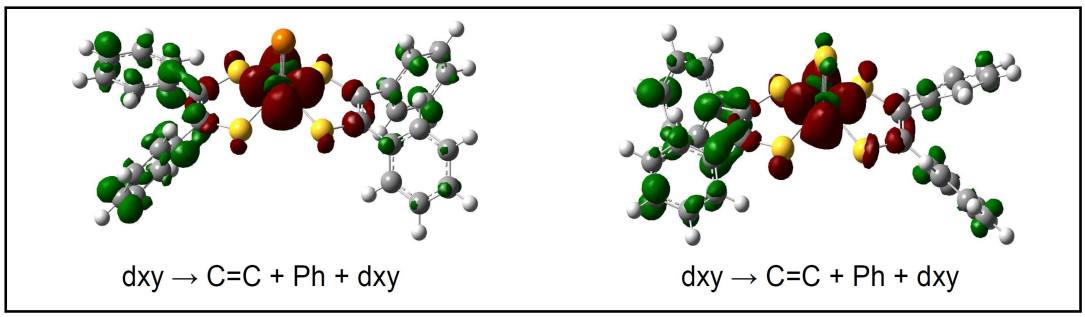

Figure 2.19: Electron density difference maps (EDDMs) for $[MoSe(L^{Ph})_2]^{2-}$ (left) and $MoS(L^{Ph})_2]^{2-}$ (right) showing the MLCT transition, where red indicates electron donation in the transition and green electron acceptance in the transition for band 1.

Band 2: This band is assigned as a combination of HOMO → LUMO, HOMO-1 → LUMO and HOMO → LUMO+1 transitions in both the $[MoSe(L^{Ph})_2]^{2-}$ and $[MoS(L^{Ph})_2]^{2-}$ compounds. The HOMO and HOMO-1 orbitals possess

asymmetric S_{op} + Se/Sπ^* and Mo-d_{xy} character, whereas the LUMO and LUMO+1 possess C=Cπ^* antibonding and phenyl ring character mainly from one side of dithiolene with some Mo-d_{xy} while the latter possesses phenyl ring ligand with small amount of Mo-d_{xy} character. The presence of C=Cπ^* antibonding, phenyl ring and Mo-d_{xy} character in these orbitals is supported by the rR excitation profiles in Figure 2.20 that show a decrease in enhancement for the υ(C=C) and υ(Ph-ring) stretches from the 19,455 cm^{-1} (514 nm) laser line to low energy concurrently with the υ(Mo-S) stretch being resonantly enhanced. This is the first low energy intraligand charge transfer transition observed in these compounds.

Band 3: The strong enhancement of υ(Mo≡S/Se), υ(C=C) and υ(Ph-ring) stretches accompanied with a small enhancement of the υ(C-C-Ph) stretch and a decrease in enhancement of the υ(Mo-S) stretch are observed in band 3 for $[MoS(L^{Ph})_2]^{2-}$ and $[MoSe(L^{Ph})_2]^{2-}$. We assign band 3 as a combination of HOMO → LUMO+2, HOMO → LUMO+3, HOMO-1 → LUMO+2, HOMO-1 → LUMO+3, HOMO → LUMO+5 and HOMO → LUMO+7 transitions respectively (Note: LUMO+7 is equivalent to LUMO+6 in $[MoS(L^{Ph})_2]^{2-}$). The HOMO possesses asymmetric Sop + S/Seπ^* + Mo-d_{xy} character and the HOMO-1 has Mo-d_{xy} character, whereas the LUMO+2 and LUMO+3 orbitals possess mainly phenyl ligand character with ~83 and 97% L^{Ph} character, respectively. The LUMO+5 possesses phenyl ring character with 6.3% Mo-d_{xz} character, and the LUMO+7 possesses ~30.5% Mo-d_{xz} + ~9.5% Se/Sπ^* + ~48.6% phenyl ring character. The

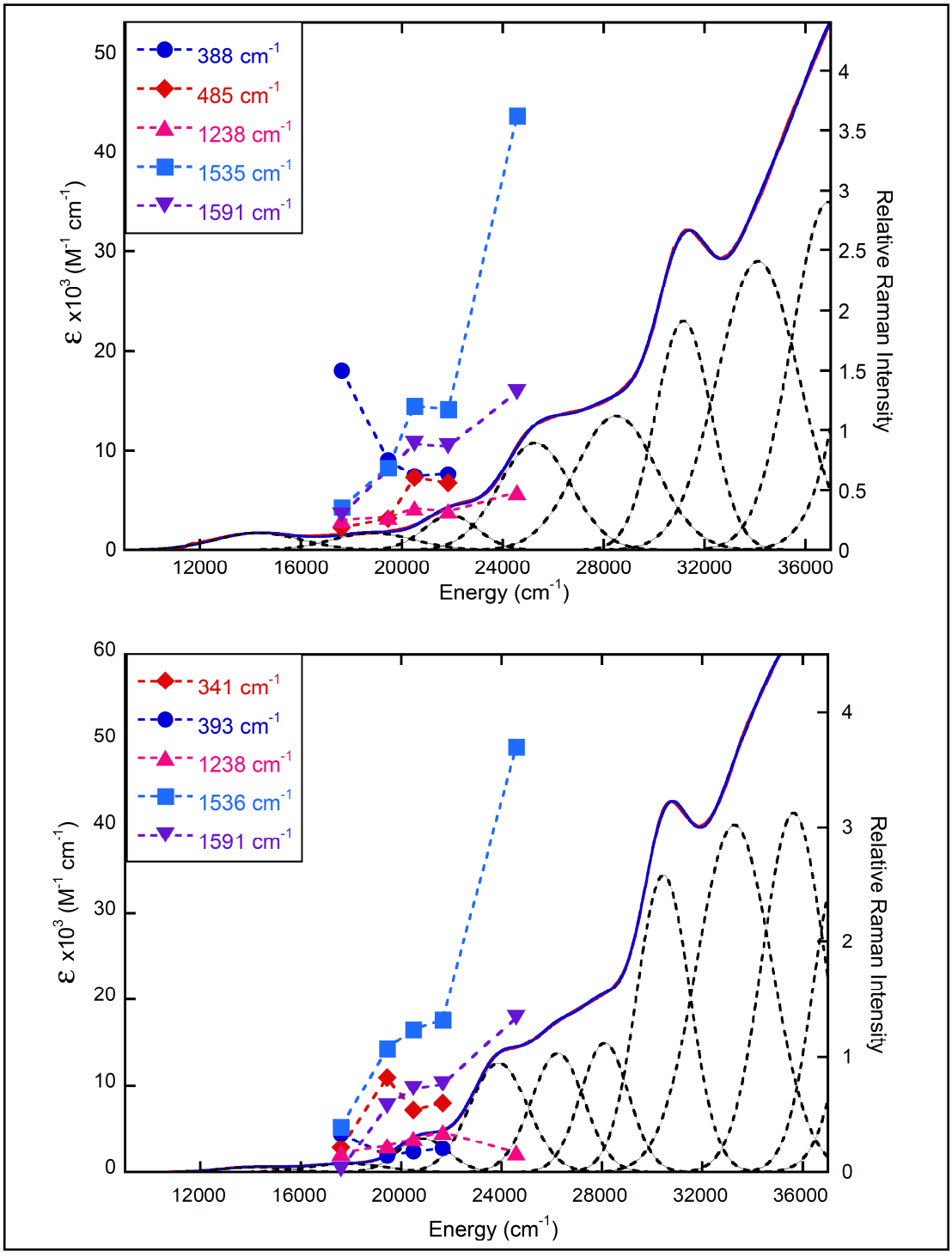

Figure 2.20: Resonance Raman excitation profile for $[MoS(L^{Ph})_2]^{2-}$ (top) showing the υ(M-S) stretch at 388 cm^{-1}, υ(Mo≡S) stretch at 485 cm^{-1}, υ(C-C-(Ph)) stretch at 1238 cm^{-1}, υ(C=C) stretch at 1535 cm^{-1} and υ(Ph-ring) stretch at 1591 cm^{-1}.

$[MoSe(L^{Ph})_2]^{2-}$ (bottom) showing the υ(Mo≡Se) stretch at 341 cm^{-1}, υ(Mo-S) stretch at 393 cm^{-1}, υ(C-C-(Ph)) stretch at 1238 cm^{-1}, υ(C=C) stretch at 1536 cm^{-1} and υ(Ph-ring) stretch at 1591 cm^{-1}.

electron density difference map for the HOMO→LUMO+5 and HOMO→LUMO+7 transitions are displayed in Figure 2.21 showing mainly the intraligand and ligand to metal charge transfer, respectively.

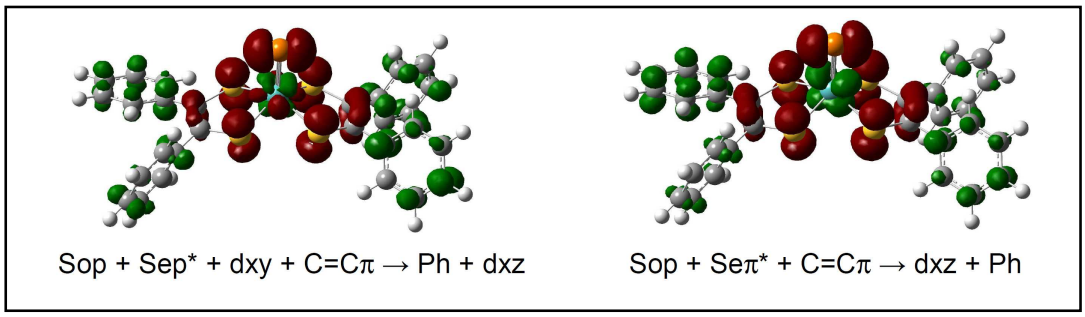

Figure 2.21: Electron density difference map (EDDM) for $[MoSe(L^{Ph})_2]^{2-}$ showing a combination of intraligand and ligand to metal charge transfer transition, where red indicates electron donation in the transition and green electron acceptance in the transition for band **3.**

Band 4: Band 4 is assigned as a combination of HOMO-1 → LUMO+5, HOMO-1 → LUMO+6, HOMO → LUMO+9 and HOMO-1 → LUMO+9 transitions. The HOMO has asymmetric Sop + Se/Sp* + C=Cπ bonding character and the HOMO-1 possesses Mo-d_{xy} character. The LUMO+5 contains phenyl ligand character from both dithiolenes and small amount of Mo-d_{xz} character. The

LUMO+6 possesses phenyl ligand character from one dithiolene side and the LUMO+9 has Mo-d_{yz} + Se/Sπ^* character. EDDMs for the HOMO-1 → LUMO+6 and HOMO → LUMO+9 transitions are given in Figure 2.22, and they show ligand field and ligand to metal charge transfer character. This assignment is supported by rRaman data that display a strong resonance enhancement of υ(Ph-ring) and υ(C-C-(Ph)) stretches using 407 nm (24,570 cm^{-1}) excitation.

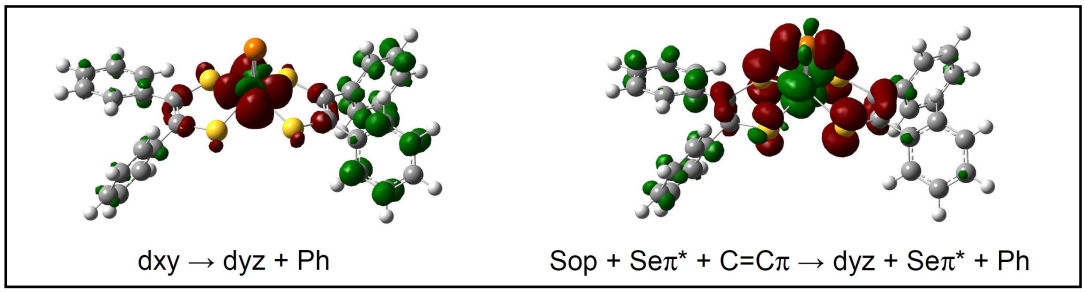

Figure 2.22: Electron density difference map (EDDM) for $[MoSe(L^{Ph})_2]^{2-}$ showing ligand field (left) and ligand to metal charge transfer (LMCT) (right), where red indicates electron donation in the transition and green electron acceptance in the transition for band 4.

Bands 5, 6, 7 and 8 were assigned solely based on the ground and excited state calculations, and their oscillator strengths were determined for a partially optimized geometry by freezing the apical chalcogen and all four sulfur atoms bound to the molybdenum to match the crystal structure geometry.

Band 5: Band 5 is assigned as a combination of HOMO-2 → LUMO (f =0.0323), HOMO-3 → LUMO (f =0.0393), HOMO-2 → LUMO+2 (f =0.0225) and HOMO →

LUMO+10 (f =0.0100) transitions for $[MoSe(L^{Ph})_2]^{2-}$. However, for $[MoS(L^{Ph})_2]^{2-}$ compound this band is assigned as arising from a combination of HOMO-2 → LUMO+1 (f =0.0082), HOMO-3 → LUMO (f =0.0441), HOMO-3 → LUMO+1 (f =0.0868) and HOMO → LUMO+10 (f =0.0064) transitions. This assignment is a combination of intraligand charge transfer and LMCT transitions where the LUMO+10 orbital possesses Mo-d_{z2} + Se/Sπ^* + totally symmetric S_{op} character, while the other orbital descriptions have been covered in the band assignments above. The intensity of this band is consistent with the calculated oscillator strength, providing further support the assignment.

Band 6: This band is assigned as a combination of HOMO-2 → LUMO+1 (f =0.0201), HOMO-3 → LUMO+2 (f =0.0094), HOMO-4 → LUMO (f =0.0289) and LUMO-2 → LUMO+4 (0.0105) transitions for the $[MoSe(L^{Ph})_2]^{2-}$ compound. However, this band is missing in the $[MoS(L^{Ph})_2]^{2-}$ compound. This is an intraligand charge transfer transition where the calculated oscillator strength is proportional to the observed band intensity.

Band 7: Band 7 is assigned as a combination of HOMO-3 → LUMO+3 (0.0161), HOMO-5 → LUMO (f =0.0859) and HOMO-3 → LUMO+4 (f =0.0385) transitions for $[MoSe(L^{Ph})_2]^{2-}$ and as HOMO-2 → LUMO+2 (0.0155), HOMO-3 → LUMO+2 (f =0.0064), HOMO-4 → LUMO (f =0.2379) and HOMO-2 → LUMO+4 (f =0.0144) transitions for $[MoS(L^{Ph})_2]^{2-}$. All of the orbital descriptions have been covered above. Additionally, these transitions have been assigned as intraligand charge

transfers, and the band intensity is consistent with the calculated oscillator strength.

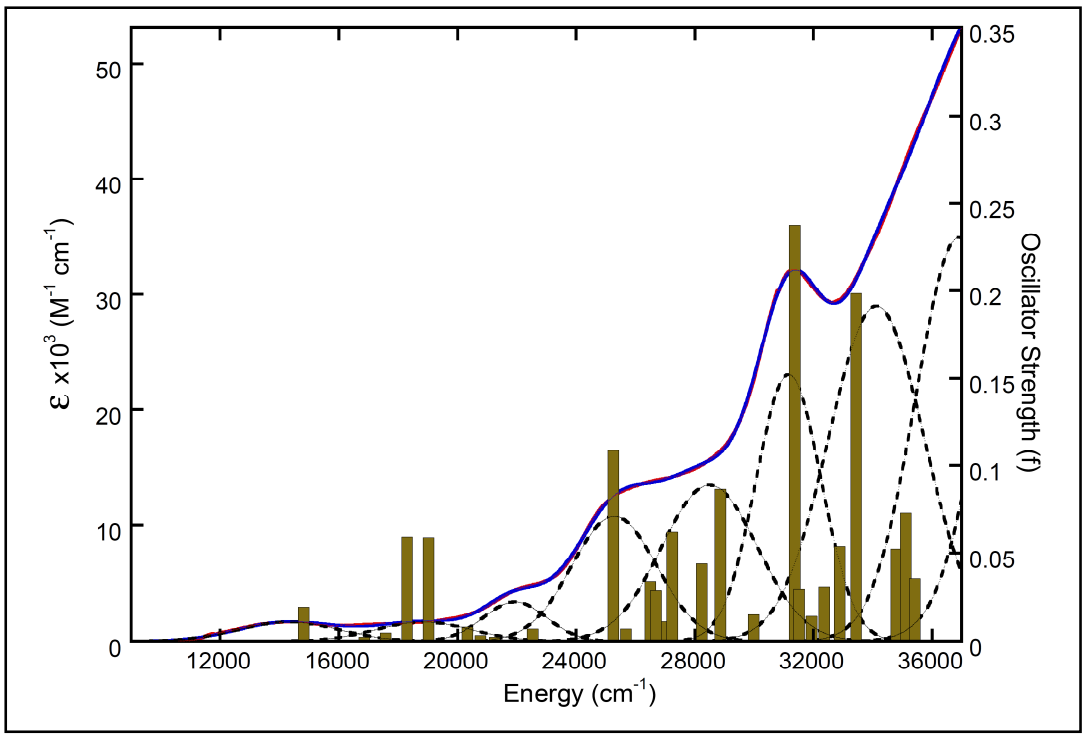

Figure 2.23: $[MoS(L^{Ph})_2]^{2-}$ Gaussian resolved electronic absorption with overlayed calculated oscillator strengths.

Bands 8 and 9: These bands are assigned as combination of HOMO-6 → LUMO (f =0.0828), HOMO-2 → LUMO+9 (0.0851), HOMO-5 → LUMO+2 (f =0.0410) and HOMO-4 → LUMO+2 and LUMO+4 (f =0.0106) transitions for $[MoSe(L^{Ph})_2]^{2-}$ while for $[MoS(L^{Ph})_2]^{2-}$ they are assigned as a combination of HOMO-3 → LUMO+4 (f =0.0132), HOMO-5 → LUMO+1 (f =0.1985), HOMO-2 → LUMO+5 (f =0.0107) and HOMO-4 → LUMO+2 and LUMO+4 (f =0.0524) respectively. These transitions have been shifted by ~3000 cm^{-1} to fit the experimental results

(Figure 2.23). Furthermore, the computational results show that these bands are dominated by intraligand charge transfer character, with the band intensity in agreement with the strong calculated oscillator strength for these transitions.

2.6.2 Discussion

2.6.2.1 Electronic Structure of $[MoS(L^{Ph})_2]^{2-}$ and $[MoSe(L^{Ph})_2]^{2-}$ Compounds

Little spectroscopic information is available on compounds with terminal sulfido or selenido ligation coupled with bis-ene-1,2-dithiolate ligation. Therefore, the use of $[MoS(L^{Ph})_2]^{2-}$ and $[MoSe(L^{Ph})_2]^{2-}$ has allowed an evaluation on the effect of terminal sulfido or selenido and ene-1,2-dithiolate coordination on the underpinning electronic structure of these types of compounds. Our results show a progressive energy shift in the order of S > Se due to the effect of the apical chalcogen. The same trend has been previously reported by Kirk and coworkers[62] on $[MoO/S/Se(Ad)(S_2C_2Me_2)_2]^{2-}$ compounds. The effect of the apical ligands on the low energy bands in the $[MoO/S/Se(Ad)(S_2C_2Me_2)_2]^{2-}$ compounds is associated with the presence of only two p-orbitals (pz and px orbitals) that are available for bonding with the metal center, since the third orbital (py orbital) forms a σ-bond with the adamantyl carbon. This is to be compared with the three p-orbitals (px, py and pz orbitals) available for bonding with Mo when the apical ligand is a single atom. The two p-orbitals in $[MoO/S/Se(Ad)(S_2C_2Me_2)_2]^{2-}$ destabilize the Mo-d_{z^2} and Mo-d_{xz} orbitals while for mono-oxo systems, the three p-orbitals destabilize the Mo-d_{z^2}, Mo-d_{xz} and Mo-d_{yz} orbitals.

The effect of the ene-1,2-dithiolate ligand with 1,2–diphenyl substitution has been observed in the electronic absorption and Raman spectra of these compounds, and the results have been corroborated by and DFT calculations. In the electronic absorption spectrum, the low energy bands below 20,000 cm^{-1} do not possess a progressive energy shift as observed for the higher energy ones. This indicates the absence of apical ligand involvement and the presence of ene-1,2-dithiolate 1,2–diphenyl ligand involvement. McNaughton et al. [62] and Lim et al. [61] reported the absence of progressive energy shift in low energy bands below 15,000 cm^{-1} for $[MoO/S/Se(Ad)(S_2C_2Me_2)_2]^2$ compounds. However this effect occurs at lower energy than in our results due to the lack of a terminal chalcogenide ligand. Otherwise, there is good agreement. In addition, Goddard and coworkers[60] reported the electronic absorption spectra of $[WO/S/Se(L^{Ph})_2]^{2-}$ compounds that showed a progressive energy shift in only the higher energy bands above 33,000 cm^{-1} and assigned them as Q (apical ligand) → W charge transfer bands. The differences in metal centers accounts for the higher energy of the transitions in these W compounds compared to the Mo systems, and this relates to the relative valence ionization energies of the metal.

DFT calculations show that the d_{xy} orbital energy is at ~1.45 eV, while the d_{xz}, d_{yz} orbitals are more destabilized and occur at 4.73 and 5.00 eV for $[MoS/Se(L^{Ph})_2]^{2-}$ compounds. The d_{xy} orbital is more stabilized compared to $[MoO(L^{H})_2]^{2-}$ and $[MoO(L^{O})_2]^{2-}$ compounds where the d_{xy} orbital energy is at ~2.50 and 2.25 eV (Section 2.7). The stabilization energy in $[MoS/Se(L^{Ph})_2]^{2-}$ is comparable with the

~1.37 eV observed for $[MoS/Se(L^{COOMe})_2]^{2-}$ compounds. This result agrees well with the poor electron donating nature of the L^{Ph} and L^{COOMe} ligands that weakens their interaction with the metal center, compared with stronger interactions for electron donating L^{H} and L^{O} ligands. Kirk and coworkers reported a small stabilization energy of ~1.50 eV relative to the d_{xz}, d_{yz} orbitals for *des*-oxo $[MoO/S/Se(Ad)(S_2C_2Me_2)_2]^{2-}$ compounds [62], which is in good agreement with what we observed for $[MoS/Se(L^{Ph})_2]^{2-}$ compounds.

2.6.2.2 The Effect of 1,2–diphenyl ene-1,2-dithiolate Ligand on Redox Potential

The nature of ene-1,2-dithiolene substituents have a large effects on redox process to regenerate the corresponding Mo(V) center. Our DFT results on $[MoS/Se(L^{Ph})_2]^{2-}$ compounds show that d_{xy} orbital is more stabilization relative to d_{xz}, d_{yz} orbitals and occurs at 1.43 and 1.48 eV compared with 2.49 and 2.25 eV for $[MoO(L^{H})_2]^{2-}$ and $[MoO(L^{O})_2]^{2-}$ compounds (Section 2.7). The stabilization of d_{xy} orbital in $[MoS/Se(L^{Ph})_2]^{2-}$ compounds disfavor metal oxidation. In addition our DFT calculations results agree well with cyclic voltammetry results by Sugimoto and coworkers showing a cyclic potential of -0.45 and -0.46 V [57] for $[MoS(L^{Ph})_2]^{2-}$ and $MoSe(L^{Ph})_2]^{2-}$ compounds. Davis et al. reported a redox potential of -0.48 V for $[MoO(sdt)_2]^{2-}$ (Note: sdt = 2-phenylethene-1,2-dithiolate).[72] This result agrees well with the Sugimoto results. Although the $[MoO(sdt)_2]^{2-}$ compound has only one phenyl ring attached to the ene-1,2-dithiolene, the effect of the ligand strength observed is similar to our compounds that possess two

phenyl rings. Donahue, et al. [73] reported a redox potential of -0.39 V for $[MoO(bdt)_2]^{2-}$ which is slightly positive compared to reported values for $[MoS/Se(L^{Ph})_2]^{2-}$ compounds. This is due to the poor donating power of the benzene ring as a result of π-electron delocalization stability present in $[MoO(bdt)_2]^{2-}$. A similar effect is manifested with the phenyl ring in $[MoOS/Se(L^{Ph})_2]^{2-}$ compounds. Additionally, Sugimoto et al. reported redox potentials of -0.75 and -0.74 V for $[MoS(L^{H})_2]^{2-}$ and $[MoSe(L^{H})_2]^{2-}$ compounds.[66] These redox potentials are more negative compared to the $[MoS/Se(L^{Ph})_2]^{2-}$ potential. Therefore, we propose a relative destabilization of the Mo(IV) species for $[MoS/Se(L^{H})_2]^{2-}$ and stabilization for $[MoS/Se(L^{Ph})_2]^{2-}$ compounds. By considering DFT and cyclic voltammetry results for $[Mo/S/Se(L^{Ph})_2]^{2-}$ compounds, we can explain the relative stability of the Mo(IV) oxidation state compared to Mo(V), and this is due to the presence of L^{Ph} ligands which possess electron withdrawing groups.

2.7 Cyclohexene-1,2-dithiolate (L^H) and 2,3-dihydro-2H-pyran-4,5-dithiolate (L^O) Mono-Oxo Molybdenum Compounds

$[MoO(L^H)_2]^{2-}$ and $[MoO(L^O)_2]^{2-}$ compounds have been synthesized and crystallographically characterized by the Sugimoto group.[57] These compounds possess square pyramidal geometries, with four sulfurs from two bis-dithiolenes attached to the molybdenum ion and an apical oxo group similar to that in reduced arsenite oxidase. Crystal structures for these models show that the molybdenum atom is located 0.70 and 0.75 Å above the basal planes made by the four sulfurs donors at equatorial positions for $[MoO(L^H)_2]^{2-}$ and $[MoO(L^O)_2]^{2-}$.[66] This is close to the 0.8 Å displacement observed in reduced arsenite oxidase.[6] The $[MoO(L^H)_2]^{2-}$ and $[MoO(L^O)_2]^{2-}$ compounds possess Mo-S bonds that averaged to 2.40 and 2.39 Å with a 1.754 Å Mo≡O bond.[57] This is similar to the 2.37 Å Mo-S bond lengths and the 1.70 Å bond length for the Mo≡O bond observed in the enzyme.[7] The general structures of $[MoO(L^H)_2]^{2-}$ and $[MoO(L^O)_2]^{2-}$ compounds are displayed in Figure 2.24.

Very few spectroscopic studies have been performed on arsenite oxidase due to the presence of iron-sulfur clusters which interferes with the molybdenum active site during spectroscopic characterization. Therefore, we are interested in using $[MoO(L^H)_2]^{2-}$ and $[MoO(L^O)_2]^{2-}$ model compounds in order to study the effect of equatorial 1,2-ene dithiolene ligands on the nature of charge transfer transitions. This may contribute to a greater understanding of the electronic structure of

reduced arsenite oxidase. We will attempt to accomplish this by employing various spectroscopic techniques coupled with detailed bonding calculations.

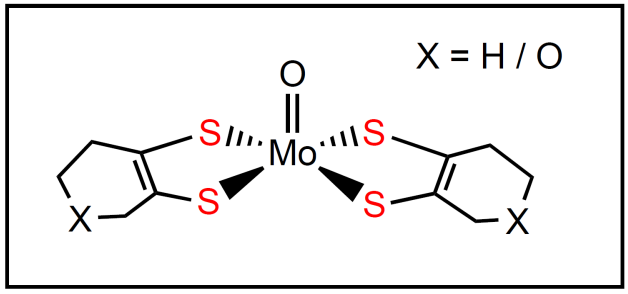

Figure 2.24: Structure of $[MoO(L^{O/H})_2]^{2-}$ compounds.

2.7.1 Results and Analysis

2.7.1.1 Electronic Absorption and rRaman Spectra

Room temperature electronic absorption spectra for $[MoO(L^{H})_2]^{2-}$ and $[MoO(L^{O})_2]^{2-}$ compounds are displayed in Figure 2.25. These two compounds contain a similar number of bands in their electronic absorption spectrum with similar intensity, except for the higher energy band at ~34,000 cm^{-1} where $[MoO(L^{O})_2]^{2-}$ has higher intensity than $[MoO(L^{H})_2]^{2-}$. The first low energy band occurs at 12,480 cm^{-1} in both $[MoO(L^{H})_2]^{2-}$ and $[MoO(L^{O})_2]^{2-}$, and the weak intensity (ε ~175 $M^{-1}cm^{-1}$) of this band indicates a ligand field transition. The second observable band is slightly more intense compared to the first band, with ε ~315 $M^{-1}cm^{-1}$ for $[MoO(L^{H})_2]^{2-}$ and ~400 $M^{-1}cm^{-1}$ for $[MoO(L^{O})_2]^{2-}$. The slight intensity increase observed in this band is associated with ligand to metal charge transfer character, which agrees well with the rRaman data in Figure 2.7.4. A shoulder is observed at ~29,000 cm^{-1} (ε ~2,000 $M^{-1}cm^{-1}$) followed by an intense

band at ~34,000 cm^{-1} (ε ~6,790 and 8,810 $M^{-1}cm^{-1}$ for $[MoO(L^H)_2]^{2-}$ and $[MoO(L^O)_2]^{2-}$, and are associated with ligand to metal charge transfer transitions.

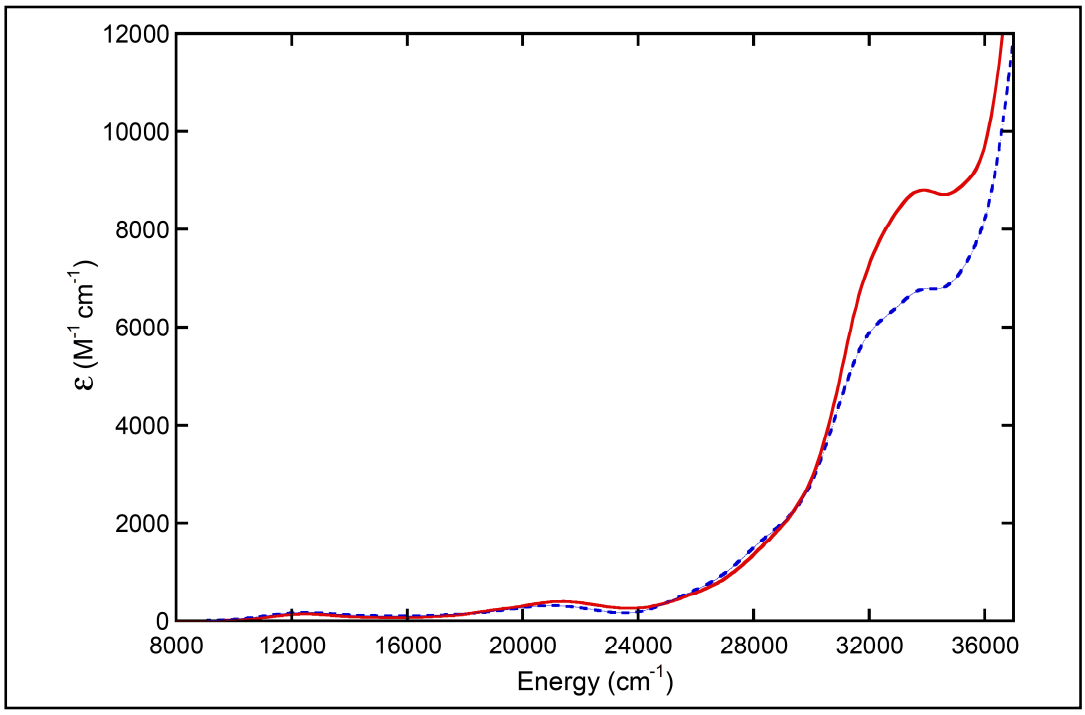

Figure 2.25: Room temperature electronic absorption for $[MoO(L^H)_2]^{2-}$ (– – –) and $[MoO(L^O)_2]^{2-}$ (——) compounds.

Resonance Raman Spectroscopy

Raman spectra for $[MoO(L^H)_2]^{2-}$ collected with 568 nm excitation, and for $MoO(L^O)_2]^{2-}$ using 514 nm excitation are displayed in Figure 2.26. A peak associated with a υ(S-Mo-S) bending is revealed at 352 cm^{-1} for $[MoO(L^H)_2]^{2-}$ and at 350 cm^{-1} for $[MoO(L^O)_2]^{2-}$ while the υ(Mo-S) stretch is revealed at 418 and 419 cm^{-1}, respectively. The υ(Mo-S) stretch occurs at relatively high energy (418 and 419 cm^{-1}) due to the strong electron donating ability of the L^H and L^O ligands.

Also, an intense peak observed at 893 and 899 cm^{-1} in $[MoO(L^{H})_2]^{2-}$ and $[MoO(L^{O})_2]^{2-}$ compounds is associated with the $\upsilon(Mo\equiv O)$ stretch. The occurrence of this stretch at lower frequency in $[MoO(L^{H})_2]^{2-}$ is due to the L^{H} strong electron donating power of this ligand, which is found to be slightly less for L^{O}. Strongly donating dithiolenes decreases the effective nuclear charge of the metal and consequently weaken the $Mo\equiv O$ bond. The observed υ(Mo-S) and $\upsilon(Mo\equiv O)$ stretches are within the range found in other bis-dithiolene compounds.[74] In addition, the higher frequency region of the spectra contains a band at 1597 and 1599 cm^{-1} for $[MoO(L^{H})_2]^{2-}$ and $[MoO(L^{O})_2]^{2-}$, respectively, that is associated with the υ(C=C) stretch. The higher frequency υ(C=C) stretch observed in both compounds is associated with the strong electron donating power of the L^{O} and L^{H} ligands. However, these frequencies are within the range reported for bis-dithiolene compounds between (1450-1575 cm^{-1}),[71,74,75] and 1572 cm^{-1} in reduced DMSOR.[22]

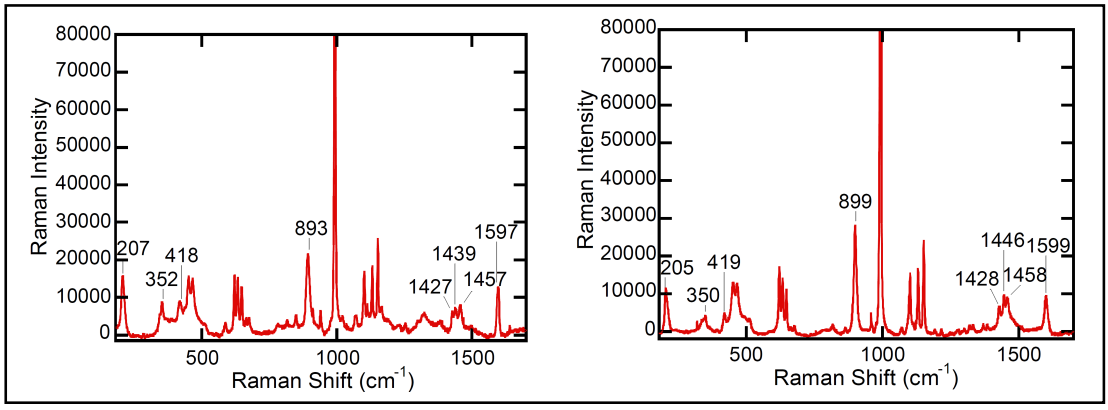

Figure 2.26: Raman spectra for $[MoO(L^{H})_2]^{2-}$ (left) at 568 nm (17,606 cm^{-1}) excitation laser line showing υ(S-Mo-S) bending at 353 cm^{-1}, υ(Mo-S) stretch at

418 cm^{-1}, υ(Mo≡O) stretch at 893 cm^{-1} and υ(C=C) stretch at 1597 cm^{-1} and for $[MoO(L^O)_2]^{2-}$ (right) at 514 nm showing υ(S-Mo-S) bending at 350 cm^{-1}, υ(Mo-S) stretch at 419 cm^{-1}, υ(Mo≡O) stretch at 899 cm^{-1} and υ(C=C) stretch at 1599 cm^{-1}.

Resonance Raman Excitation Profiles

Solid state resonance Raman spectra for $[MoO(L^H)_2]^{2-}$ and $[MoO(L^O)_2]^{2-}$ were collected using laser excitation lines at 407, 458, 488, 514, 568 and 647 nm, and the data are displayed in Figure 2.27. The resonance Raman excitation profiles for $[MoO(L^H)_2]^{2-}$ show a resonance enhancement of the υ(Mo-S), υ(C=C) stretches and strong resonance enhancement of the υ(Mo≡O) stretch. The latter enhancement pattern predicts strong excited state distortions along the z-axis and not along the xy plane, and result from one electron promotions orbitals that possess Mo-d_{xz} or d_{yz} metal character. Enhancement of the υ(Mo-S) stretch and υ(C=C) stretch in $[MoO(L^H)_2]^{2-}$ indicates a strong excited state distortion in the x-y plane and along the C=C bond, suggesting one electron promotion to the excited state possessing Mo-d_{x2-y2} and C=C character. As a result, we anticipate band 5 will involve one electron promotion to the excited state that possesses Mo-$d_{xz/yz}$ or d_{z2} with some L^H ligand character. The $[MoO(L^O)_2]^{2-}$ compound has similar rRaman excitation profile trend as observed in $[MoO(L^H)_2]^{2-}$.

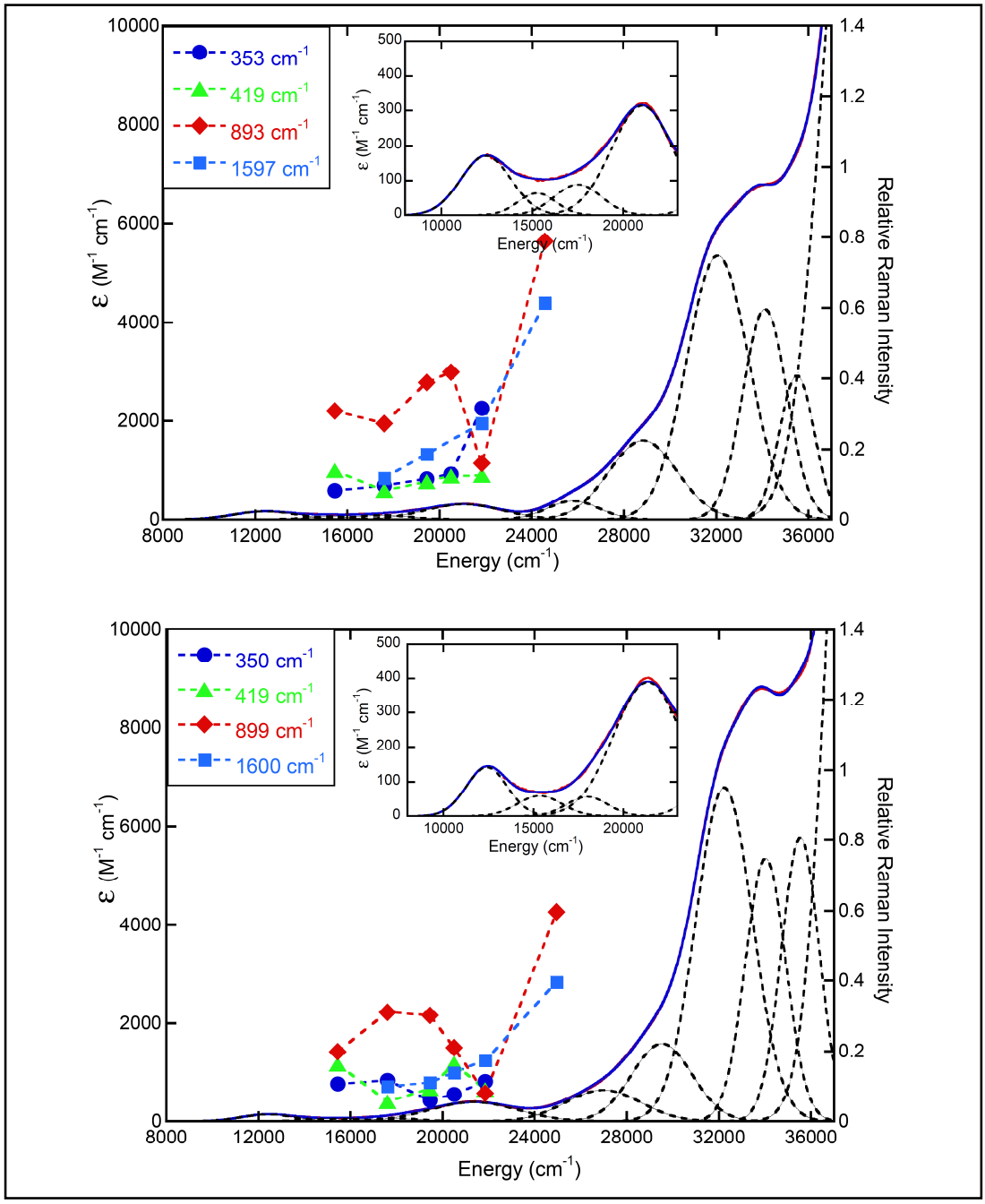

Figure 2.27: Resonance Raman excitation profiles for $[MoO(L^{H})_2]^{2-}$ (top) showing υ(S-Mo-S) bending at 352 cm^{-1}, υ(Mo-S) stretch at 418 cm^{-1}, υ(Mo≡O) stretch at 893 cm^{-1} and υ(C=C) stretch at 1597 cm^{-1}. $[MoO(L^{O})_2]^{2-}$ (bottom) showing υ(S-

Mo-S) bending at 350 cm^{-1}, υ(M-S) stretch at 419 cm^{-1}, υ(Mo≡O) stretch at 899 cm^{-1} and υ(C=C) stretch at 1600 cm^{-1}.

2.7.1.2 Effect of L^H and L^O Ligands Substituents on the Electronic Structure of $[MoO(L^H)_2]^{2-}$ and $[MoO(L^O)_2]^{2-}$ Compounds

Substitution on ene-1,2-dithiolenes ligands has a large effect on the electronic structure of $[MoO/S/Se(L^{COOMe})_2]^{2-}$, $[MoS/Se(L^{Ph})_2]^{2-}$, $[MoOCl(L_2{}^{ipro/meth})]^{+}$ and $[MoO(L^{ipro})(SPh)_2]$ compounds. Geometry optimized DFT results from $[MoO(L^{H/O})_2]^{2-}$ compounds show that the LUMO, LUMO+1, LUMO+2, LUMO+3 and LUMO+5 orbitals possess metal character as opposed to the ligand character observed in $[MoO/S/Se(L^{COOMe})_2]^{2-}$ and $[MoS/Se(L^{Ph})_2]^{2-}$ compounds. Table 2-4 summarizes the percentage composition of the LUMO - LUMO+4 orbitals for $[MoO(L^H)_2]^{2-}$ and $[MoO(L^O)_2]^{2-}$ and the molecular orbital contour plots are displayed in Figure 2.28. The four sulfur atoms in the equatorial position that derive from the L^O/L^H ligands dominantly interact with molybdenum through σ bonding and destabilize the $d_{x^2-y^2}$ orbital, while the apical oxo dominantly destabilizes the d_{z^2}, d_{xz} and d_{yz} respectively. The combined effects of equatorial and apical ligands interacting with the metal center lead to a $d_{x^2-y^2}$, d_{z^2}, $d_{xz/dyz}$ and d_{xy} splitting pattern, where d_{xy} is the redox orbital. The absence of ligand character in the low-energy unoccupied orbitals results from the L^H and L^O ligands possessing strong donor properties. This is supported by rRaman excitation profiles shown in Figure 2.27 which indicate an enhancement of the

υ(Mo=O) stretch from low to higher energy excitation indicating the presence of $d_{xz/yz}$ acceptor orbitals in these one-electron promotions. Additionally, DFT results show that the d_{xy} orbital occurs at 2.49 and 2.25 eV while the d_{xz} and d_{yz} orbital energies occur at 6.49 eV and at ~6.30 eV in the $[MoO(L^{H})_2]^{2-}$ and $[MoO(L^{O})_2]^{2-}$ compounds.

Table 2-4: Molecular orbital description of $[MoO(L^{H})_2]^{2-}$ and $[MoO(L^{O})_2]^{2-}$ compounds.

Wave functions	Fragments	$MoO(LH)_2$	$MoO(LO)_2$
LUMO	Mo	69.49	65.42
	Oxo	11.97	15.93
	$S_{dithiolene}$	4.53	6.52
LUMO+1	Mo	73.16	76.44
	Oxo	8.75	11.79
	$S_{dithiolene}$	3.51	7.46
LUMO+2	Mo	46.49	53.23
	Oxo	11.08	4.81
	$S_{dithiolene}$	14.39	12.40
LUMO+3	Mo	94.34	94.28
	Oxo	1.48	1.97
	$S_{dithiolene}$	-1.36	-1.04
LUMO+4	Mo	82.09	87.25
	Oxo	2.79	2.53
	$S_{dithiolene}$	0.21	-0.53

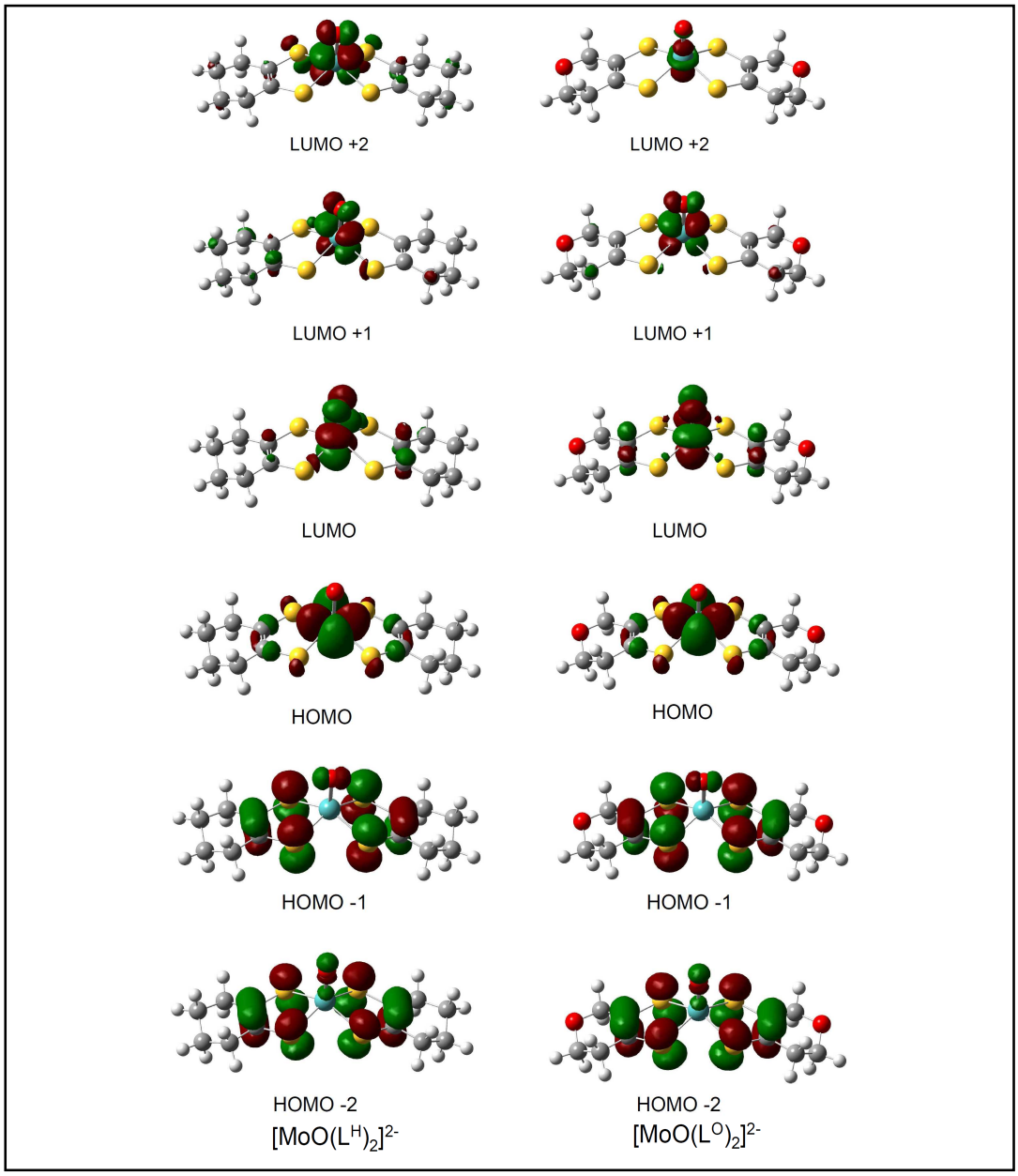

Figure 2.28: Molecular orbital electron density contours for valence orbitals in $[MoO(L^{H})_2]^{2-}$ and $[MoO(L^{O})_2]^{2-}$ compounds.

2.7.1.3 Band Assignments and the Nature of Charge Transfer Transitions

Geometry optimization calculations, followed by ground state and excited calculations, were performed on a frozen first coordination sphere that contained four sulfurs and the molybdenum atom as described by crystal structure geometry for $[MoO(L^{H})_2]^{2-}$ and $[MoO(L^{O})_2]^{2-}$. A combination of Gaussian resolved room temperature electron absorption, rRaman experiments, bonding calculation and ground state and excited state calculations have been utilized in band assignments. $[MoO(L^{H})_2]^{2-}$ and $[MoO(L^{O})_2]^{2-}$ have very similar electronic absorption spectra and rRaman excitation profiles. Therefore, their electronic structures are expected to be similar, so their band assignments will be discussed together.

Band 1: This band (12,520 cm^{-1}) can be assigned as a ligand field HOMO → LUMO transition, where the HOMO possesses Mo-d_{xy} character and the LUMO has Mo-d_{yz} + Oπ^* character in both $MoO(L^{H})_2]^{2-}$ and $[MoO(L^{O})_2]^{2-}$ compounds. The small oscillator strength (f =0.00085) calculated for this transition and the small intensity of this band are consistent with its assignment as ligand field transition.

Bands 2 and 3: Band 2 (15,280 cm^{-1}) is assigned as a combination of one electron promotions from HOMO → LUMO+1 and HOMO → LUMO+2 whereas band 3 (17,520 cm^{-1}) is assigned as the HOMO-1 → LUMO+1 transition in both

$[MoO(L^{H})_2]^{2-}$ and $[MoO(L^{O})_2]^{2-}$ compounds. The HOMO possesses Mo-d_{xy} character and the HOMO-1 possesses asymmetric S_{op} + Oπ^* character, while the LUMO+1 and LUMO+2 possess Mo-d_{xz} + Oπ^* character. The HOMO → LUMO+1 and HOMO → LUMO+2 one electron promotions are manifested in the electron density difference map (EDDM) in Figure 2.29. This assignment is supported by rRaman excitation profiles (Figure 2.27) that show the υ(Mo=O) stretch is resonantly enhanced with 15,456 (647 nm) and 17,606 cm^{-1} (568 nm) excitation. The weak intensity of band 2 is indicative of their ligand field character.

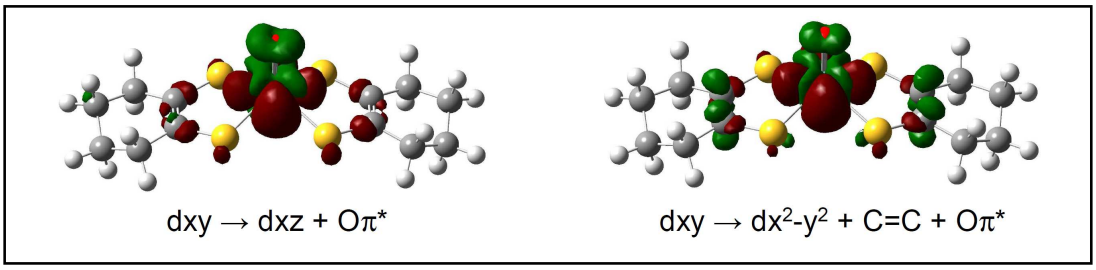

Figure 2.29: Electron density difference map (EDDM) for $[MoO(L^{H})_2]^{2-}$ showing the ligand field transitions observed in bands 2 (left) and 5 (right), where red indicates electron donation in the transition and green indicates electron acceptance in the transition.

Band 4: Resonance enhancement of the C=C and Mo-S stretches, concurrently with an Mo=O stretch enhancement decrease in the 21,834 cm^{-1} (458 nm) excitation laser lines, are observed in the rRaman excitation profile at band 4 (21,150 cm^{-1}). This band is assigned as the HOMO → LUMO+6 transition since

the HOMO possesses Mo-d_{xy} character and the LUMO+6 has Mo-d_{x2-y2} + C=Cπ^* characters. Therefore, we anticipate enhancement of υ(C=C) and υ(Mo-S) stretches and not the υ(Mo=O) stretch, which is consistent with what is observed in the rRaman excitation profile and hence confirms the assignment.

Band 5: This band (25,780 cm^{-1}) is assigned as HOMO → LUMO+3, and a combination of one electron promotions that include HOMO → LUMO+2 and HOMO → LUMO+6. Since the HOMO-1 possesses Mo-d_{xy} character, the LUMO+2 has Mo-d_{xz} + Oπ^* character, the LUMO+3 possesses Mo-d_{z2} character, and the LUMO+6 has Mo-d_{x2-y2} + C=Cπ^* character we anticipate resonance enhancement of υ(C=C) and υ(Mo=O) stretches. This is what is observed in the rRaman excitation profile (Figure 2.7.4) where we observe a strong enhancement of the υ(C=C) and υ(Mo=O) stretches which confirm our assignment.

Band 6: Band 6 (28,850 cm^{-1}) is assigned as a metal to ligand charge transfer band involving HOMO-1 → LUMO+2 and HOMO-1 → LUMO+3 transitions for $[MoO(L^H)_2]^{2-}$. However, for $[MoO(L^O)_2]^{2-}$ this band is assigned as HOMO-1 → LUMO+2 and HOMO-1 → LUMO+4 respectively. The HOMO-1 has asymmetric S_{op} bonding character with the metal and C=Cπ ligand bonding character. The LUMO+2 for $[MoO(L^H)_2]^{2-}$ is similar to LUMO+4 orbital in the $[MoO(L^O)_2]^{2-}$ and possesses Mo-d_{xz} + Oπ^* character. The LUMO+3 is similar to LUMO+2 in $[MoO(L^O)_2]^{2-}$ and has Mo-d_{z2} character. The intensity observed for this band is consistent with the calculated oscillator strengths (f = 0.0155 and 0.0169 for

$[MoO(L^{H})_2]^{2-}$ and f = 0.0092 and 0.0126 for $[MoO(L^{O})_2]^{2-}$) supporting the LMCT assignment.

Band 7: This band (32,060 cm^{-1}) is assigned as a combination of HOMO-2 → LUMO+1, HOMO-2 → LUMO+3 and HOMO-1 → LUMO+6 transitions. The HOMO-2 possesses totally symmetric S_{op} bonding character with respect to the metal and C=Cπ bonding character. The HOMO-1 possesses antisymmetric S_{op} character and C=Cπ bonding character, while the LUMO+1 and LUMO+3 orbitals possess d_{yz} + Oπ* and Mo-d_{z2} character. The LUMO+6 possesses Mo-d_{x2-y2} + C=Cπ* character, which is apparently in the electron density difference map (EDDM) presented in Figure 2.30.

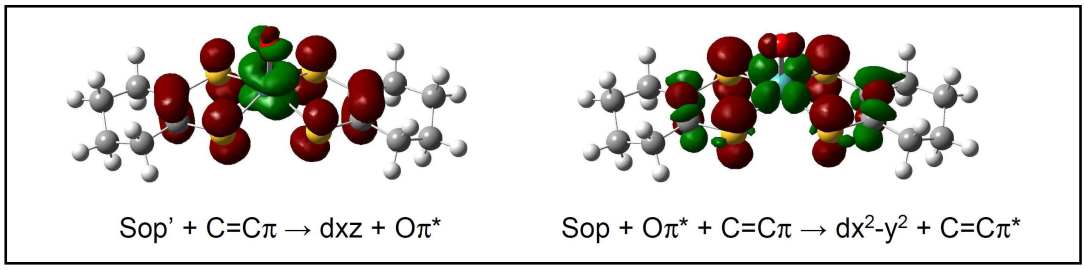

Figure 2.30: Electron density difference map (EDDM) for $[MoO(L^{H})_2]^{2-}$ showing the LMCT transitions present in band 7, where red indicates electron donation in the transition and green indicates electron acceptance in the transition.

Band 8 and 9: Band 8 (34,110 cm^{-1}) is assigned as HOMO → LUMO+9 transition (f = 0.0072 for $[MoO(L^{H})_2]^{2-}$), whereas band 9 (35,500 cm^{-1}) is assigned as a transition originating from a combination of one electron promotions from the

HOMO-3 → LUMO and HOMO-1 → LUMO+7 (f = 0.0105). The HOMO, HOMO-1 and LUMO descriptions have been covered above, therefore HOMO-3 possesses antisymmetric S_{op} character, while LUMO+7 and LUMO+9 possess $d_{x^2-y^2}$ and d_{z^2} + Oπ* + S_{op} character. The intensities for these bands are consistent with the calculated oscillator strengths.

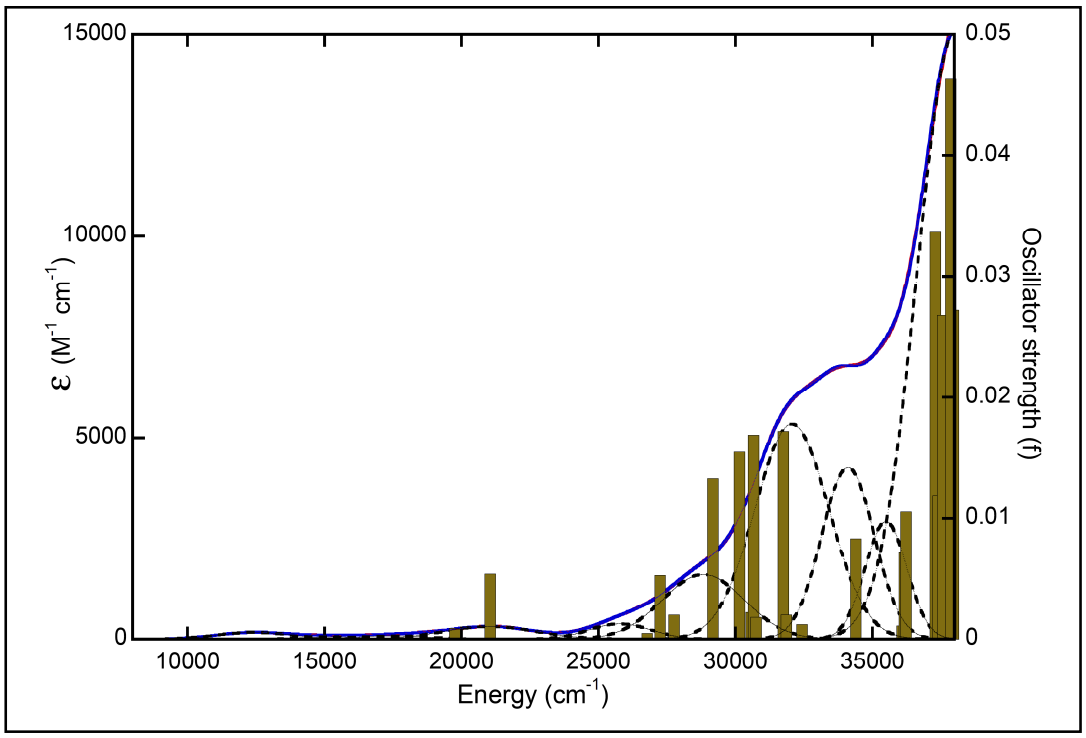

Figure 2.31: $[MoO(L^{H})_2]^{2-}$ Gaussian resolved electronic absorption spectrum with calculated transitions and oscillator strengths.

Band 10: This is an intense band (38,000 cm^{-1}) and is assigned comprised of HOMO-3→LUMO+1, HOMO-4→LUMO and HOMO-4→LUMO+1 transitions with oscillator strengths of 0.0337, 0.0268, and 0.0463, respectively. The HOMO-3

orbital possesses asymmetric S_{op} character and displays a non-bonding interaction with the metal. The HOMO-4 has symmetric S_{ip} ligand character while the LUMO and LUMO+1 possess Mo-d_{yz} + Oπ^* and Mo-d_{xz} + Oπ^* character, respectively. The strong oscillator strength calculated (Figure 2.31) for this transition is consistent with the strong intensity of this band.

2.7.2 Discussion

The Effect of LH and LO Ligands in the Redox Processes

The DFT results show that the d_{xy} orbital is at 2.49 and 2.25 eV, while the d_{xz}, d_{yz} orbitals occurs at 6.49 and ~6.30 eV for the $[MoO(L^H)_2]^{2-}$ and $[MoO(L^O)_2]^{2-}$ compounds, respectively. Electrochemical results reported by Sugimoto et al.[66,57] show redox potentials of -0.70 and -0.56 V for the $[MoO(L^H)_2]^{2-}$ and $[MoO(L^O)_2]^{2-}$ compounds, respectively. The lower potential observed for $[MoO(L^H)_2]^{2-}$ agrees with the LUMO energies that indicate $[MoO(L^H)_2]^{2-}$ is less stabilized than $[MoO(L^O)_2]^{2-}$ with respect to one-electron oxidation. Therefore, the negative potentials observed in these compounds are consistent with the relative donating power of the L^H and L^O ligands. However, the greater electron donating ability of the ligands makes them easier to oxidize with respect to the electron withdrawing dithiolenes discussed earlier. Lim and coworkers reported a redox potential of -0.62 V for $[MoO(S_2C_2Me_2)_2]^{2-}$,[76] that lies in between the $[MoO(L^H)_2]^{2-}$ and $[MoO(L^O)_2]^{2-}$ redox potentials. In summary, all three compounds have electron donating ligands that result in more facile Mo(IV) → Mo(V) oxidations. Both DFT calculation and electrochemical results on $[MoO(L^{H/O})_2]^{2-}$

compounds agree well in terms of their redox properties and therefore support a hypothesis that L^{O} and L^{H} ligands are electron donating in nature.

2.8 Cyclohexene-1,2-dithiolate (L^H) and 1,2–diphenyl (L^{Ph}) Mono-oxo Tungsten Compounds

The tungsten enzymes are similar to Mo DMSO Reductase family enzyme members. The gene sequence and active site crystal structure of the oxidized tungsten enzyme formate dehydrogenase from *D. gigas* have been reported. The active site possesses two pyranopterin dithiolenes, a selenocysteine, and thiol/hydroxyl ligand coordinated to the molybdenum ion to form a distorted trigonal prismatic geometry.[9,38,42] Very few spectroscopic studies have been performed on the oxidized or reduced form of this enzyme, and the crystal structure of the reduced tungsten containing formate dehydrogenase has not been reported thus far.

W-dithiolene model compounds have been utilized to study oxygen transfer reactivity,[77] the influence of the apical chalcogen substituent on reactivity [60] and electronic structure,[74,78] as active site mimics[79-81] in order to develop a better understanding of W containing enzymes like formate dehydrogenase. In this study we use $[WO/S(L^{Ph})_2]^{2-}$ and $[WO(L^H)_2]^{2-}$ as first generation analogues for the formate dehydrogenase active site in order to understand the effect of the apical chalcogen and ene-1,2-dithiolene ligands on their electronic structure. This has been accomplished by utilizing a combination of spectroscopic and computational methods. Figure 2.32 displays the structure of the $[WO(L^H)_2]^{2-}$ and $[WO(L^{Ph})_2]^{2-}$ models which have a square pyramid geometry with four equatorial sulfur donors and an apical sulfur or oxygen donor bound to tungsten.

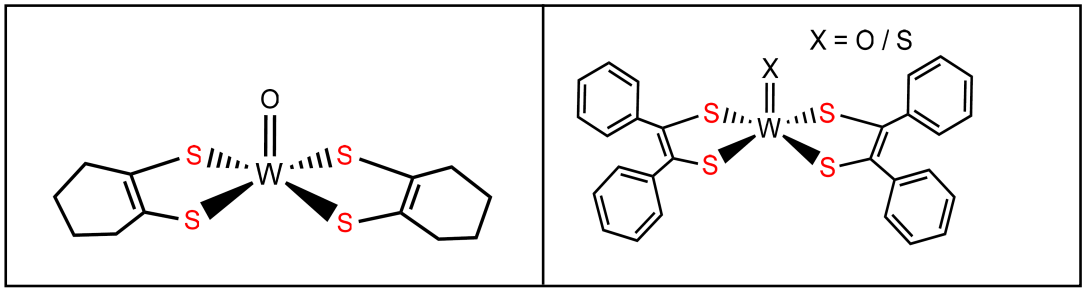

Figure 2.32: Structure of $[WO(L^{H})_2]^{2-}$ and $[WO/S(L^{Ph})_2]^{2-}$ compounds.

2.8.1 Results and Analysis

2.8.1.1 Electronic Absorption and rRaman Spectra

Room temperature electronic absorption spectra for $[WO/S(L^{Ph})_2]^{2-}$ and $[WO(L^{H})_2]^{2-}$ are displayed in Figures 2.33 and 2.34. The electronic absorption spectra show clearly four well resolved bands for $[WS(L^{Ph})_2]^{2-}$ and six bands are present in both $[WO(L^{Ph})_2]^{2-}$ and $[WO(L^{H})_2]^{2-}$ compounds. Three less intense peaks are observed at 13800 (ε ~1,430 $M^{-1}cm^{-1}$), 19500 (1,960 $M^{-1}cm^{-1}$) and 22950 cm^{-1} (3,580 $M^{-1}cm^{-1}$) for $[WO(L^{Ph})_2]^{2-}$ while for $[WS(L^{Ph})_2]^{2-}$ these are observed at 14800 (ε ~550 $M^{-1}cm^{-1}$), 16400 (640 $M^{-1}cm^{-1}$) and 23800 cm^{-1} (5,180 $M^{-1}cm^{-1}$). The intensities of these bands indicate the presence of metal to ligand charge transfer and intraligand charge transfer transitions and not ligand field transitions. Additionally, two intense peaks are observed in the higher energy region at 29,200 (18,900 $M^{-1}cm^{-1}$) and 32,700 cm^{-1} (29,280 $M^{-1}cm^{-1}$) for $[WO(L^{Ph})_2]^{2-}$ and at 28,200 (16,460 $M^{-1}cm^{-1}$) and 33,250 cm^{-1} (33,100 $M^{-1}cm^{-1}$) for $[WS(L^{Ph})_2]^{2-}$ respectively. These bands have a higher intensity that is likely associated with intraligand charge transfer transitions. The electronic absorption spectra overlay for the $[WO/S(L^{Ph})_2]^{2-}$ compounds in Figure 2.33 do not show a

clear progressive spectral shift at low energy as observed in $[MoS/Se(L^{Ph})_2]^{2-}$, and this is not common for compounds possessing apical sulfido or selenido ligands a parity of the coordinated dithiolenes.

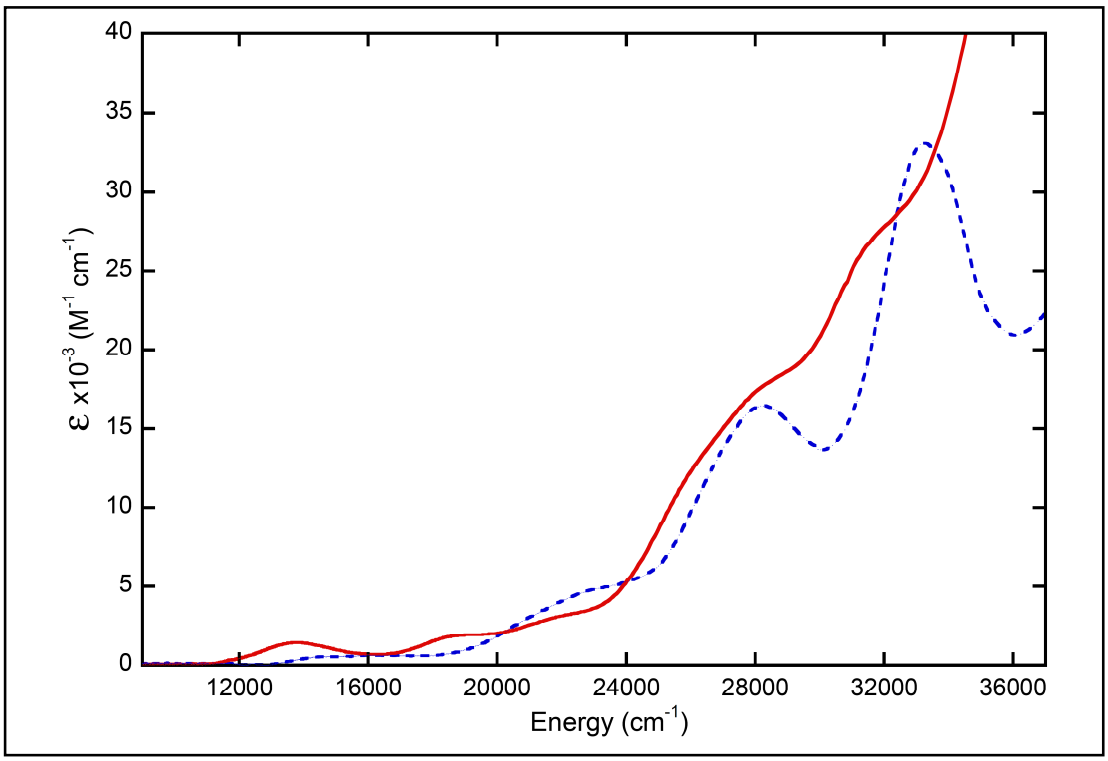

Figure 2.33: Room temperature electronic absorption spectra overlay for $[WO(L^{Ph})_2]^{2-}$ (——) and $[WS(L^{Ph})_2]^{2-}$ (- - -) compounds.

An overlay of $[WO(L^{H})_2]^{2-}$ and $[WO(L^{Ph})_2]^{2-}$ room temperature electronic absorption spectra is given in Figure 2.34. These spectra reveal a similar total number of bands in the 9,000 to 40,000 cm^{-1} region. Three low energy bands are observed at 14540 cm^{-1}, 19150 cm^{-1} and 22,400 cm^{-1} for $[WO(L^{H})_2]^{2-}$ which occur at slightly higher energy compared to $[WO(L^{Ph})_2]^{2-}$ where band maxima are

observed at 13750 cm^{-1}, 18800 cm^{-1} and at 22,350 cm^{-1}. Using our prior Mo results as a guide, we would expect to observe low energy LF and LMCT transitions in $[WO(L^{H})_2]^{2-}$ and MLCT and ILCT transition with $[WO(L^{Ph})_2]^{2-}$ due to the electron donating L^{H} and electron withdrawing L^{Ph} dithiolene ligands.

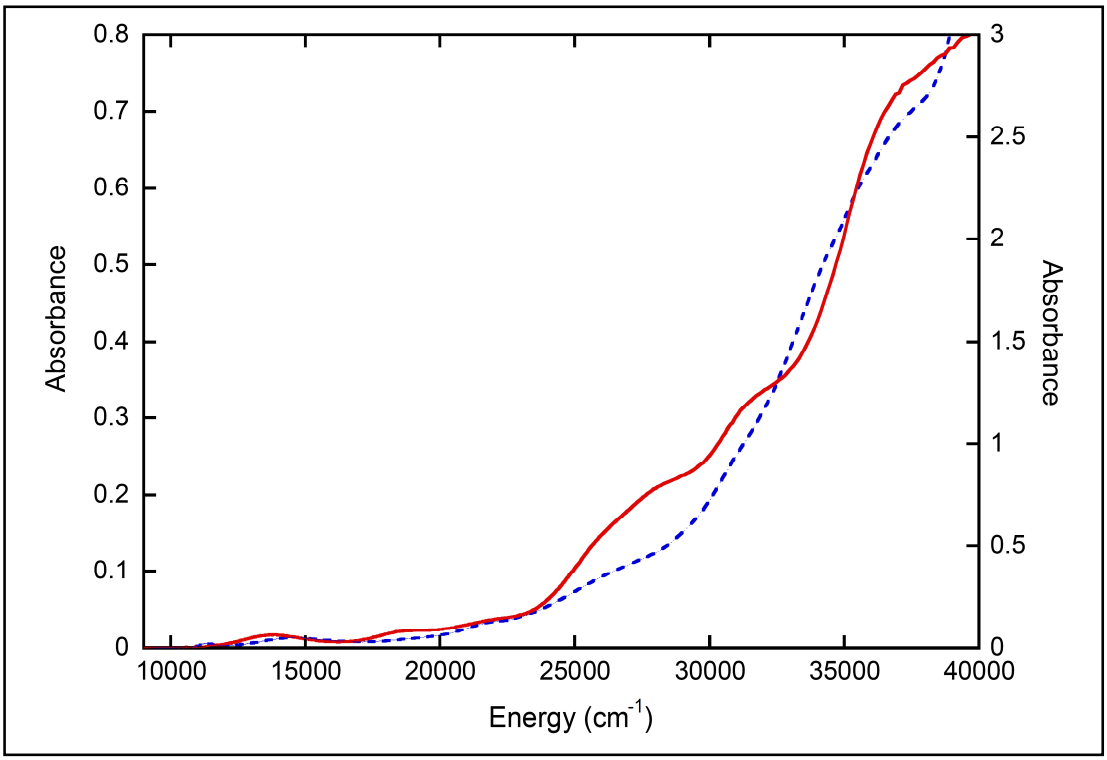

Figure 2.34: Room temperature electronic absorption spectral overlay for $[WO(L^{H})_2]^{2-}$ (– – –) and $[WO(L^{Ph})_2]^{2-}$ (——).

Resonance Raman Spectroscopy

Resonance Raman spectroscopy is a useful tool in studying the excited state properties of metallodithiolenes. Figure 2.35 shows Raman spectra for $[WO(L^{Ph})_2]^{2-}$ and $[WS(L^{Ph})_2]^{2-}$ compounds that reveal $\upsilon(W\text{-}S_{dithiolene})$ dithiolene

bends at 362 and 365 cm^{-1} and $\upsilon(W\text{-}S_{dithiolene})$ stretches at 392 and 397 cm^{-1} respectively. The vibrational energy differences observed in the $W\text{-}S_{dithiolene}$ bending and stretching modes for $[WS(L^{Ph})_2]^{2-}$ and $[WO(L^{Ph})_2]^{2-}$ are observed to be quite small. A strong $\upsilon(W\equiv O)$ stretch appears at 890 cm^{-1} in $[WO(L^{Ph})_2]^{2-}$ and the $\upsilon(W\equiv S)$ stretch occurs at 496 cm^{-1} for $[WS(L^{Ph})_2]^{2-}$. The observed frequency of the $\upsilon(W\equiv O)$ stretch is within the range observed for oxo-tungsten compounds.[60,72,74] The higher frequency region contains two stretches at 1176 and 1240 cm^{-1} associated with υ(C-C) attached to the phenyl for $[WO(L^{Ph})_2]^{2-}$ and at 1170 and 1240 cm^{-1} for $[WS(L^{Ph})_2]^{2-}$ compound. In addition, two intense bands are observed at 1547 and at 1591 cm^{-1} for $[WO(L^{Ph})_2]^{-2}$ and at 1532 and 1590 cm^{-1} for $[WS(L^{Ph})_2]^{2-}$ are associated with υ(C=C) and υ(Ph-ring) stretches respectively. The higher υ(C=C) stretch observed in $[WO(L^{Ph})_2]^{2-}$ is associated with the resonance stability of phenyl group which acts as π-acceptor.

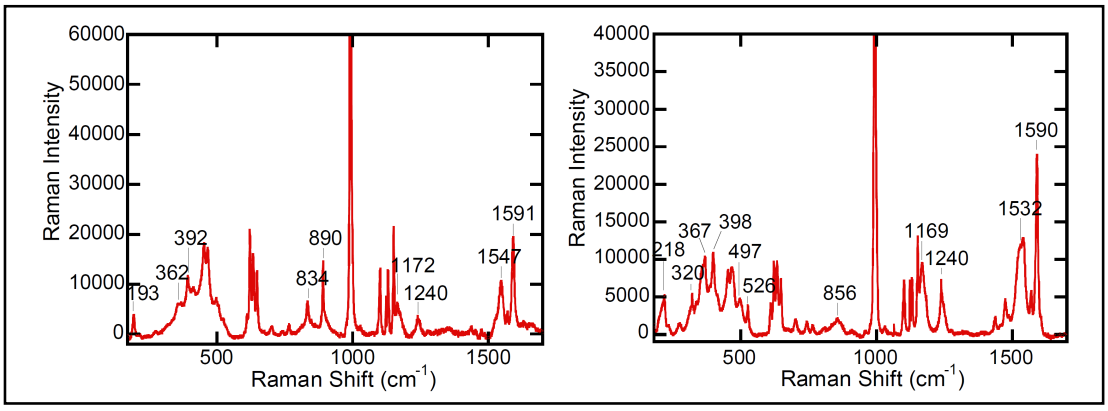

Figure 2.35: Resonance Raman spectrum for $[WO(L^{Ph})_2]^{2-}$ (left) showing υ(S-W-S) bending at 362 cm^{-1}, υ(W-S) stretch at 392 cm^{-1}, $\upsilon(W\equiv O)$ stretch at 890 cm^{-1}, υ(C-C-(Ph)) stretch at 1165 and 1240 cm^{-1}, υ(C=C) stretch at 1547 cm^{-1} and

υ(Ph-ring) stretch at 1591 cm^{-1}. $[WS(L^{Ph})_2]^{2-}$ (right) spectrum showing υ(S-W-S) bending at 367 cm^{-1}, υ(W-S) stretch at 398 cm^{-1}, υ(W≡S) stretch at 497 cm^{-1}, υ(C-C-(Ph)) stretch at 1169 and 1240 cm^{-1}, υ(C=C) stretch at 1539 cm^{-1} and υ(Ph-ring) stretch at 1590 cm^{-1}.

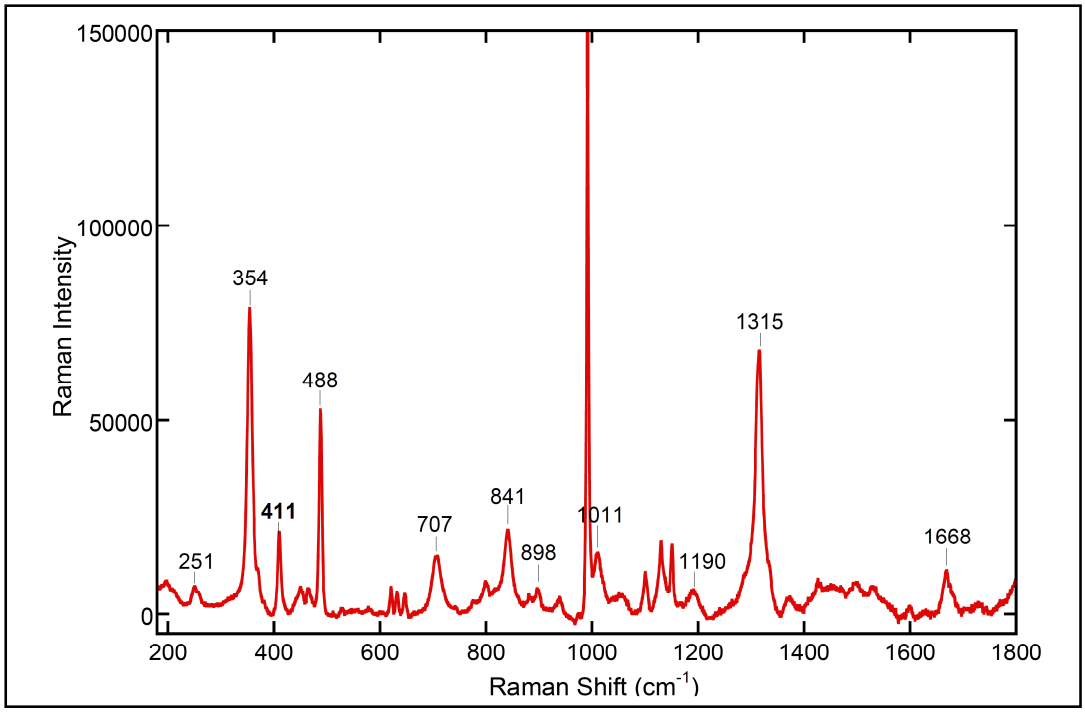

Figure 2.36: Resonance Raman spectrum for $[WO(L^{H})_2]^{2-}$ showing the υ(W-$S_{dithiolene}$) bending mode at 354 cm^{-1}, υ(W-S) stretch at 411 cm^{-1}, υ(W≡O) stretch at 898 cm^{-1}, υ(L^{H} ring) stretch at 1315 cm^{-1} and υ(C=C) stretch at 1668 cm^{-1}.

The resonance Raman spectrum for $[WO(L^{H})_2]^{2-}$ is presented in Figure 2.36 and shows a υ(W-$S_{dithiolene}$) bend at 354 cm^{-1} this is at slightly low frequency compared to the υ(W-$S_{dithiolene}$) bend for $[WO(L^{Ph})_2]^{2-}$. The υ(W-S) and υ(W≡O)

stretches are observed at 411 and 898 cm^{-1}, and this is within the range observed for oxo-tungsten compounds.[74] We note that the W-$S_{dithiolene}$ stretch is at slightly higher frequency than that observed in $[WO(L^{Ph})_2]^{2-}$ due to the stronger electron donating ability of L^H compared with L^{Ph}. The higher frequency region contains two stretches observed at 1315 and 1668 cm^{-1} associated with the L^H ring stretch and the symmetric C=C stretch. The υ(C=C) stretch is at higher frequency due to the strong donation ability of L^H ligand.

Resonance Raman Excitation Profiles

Resonance Raman excitation profiles for $[WO(L^{Ph})_2]^{2-}$ and $[WS(L^{Ph})_2]^{2-}$ are displayed in Figures 2.37 and 2.38. Strong enhancement of the υ(C=C) stretch and υ(Ph-ring) stretch are observed with increasing excitation energies. No enhancement of the υ(Mo=O) and υ(Mo-S) stretches have been observed which shows the absence of a dominant distortion along these modes in the excited states. Therefore, we anticipate that all of the transitions assigned for bands 2, 3 and 4 to possess L^{Ph} ligand character in their excited state due to strong distortions along C=C, C-C-(Ph) and Ph-ring stretching modes that are observed in the rRaman profile data.

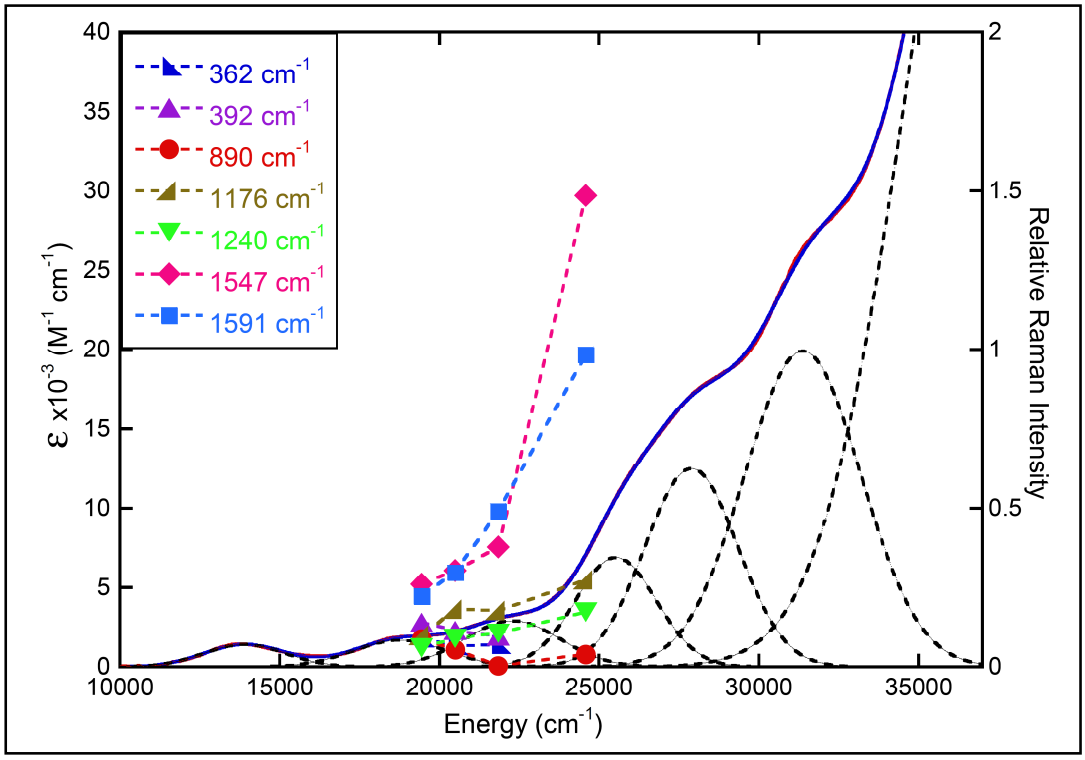

Figure 2.37: Resonance Raman excitation profiles for $[WO(L^{Ph})_2]^{2-}$ showing the υ(S-W-S) bend at 362 cm^{-1}, υ(W-S) stretch at 392 cm^{-1}, υ(W≡O) stretch at 890 cm^{-1}, υ(C-C-(Ph)) stretch at 1176 and 1240 cm^{-1}, υ(C=C) stretch at 1547 cm^{-1} and υ(Ph-ring) stretch at 1591 cm^{-1}.

The resonance Raman excitation profiles for $[WS(L^{Ph})_2]^{2-}$ (Figure 2.38) show weak enhancement of the υ(Mo≡O) stretch and υ(C-C-(Ph)) stretch accompanied by a strong enhancement of the υ(C=C) and υ(Ph-ring) stretches to higher energy. A progressive decrease in the enhancement of the υ(Mo-$S_{dithiolene}$) bend and the υ(Mo-S) stretch is observed going to higher energy, signifying a smaller distortion along these coordinates in the excited state. The

strong distortions along C=C and phenyl ring coordinates suggest excited states probed in bands 2, 3 and 4 to possess L^{Ph} and C=C ligand character.

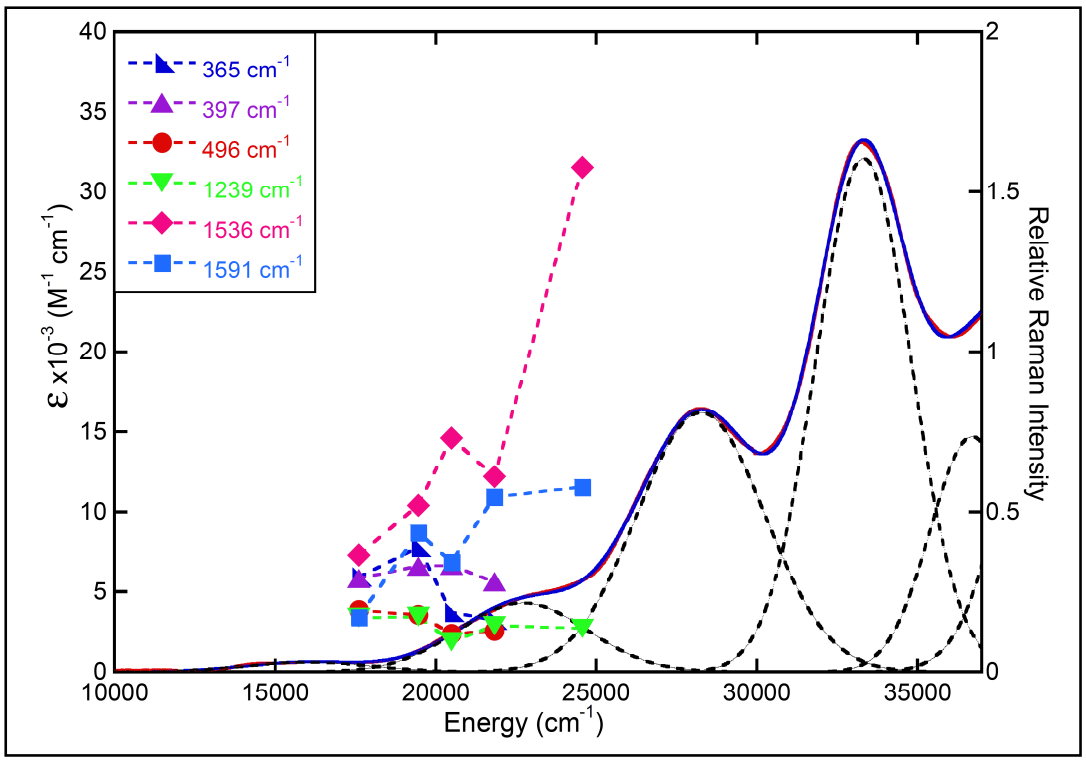

Figure 2.38: Resonance Raman excitation profiles for $[WS(L^{Ph})_2]^{2-}$ showing the υ(W-S) bend at 365 cm^{-1}, υ(W-S) stretch at 397 cm^{-1}, υ(W≡S) stretch at 496 cm^{-1}, υ(C-C-(Ph)) stretch at 1239 cm^{-1}, υ(C=C) stretch at 1536 cm^{-1} and υ(Ph-ring) stretch at 1591 cm^{-1}.

The resonance Raman excitation profile for $[WO(L^{H})_2]^{2-}$ is shown in Figure 2.39 and displays a strong enhancement of the $\upsilon(W\text{-}S_{dithiolene})$ bend and the $\upsilon(L^{H}$ ring) stretch accompanied with a weak enhancement of the υ(W≡O) stretch, υ(W-S) stretch, and υ(C=C) stretch. We anticipate from this data that the excited state

transition involved in band 3 will possess Mo-d_{xy} and L^H ligand character, whereas band 4 will possess Mo-$d_{xz/yz}$ and C=C ligand characters.

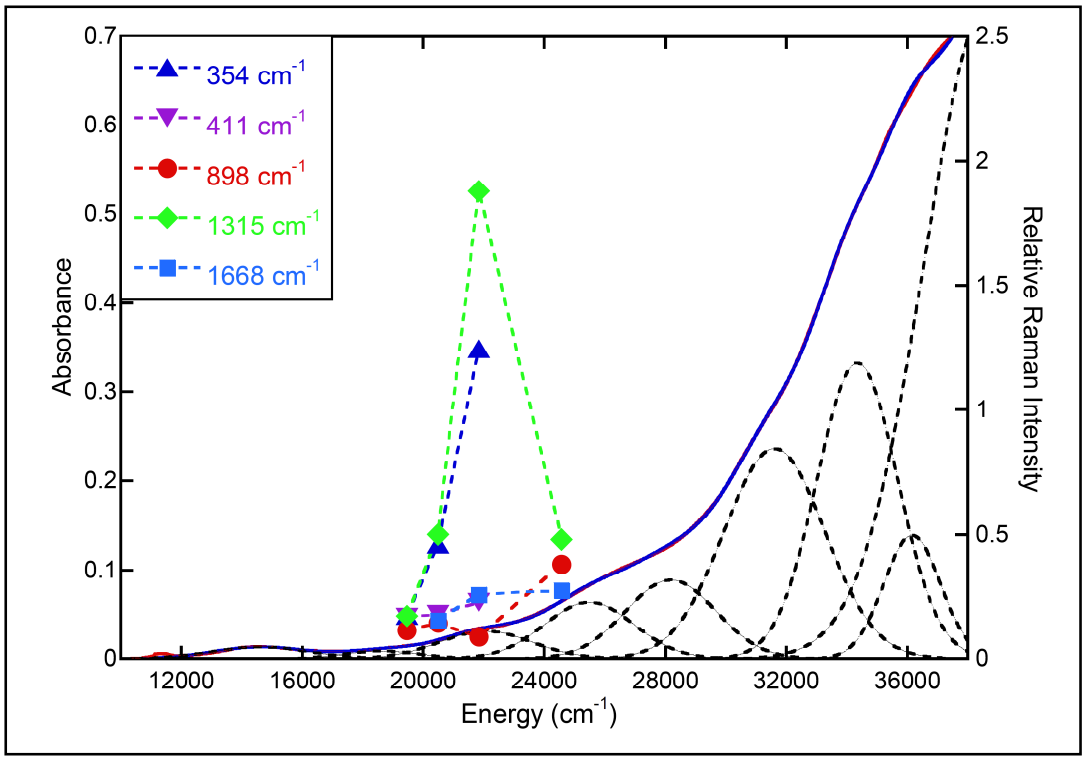

Figure 2.39: Resonance Raman excitation profiles for $[WO(L^H)_2]^{2-}$ showing the υ(S-W-S) bending at 354 cm^{-1}, υ(W-S) stretch at 411 cm^{-1}, υ(W≡O) stretch at 898 cm^{-1}, υ(L^H ring) stretch at 1315 cm^{-1} and υ(C=C) stretch at 1668 cm^{-1}.

2.8.1.2 Low Energy Ligand Field, LMCT, and LLCT Transitions and Band Assignments

Figure 2.33 shows the electronic absorption spectral overlay for $[WO(L^{Ph})_2]^{2-}$ and $[WS(L^{Ph})_2]^{2-}$ compounds. No progressive higher energy spectral shifts are observed in these two compounds from the different apical chalcogen ligands.

Band 1 in $[WO(L^{Ph})_2]^{2-}$ occurs at lower energy than in $[WS(L^{Ph})_2]^{2-}$, which is contrary to our expectation. As such, we have not been able to make a definitive assignment for this band in $[WO(L^{Ph})_2]^{2-}$. In addition, all other bands in the $[WO(L^{Ph})_2]^{2-}$ and $[WS(L^{Ph})_2]^{2-}$ compounds have been very tentatively assigned based on the rRaman and the ground and excited state transitions obtained from time dependent DFT calculations (TD-DFT). Here, we focus on band assignments for the $[WS(L^{Ph})_2]^{2-}$ compound as it relates to our data for $[WO(L^{Ph})_2]^{2-}$. The band assignment section represents a project report on these compounds, as work here is ongoing.

Band 1: Band 1 (16,100 cm^{-1}) in $[WS(L^{Ph})_2]^{2-}$, is assigned as a combination of the HOMO → LUMO+1, HOMO → LUMO+2 and HOMO-1 → LUMO transitions. Molecular orbital characters are presented in Table 2.46 below and should be used in understanding the nature of these band assignments.

Band 2: Bands 4 and 5 in the $[WO(L^{Ph})_2]^{-2}$ are similar to band 2 (22,700 cm^{-1}) in $[WS(L^{Ph})_2]^{2-}$. Band 2 in $[WS(L^{Ph})_2]^{2-}$ is assigned comprised of HOMO → LUMO+4, HOMO → LUMO+6 and HOMO-1 → LUMO+5 transitions. HOMO possesses Mo-d_{xy} character and HOMO-1 possesses asymmetric S_{op} character with apical $S\pi^*/O\pi^*$ ligand character. The LUMO+4, LUMO+5, and LUMO+6 orbitals possess mainly phenyl ring ligand character in both the $[WS(L^{Ph})_2]^{2-}$ and $[WO(L^{Ph})_2]^{2-}$ compounds. Figure 2.40 displays the electron density deference map (EDDM) showing intraligand charge transfer in both $[WS(L^{Ph})_2]^{2-}$ and

$[WO(L^{Ph})_2]^{2-}$ compounds. The υ(C=C) and υ(Ph-ring) stretches are resonantly enhanced with 458 nm (21,834 cm^{-1}) excitation in $[WS(L^{Ph})_2]^{2-}$. However, for $[WO(L^{Ph})_2]^{2-}$ a strong enhancement of υ(C=C) and υ(Ph-ring) stretches occur with a slight enhancement of the υ(C-C-(Ph)) stretch using 407 nm (24,570 cm^{-1}) excitation (Figure 2.37). The strong distortions along C=C and phenyl ring modes support an assignment as a combination of metal to ligand and Intraligand charge transfer transitions.

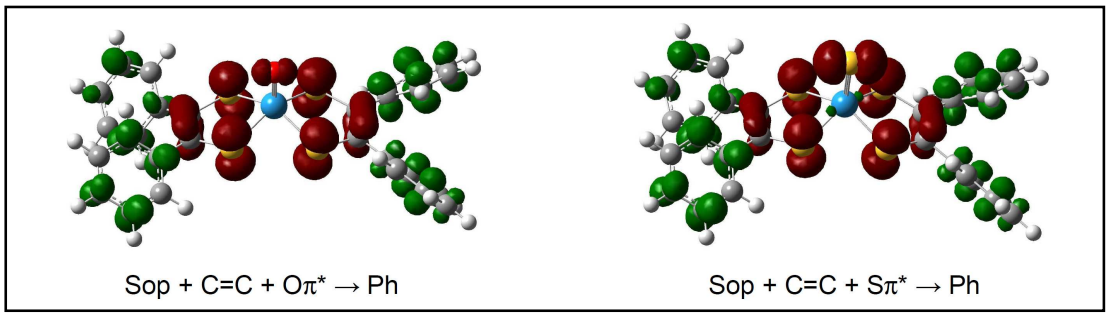

Figure 2.40: Electron density difference maps (EDDMs) for $[WO(L^{Ph})_2]^{2-}$ (left) and $[WS(L^{Ph})_2]^{2-}$ (right) showing the intraligand charge transfer transition for band 2.

Bands 3 and 4 in the electronic absorption spectrum for $[WS(L^{Ph})_2]^{2-}$ are assigned based on initial ground and excited state calculations. Figures 2.41 and 2.42 display Gaussian resolved electronic absorption spectra for $[WS(L^{Ph})_2]^{2-}$ and $[WO(L^{Ph})_2]^{2-}$ with calculated oscillator strengths and transition energies.

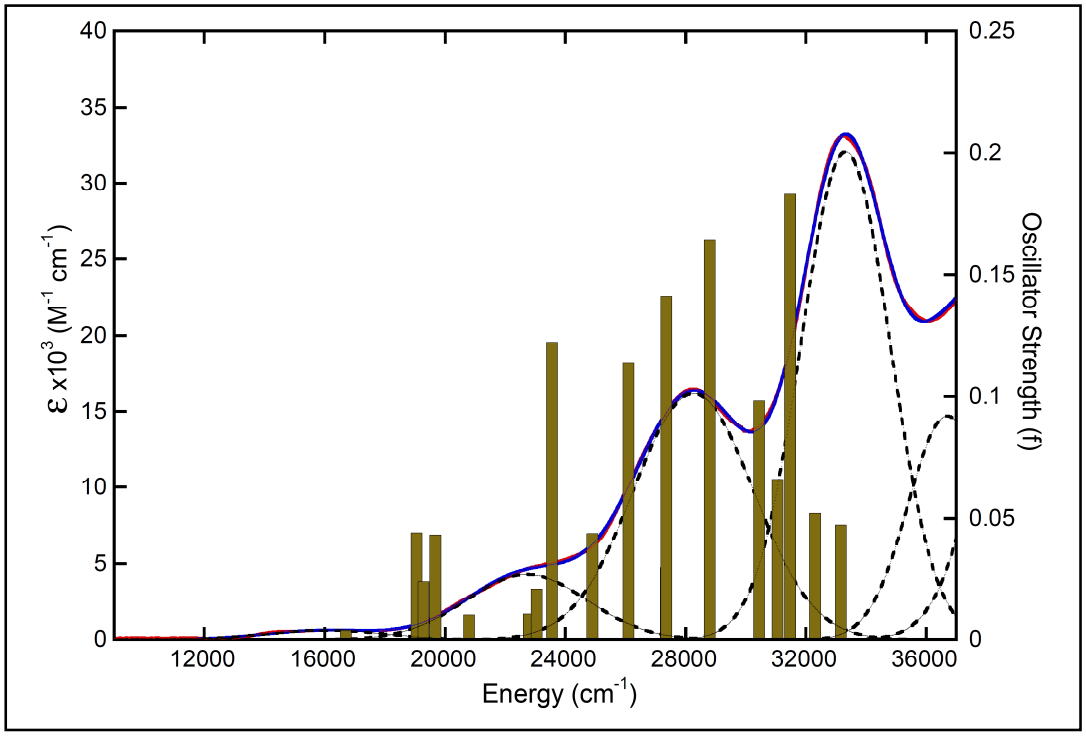

Figure 2.41: $[WS(L^{Ph})_2]^{2-}$ Gaussian resolved electronic absorption with calculated oscillator strength.

Band 3: This band (28,230 cm^{-1}) is similar to band 6 in $[WO(L^{Ph})_2]^{2-}$ and is assigned as a combination of HOMO-1 → LUMO+7 (f =0.0438), HOMO-2 → LUMO (f =0.11420, HOMO-3 → LUMO+1 (f =0.1413), HOMO-4 → LUMO (f =0.1644) and HOMO-2 → LUMO+2 (f =0.0983) transitions for $[WS(L^{Ph})_2]^{2-}$. However, a combination of HOMO-2 → LUMO (f =0.1195), HOMO-1 → LUMO+7 (f =0.0362), HOMO-3 → LUMO (f =0.2192), HOMO-2 → LUMO+2 (f =0.0439) and HOMO-4 → LUMO+1 (f 0.1134) transitions are assigned for $[WO(L^{Ph})_2]^{2-}$. The strong oscillator strength (calculated oscillator strengths are in brackets) observed in these transitions are consistent with the greater intensity for this band.

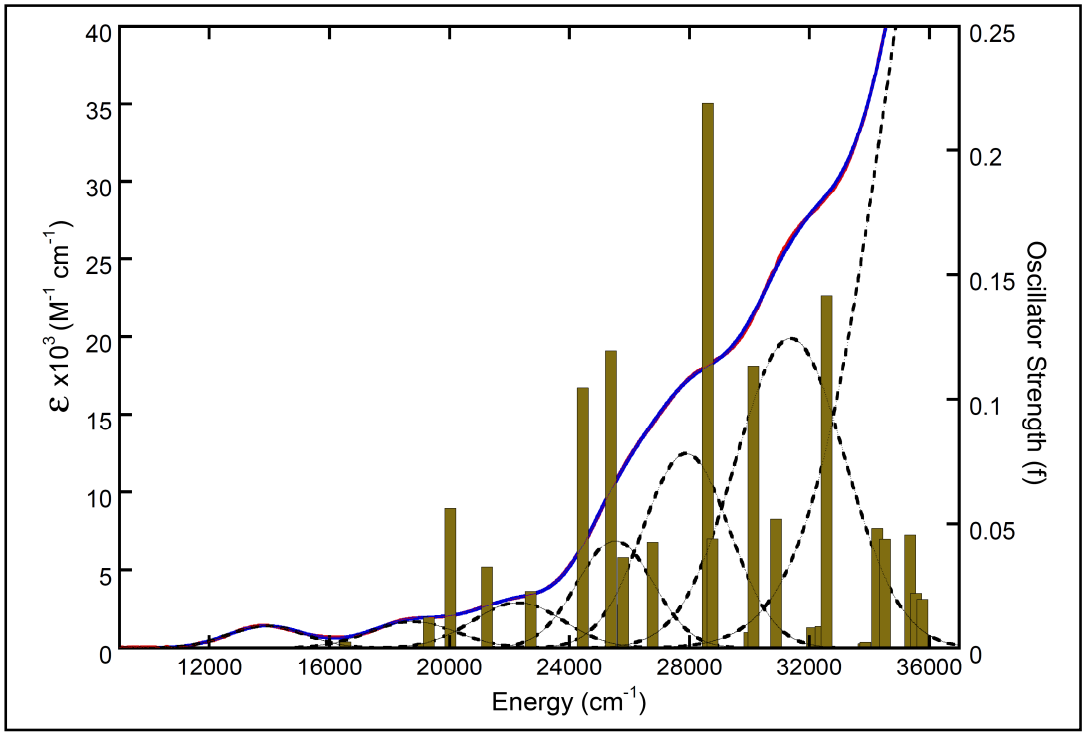

Figure 2.42: $[WO(L^{Ph})_2]^{2-}$ Gaussian resolved room temperature electronic absorption with calculated oscillator strength (f).

Band 4: Band 4 (33,250 cm^{-1}) is assigned as a combination of HOMO-5 → LUMO+1 (f =0.0657), HOMO-2 → LUMO+4 (f =0.1832) and HOMO-3 → LUMO+5 (f =0.0520) transitions for $[WS(L^{Ph})_2]^{2-}$. This band is similar to band 7 in $[WO(L^{Ph})_2]^{2-}$ and assigned as HOMO-2 → LUMO+5 (f =0.0518), HOMO-5 → LUMO+1 (f =0.1417) and HOMO-3 → LUMO+5 (f =0.0481) respectively. Molecular orbital characters are presented in Table 2.46 below. This band contains higher energy intraligand charge transfer transitions for both $[WS(L^{Ph})_2]^{2-}$ and $[WO(L^{Ph})_2]^{2-}$ and the tentative assignment is supported with their strong oscillator strengths that agree with a strong intensity observed for this band.

$[WO(L^{H})_2]^{2-}$ Compound

Band assignments for this compound are different than those posited for the $[WO/S(L^{Ph})_2]^{2-}$ compounds. Band assignment differences are due to differences in the nature of the dithiolene coordinated to the tungsten center. Therefore, all bands are assigned based on electronic absorption and rRaman spectra, combined with ground and excited state calculations performed on the fully optimized geometry.

Band 1: This band (14,600 cm^{-1}) is assigned as the HOMO → LUMO+1 transition, where HOMO possesses W-d_{xy} character and the LUMO+1 has W-d_{yz} + Oπ^* + C=Cπ^* character. Molecular orbital characters are presented in Table 2.46 below. The low calculated oscillator strength for this transition is consistent with the weak band intensity and supports this assignment as a ligand field transition.

Band 2: This band (18,650 cm^{-1}) is assigned as the HOMO → LUMO transition where the LUMO contains W-d_{yz} character. Molecular orbital characters are presented in Table 2.46 below. A slight enhancement of the υ(W=O) stretch is observed in the rRaman excitation profile (Figure 2.39) that supports the assignment as a ligand field transition.

Band 3: Band 3 (22,070 cm^{-1}) is assigned as the HOMO → LUMO+2 transition, where the LUMO+2 orbital possesses W-d_{xz} + Oπ^* + C=Cπ^* character.

Molecular orbital characters are presented in Table 2.46 below. Therefore, we anticipate an excited state distortion along the W≡S and C=C bonds. This is observed in the rRaman excitation profile of $[WO(L^{Ph})_2]^{2-}$ that shows enhancement of W-S, L^H ring, C=C and W=O stretches. The electron density different map (EDDM) in Figure 2.43 shows the ligand field transition.

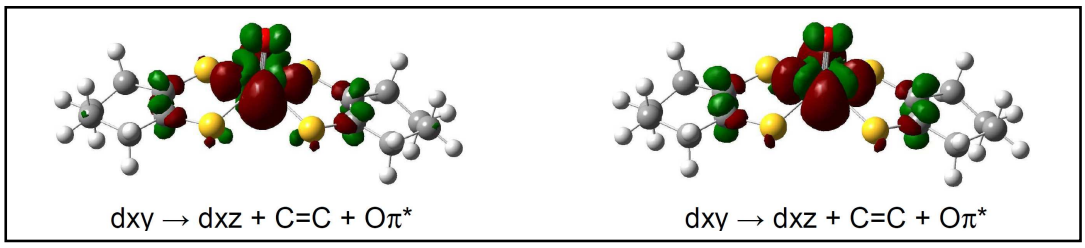

Figure 2.43: Electron density difference map for $[WO(L^H)_2]^{2-}$ showing the ligand field transitions assigned for band 3 (left) and band 4 (right), where an electron density loss in the transition is shown in red, and an electron density gain in green.

Band 4: Combinations of HOMO → LUMO+4 and HOMO → LUMO+6 one electron promotions are assigned for band 4 (25,500 cm^{-1}). The HOMO possesses W-d_{xy} character while LUMO+4 has d_{z2} character and the LUMO+6 possesses bent W-d_{xz} + Oπ* + C=Cπ* + asymmetric S_{op} characters. The rRaman excitation profiles in Figure 2.39 display resonance enhancement of υ(W=O), υ(C=C) stretches with a decrease in υ(L^H ring) stretch intensity using 24,570 cm^{-1} (407 nm) excitation which provides some support for this assignment. The ligand field transition for this band is depicted in Figure 2.43 which is consistent with the

enhancement of C=C and W=O stretching modes observed in the rRaman spectra.

Bands 5 to 9 have been assigned solely based on bonding calculations combined with ground and excited state calculations performed on the fully optimized $[WO(L^{H})_2]^{2-}$ geometry. Band assignments here are very tentative.

Band 5: This band (28,180 cm^{-1}) is assigned as combination of HOMO-1 → LUMO+2 and HOMO → LUMO+8 transitions with 0.0158 and 0.0051 oscillator strength. Asymmetric Sop + C=Cπ + Oπ* character are contained in the HOMO-1 orbital, while the LUMO+2 possesses W-d_{xz} + Oπ* + C=Cπ* + asymmetrical S_{op} characters and LUMO+8 has Mo-d_{yz} + Oπ* + C=Cπ* characters respectively. This is the first ligand to metal charge transfer (LMCT) transition observed in this compound and it is depicted in the EDDM in Figure 2.44. The intensity of this band agrees well with the calculated oscillator strengths.

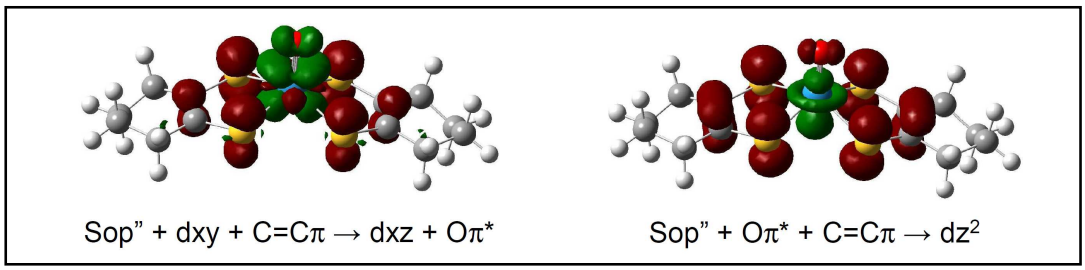

Figure 2.44: Electron density different maps (EDDMs) showing the ligand to metal charge transfer (LMCT) for band 5 (left) and band 6 (right), where an

electron density loss in the transition is shown in red, and an electron density gain in green.

Band 6: A combination of HOMO-1 → LUMO+4 and HOMO-2 → LUMO+1 transitions are assigned for this band (31,600 cm^{-1}). The HOMO-1 → LUMO+4 transition has a calculated oscillator strength of 0.0404 and the LUMO+4 orbital contains pure Mo-d_{z2} character. Symmetric S_{op} + C=Cπ* character is present in the HOMO-1 orbital as depicted in the EDDM (Figure 2.44). In addition HOMO-2 → LUMO+1 (f =0.0033) transition has only a small contribution in this band. Here, the HOMO-2 orbital possesses symmetric S_{op} + C=Cπ character and the LUMO+2 has Mo-d_{yz} + Oπ* + C=Cπ* character.

Band 7: This band (34,350 cm^{-1}) involves a combination of ligand field and LMCT transitions with calculated oscillator strengths of 0.0055 and 0.0169. The individual transitions that contribute to this band are assigned as HOMO-2 → LUMO and HOMO-1 → LUMO+6. The HOMO, HOMO-1 and LUMO characters have been described above while LUMO+6 possesses bent Mo-d_{xz} + C=Cπ* + Oπ* + asymmetric S_{op} character.

Band 8: A ligand field HOMO → LUMO+9 transition is assigned for band 8 (36,170 cm^{-1}), with Mo-d_{xy} character in the HOMO and Mo-d_{xz} + Oπ* characters in LUMO+9 orbital. This weaker band in the high energy region of the electronic

absorption spectrum with small a calculated oscillator strength (f =0.0138) that correlates well with its assignment as ligand field transition.

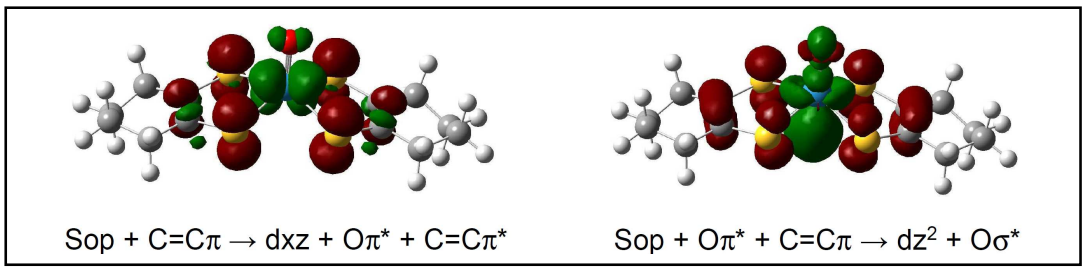

Figure 2.45: Electron density difference maps (EDDMs) showing LMCT transitions for band 7 (left) and band 9 (right), where an electron density loss in the transition is shown in red, and an electron density gain is in green.

Band 9: This is the highest energy (38,700 cm^{-1}) and most intense band assigned in this compound. We assign this band as arising from a HOMO-1 → LUMO+7 transition, with asymmetric S_{op} + C=Cπ* + Oπ* character in the HOMO-1 and Mo-d_{z2} + Oσ* + total symmetric S_{op} character in the LUMO+7. The electron density different map (EDDM) in Figure 2.8.14 shows the ligand to metal charge transfer character in this transition. The intensity of this band agrees well with the calculated oscillator strength (0.0412).

2.8.3 Discussion

Effect of L^{Ph} Ligands on the Electronic Structure of $[WO/S(L^{Ph})_2]^{2-}$

The electronic structure of $[WO/S(L^{Ph})_2]^{2-}$ and $[WO(L^{H})_2]^{2-}$ have been studied spectroscopically and computationally. The effect of the L^{Ph} ligands have been

observed in rRaman excitation profiles for $[WO/S(L^{Ph})_2]^{2-}$ and indicates a strong resonance enhancement of υ(C=C) and υ(phenyl ring) stretches from low to higher energy, confirming the presence of orbitals with ligand character in specific charge transfer excited states. This observation is supported by DFT calculations that show the LUMO to LUMO+7 orbitals to possess ligand character and not metal character for both $[WO/S(L^{Ph})_2]^{2-}$ compounds as displayed in Figure 2.46. The presence of ligand characters in the unoccupied orbitals is due to the strong π-acceptor character of the dithiolene phenyl substituents that tends to destabilize the ligand orbitals and allow the dithiolene to develop electron acceptor character. This phenomenon has been observed in $[MoO/S/Se(L^{COOMe})_2]^{2-}$ (section 2.5), $[MoS/Se(L^{Ph})_2]^{2-}$ (section 2.6) and $[MoOCl(L_2^{ipro/meth})]$ (section 2.9) with electron withdrawing dithiolene ligands. However, for the $[WO(L^{H})_2]^{2-}$ compound, rRaman and DFT calculations do not show the presence of L^H ligands in the unoccupied orbitals, and this is the result of the electron donating nature of L^H ligand. This is evident in the molecular orbital electron density plot for $[WO(L^{H})_2]^{2-}$ in Figure 2.46.

Goddard et al. reported a cyclic potential of -0.62 V for $[WO(L^{Ph})_2]^{2-}$ and $[WS(L^{Ph})_2]^{2-}$ compounds from electrochemical studies.[60] These values are more negative compared to the -0.46 and -0.43 V values observed for $[MoO(L^{Ph})_2]^{2-}$ and $[MoS(L^{Ph})_2]^{2-}$ compounds.[57] The more negative potential is consistent with ability of tungsten to be easily oxidized, which is also supported with our DFT calculation that show the W-d_{xy} orbital is less stabilized and occurs at 1.76 and

1.69 eV for $[WO(L^{Ph})_2]^{2-}$ and $WS(L^{Ph})_2]^{2-}$ compared to 1.48 eV observed in the $[MoS(L^{Ph})_2]^{2-}$ compound. Therefore these results show that the tungsten compounds are easier to oxidize, but the W(IV) state can stabilized with electron withdrawing dithiolene ligands.

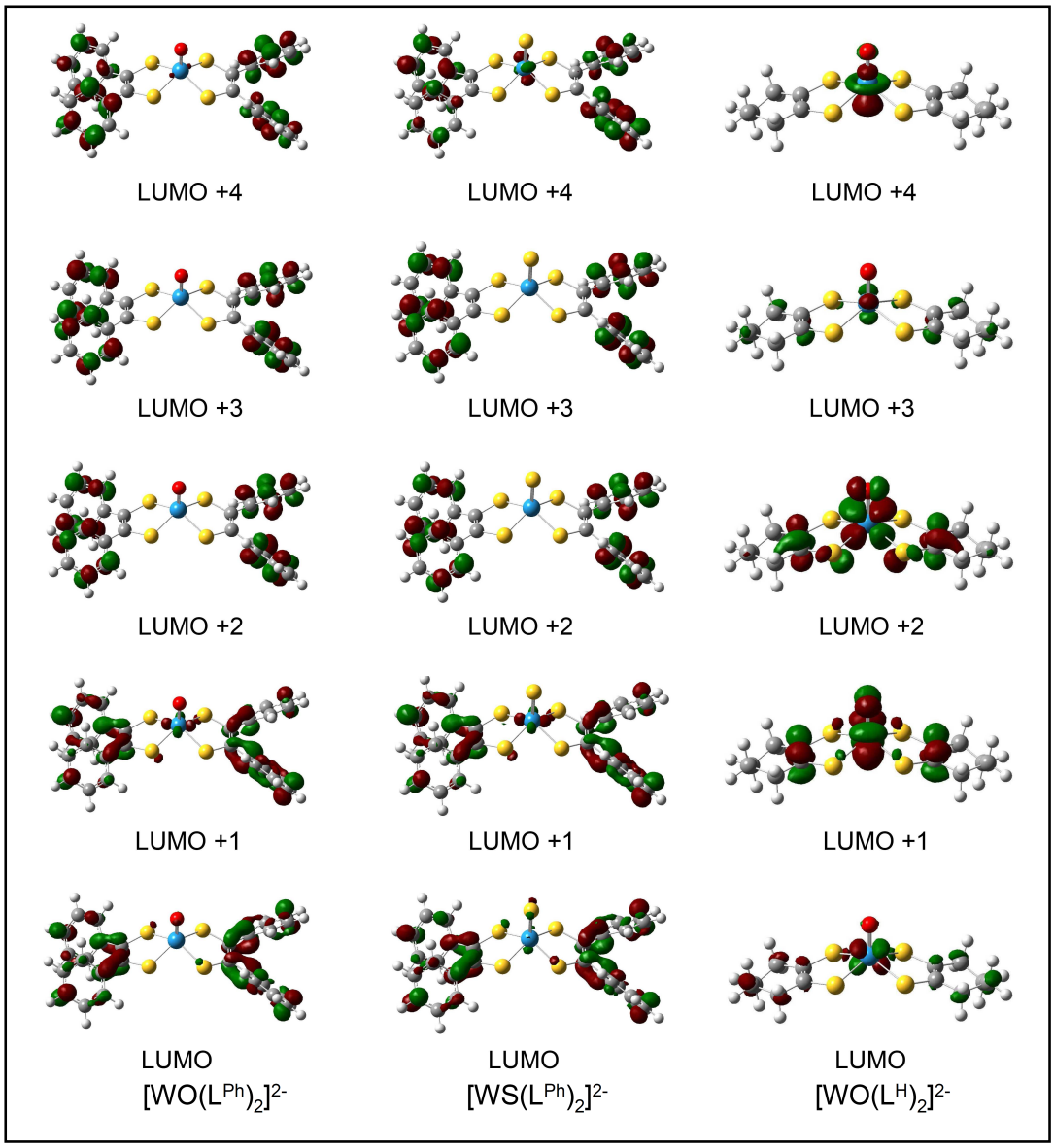

Figure 2.46: Molecular orbital electron density plots for $[WO(L^{Ph})_2]^{2-}$ and

$[WS(L^{Ph})_2]^{2-}$ compounds showing the ligand characters in the unoccupied orbitals whereas $[WO(L^{H})_2]^{2-}$ has metal based unoccupied orbitals.

2.9 Oxo Molybdenum Chloro Bis-1,4-dimethyl/isopropyl-piperazine-2,3-dithione $[MoOCl(L_2^{ipro/meth})]^+$ and Oxo-Molybdenum-1,4-diisopropyl piperazine-2,3-dithione Benzene Thiolate $[MoO(L^{ipro})(S_2Ph_2)]$ Compounds

Molybdenum and tungsten containing compounds have been synthesized as model for the active sites of pyranopterin molybdenum enzymes. These enzymes possess one or two pyranopterin dithiolenes attached to the metal center. The DMSO reductase enzyme family has two pyranopterin dithiolenes attached to the molybdenum as a unique characteristic of this enzyme family. Pyranopterin dithiolenes are known as redox non-innocent ligands and the pyranopterin dithiolene has been implicated in electron transfer processes in the enzymes.[55] Therefore, the pyranopterin ene-1,2-dithiolene ligand can exist as i). a radical mono ionic form (one electron oxidation), ii). an oxidized form (thione/thiete) and, iii). a reduced form (thiolene/thiolate).[46,55,82] Recently Matz et al.[71] reported the synthesis of Tp*MoO(S2BMOQO) that possessed a unique thiol/thione ligand system. The mixture of thiol/thione ligand character suggested by spectroscopic and computational investigations was observed in the crystal structure of the compound.

Figure 2.47 shows the structure of $[MoOCl(L_2^{ipro})]^+$, $[MoOCl(L_2^{meth})]^+$ and $[MoO(SPh)(L^{ipro})]$ compounds that are discussed in this section. These compounds possess dithione type ligands that representing an oxidized form of the pyranopterin dithiolene ligand. Electronic absorption and rRaman

spectroscopies, combined with DFT calculations, have been used to probe the nature of the low energy charge transfer transitions in these compounds and the effect of the dithione ligand on electronic structure in these compounds.

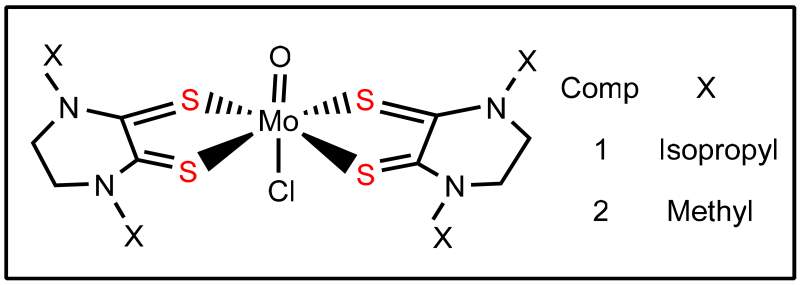

Figure 2.47: Structure of the $[MoOCl(L_2^{ipro/meth})]^+$ compounds.

2.9.1 Results and Analysis

2.9.1.1 Electronic Absorption and rRaman Spectra

Electronic Absorption Spectra

Room temperature electronic absorption spectra for $[MoOCl(L_2^{ipro/meth})]^+$ and $[MoO(L^{ipro})(SPh)_2]$ are displayed in Figures 2.48 and 2.49. The electronic absorption spectra for $[MoOCl(L_2^{ipro})]^+$ and $[MoOCl(L_2^{meth})]^+$ show a similar number of bands. Three well resolved bands that possess intensity below 5,000 $M^{-1}cm^{-1}$ are observed at ~13,500, at 19,500 and 24,400 cm^{-1} while an intense absorption peak with ε ~30,000 $M^{-1}cm^{-1}$ is observed at 31,150 and at 32,050 cm^{-1} for $[MoOCl(L_2^{ipro})]^+$ and $[MoOCl(L_2^{meth})]^+$. The energy differences in the higher energy bands is associated with strong electron donation from the isopropyl group attached to piperazine-2,3-dithione ring. The electronic absorption spectrum for $[MoO(L^{ipro})(SPh)_2]$ differs considerably from the bis-dithione

compound spectra and this is due to the substitution of two benzene thiolate ligands for the 1,2-dithione ligand.

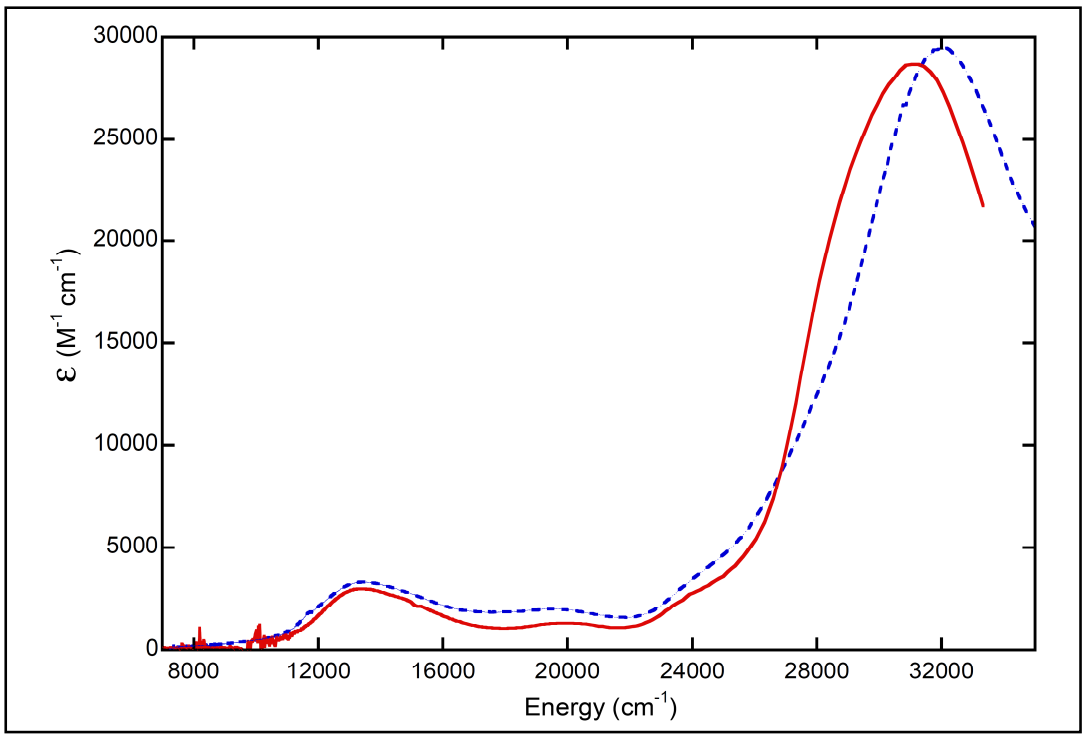

Figure 2.48: Room temperature electronic absorption overlay for $[MoOCl(L_2^{methyl})]^+$ (- - -) and $[MoOCl(L_2^{ipro})]^+$ (——) compounds.

The electronic absorption spectrum for $[MoO(L^{ipro})(SPh)_2]$ has three well resolved bands and two shoulders in the 8,000cm^{-1} to 37,000 cm^{-1} spectral region. The low energy region contains a weak shoulder at 15,350 cm^{-1} and a strong band at 18,250 cm^{-1}. These bands occur at higher energy when compared to $[MoOCl(L_2^{ipro})]^+$ the compound were the low-energy intense band occurs at 13,500cm^{-1}. The second band occurs at 23,650 cm^{-1}, while the third band appears as a well resolved peak at 29,850 cm^{-1}.

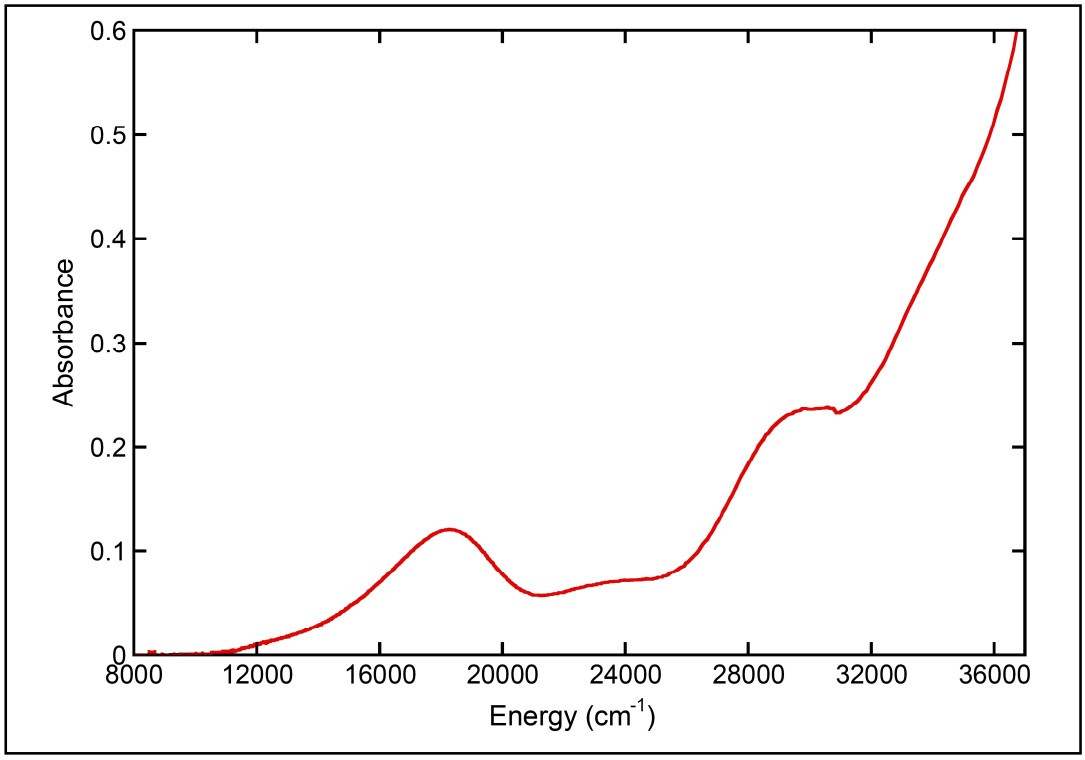

Figure 2.49: Room temperature electronic absorption spectrum for $[MoO(L^{ipro})(SPh)_2]$.

Resonance Raman Spectra

Solid state resonance Raman for $[MoOCl(L_2^{ipro})]^+$, $[MoOCl(L_2^{meth})]^+$ and $[MoO(L^{ipro})(SPh)_2]$ were collected using 407, 458, 488, 514, 568 and 647 nm laser excitation wavelengths. Figure 2.50 shows the resonance Raman spectra with the υ(Mo-S) stretches at 339 and 373 cm^{-1} for $[MoOCl(L_2^{ipro})]^+$ and at 383 cm^{-1} for $[MoOCl(L_2^{methyl})]^+$. These υ(Mo-S) vibrations are within the range of reported values for other υ(Mo-S) stretches.[74] A strong band is observed at 941 cm^{-1} in $[MoOCl(L_2^{ipro})]^+$ that appears as a weak band at 946 cm^{-1} in $[MoOCl(L_2^{methyl})]^+$. This band is assigned as the $\upsilon(Mo \equiv O)$ stretch consistent with

previously reported Mo≡O stretches for mono-oxo molybdenum bis-dithiolene compounds.[74,83] In the higher frequency region, these spectra contain very intense bands at 1120 cm^{-1} associated with υ(C-C & C=S) stretches and at 1227 cm^{-1} for the υ(C-C) stretch in $[MoOCl(L_2^{ipro})]^+$. However, for $[MoOCl(L_2^{methyl})]^+$ strong intense bands associated with C-C & C=S and C-C stretches occur at 1122 cm^{-1} and at 1260 cm^{-1} respectively. Figure 2.51 shows vibrational bands associated with υ(Mo≡O), υ(C-C & C=S), υ(C-C) and υ(C-N) stretches for the $[MoOCl(L_2^{ipro})]^+$ compound.

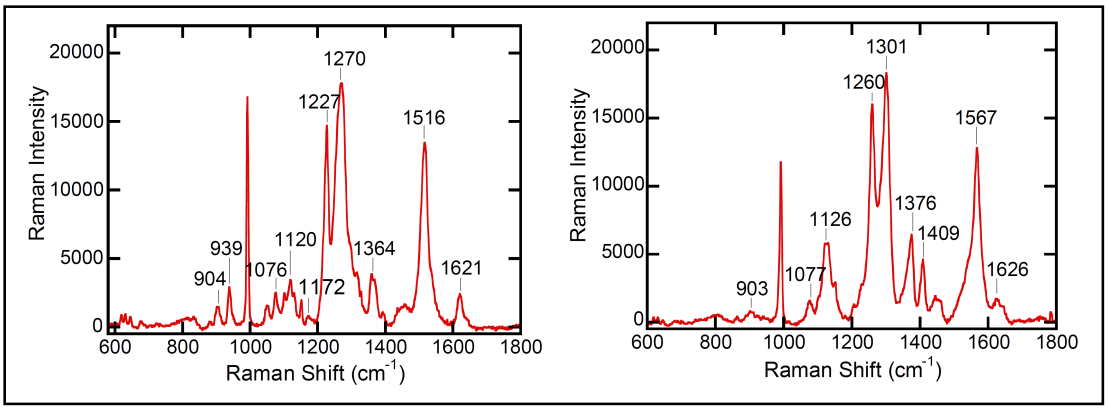

Figure 2.50: Solid state rRaman spectrum at 407 nm (24,570 cm^{-1}) excitation laser line for $[MoOCl(L_2^{ipro})]^+$ (left) showing υ(Mo≡O) at 940 cm^{-1}, υ(C-C & C=S) stretch at 1120 cm^{-1}, υ(C-C) stretch at 1227 $cm^{-1}$and υ(C-N) stretch at 1516 cm^{-1}. (Right) $[MoOCl(L_2^{meth})]^+$ at 407 nm excitation laser line showing υ(C-C & C=S) stretch at 1126 cm^{-1}, υ(C-C) stretch at 1260 cm^{-1}, υ(L^{meth}) stretch at 1301 cm^{-1} and υ(C-N) stretch at 1567 cm^{-1}.

These results show that bands associated with the υ(C-C) stretch occur at low frequency compared to reported υ(C=C) stretches which normally occur between 1400 and 1600 cm^{-1} in oxo-molybdenum bis-dithiolene compounds. Raman data also shows a υ(C=S) stretch band at higher energy compared to reported C-S stretches which occurs between 600 and 800 cm^{-1} in metallodithiolenes.[84] These results are consistent with the reduction of bond order from C=C to C-C and an increase in bond order from C-S to C=S present in our structures. The υ(C-N) symmetric stretch appears at 1516 cm^{-1} in $[MoOCl(L_2^{ipro})]^+$ whereas in $[MoOCl(L_2^{meth})]^+$ it occurs at 1563 cm^{-1}. The higher frequency υ(C-N) stretch observed in $[MoOCl(L_2^{ipro})]^+$ is due to the electron donating power of isopropyl group at 1,4 positions in the piperazine that neutralize partial positive charge on the carbon and result in a strengthening of the N-C bond.

The resonance Raman spectrum for $[MoO(L^{ipro})(SPh)_2]$ is shown in Figure 2.51 and displays a band at 949 cm^{-1} associated with the υ(Mo≡O) stretch, which is close to 941 and 946 cm^{-1} observed in the $[MoOCl(L_2^{ipro/meth})]^+$ compounds. Furthermore, a rRaman band observed at 264 cm^{-1} is associated with the υ(Mo-S^{ipro}) bending mode and the bands at 330 and 385 cm^{-1} are associated with the υ(Mo-S^{ipro}) stretch. The band at 358 cm^{-1} is associated with υ(Mo-S^{Ph}) stretch in $[MoO(SPh)(L^{ipro})]$. The υ(Mo-$S_{dithiolene}$) stretch observed in this compound is typical for mono-oxo bis-dithiolene molybdenum compounds. Furthermore, the higher frequency region contains peaks at 1,221 and 1,267 cm^{-1} associated with

$\upsilon(L^{ipro}$ ring) and υ(C-C) stretches. The υ(C-C) stretch is at lower frequency as expected for a single bond and the υ(C-N) stretch is observed at 1576 cm^{-1}.

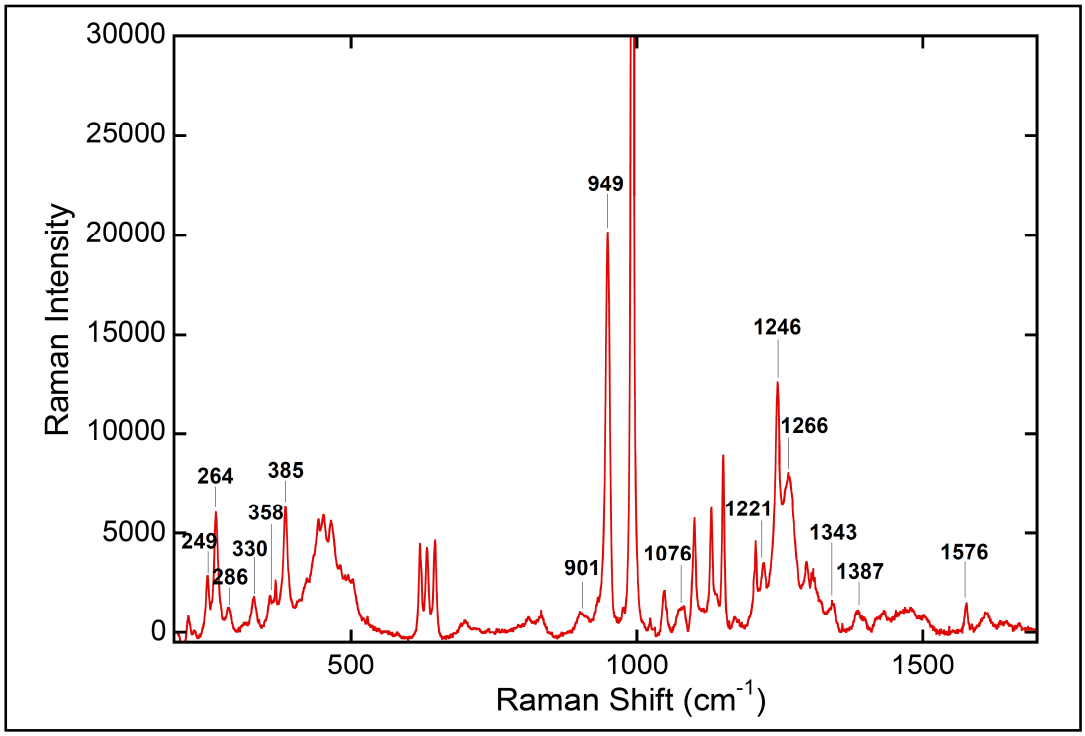

Figure 2.51: Solid state rRaman spectrum for [MoO(SPh)(L^{ipro})] using 458 nm (21,834 cm^{-1}) excitation showing υ(Mo≡O) at 940 cm^{-1}, υ(C-C & C=S) stretch at 1120 cm^{-1}, υ(C-C) stretch at 1227 $cm^{-1}$and υ(C-N) stretch at 1516 cm^{-1}.

Resonance Raman Excitation Profiles

Solid state resonance Raman excitation profiles have been constructed for the υ(Mo-S), υ(Mo≡O), υ(C-C & C=S), υ(C-C) and υ(C-N) stretches in [MoOCl(L_2^{ipro})]$^+$, [MoOCl(L_2^{meth})]$^+$ and [MoO(L^{ipro})$(SPh)_2$] using laser excitation wavelength between 407 and 676 nm. The data are displayed in Figures 2.52,

2.53 and 2.54 respectively. All vibrational band intensities were normalized relative to a Na_2SO_4 internal standard peak at 902 cm^{-1}. For $[MoOCl(L_2^{ipro})]^+$ the absorption maxima are observed at 13,400 cm^{-1}, at 19,500 cm^{-1}, at 24,400, and at 32,000 cm^{-1} while for $[MoOCl(L_2^{meth})]^+$ band maxima appear at 13,500, at 19,510, at 24,300, at 27,810 and at 32,000 cm^{-1}. Both compounds show enhancement of υ(C-C & C=S), υ(C-C) and υ(C-N) stretches from 20,000 cm^{-1} to lower energy. This result shows distortion along the $L^{ipro/meth}$ ligand in the excited state. Therefore, it is anticipated that we will observe one-electron promotions to virtual orbitals that possesses $L^{ipro/meth}$ ligand character.

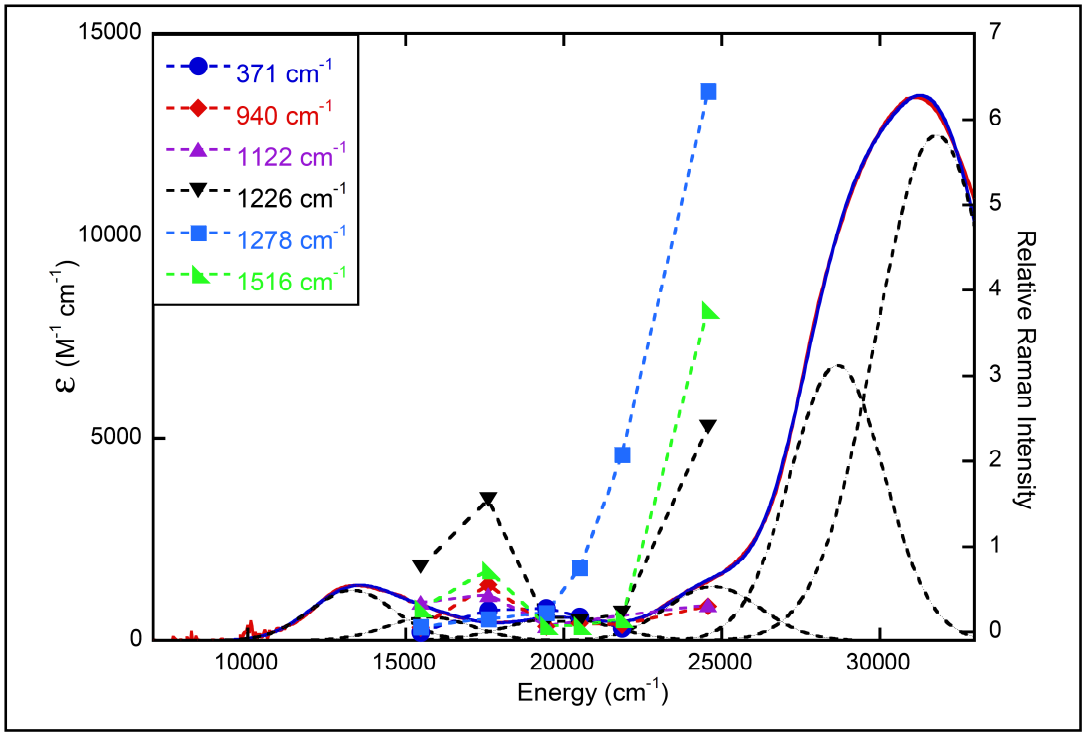

Figure 2.52: Solid state rRaman excitation profiles and electronic absorption spectrum for $[MoOCl(L_2^{ipro})]^+$ showing υ(Mo-$S_{dithiolene}$) at 371 cm^{-1}, υ(Mo≡O) at

940 cm^{-1}, υ(C-C & C=S) stretch at 1122 cm^{-1}, υ(C-C) stretch at 1226 cm^{-1}, $\upsilon(L^{ipro}$ ring) stretch at 1278 cm^{-1} and υ(C-N) stretch at 1516 cm^{-1}.

A small progressive enhancement of the $\upsilon(M\equiv O)$ stretch is observed only in the $[MoOCl(L_2^{ipro})]^+$ compound starting from 20,000 cm^{-1} to higher energy, that occurs concurrently with a strong enhancement of υ(C-C), $\upsilon(L^{ipro}$ ring) and υ(C-N) stretches, and a small enhancement of the υ(C-C & C=S) stretch in the two compounds. This results show a strong distortion along $L^{ipro/meth}$ ligand modes and along the molecular z-axis bonds. Therefore, we anticipate one electron promotions to virtual orbitals to possess a combination of $L^{ipro/meth}$ ligand and d_{xz}/d_{yz} orbital characters for $[MoOCl(L_2^{ipro})]^+$. The presence of ligand character in the unoccupied orbitals is consistent with the electron withdrawing nature of the 1,4-diisopropyl piperazine-2,3-dithione and 1,4-dimethyl piperazine-2,3-dithione ligands.

The absorption maxima for $[MoOCl(L^{ipro})(SPh)_2]$ are observed at 13,500 cm^{-1} for band 1, at 19,510 cm^{-1} for band 2, at 24,300 cm^{-1} for band 3, at 27,810 cm^{-1} for band 4, and at 32,000 cm^{-1} for band 5 respectively. Three low energy excitation laser lines at 647nm (15,458 cm^{-1}), 568nm (17,606 cm^{-1}) and 514nm (19,455 cm^{-1}) are on resonance with bands 1 and 2. Therefore, we observe a strong resonance enhancement of the $\upsilon(Mo\text{-}S^{ipro})$ stretch (Figure 2.54). This result suggests a strong distortion along in xy plane and therefore we anticipate one

electron promotions to excited state orbitals with d_{xy} character to be responsible for this distortion. Also, a strong resonance enhancement of the υ(Mo≡O)

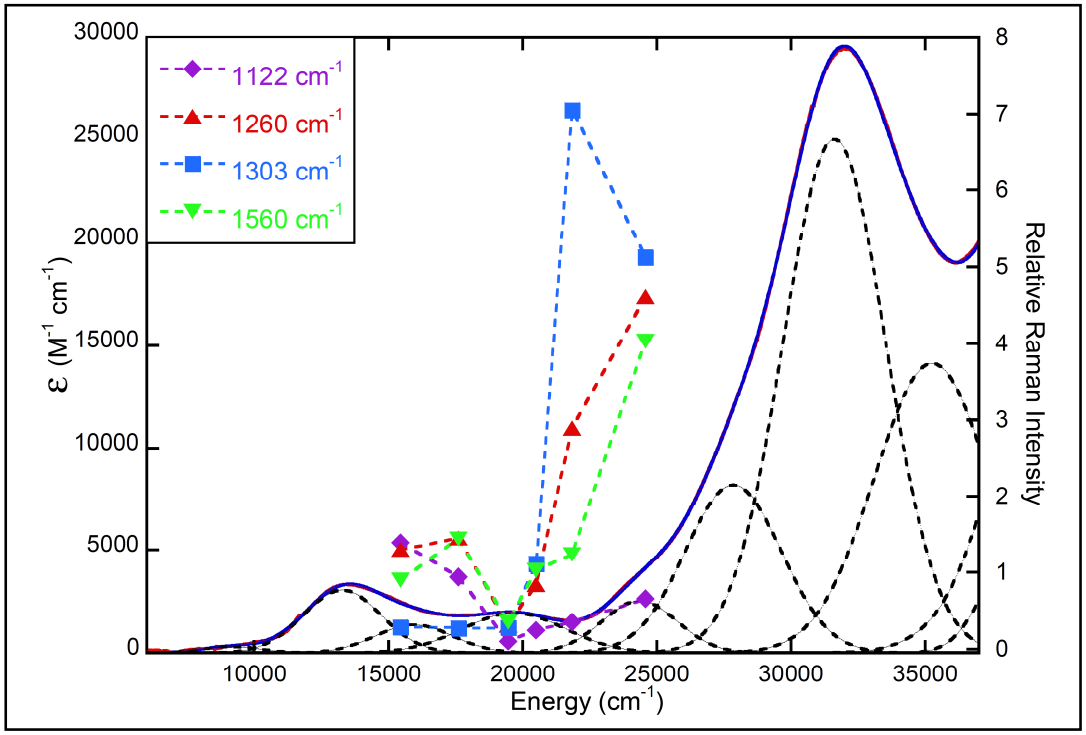

Figure 2.53: Solid state rRaman excitation profile spectrum for $[MoOCl(L_2^{methyl})]^+$ showing the υ(C-C & C=S) stretch at 1122 cm^{-1}, υ(C-C) stretch at 1260 cm^{-1}, $\upsilon(L^{meth}$ ring) stretch at 1303 cm^{-1} and υ(C-N) stretch at 1560 cm^{-1}.

stretch is observed with 20,492 cm^{-1} (488nm) excitation indicating the presence of d_{xz}, d_{yz} orbital character in unoccupied orbitals associated with transition that comprise bands 2 and 3 respectively. In addition, excitation into band 3 displays resonance enhancement of υ(C-C) and $\upsilon(L^{ipro}$ ring) stretches that indicate one electron promotion to the unoccupied L^{ipro} ligand orbital. The presence of L^{ipro}

ligand character in the unoccupied orbital agrees well with the electron withdrawing nature of the 1,4-diisopropyl piperazine-2,3-dithione ligand.

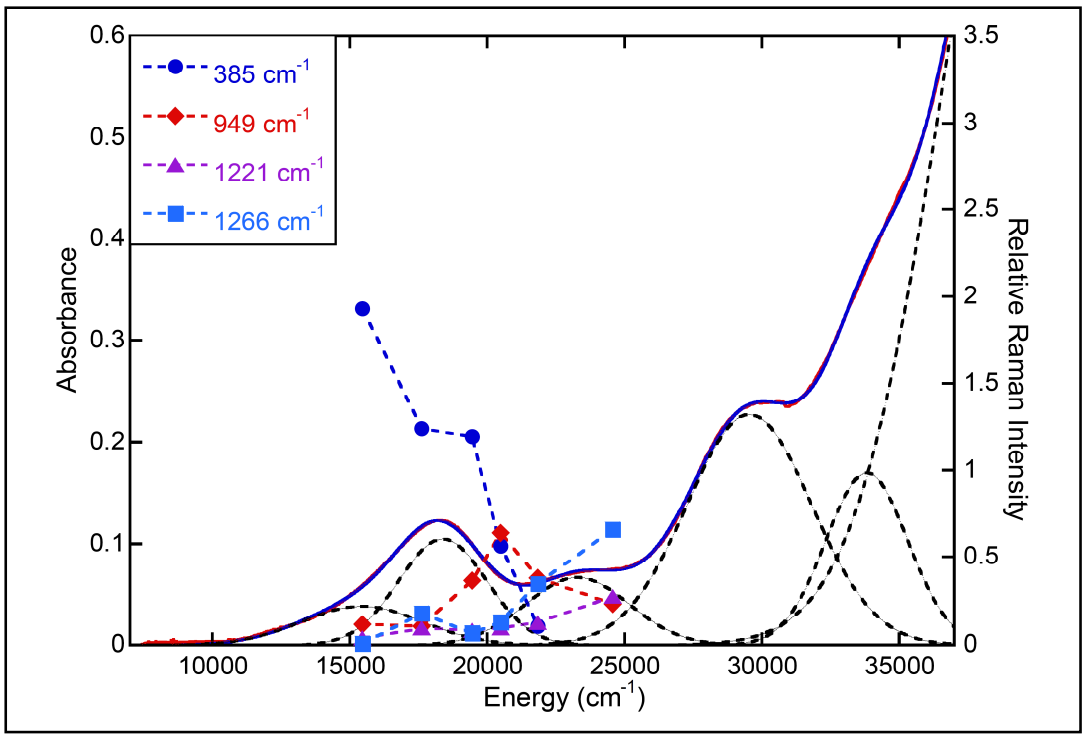

Figure 2.54: Solution electronic absorption spectrum and solid state rRaman excitation profiles for [MoO(L^{ipro})($SPh)_2$] showing υ (Mo-S^{ipro}) stretch at 385 cm^{-1}, υ (Mo≡O) stretch at 949 cm^{-1}, υ (L^{ipro} ring) stretch at 1221 cm^{-1} and υ (C-C) stretch at 1267 cm^{-1}.

2.9.1.2 Band Assignments

Time dependent DFT calculations, and electronic absorption and rRaman spectroscopy have been utilized to study the nature of charge transfer bands and their assignments for $[MoOCl(L_2^{ipro/meth})]^+$ and $[MoO(L^{ipro})(SPh)_2]$ compounds. Table 2-5 displays the electronic absorption, calculated band maxima, oscillator strength, and band assignments for $[MoOCl(L_2^{ipro})]^+$, $[MoOCl(L_2^{meth})]^+$ and $[MoO(L^{ipro})(SPh)_2]$ compounds. $[MoOCl(L_2^{ipro})]^+$ and $[MoOCl(L_2^{meth})]^+$ show a similar number of bands in the 8,000–37,000 cm^{-1} regions, while for $[MoO(L^{ipro})(SPh)_2]$, Gaussian the resolved electronic absorption spectrum shows six bands from 8,000 to 37,000 cm^{-1}. Therefore due to structural similarities between $[MoOCl(L_2^{ipro})]^+$ and $[MoOCl(L_2^{meth})]^+$ compounds their band assignments will be discussed together.

Table 2-5: Experimental vs. theoretical band maxima energies and their oscillator strength for $[MoOCl(L_2^{ipro})_2]^+$, $[MoOCl(L_2^{meth})]^+$ and $[MoO(L^{ipro})(SPh)_2]$ compounds.

$[MoOCl(L_2^{ipro})]^+$					
Band #	Expt Energy (cm^{-1})	Calc Energy (cm^{-1})	Expt (f)	Calc (f)	Assignment
1	13467	14270	0.0467	0.0595	dxy → Sop" + C=C + dxz
2	16267	16364	0.0123	0.0040	dxy → Sop' + C=C + dxy
3	19772	19056	0.0217	0.0503	dxy → dxz + Oπ*
4	24867	24067 24707	0.0536	0.0264 0.0355	dxy → dx^2-y^2 + Sσ* Sip' + Clσ* → Sop" + C=C + dxz
5	28750	29510	0.2462	0.0528	Sip' + Clπ → Sop" + C=C + dxy
6	31778	32850 32,980 34602	0.4199	0.1080 0.0345 0.0609	Sip" + Clπ → Sop' + C=C + dxy Sip" + Clπ* → Sop" + C=C + dxz Sop' + Clπ* → dx^2-y^2 + Sipσ*

$[MoOCl(L_2^{meth})]^+$					
Band #	Expt Energy (cm^{-1})	Calc Energy (cm^{-1})	Expt (f)	Calc (f)	Transition
1	13030	14110	0.0501	0.0671	dxy → Sop" + C=C + dxz
2	15230	16483	0.0199	0.0042	dxy → Sop" + C=C + dxy
3	19660	19695	0.0403	0.0582	dxy → dxz + Oπ*
4	24125	23819 24170	0.0394	0.0210 0.0319	Sip' + Clσ* → Sop" + C=C + dxz dxy → dx^2-y^2 + Sipσ*
5	27300	29490	0.1581	0.0350	Sop" + Clπ* → Sop' + C=C + dxy
6	31875	32753 32818 34318	0.5184	0.0243 0.0998 0.1717	Sip" + Clπ* → Sop" + C=C + dxz Sop" + Clπ* → Sop' + C=C + dxy Sop' + Clπ* → dx^2-y^2 + Sipσ*

$[MoO(L^{ipro})(SPh)_2]$				
Band #	Expt Energy (cm^{-1})	Calc Energy (cm^{-1})	Calc (f)	Transition
1	15,430	12,670	0.0197	Sop" (SPh) → dxy + Sop' + C=C
2	18,290	17,130	0.0607	Sop' (SPh) + dxy → dxy + Sop' + C=C
3	23,250	21,600 24,850	0.0378 0.0371	dxy + Sop' (SPh) → dxy + Sop' + C=C Sop" (SPh) → dxz + Oπ*
4	29,560	25,670 29,630	0.0758 0.0373	Sop" (SPh) → dyz + Oπ* dxy + Sop → dxz + Oπ*
5	33,800	31,810 33,440	0.0384 0.0076	dxy + SPh → dyz + Oπ* Sop (SPh) + Sop" → dxz + Oπ*
6	40,075	34,570 38,330	0.0246 0.1098	dxy + Sop' (SPh) → dx^2-y^2 + Sipσ* Sop" (SPh) → Ph

Band 1: Band 1 is assigned as the HOMO → LUMO transition that possesses Mo-d_{xy} character in the HOMO while LUMO has L^{ipro} ligand + Mo-d_{xz} character in both $[MoOCl(L_2^{ipro/meth})]^+$ compounds. This assignment is supported by the rRaman data in Figure 2.9.6 that shows enhancement of υ(C-C & C=S), υ(C-C) and υ(C-N) stretches using 15,456 cm^{-1} excitation. The strong intensity of this band is consistent with its assignment as a metal to ligand charge transfer (MLCT) transition as depicted in the electron density difference map in Figure

2.55. For [MoO(L^{ipro})($SPh)_2$], band 1 is assigned as the HOMO → LUMO transition, where the HOMO possesses asymmetric S_{op} (SPh) and some phenyl ligand character and the LUMO contains L^{ipro} ligand + Mo-d_{xy} character. These transitions are depicted in the electron density difference maps (EDDMs) of Figure 2.55. A strong enhancement of the υ(Mo-S^{ipro}) stretch using 15,456 cm^{-1} excitation observed in the rRaman spectrum (Figure 2.54) supports this assignment.

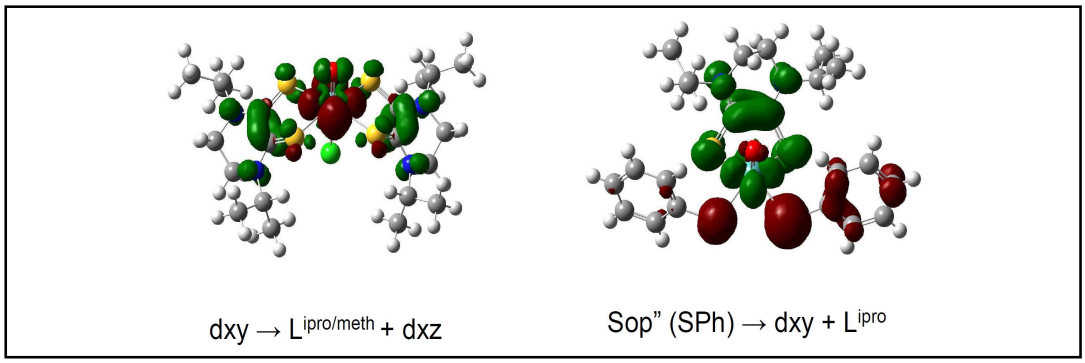

Figure 2.55: Electron density difference maps (EDDMs) for (left) [MoOCl(L_2^{ipro})]$^+$ and (right) [MoOCl(L^{ipro})($SPh)_2$] compounds showing the MLCT and intraligand charge transfer for band 1.

Band 2: A HOMO → LUMO+1 transition is assigned for band 2 in [MoOCl($L^{ipro/meth}$)]$^+$, where the HOMO possesses mainly Mo-d_{xy} character and the LUMO+1 has $L^{ipro/meth}$ ligand + Mo-d_{xy} character, respectively. Enhancement of υ(C-C & C=S), υ(C-C) and υ(C-N) stretches is observed using 17,606 cm^{-1} laser excitation and support the assignment of this band as a MLCT transition with L^{ipro} ligand character in the excited state. For the [MoO(L^{ipro})($SPh)_2$] compound, band

2 is assigned as the HOMO-1 → LUMO transition, where the HOMO-1 possesses symmetric S_{op} (SPh) + Mo-d_{xy} character and the LUMO orbital has L^{ipro} + d_{xy} character. This assignment is supported by rRaman data that shows a strong resonance enhancement of the υ(Mo-S) stretch at 17,606 using 19,455 cm^{-1} laser excitation, and enhancement of the υ(Mo≡O) stretch using 19,455 and at 20,492 cm^{-1} laser excitation. The intensity of this band agrees well with the assignment as a combination of a ligand field transition and an intraligand charge transfer transition. These transitions are depicted in the electron density maps (EDDMs) of Figure 2.56.

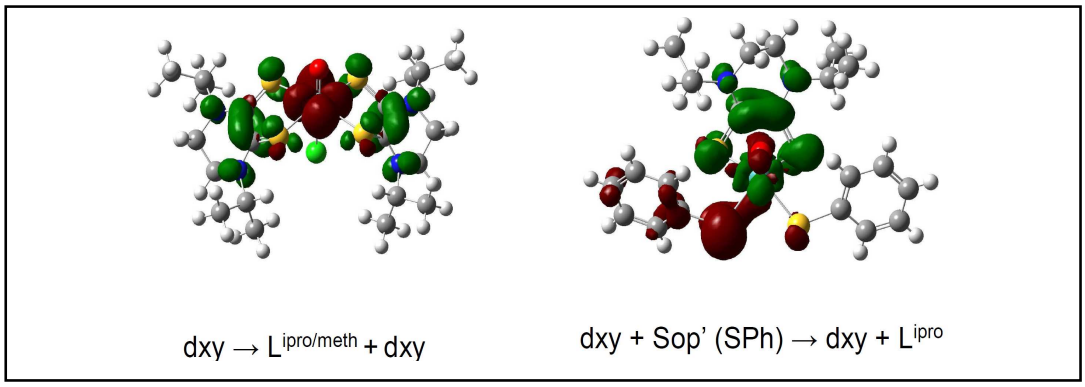

Figure 2.56: Electron density difference maps (EDDMs) for (left) $[MoOCl(L_2^{ipro})]^+$ and (right) $[MoOCl(L^{ipro})(SPh)_2]$ describing the nature of band 2.

Band 3: Band 3 is assigned as the HOMO → LUMO+3 transition in both $[MoOCl(L_2^{ipro/meth})]^+$ compounds. The HOMO contains Mo-d_{xy} character whereas the LUMO+3 possesses Mo-d_{xz} with Oπ* character. A very weak resonance enhancement of the υ(C-C & C=S), υ(C-C), υ($L^{ipro/meth}$) and υ(C-N) stretches

were observed in the rRaman spectra supporting the assignment of this band. For the [MoO(L^{ipro})$(SPh)_2$] compound, resonance enhancement of the υ(Mo≡O) stretch, and υ(C-C) and $\upsilon(L^{ipro})$ stretches were observed with 24,570 cm^{-1} excitation. The Raman data supports the assignment of this band as a combination of the HOMO-2 → LUMO and HOMO → LUMO+1 transitions. The HOMO possesses asymmetric S_{op} (SPh) character plus some Ph ligand character and the HOMO-2 has symmetric S_{op} (SPh) + Mo-d_{xy} character. The LUMO contains L^{ipro} ligand + Mo-d_{xy} character and the LUMO+1 possesses Mo-d_{xz} + Oπ^* character.

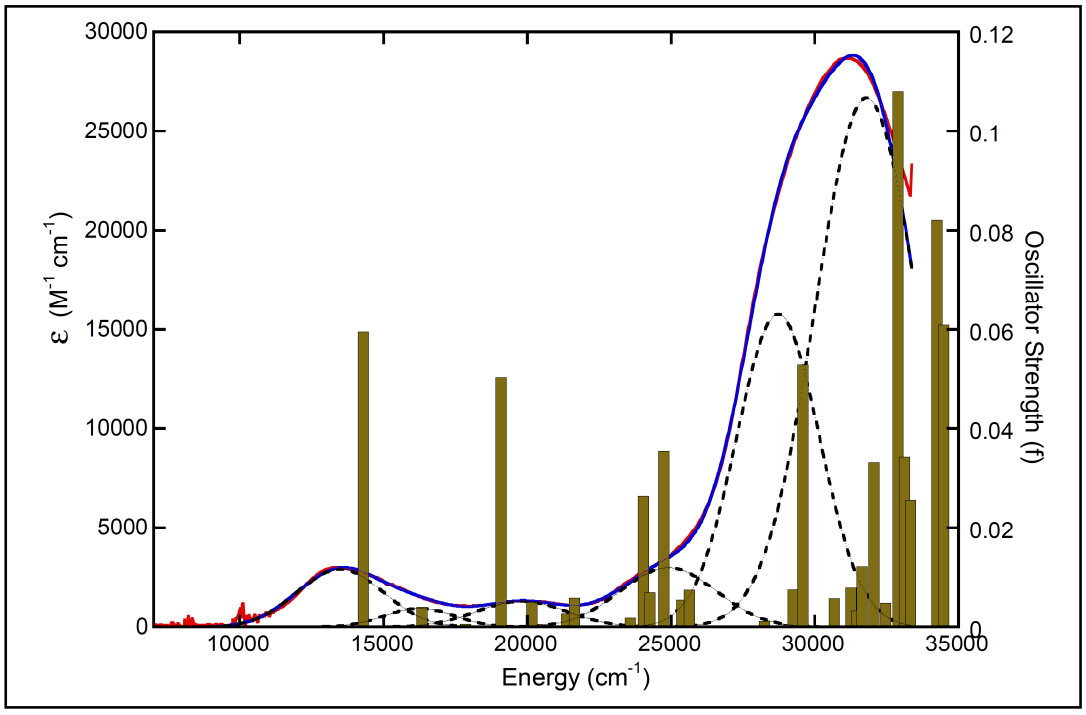

Figure 2.57: Room temperature Gaussian resolved electronic absorption spectrum of [MoOCl(L_2^{ipro})]$^+$ with calculated transitions and oscillator strengths obtained from TD-DFT calculations.

Band 4: A strong resonance enhancement of υ(C-C), υ(C-N), $\upsilon(L^{ipro/meth})$ ligand stretches, concomitant with a weak enhancement of υ(Mo=O) and υ(C-C & C=S) stretches, support the assignment of this band as HOMO-5 → LUMO and HOMO → LUMO+4 transitions. The HOMO possesses Mo-d_{xy} character and the HOMO-5 contains totally symmetric S_{op} + Clσ* ligand character, whereas LUMO orbital has a combination of $L^{ipo/meth}$ ligand + Mo-d_{xz} character and the LUMO+4 possesses $d_{x^2-y^2}$ + $S_{ip}\sigma$* character. The strong enhancement of υ(C-C), υ(C-N), and $\upsilon(L^{ipro/meth})$ stretches observed in the rRaman spectrum allows us to propose a HOMO-5 → LUMO transition as the major contributor in this band.

For [MoO(L^{ipro})$(SPh)_2$], bands 4, 5 and 6 have been assigned solely based on the ground and excited state calculation and their calculated oscillator strengths and observed band intensities. Thus, these transitions should be considered tentative at this stage. A combination of HOMO → LUMO+2 and HOMO-2 → LUMO+1 excitations are assigned for band 4. The HOMO-2 possesses symmetric S_{op} (SPh) + Mo-d_{xy} character and the HOMO has asymmetric S_{op} (SPh) character plus some phenyl ligand character, whereas the LUMO+1 and LUMO+2 orbitals possesses Mo-d_{xz} + Oπ* and Mo-d_{yz} + Oπ* character respectively. The calculated oscillator strength (f = 0.0758, Table 2-5) for this transition is in line with the intensity of this band.

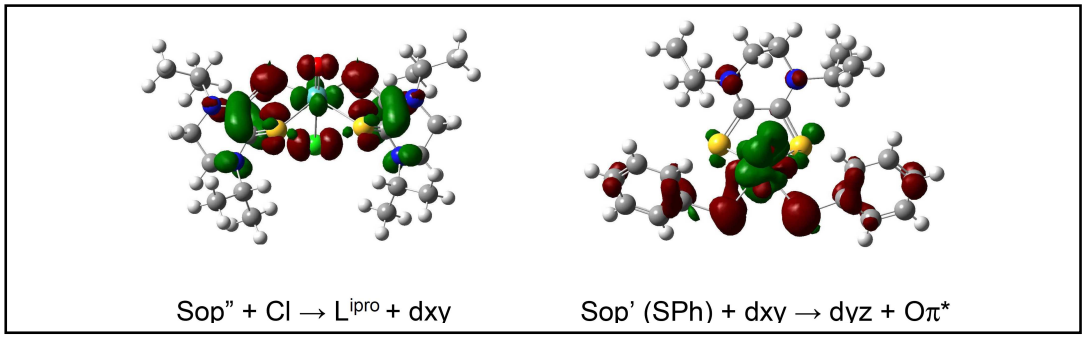

Figure 2.58: Electron density difference map (EDDMs) for (left) $[MoOCl(L_2^{ipro/meth})]^+$ and (right) $[MoOCl(L^{ipro})(SPh)_2]$ compounds showing the intraligand charge transfer and LMCT transitions for band 5.

Band 5: An intensity increase observed in band 5 in both $[MoOCl(L_2^{ipro/meth})]^+$ compounds is consistent with the assignment of this band as HOMO-6 → LUMO+ with a calculated oscillator strength of ~0.530 (Figure 2.57). This is a higher energy intraligand charge transfer transition that involves asymmetric S_{ip} + Clπ* + Oπ* character in the HOMO-6 while the LUMO+1 orbital possesses $L^{ipo/meth}$ ligand and Mo-d_{xy} character. The calculated electron density difference map (EDDM) is presented in Figure 2.58. For $[MoO(L^{ipro})(SPh)_2]$, band 5 is assigned as arising from HOMO-2 → LUMO+2 and HOMO-3 → LUMO+1 transitions with 0.0384 and 0.0076 oscillator strengths. These transitions involve symmetric S_{op} (SPh) ligand + Mo-d_{xy} character in the HOMO-3, whereas S_{op} (SPh) + $S_{op'}$ (L^{ipro}) ligand character and Mo-$d_{yz/xz}$ + Oπ* characters are present in the LUMO+2 and LUMO+3 orbitals, respectively. A decrease in intensity observed in this band compared to bands 4 and 6 is proportional to the

calculated oscillator strength (f = 0.0384, Table 2-5) for the HOMO-2 → LUMO+2 transition displayed in Figure 2.58 that agrees well with the LMCT assignment.

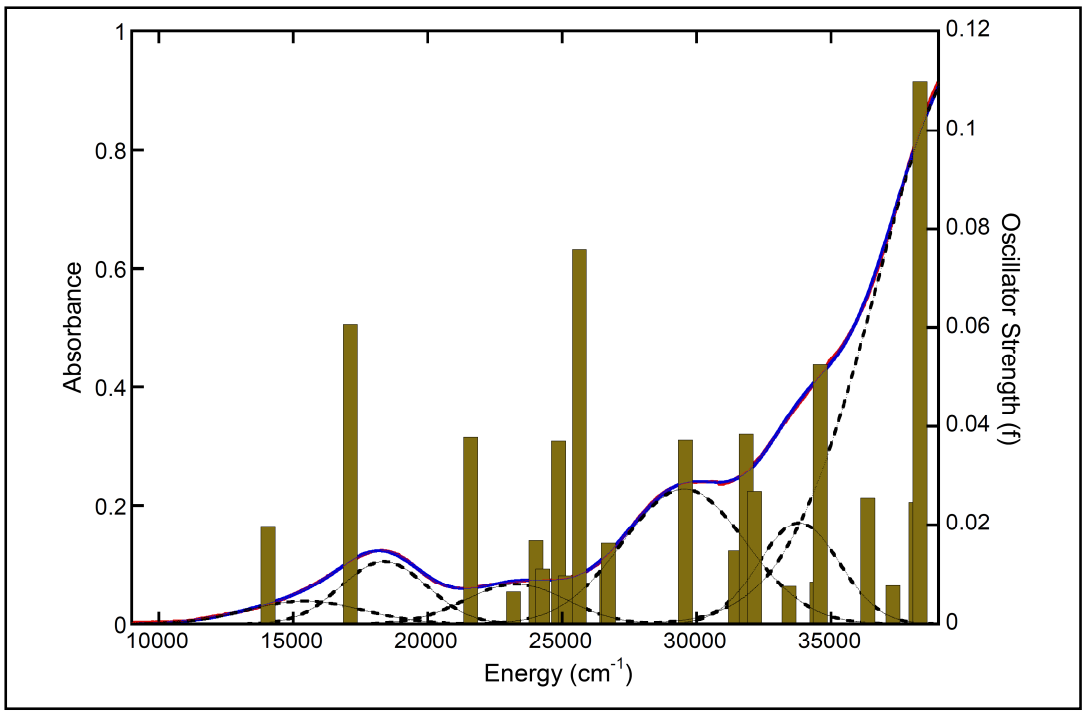

Figure 2.59: Gaussian resolved room temperature electronic absorption spectrum of [MoO(L^{ipro})($SPh)_2$] with calculated transition energies and oscillator strengths obtained from TD-DFT calculations.

Band 6: This is the most intense band observed in the electronic absorption spectrum for all three compounds. In the [MoOCl($L_2^{ipro/meth}$)]$^+$ compounds, this band is assigned as arising from the HOMO-8 → LUMO+1, HOMO-8 → LUMO and HOMO-1 → LUMO+4 transitions (Table 2-5). The HOMO-8 orbital possesses a combination of asymmetric S_{ip} and Clπ^* ligands character, the HOMO-1 has symmetric S_{op} + Clπ^* character, whereas LUMO contains $L^{ipro/meth}$

ligand with Mo-d_{yz} metal character. The LUMO+1 has $L^{ipro/meth}$ ligand + Mo-d_{xy} and the LUMO+4 contains d_{x2-y2} + antisymmetric $S_{ip}\sigma^*$ character. Regarding [MoO(L^{ipro})$(SPh)_2$], this band is assigned as HOMO-2 → LUMO+3 and HOMO → LUMO+6 transitions. The HOMO orbital possesses antisymmetric S_{op} (SPh) + phenyl character, the HOMO-2 involves symmetric S_{op} (SPh) + Mo-d_{xy} character, whereas the LUMO+3 orbital has Mo-d_{x2-y2} + $S_{ip}\sigma^*$ character. The LUMO+6 orbital is dominated by phenyl ligand character only. The intensity of this band agrees well with the strong calculated oscillator strength (f = 0.0525 and 0.1098) that is depicted in figure 2.59.

2.9.2 Discussion

2.9.2.1 The Effect of 1,4-dimethyl/ipro-piperazine-2,3-dithione and Benzene Thiolate Ligands on the Electronic Structure of the Compounds

DFT calculations and AOMix analysis on [MoOCl($L_2^{ipro/meth}$)]$^+$ compounds reveal the presence of orbitals with ligand character in the unoccupied orbitals (Figure 2.61). Our results show that the LUMO and LUMO+1 orbitals for [MoOCl($L_2^{ipro/meth}$) contain predominantly piperazine dithione ligand character and a small amount of metal. The LUMO orbital possesses 88% L^{ipro} character in [MoOCl(L_2^{ipro})]$^+$ and 86% L^{meth} ligand character in [MoOCl(L_2^{meth})]$^+$, while only 5% of metal character is present in both compounds.

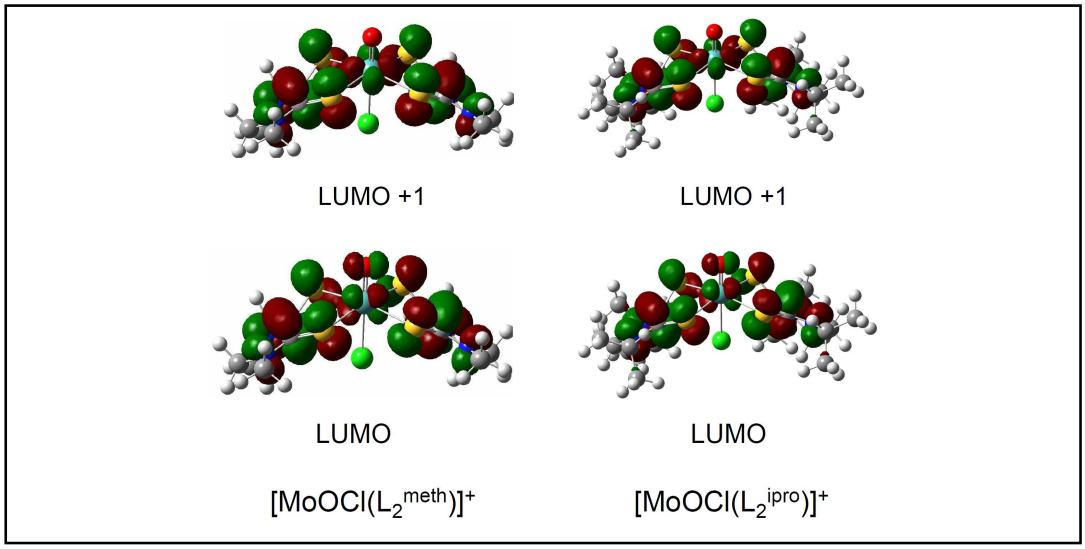

Figure 2.60: LUMO and LUMO+1 molecular orbital density plots for $[MoOCl(L_2^{meth})]^+$ and $[MoOCl(L_2^{ipro})]^+$ compounds.

Additionally, the two compounds contain a comparably (~10%) small amount of metal character in the LUMO+1 orbital with 89% L^{ipro} and 86% L^{meth} ligand character in $[MoOCl(L_2^{ipro})]^+$ and $[MoOCl(L_2^{meth})]^+$ respectively (Figure 2.60).

The presence of piperazine dithione ligand character in low-energy unoccupied orbitals is supported by TD-DFT calculations. Additionally, rRaman results (Figure 2.52 and 2.53) show a strong resonance enhancement of the υ(C-C & C=S), υ(C-C) and $\upsilon(L^{ipro/meth}$ ring) stretches from 20,000 cm^{-1} to higher energy in the two compounds that confirm the presence of piperazine dithione ligand character in the LUMO and LUMO+1 orbitals. The electron withdrawing nature of the $L^{ipro/meth}$ ligands destabilizes the ligand orbitals, which in turn allows them to act as electron acceptor ligands. Matz et al.,[71] reported the presence of

quinoxalline ligand character in the LUMO and LUMO+1 orbitals of Tp*MoO(S_2BMOQO) that also acts as an electron acceptor in this compound. Similar results have been observed in the $[MoS/Se(L^{Ph})_2]^{2-}$ compounds (Section 2.6) where ligands orbital character is dominant in the low-energy unoccupied molecular orbitals.

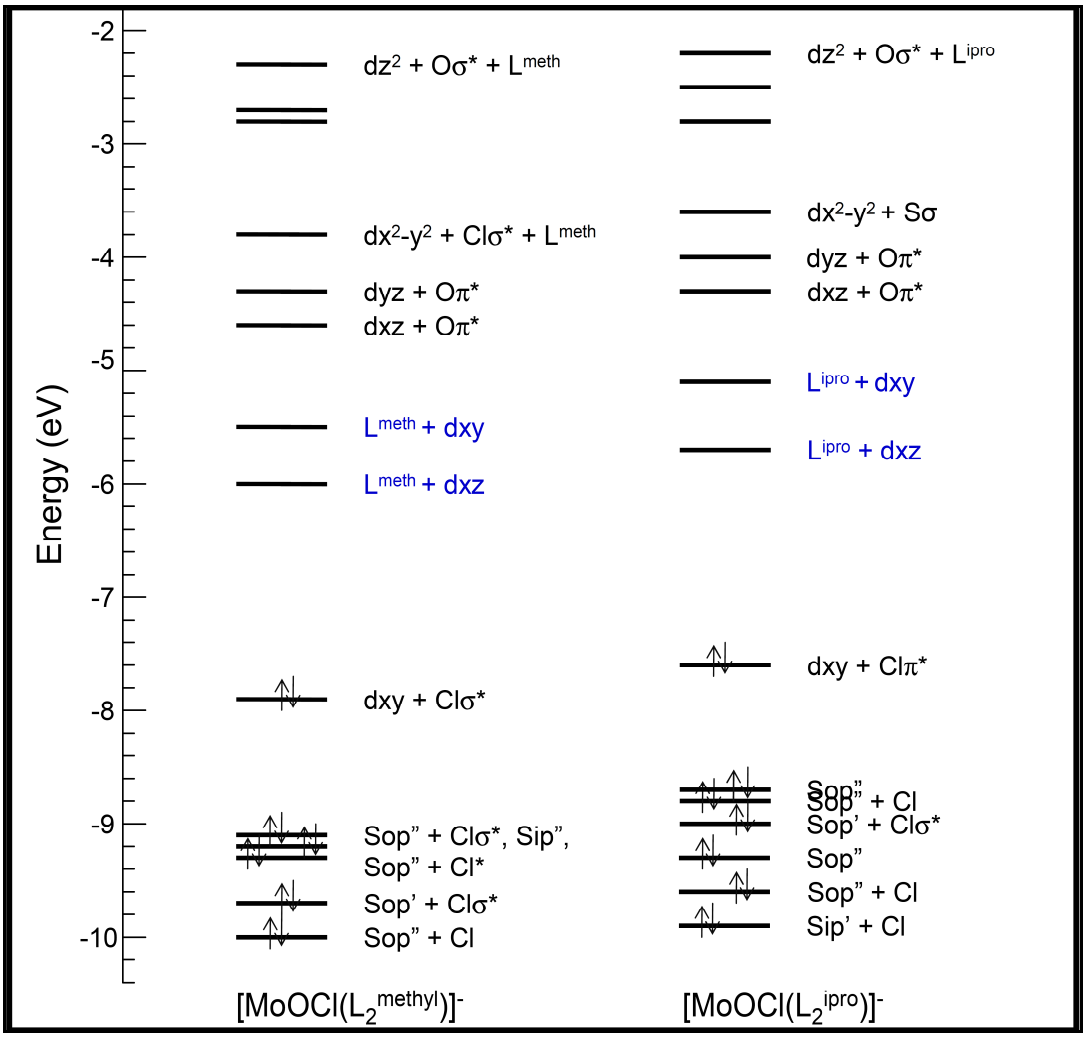

Figure 2.61: Molecular orbital energy diagram showing the presence of ligand character in the LUMO and LUMO+1 orbitals for $[MoOCl(L_2^{ipro/meth})]^+$ compounds.

The $[MoO(L^{ipro})(SPh)_2]$ compound differs from $[MoOCl(L^{ipro/meth})]^+$ compounds since it possesses only a single dithione ligand. DFT and AOMix analysis for $[MoO(L^{ipro})(SPh)_2]$ reveal the presence of piperazine dithione ligand character only in the LUMO orbital. This result is different when compared to the $[MoOCl(L_2{}^{ipro/meth})]^+$ compounds which possesses piperazine dithione ligand characters in both the LUMO and LUMO+1 orbitals. The LUMO orbital for $[MoO(L^{ipro})(SPh)_2]$ contains 65% L^{ipro}, 5% SPh ligand, and 28% metal character, while the LUMO+1 has 22% L^{ipro}, 11% SPh ligands and 49% metal character (Figure 2.62). The presence of L^{ipro} ligand character in these orbitals is also manifested in the rRaman data in Figure 2.54, where a strong resonance enhancement of υ(C-C) and $\upsilon(L^{ipro}$ ring) stretches are observed starting from 19,455 cm^{-1} excitation laser line to higher energy.

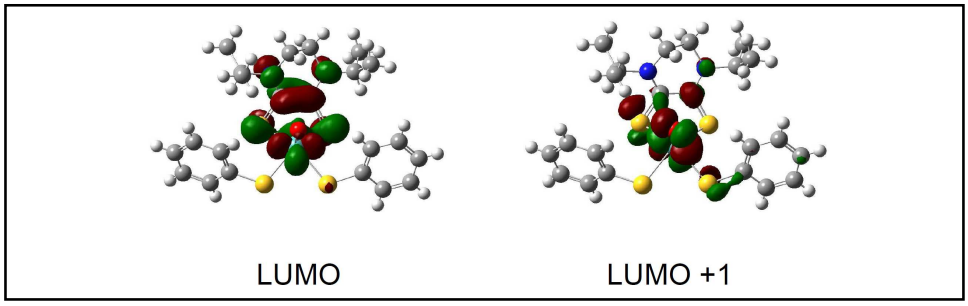

Figure 2.62: LUMO and LUMO+1 molecular orbital density plots for $[MoO(L^{ipro})(SPh)_2]$.

Therefore, the electron withdrawing nature of the L^{ipro} ligand destabilizes the piperazine dithione ligand, which in turn acts as an electron acceptor. This explains why in $[MoOCl(L_2{}^{ipro/meth})]^+$ compounds, both the LUMO and LUMO+1

have ligand character. This study is important in determining the role and electronic structure of N-heterocyclic rings present in the active sites of pyranopterin Mo enzymes.

2.10 Implication for DMSO Reductase Family Enzymes

DMSO reductase family enzymes possess two pyranopterin dithiolenes attached to the molybdenum center as its unique characteristic feature. It has been reported that pyranopterin ene-1,2-dithiolene can exist in three different forms, i.e. a radical ionic form, a dithione/dithiete (oxidized form) and a dithiolene/dithiolate (reduced form).[55,82] Recently Matz et al.[71] reported on an oxo molybdenum compound with a thiol/thione ligand system of the pyranopterin ene-1,2-dithiolene ligand. Garton and coworkers reported that in pyranopterin dithiolenes, a substantial π-delocalization or dithioketone character with a characteristic υ(C-S) stretch should occur at higher frequency and presumably a υ(C=C) stretch at lower frequency.[22] This is consistent with our results that show a υ(C-C & C=S) stretch at 1120-1122 cm^{-1} and a υ(C=C) stretch at 1230-1260 cm^{-1} for $[MoO(L_2^{ipro})]^+$ and $[MoOCl(L_2^{meth})]^+$. The rRaman excitation profiles for $[MoOCl(L_2^{ipro})]^+$ and $[MoOCl(L_2^{meth})]^+$ reveal the presence of ligand character in the low energy unoccupied orbitals, and the same results was reported by Matz and coworkers for Tp*MoO(S2BMOQO) and is also anticipated for enzymes with a dithione ligand character.

Comparison of electronic absorption between DMSO reductase and $[MoOCl(L_2^{meth})]^+$ are presented in Figure 2.63 and show energy and intensity differences in the low energy region. For $[MoOCl(L_2^{meth/ipro})]^+$ the low energy bands occur at 13,470 and 14,200 cm^{-1} which is at lower energy compared to reduced Mo(IV) DMSOR enzyme. This may be due to the presence of an apical oxo in these compounds, since DMSOR does not possesses an apical oxo ligand in the reduced form. The first two low energy bands are assigned as MLCT transitions for $[MoOCl(L_2^{meth/ipro})]^+$, while ligand field and LMCT transitions have been assigned for the higher energy bands. Differences in the nature of the dithiolene ligands for the model and enzyme may also account for the difference in their electronic absorption spectra.

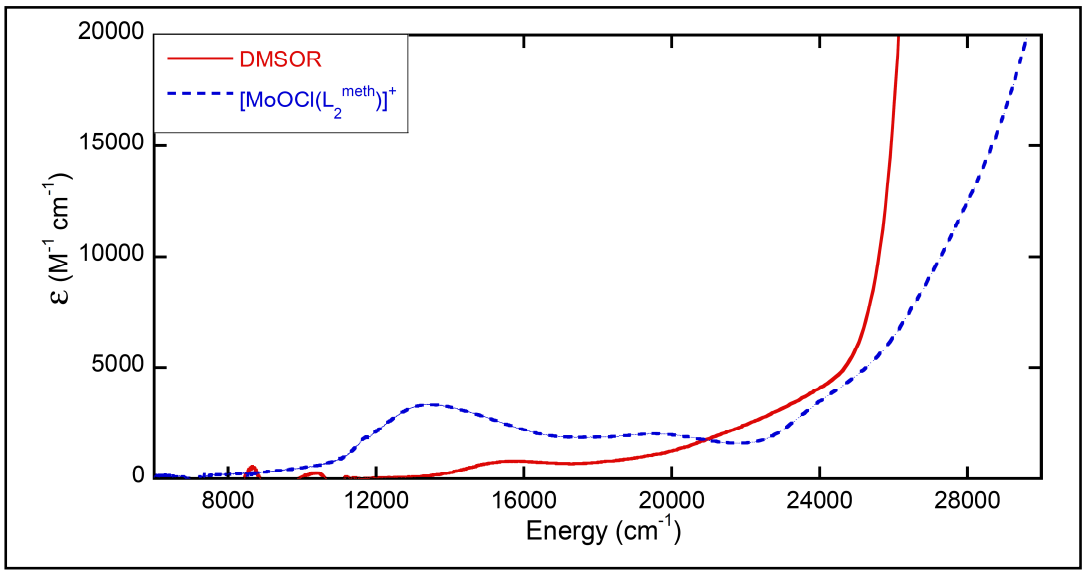

Figure 2.63: Electronic absorption spectra overlay for DMSOR and $[MoOCl(L_2^{meth})]^+$ compounds.

Electronic absorption spectra for $[MoO/S/Se(L^{COOMe})_2]^{2-}$, $[MoS/Se(L^{Ph})_2]^{2-}$ and $[MoO(L^{H/O})_2]^{2-}$ compounds possess absorption features at energies lower than the Mo(IV) form of DMSO reductase. The low energy bands observed for $[MoO/S/Se(L^{COOMe})_2]^{2-}$ and $[MoS/Se(L^{Ph})_2]^{2-}$ derive from intraligand charge transfer transitions, as opposed to the ligand field transitions observed in $[MoO(L^{H/O})_2]^{2-}$. This is a direct result of differences in the substituents attached to the S-C=C-S backbone. The electron donating power of the L^H/L^O dithiolene ligands reduces the strength of apical Mo-oxo interaction bond and this is reflected in a reduced Mo-d_{xy}-Mo-$d_{xz,yz}$ d-orbital splitting energy.

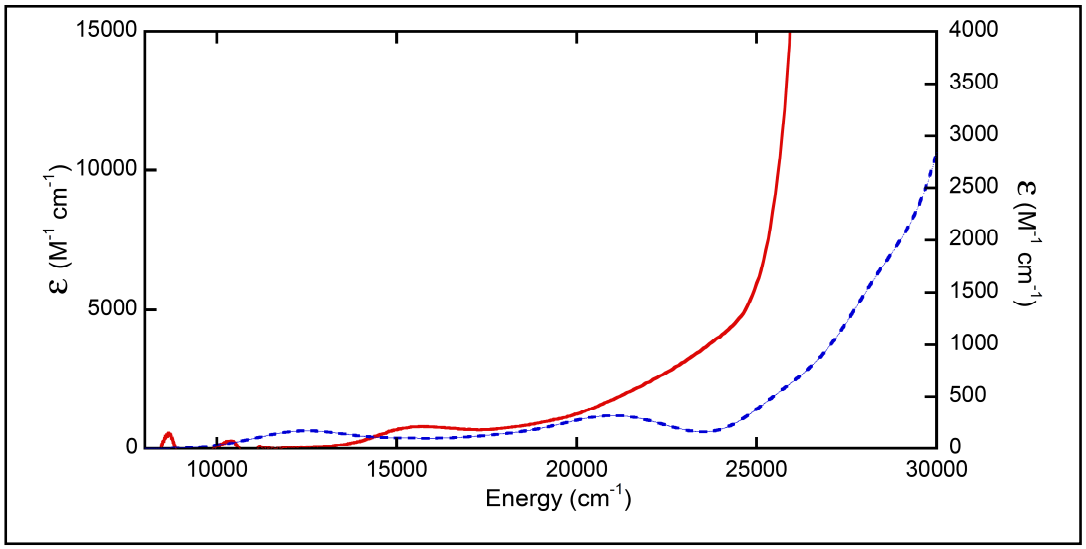

Figure 2.64: Electronic absorption spectral overlay between Mo(IV) DMSOR enzyme (——) and $[MoO(L^H)_2]^{2-}$ (·····) highlighting the low energy bands.

Garton and coworkers reported a υ(Mo-S) stretch at 367 cm^{-1} for DMSOR[19,22] and at 363 cm^{-1} υ(Mo-S) stretch for biotin sulfoxide,[20] and this is in good

agreement with symmetric υ(Mo-S) stretches observed at 353, 350 and 364 cm^{-1} for the $[MoOL^{H})_2]^{2-}$, $[MoOL^{O})_2]^{2-}$ and $[MoO(L^{COOMe})_2]^{2-}$ model compounds. Comparing rRaman and electronic absorption data for our model compounds with similar spectra for arsenite oxidase is not possible due to the presence of highly absorbing Fe/S clusters.[7]

2.11 Conclusion

The electronic structures for the square pyramidal complexes $[MoO/S/Se(L^{COOMe})_2]^{2-}$, $[MoS/Se(L^{Ph})_2]^{2-}$, $[MoO(L^{H/O})_2]^{2-}$, $[MoOCl(L_2{}^{ipro/meth})]^{+}$, $[MoO(L^{ipro})(SPh)_2]$, $[WO/S(L^{Ph})_2]^{2-}$ and $[WO(L^{H})_2]^{2-}$ have been probed spectroscopically and computationally. Both spectroscopy and DFT studies have shown the nature of the apical chalcogen and ene-1,2-dithiolenes affect the electronic structure of these complexes. The electron withdrawing nature of dithiolene substituents and the effect of extended conjugation are evident in the spectra of $[MoO/S/Se(L^{COOMe})_2]^{2-}$, $[MoS/Se(L^{Ph})_2]^{2-}$, $[MoOCl(L_2{}^{ipro/meth})]^{+}$ and $[WO/S(L^{Ph})_2]^{2-}$ compounds, which show ligand character in the low energy unoccupied orbitals and display low energy intraligand charge transfer transitions from S_{op} to either the carbon backbone or the dithiolene ligand substituents.

The origin of the spectra shifts observed in $[MoO/S/Se(L^{COOMe})_2]^{2-}$, and $[MoS/Se(L^{Ph})_2]^{2-}$ have been explained in terms of two factors i). the nature of the ligand field that results from Mo≡E bonding (E = O, S, Se) which leads to higher energy ligand field bands for Mo≡O compounds and ii). the nature of both the

LUMO and LUMO+1 wavefunctions, which have been shown to possess apical ligand (E) character and lead to lower energy charge transfer transitions as the apical chalcogenido electronegativity decreases.

The enzyme catalytic geometry is suggested to be the one similar to model compounds with EDGs (L^H, L^O) as these should destabilize the Mo(IV) geometry for oxidation to the Mo(V) state and eventually to the resting state of the enzyme. Fortunately, these are compounds that have true ene 1,2-dithiolene ligands similar those proposed for the enzyme active sites, allowing for detailed spectroscopic probing of enzyme electronic structure through model compound studies.

CHAPTER 3

Molybdenum and Tungsten (V) Bis-dithiolenes Models for Arsenite Oxidase

3.1 Introduction

Most of pyranopterin molybdenum enzymes catalyze oxygen atom transfer reactions by starting catalysis in either the Mo(IV) or Mo(VI) resting states. During catalysis, these enzymes cycle between Mo(IV) and Mo(VI) with an obligatory Mo(V) intermediate in the electron transfer half reaction. This Mo(V) species has also been observed in redox titrations or freeze-quench kinetic experiments when using one-electron redox partners. The Mo(V) form of several dimethyl sulfoxide reductase (DMSOR) family members including nitrate reductase,[23,29,85-87] formate dehydrogenase,[38,40] and dimethylsulfoxide reductase[14,19,88-92] has been observed. However, to date there is no evidence for the existence of a Mo(V) intermediate in arsenite oxidase.

Arsenite oxidase is involved in arsenite detoxification and its active site has a square pyramidal geometry with four sulfur atoms from the two pyranopterin dithiolenes bound to molybdenum.[6,7] The enzyme also contains two iron-sulfur clusters which are involved in electron transfer regeneration processes. Electronic absorption,[31] EPR,[31] and rRaman data [7] for arsenite oxidase are dominated by iron-sulfur clusters, resulting in an effectively spectroscopically silent molybdenum active site. This severely complicates the electronic structure characterization of the Mo active site. Protein film voltammetric studies have been performed on arsenite oxidase and reveal an unusual highly cooperative

two electron process at the molybdenum center and the authors of this work propose that Mo(V) is not observed due to the highly unstable nature of this intermediate.[32] However, both formate dehydrogenase and nitrate reductase enzymes have been shown to possess a Mo(V) intermediate, but the presence of iron sulfur clusters complicates their spectroscopic characterization. [23,36,40,85,87,93]

Several molybdenum and tungsten model compounds such as $[MoO(bdt)_2]^-$ (where bdt = 1,2-benzenedithiolate),[80,94] $[MoO(edt)_2]^-$ (where edt = ethylene-1,2-dithiolate),[72,95,96] $[MoO(S_2C_2Me_2)_2]^-$ (where $S_2C_2Me_2$ = 1,2-dimethyl-1,2-ethylenedithiolate,,[76] $[MoO(S_2C_2Ph_2)_2]^-$ (where $S_2C_2Ph_2$ = 1,2-diphenyl-1,2-ethylenedithiolate,[60] $[MoO(mnt)_2]^-$ (where mnt =1,2-dicyanoethenedithiolato),[97] $[MoO(4\text{-}pedt)_2]^-$ (where 4-pedt =1-(4-pyridine)-1,2-ethylene-dithiolate),[71] $[MoO(p\text{-}SC_6H_4X)_4]$- (X=H, Cl, OMe),[96] $[WO(bdt)_2]^-$,[77,98] $[WO(S_2C_2Ph_2)_2]^-$,[59] $[WO(S_2C_2Me_2)_2]^-$,[99] have been synthesized and electrochemically characterized in order to model Mo/W(V) intermediates in DMSOR family enzymes. However, very few spectroscopic studies have been performed that have determined the nature of their charge transfer transitions and the effect of dithiolene substituents on the reactivities and electronic structure of these compounds. Therefore, we have undertaken a detailed spectroscopic study of $[MoO(L^H)_2]^-$, $[MoO(L^O)_2]^-$, $[MoO(L^{COOMe})_2]^-$, $[MoO(bdt)_2]^-$ and $[WO(L^H)_2]^-$ model compounds that possess a square pyramidal geometry similar to that found at the active site of the reduced arsenite oxidase enzyme. Our work reveals the nature of charge transfer transitions related to the Mo(V) enzyme form, and how the dithiolene affects

reactivity and electron transfer regeneration of the Mo(VI) active site in the catalytic cycle of arsenite oxidase.

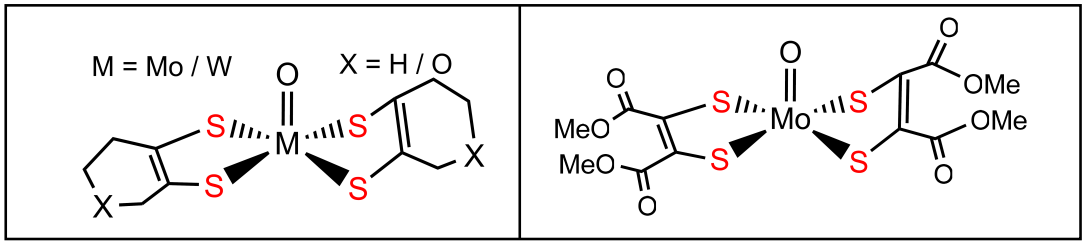

Figure 3.1: Structure of $[Mo/WO(L^{O/H})_2]^-$ and $[MoO(L^{COOMe})_2]^-$ compounds.

3.2 Statement of the Problem

Few spectroscopic studies have been performed on model compounds that mimic the putative Mo(V) intermediate of arsenite oxidase. Furthermore no detailed spectroscopic studies of oxomolybdenum bis-dithiolene Mo(V) compounds that possess L^H, L^O, L^{COOMe} or bdt dithiolenes have been performed. It is not known which pyranopterin dithiolene in arsenite oxidase is actively involved in electron transfer regeneration of the enzyme active site. Therefore, we aim to address this issue by understanding the nature of the low energy charge transfer bands in these model systems and probing covalency contributions to the Mo-dithiolene bonding scheme.

3.3 Hypotheses

Electron transfer regeneration in arsenite oxidase utilizes a pathway that involves a pyranopterin dithiolene ligand that does not possess an appreciable sulfur fold. Additionally, we hypothesize that a Mo(V) intermediate exists for arsenite oxidase and possesses a geometry that lies between square pyramidal and trigonal bipyramidal, and possesses low energy ligand (Sop) to metal (d_{xy}) charge transfer transitions.

3.4 Materials and Methods

The $[MoO(L^{H})_2]^-$, $[MoO(L^{O})_2]^-$, $[MoO(L^{COOMe})_2]^-$ and $[WO(L^{H})_2]^-$ compounds were generated *in situ* by reaction of 1:0.8 mole ratios of $[MoO(L^{H})_2]^{2-}$, $[MoO(L^{O})_2]^{2-}$, $[MoO(L^{COOMe})_2]^{2-}$ and $[WO(L^{H})_2]^{2-}$ with ferrocenium hexaflourophosphate ($C_{10}H_{10}F_6P$). All of these reactions were carried out in a glove box under a nitrogen atmosphere. The synthetic procedure for $[MoO(bdt)_2]^-$ was adopted from reference 94.

Electronic Absorption

Room temperature electronic absorption spectra were collected using a Hitachi U-3501 UV-Vis spectrophotometer that possesses a 180–3000 nm wavelength range. Anaerobic experiments were performed in a specialized 1 cm cuvette cell sealed with Teflon cap. All spectral bands were Gaussian resolved using the Grams/AI (7.02) software package.

Magnetic Circular Dichroism Spectroscopy

MCD spectra were collected on samples prepared as polystyrene thin films or as optical glasses using 2-methyl tetrahydrofuran as a glassing agent. For the polystyrene films, polystyrene beads were degassed using a Schlenk line and dissolved in a anhydrous dichloromethane or N,N-dimethylformamide in order to obtain a clear thick glassy matrix. The *in situ* generated Mo(V) compounds were mixed with this polystyrene matrix in order to obtain a uniform mixture which was then poured onto a glass slide and left to dry for three days. High quality thin films were routinely obtained using this method. Alternatively, 2-Methyl tetrahydrofuran was used to give a clear optical glass at low temperatures. The ratio of 0.6:0.4 Mo(V) compounds and 2-methyl tetrahydrofuran is suitable for a good MCD glass where 0.5 ml was withdrawn from the mixture, injected into the MCD cell and immediately frozen in the liquid nitrogen. The sample cell was connected into the sample rod while immersed in the liquid nitrogen and quickly inserted into the sample space. Before data collection standard Ni (+)-tartrate solution was used to calculate the depolarization, when the depolarization is less than 10% the sample is good for data collection.

Electron Paramagnetic Resonance Spectroscopy

Samples for EPR characterization were prepared the same way as described in the electronic absorption section. The mixture was placed in an EPR tube and quickly frozen in liquid nitrogen. EPR measurements were obtained using Bruker EMX EPR Spectrometer operating at ~ 9.5 GHz (X-band) with the following

instrument settings: 100 kHz modulation frequency, 6 gauss modulation amplitude, 500 gauss sweep width and 0.2 milliwatts of microwave power. Spectral simulations were done using Bruker XSophe and Easy spin simulation programs.

Computational Details

All calculations on Mo(V) models were performed at the density functional level of theory using ORCA, and Gaussian 03W software packages. In Gaussian 03W program a hybrid B3LYP functional with 6-31G* basis set were used for carbon, oxygen and sulfur, while LANL2DZ and LANL2 effective core potential basis sets were used for molybdenum. All Mo(V) model compounds were optimized in spin-unrestricted mode (UB3LYP). The lowest-energy excited states for computational model were predicted using time dependent density functional theory (TD DFT) as implemented by Gaussian 03W program. EPR spin Hamiltonian parameters were calculated at the DFT level using ORCA 2.7.0. Relativistic corrections were incorporated self-consistently in the ORCA calculations with the ZORA scalar relativistic Hamiltonian. The GaussView input interface was used to prepare Input files.

3.5 Results and Analysis

3.5.1 Electronic Absorption and Magnetic Circular Dichroism (MCD) Spectra

$[MoO(L^H)_2]^-$ and $[MoO(L^O)_2]^-$ Compounds

Room temperature acetonitrile solution electronic absorption and 5K, 7T polystyrene film magnetic circular dichroism (MCD) overlay spectra for $[MoO(L^H)_2]^-$ and $[MoO(L^O)_2]^-$ compounds from 6,000 to 37,000 cm^{-1} are displayed in Figure 3.2. The electronic absorption spectra for the two compounds clearly show three well resolved low energy bands that occur between 6000 and 20,000 cm^{-1} region and appear as negative-positive-positive C-term peaks in the MCD spectra. Several bands were observed in the higher energy region of electronic absorption spectra which correspond to positive-negative-positive peaks pattern in the MCD spectra between 25,000 and 37,000 cm^{-1} region. Figure 3.3 shows variable-temperature MCD spectra for the two compounds collected at 5K, 10K, and 20K, which show that all bands are C-terms.

A weak band that occurs at 8,750 cm^{-1} and at 9,000 cm^{-1} for $[MoO(L^H)_2]^-$ and $[MoO(L^O)_2]^-$ respectively, with extinction coefficient below 300 $M^{-1}cm^{-1}$ in the electronic absorption spectra, appears as a weak negative C-term peak in the MCD spectra at 8,710 cm^{-1} for $[MoO(L^H)_2]^-$ and at 8,830 cm^{-1} for $[MoO(L^O)_2]^-$. The second band which is the first intense band in the electronic absorption spectra of $[MoO(L^H)_2]^-$ and $[MoO(L^O)_2]^-$ compounds, occurs at 12,260 cm^{-1} (ε ~2000 $M^{-1}cm^{-1}$) and 12,100 cm^{-1} (ε ~2000 $M^{-1}cm^{-1}$) respectively. This band corresponds to

an intense positive C-term band occurring at 11,850 cm^{-1} and at 12,000 cm^{-1} in the MCD spectra for $[MoO(L^{H})_2]^-$ for $[MoO(L^{O})_2]^-$ respectively.

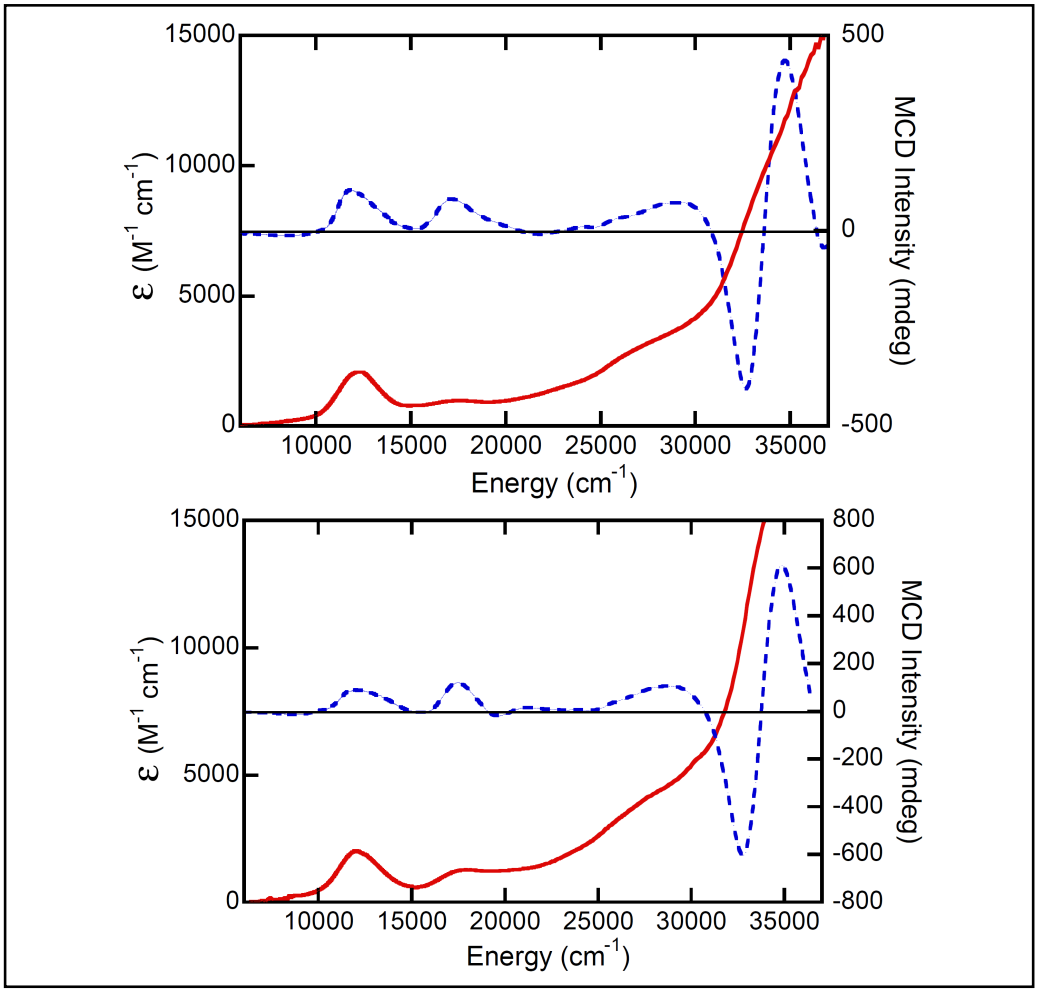

Figure 3.2: Room temperature electronic absorption (——) and 5K, 7T frozen glass MDC (– – –) spectral overlay for $[MoO(L^{H})_2]^-$ (top) and $[MoO(L^{O})_2]^-$ (bottom) compounds.

The second intense band (band 3) in the electronic absorption spectra of $[MoO(L^{H})_2]^-$ and $[MoO(L^{O})_2]^-$ compounds occurs at 17,550 cm^{-1} (ε ~975 $M^{-1}cm^{-1}$)

and 17,950 cm^{-1} (ε ~1275 $M^{-1}cm^{-1}$) and this corresponds to the second intense positive C-term peak at 17,150 cm^{-1} and at 17,450 cm^{-1} in the MCD spectra for the two compounds respectively. A shoulder at approximately 24,500 cm^{-1} in the electronic absorption spectrum consists of two bands that occur at 21,730 cm^{-1} and at 24,240 cm^{-1} for $[MoO(L^H)_2]^-$, while in $[MoO(L^O)_2]^-$ the two bands occur at 20,570 and 23,500 cm^{-1}. These bands correspond to positive (21,640 cm^{-1}) and negative (24,000 cm^{-1}) C-term peaks in the $[MoO(L^H)_2]^-$ MCD spectrum, while for $[MoO(L^O)_2]^-$, it the band appears as negative C-term peak at 19,660 cm^{-1} and three consecutive positive C-term peaks at 21,155 cm^{-1}, at 22,720 cm^{-1} and at 23,860 cm^{-1} respectively. Two consecutive positive C-term peaks at 26,000 and 29,100 cm^{-1} in the MCD spectrum of $[MoO(L^H)_2]^-$ appear as bands 5 and 6 at 26,520 cm^{-1} and at 29,300 cm^{-1} in the electronic absorption spectrum. However, for $[MoO(L^O)_2]^-$ the two positive MCD C-term peaks occur at 26,300 and 28,750 cm^{-1} and correspond to bands 5 and 6 that appear at 26,160 and 28,930 cm^{-1} in the electronic absorption spectrum, respectively. Furthermore, two strong negative and positive C-term (+ve pseudo A-term) peaks are observed at 32,650 cm^{-1} and at 34,700 cm^{-1} in the MCD spectra for $[MoO(L^H)_2]^-$ while in $[MoO(L^O)_2]^-$, these occur at 32,760 and 34,820 cm^{-1}. These bands correspond to band 7 and band 8 in the electronic absorption spectrum of $[MoO(L^H)_2]^-$ at ~32,700 cm^{-1} (ε ~4,000 $M^{-1}cm^{-1}$) and at 34,500 cm^{-1} (ε ~6100 $M^{-1}cm^{-1}$) while in $[MoO(L^O)_2]^-$ compound, they occur at 32,700 cm^{-1} (ε ~5,800 $M^{-1}cm^{-1}$) and at 34580 cm^{-1} (ε ~10,800 $M^{-1}cm^{-1}$) respectively. In general the electronic absorption spectra for all

compounds show intensity increases going to higher energy bands which signifies the presence of ligand to metal charge transfer (LMCT) transitions.

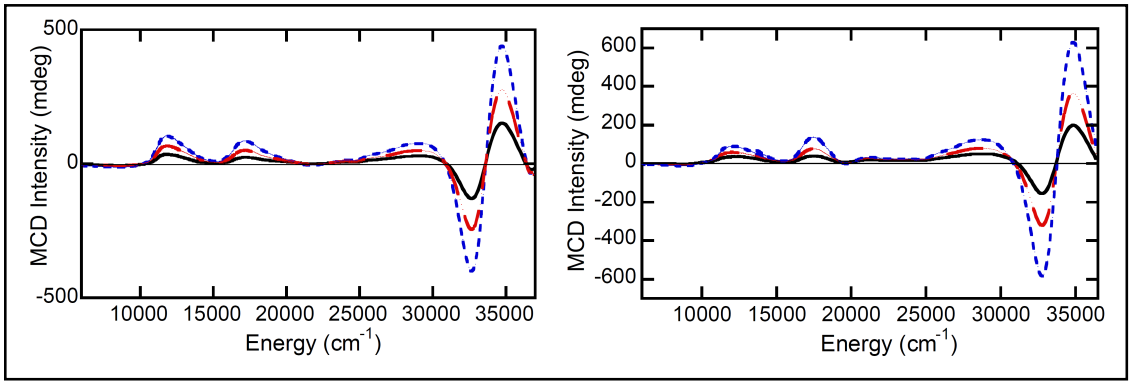

Figure 3.3: Variable temperature MCD spectra for $[MoO(L^{H})_2]^-$ (left), $[MoO(L^{O})_2]^-$ (right) at 5K (—·--), 10K (– – –) and 20K(——).

$[MoO(L^{COOMe})_2]^-$ and $[MoO(bdt)_2]^-$ Compounds

Room temperature acetonitrile solution electronic absorption and 5K, 7T frozen glass magnetic circular dichroism (MCD) spectral overlay for $[MoO(L^{COOMe})_2]^-$ and $[MoO(bdt)_2]^-$ compounds from 6,000 to 37,000 cm^{-1} are shown in Figure 3.4. The electronic absorption spectra for the two compounds reveal five well resolved bands below 27,000 cm^{-1} that appear as negative-three positive-negative pattern of C-term peaks in the MCD spectrum for $[MoO(L^{COOMe})_2]^-$. However, the electronic absorption spectrum for $[MoO(bdt)_2]^-$ shows four bands that appear as negative-two positive-negative C-term peaks in the MCD spectrum. The electronic absorption spectra of the two compounds show two intense peaks at higher energy that appear as two intense positive and negative (-ve pseudo-A) MCD C-term peaks in $[MoO(L^{COOMe})_2]^-$ and vice versa for the $[MoO(bdt)_2]^-$ MCD

spectra. Figure 3.5 shows variable temperature MCD spectra collected at 5K, 10K, and 20K that reveal seven temperature dependent C-term bands for both the $[MoO(^{LCOOMe})_2]^-$ and $[MoO(bdt)_2]^-$ compounds.

A weak band observed in the electronic absorption spectra for $[MoO(L^{COOMe})_2]^-$ and $[MoO(bdt)_2]^-$ compounds at 10,330 cm^{-1} (ε ~145 $M^{-1}cm^{-1}$) and at 10,940 cm^{-1} (ε ~295 $M^{-1}cm^{-1}$), respectively, appears as a weak negative MCD C-term band in the MCD spectra at ~10,000 cm^{-1} and at 11,415 cm^{-1} for $[MoO(L^{COOMe})_2]^-$ and $[MoO(bdt)_2]^-$, respectively. This band occurs at slightly higher energy (>10,000 cm^{-1}) in these compounds compared to the same band that occurs below 9,000 cm^{-1} in the $[MoO(L^H)_2]^-$ and $[MoO(L^O)_2]^-$ compounds. This may indicate less ligand-metal covalency in $[MoOL^{COOMe})_2]^-$ and $[MoO(bdt)_2]^-$ compared to $[MoO(L^H)_2]^-$ and $[MoO(L^O)_2]^-$. The first intense band (band 2) in the $[MoO(L^{COOMe})_2]^-$ and $[MoO(bdt)_2]^-$ electronic absorption spectra occurs at 13,270 cm^{-1} (ε ~2000 $M^{-1}cm^{-1}$) and at 13,740 cm^{-1} (ε = 3,000 $M^{-1}cm^{-1}$), and appears as an intense positive C-term in the MCD spectra at 13,330 cm^{-1}, and at 13,375 cm^{-1} respectively. This band is observed at higher energy (~13,300 cm^{-1}) in $[MoO(L^{COOMe})_2]^-$ and $[MoO(bdt)_2]^-$ compared to ~12,200 cm^{-1} observed in $[MoO(L^H)_2]^-$ and $[MoO(L^O)_2]^-$ due to strong electron withdrawing nature of the L^{COOMe} ligand for $[MoO(L^{COOMe})_2]^-$ and resonance effects in the bdt ligand of $[MoO(bdt)_2]^-$.

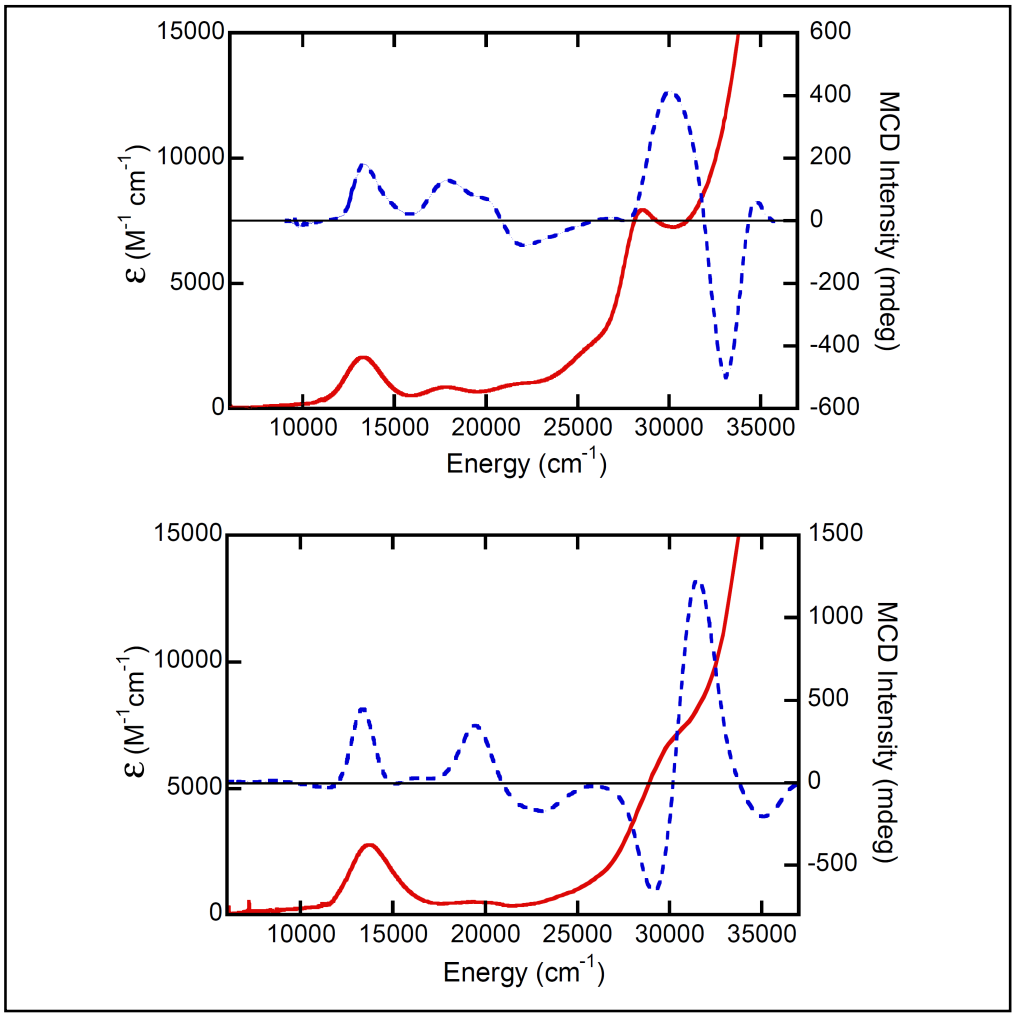

Figure 3.4: Room temperature electronic absorption (——) and 5K frozen glass MDC (– – –) spectral overlay for $[MoO(L^{COOMe})_2]^-$ (top) and $[MoO(bdt)_2]^-$ (bottom) compounds.

A weak positive C-term peak observed in the MCD spectrum for $[MoO(bdt)_2]^-$ at 16,430 cm^{-1} appears as a shoulder (band 3) in the electronic absorption at 15,300 cm^{-1}, however, this band is missing in $[MoO(L^{COOMe})_2]^-$. The second intense band in the electronic absorption spectra of $[MoO(L^{COOMe})_2]^-$ and $[MoO(bdt)_2]^-$ occurs at 17,800 cm^{-1} (ε = 800 $M^{-1}cm^{-1}$) and at 19,400 cm^{-1} (ε ~520

$M^{-1}cm^{-1}$), and appears as a positive C-term (band 4) in the MCD spectra at 17,900 cm^{-1} and at 19,450 cm^{-1} for $[MoO(L^{COOMe})_2]^-$ and $[MoO(bdt)_2]^-$ respectively. The positive and negative C-term peaks in the MCD spectrum of $[MoO(L^{COOMe})_2]^-$ compound observed at 19,680 cm^{-1} and at 22,030 cm^{-1} are contained in band 5 that occurs at 21,900 cm^{-1} in the electronic absorption spectrum. However, for $[MoO(bdt)_2]^-$, a broad negative C-term peak in the MCD spectrum is composed of two bands at 21,300 cm^{-1} and at 23,330 cm^{-1} which are contained in band 5 that occurs at ~23,900 cm^{-1} in the electronic absorption. A shoulder (band 6) that is revealed at ~26,200 cm^{-1} and at 26,600 cm^{-1} region in the electronic absorption spectra for $[MoO(L^{COOMe})_2]^-$ and $[MoO(bdt)_2]^-$ appears as a weak positive C-term peak at ~26,600 cm^{-1} for $[MoO(L^{COOMe})_2]^-$ and a weak negative C-term peak at ~25,000 cm^{-1} for $[MoO(bdt)_2]^-$ in the MCD spectra. Additionally, in the higher energy MCD spectral region, two very intense positive and negative C-term (-ve pseudo-A) peaks are observed at 30,600 and 33,050 cm^{-1} for $[MoO(L^{COOMe})_2]^-$ compound, which appear as bands 7 and 8 in the electronic absorption spectrum that occur at 30,470 cm^{-1} and at 32950 cm^{-1}. However, for $[MoO(bdt)_2]^-$, MCD the spectrum reveals two intense negative and positive C-term (+ve pseudo-A) peaks at 29,150 cm^{-1} and at 31,520 cm^{-1} that appear as bands 7 and 8 in the electronic absorption spectrum occurring at 29,330 cm^{-1} and at 31,380 cm^{-1} respectively. Progressive intensity increases, observed in the higher energy spectral bands, indicates strong ligand to metal charge transfer transitions.

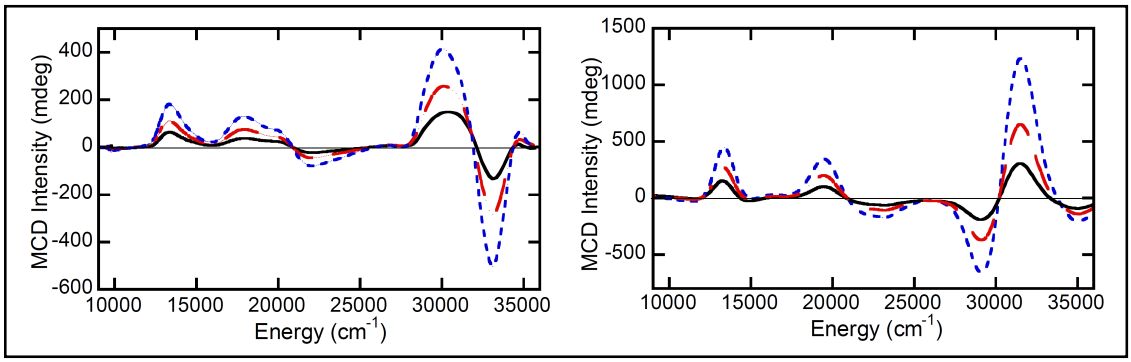

Figure 3.5: Variable temperature MCD spectra for $[MoO(L^{COOMe})_2]^-$ (left), $[MoO(bdt)_2]^-$ (right) at 5K (—·—), 10K (– – –) and 20K(——).

$[WO(L^H)_2]^-$ Compound

Room temperature acetonitrile solution electronic absorption and 5K, 7T frozen glass magnetic circular dichroism (MCD) spectral overlay for $[WO(L^H)_2]^-$ from 6,000 to 37,000 cm^{-1} is shown in Figure 3.6. The room temperature electronic absorption spectrum reveals three low energy bands in $[WO(L^H)_2]^-$,, but due to poor bands spectral resolution in the electronic absorption spectrum higher energy region bands maxima energies are obtained from Gaussian resolved spectrum that match the MCD spectrum. Figure 3.7 shows the variable temperature MCD spectra collected at 5K, 10K, and 20K that reveal nine C-term temperature dependent bands from 8,000 to 37,000 cm^{-1}. Nine MCD C-term bands observed in the variable temperature MCD spectrum have negative, three positives and negative pattern below 24,000 cm^{-1} spectral region followed by four consecutive positive MCD C-term peaks from 24,000 to 37,000 cm^{-1}.

A weak negative C-term peak in the MCD spectrum observed at 10,800 cm^{-1} appears as a weak band (band 1) in the electronic absorption spectrum at 10,710 cm^{-1}. The weakness in intensity of this band indicates poor overlap between ene-dithiolene ligands and the metal center. The first broad and intense band (band 2) in the electronic absorption spectrum that occurs at 15,100 cm^{-1} appears as an intense and broad positive C-term peak 2 in the MCD spectrum at 14,400 cm^{-1}.

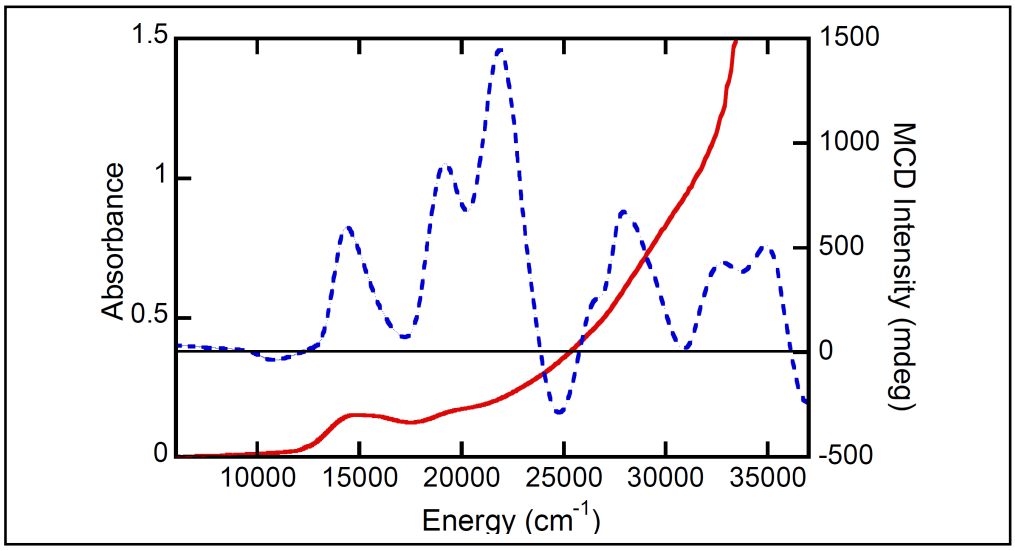

Figure 3.6: Room temperature electronic absorption (——) and 5K, 7T frozen glass MDC (– – –) spectra overlay for $[WO(L^{H})_2]^-$.

Two intense positive C-term peaks in the MCD spectrum that occur at 19,190 cm^{-1} and at 21,870 cm^{-1} appear as bands 4 and 5 in the electronic absorption at 18,895 cm^{-1} and at 22,080 cm^{-1} respectively. A negative and positive (+ve pseudo-A term) C-term peaks in the MCD spectrum which appear at 24,710 cm^{-1} and at 25,415 cm^{-1} are contained in band 6 in the electronic absorption spectrum

at 25,415 cm^{-1}. Bands 7 and 8 in the electronic absorption spectrum that occur at 27,640 and 29,490 cm^{-1} are contained in a non Gaussian positive C-term peaks in the MCD spectrum at 27,990 cm^{-1}. In addition, two intense higher energy bands in the electronic absorption spectrum that occur at 32,450 cm^{-1} (band 9) and at 34,770 cm^{-1} (band 10), appear as two positive C-term bands in the MCD spectrum at 32,800 cm^{-1} and at 34,840 cm^{-1} respectively.

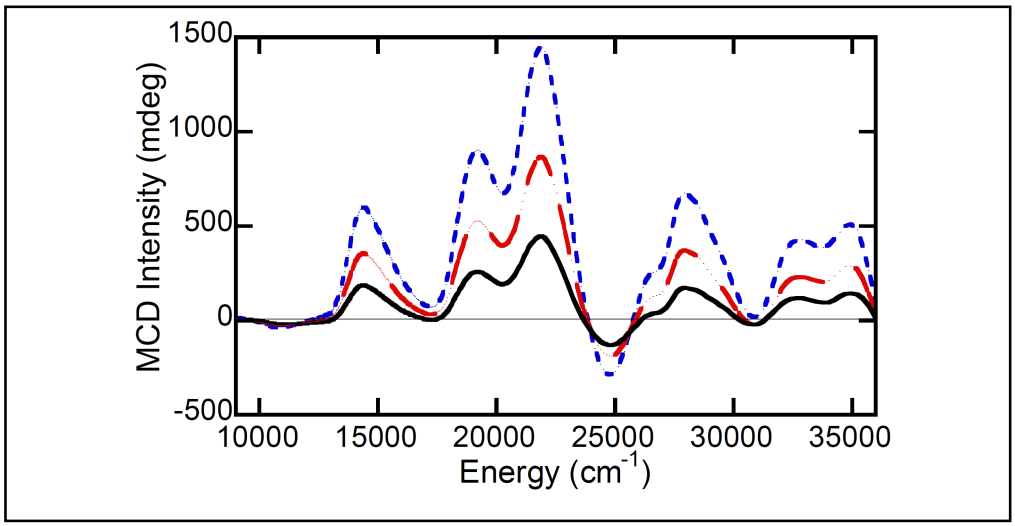

Figure 3.7: Variable temperature MCD spectra for $[WO(L^{H})_2]^-$ at 5K (— · -), 10K (- - -) and 20K(——).

3.5.2 Determination of Spin Hamiltonian Parameters

The differences in the electronic structure resulting from different ene-dithiolene substituents bound to molybdenum observed in the electronic absorption and MCD spectroscopies have been studied using EPR spectroscopy. For $[MoO(L^{H})_2]^-$, $[MoO(L^{O})_2]^-$, $[MoO(L^{COOMe})_2]^-$, $[MoO(bdt)_2]^-$ and $[WO(L^{H})_2]^-$ compounds, $^{95,97}Mo$ and ^{183}W hyperfine tensor, g-tensor and their relative

orientations (Euler angles) have not been reported to date. Figure 3.8 displays room temperature experimental solution EPR spectra and the corresponding simulations for $[MoO(L^{H})_2]^-$, $[MoO(L^{O})_2]^-$, $[MoO(L^{COOMe})_2]^-$, $[MoO(bdt)_2]^-$ and $[WO(L^{H})_2]^-$ compounds. Room temperature EPR spectral simulations reveal an isotropic g value (g_{iso}) of 2.0022 for $[MoO(L^{H})_2]^-$, 2.0024 for $[MoO(L^{O})_2]^-$, 2.0020 for $[MoO(L^{COOMe})_2]^-$, 1.9982 for $[MoO(bdt)_2]^-$ and 1.9632 for $[WO(L^{H})_2]^-$. The g_{iso} values for $[MoO(L^{H})_2]^-$, $[MoO(L^{O})_2]^-$ and $[MoO(L^{CCOMe})_2]^-$ are close to 2.00321 for free electron (g_e), however for [MoO(bdt) and $[WO(L^{H})_2]^-$ compounds g_{iso} value is lower than that of free electron (g_e).

In addition, frozen glass EPR spectra have an average g value (g_{ave}) of 1.9925 for $[MoO(L^{H})_2]^-$, 2.0018 for $[MoO(L^{O})_2]^-$, 2.0007 for $[MoO(L^{COOMe})_2]^-$, 1.9982 for $[MoO(bdt)_2]^-$ and 1.9695 for $[WO(L^{H})_2]^-$ compounds. Comparison of isotropic g (g_{iso}) with average g (g_{ave}) show a very good agreement, as g_{ave} is the averaged anisotropic g values obtained from frozen samples spectral simulation value and the isotropic g is observed at room temperature where molecules are tumbling very rapidly.[42,43]

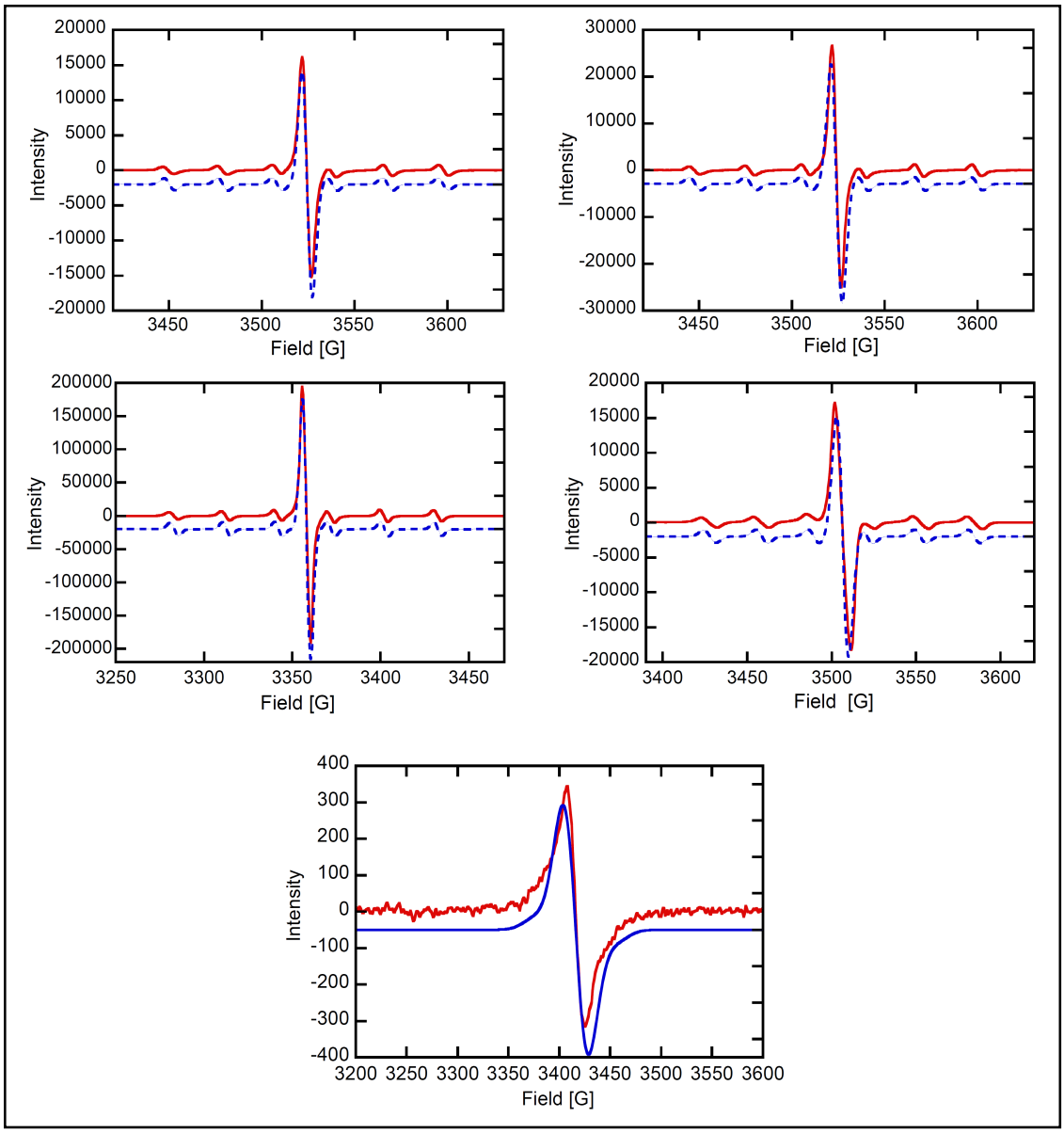

Figure 3.8: Room temperature (298K) experimental (——) and simulation (- - -) EPR spectra overlay for $[MoO(L^{H})_2]^{-1}$ (top left), $[MoO(L^{O})_2]^{-1}$ (top right), $[MoO(L^{COOMe})_2]^{-1}$ (middle left), and $[MoO(bdt)_2]^{-1}$ (middle right).

At room temperature and in solution, the molybdenum unpaired electron spin interacts with nucleus and this leads to an isotropic ^{95,97}Mo hyperfine interaction

which should be close the average A value in the x, y, and z directions according to Eq. 2.

$$\langle A \rangle = \langle A_x + A_y + A_z \rangle / 3 \quad \text{..... (2)}$$

Spectral simulation of room temperature EPR data reveal isotropic ^{95,97}Mo hyperfine of 27.33 x10^{-4} cm^{-1} for $[MoO(L^{H})_2]^-$, 28.10 x10^{-4} cm^{-1} for $[MoO(L^{O})_2]^-$, 27.67 x10^{-4} cm^{-1} for $[MoO(L^{COOMe})_2]^-$, and 28.77 x10^{-4} cm^{-1} for $[MoO(bdt)_2]^-$, whereas for $[WO(L^{H})_2]^-$ an isotropic ^{183}W hyperfine of 12.00 x10^{-4} cm^{-1} was obtained. These values are close to averaged ^{95,97}Mo hyperfine of 27.33 x10^{-4} cm^{-1} for $[MoO(L^{H})_2]^-$, 28.22 x10^{-4} cm^{-1} for $[MoO(L^{O})_2]^-$, 28.56 x10^{-4} cm^{-1} for $[MoO(L^{COOMe})_2]^-$, and 27.89 x10^{-4} cm^{-1} for $[MoO(bdt)_2]^-$ and ^{183}W hyperfine of 7.11 x10^{-4} cm^{-1} for $[WO(L^{H})_2]^-$ as obtained from low temperature anisotropic parameters by spectral simulation. A good agreement between the averaged anisotropic g_{ave} and A_{ave} with isotropic g_{iso} and A_{iso} values, indicate that there is no marked perturbation of the compounds upon freezing. Additionally these values are within a range observed in Mo(V) and W(V) bis-dithiolene compounds.[71,95,100]

Table 3-1: EPR spin Hamiltonian parameters for bis-dithiolene molybdenum and tungsten (V) complexes.

Compound	$[MoO(L^H)_2]^-$	$[MoO(L^O)_2]^-$	$[MoO(L^{COOMe})_2]^-$	$[MoO(bdt)_2]^-$	$[WO(L^H)_2]^-$
g_1	2.0210	2.0295	2.0259	2.0293	2.0550
g_2	1.9836	1.9931	1.9936	1.9902	1.9368
g_3	1.9730	1.9827	1.9825	1.9821	1.9168
g_{ave}	1.9925	2.0018	2.0007	2.0005	1.9695
g_{iso}	2.0022	2.0024	2.0020	1.9982	1.9632
A_1	45.33	46.67	47.33	48.67	14.67
A_2	18.67	19.33	20.00	18.33	3.33
A_3	18.00	18.67	18.33	16.67	3.33
A_{ave}	27.33	28.22	28.56	27.89	7.11
A_{iso}	27.33	28.10	27.67	28.77	12.00
α	-0.40	1.00	-6.10	0.00	9.60
β	30.02	30.41	32.76	26.01	39.32
γ	1.40	-1.30	8.00	0.00	-45.40

The low temperature (77K) EPR spectra for all five compounds reveal a rhombic g-tensor pattern as displayed in Figure 3.9 and spin Hamiltonian parameters are displayed in Table 3-1. High quality EPR spectral simulation gave a rhombic g tensor with g_1 = 2.0210, g_2 = 1.9836 and g_3 = 1.9730 for $[MoO(L^H)_2]^{2-}$, g_1 = 2.0295, g_2 = 1.9931 and g_3 = 1.9827 for $[MoO(L^O)_2]^{2-}$, g_1 = 2.0259, g_2 = 1.9936 and g_3 = 1.9825 for $[MoO(L^{COOMe})_2]^{2-}$ and g_1 = 2.0293 g_2 = 1.9902 and g_3 = 1.9821 for $[MoO(bdt)_2]^{2-}$ compounds. The rhombic nature of the g-tensor indicates the presence of low-symmetry (C_s symmetry) coordination environment in these Mo(V) model compounds. Figure 3.9 shows experimental EPR with the simulation overlayed. All molybdenum compounds possess a g_1 value larger than the free electron value (g_e), which is consistent with previously reported values

for mono-oxo bis-dithiolenes $[MoO(edt)_2]^-$,[95,96] $[MoO(4\text{-}pedt)_2]^-$,[71] and $[MoO(mnt)_2]^-$,[97] compounds. The larger g_1 value observed in $[MoO(L^H)_2]^-$, $[MoO(L^O)_2]^-$, $[MoO(L^{COOMe})_2]^-$ and $[MoO(bdt)_2]^-$ is due to increased metal-ligand covalency and the presence of low energy ligand to metal charge transfer (LMCT) states.[101,102] Also we calculated anisotropic g value (note: $g_{anisotropy} = g_1 - g_3$) of 0.048 for $[MoO(L^H)_2]^-$, 0.047 for $[MoO(L^O)_2]^-$, 0.043 for $[MoO(L^{COOMe})_2]^-$ and 0.047 for $[MoO(bdt)_2]^-$. These values are slightly above the range observed for molybdenum enzymes[90,85] but are within the range observed for bis-dithiolene molybdenum compounds.[97,103] Additionally, spectral simulation for $[WO(L^H)_2]^-$ compound (Figure 3.9) reveals a rhombic g tensor pattern with $g_1 = 2.0550$, $g_2 = 1.9368$ and $g_3 = 1.9168$, and average g value (g_{ave}) of 1.9695. A large g_1 value observed for the $[WO(L^H)_2]^-$ compound (Table 3-1) is consistent with what has been previously reported in $[WO(bdt)_2]^-$, $[WO(edt)_2]^-$, $[WO(mnt)_2]^-$,[104] and $[WO(SPh)_4]^-$[100,105] compounds as being due to larger spin-orbit coupling constant which is estimated to be 3-5 times larger in tungsten than in molybdenum. The spin-orbit coupling increases the g anisotropy ($g_{anisotropy} = 0.1382$) and leads to lower g_{ave} values in W(V) compared to Mo(V) compounds ($g_{anisotropy}$ ~0.043 - 0.048).

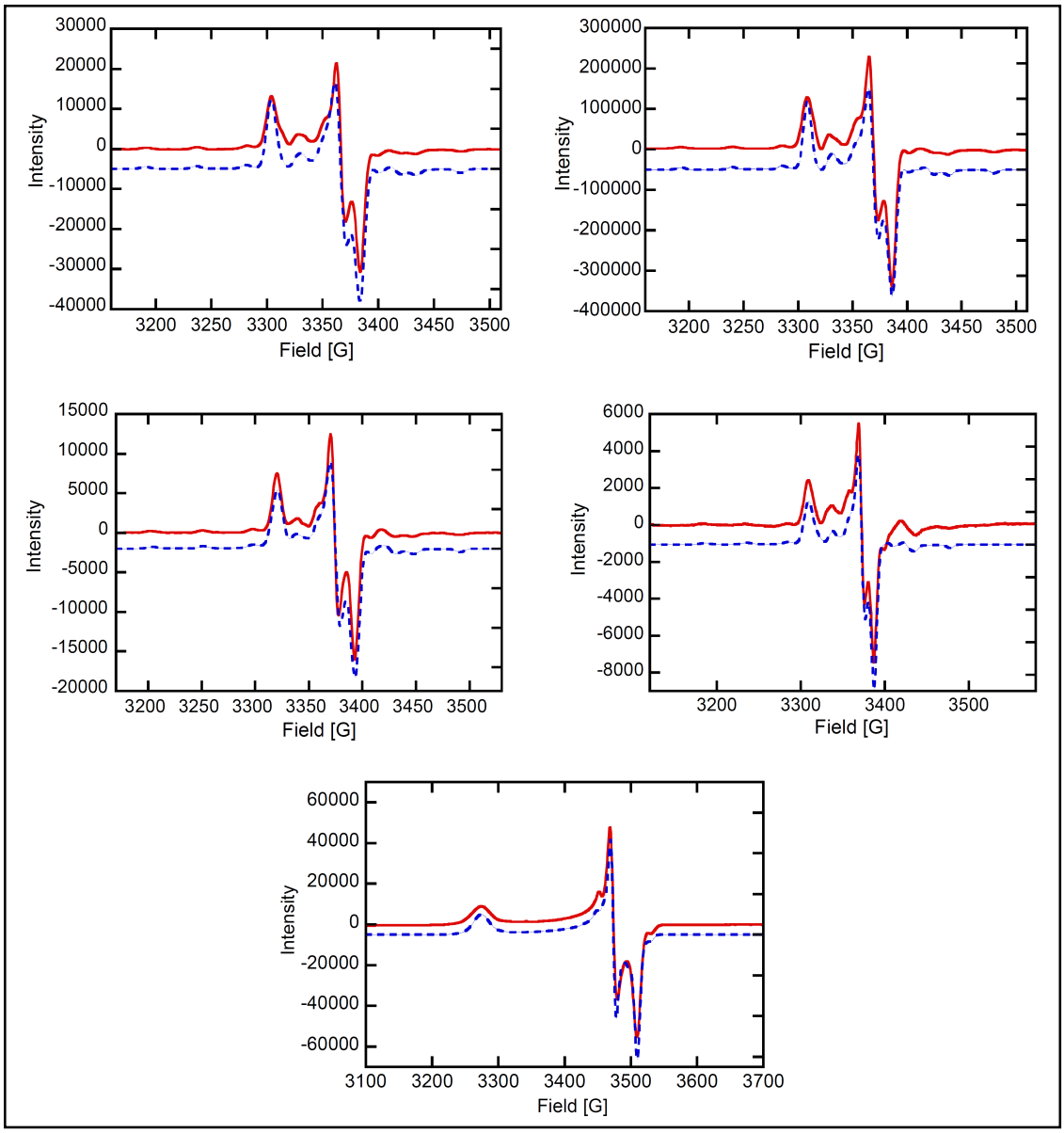

Figure 3.9: Low temperature (77K) experimental (——) and simulation (– – –) EPR spectra overlay for $[MoO(L^{H})_2]^{-1}$ (top left), $[MoO(L^{O})_2]^{-1}$ (top right), $[MoO(L^{COOMe})_2]^{-1}$ (middle left), and $[MoO(bdt)_2]^{-1}$ (middle right) showing the rhombic g-value and axial ^{95,97}Mo hyperfine and (bottom) is the $[WO(L^{H})_2]^{-1}$ compound showing the rhombic g-value and ^{183}W hyperfine.

With respect to hyperfine values, spectral simulation results show that all compounds possess axial ^{95,97}Mo hyperfine splitting patterns consistent with d^1 system (S =1/2) containing a d_{xy} redox orbital. The hyperfine interaction arises from interaction of unpaired electron spin with its nucleus and comprises of isotropic and anisotropic components.[43,101] The anisotropic component consists of the spin dipolar (A_s^{Mo}) and orbital dipolar (A_l^{Mo}) terms where the latter has less contribution. The spin dipolar contribution is proportional to the unpaired electron nuclear spin density and reflects changes in the ground state covalency.[42,43] The low temperature EPR spectral simulation gave an axial ^{95,97}Mo hyperfine tensor with A_1 = 45.33 x10^{-4} cm^{-1}, A_2 = 18.67 x10^{-4} cm^{-1}, and A_3 = 18.00 x10^{-4} cm^{-1} for $[MoO(L^H)_2]^-$, A_1 = 46.67 x10^{-4} cm^{-1}, A_2 = 19.33 x10^{-4} cm^{-1}, and A_3 = 18.67 x10^{-4} cm^{-1} for $[MoO(L^O)_2]^-$, A_1 = 47.33 x10^{-4} cm^{-1}, A_2 = 20.00 x10^{-4} cm^{-1}, and A_3 = 18.33 x10^{-4} cm^{-1} for $[MoO(L^{COOMe})_2]^-$ and A_1 = 48.67 x10^{-4} cm^{-1}, A_2 = 18.33 x10^{-4} cm^{-1}, and A_3 = 16.67 x10^{-4} cm^{-1} for $[MoO(bdt)_2]^-$ whereas for $[WO(L^H)_2]^-$ compound ^{183}W hyperfine values are A_1 = 14.67 x10^{-4} cm^{-1}, A_2 = 3.33 x10^{-4} cm^{-1}, and A_3 = 3.33 x10^{-4} cm^{-1} respectively. In addition an axial dipolar contributions A_s^{Mo} = [$2A_s^{Mo}$, $-A_s^{Mo}$, $-A_s^{Mo}$] shown in Table 3-2 was calculated from ^{95,97}Mo hyperfine in each compound, that support a d_{xy} ground state.[42,52]

Table 3-2: Experimental and theoretical dipolar contributions for $[MoO(L^{H})_2]^-$, $[MoO(L^{O})_2]^-$, $[MoO(L^{COOMe})_2]^-$ and $[MoO(bdt)_2]^-$ compounds.

Compound	$[MoO(L^{H})_2]^-$	$[MoO(L^{O})_2]^-$	$[MoO(L^{COOMe})_2]^-$	$[MoO(bdt)_2]^-$
		Experimental		
A_1	18.00	18.45	19.89	20.78
A_2	-8.66	-8.89	-7.44	-9.56
A_3	-9.33	-8.55	-9.11	-11.22
		Theoretical		
A_1	19.33	19.22	19.45	20.51
A_2	-9.01	-8.99	-8.62	-9.26
A_3	-10.32	-10.23	-10.83	-11.25

Calculated Spin Hamiltonian Parameters

ORCA calculations have been performed on fully optimized geometries for $[MoO(L^{H})_2]^-$, $[MoO(L^{O})_2]^-$, $[MoO(L^{COOMe})_2]^-$ and $[MoO(bdt)_2]^-$ in order to obtain theoretical spin Hamiltonian parameters for direct comparison with experimental results. ORCA results revealed a rhombic g tensor with $g_1 = 2.0239$, $g_2 = 1.9874$ and $g_3 = 1.9738$ for $[MoO(L^{H})_2]^{2-}$, $g_1 = 2.0238$, $g_2 = 1.9879$ and $g_3 = 1.9726$ for $[MoO(L^{O})_2]^{2-}$, $g_1 = 2.0265$, $g_2 = 1.9914$ and $g_3 = 1.9812$ for $[MoO(L^{COOMe})_2]^{2-}$, $g_1 = 2.0204$, $g_2 = 1.9865$ and $g_3 = 1.9741$ for $[MoO(bdt)_2]^{2-}$ and $g_1 = 2.0282$, $g_2 = 2.0037$ and $g_3 = 1.9539$ for $[WO(L^{H})_2]^{2-}$. These values are similar to the experimental g tensor values and support a C_s low symmetry coordination environment. ORCA results also produced a larger g_1 value than g_{iso}, similar to what have been observed experimentally due to metal-ligand covalency and the presence of low energy ligand to metal charge transfer (LMCT) state in

molybdenum compounds and the larger spin orbital coupling constant for $[WO(L^{H})_2]^-$ compound.

Furthermore ORCA calculations produced axial ^{95,97}Mo hyperfine and ^{183}W hyperfine values with A_1 = 43.72 x10^{-4} cm^{-1}, A_2 = 15.38 x10^{-4} cm^{-1}, and A_3 = 14.06 x10^{-4} cm^{-1} for $[MoO(L^{H})_2]^-$, A_1 = 43.76 x10^{-4} cm^{-1}, A_2 = 15.56 x10^{-4} cm^{-1}, and A_3 = 14.32 x10^{-4} cm^{-1} for $[MoO(L^{O})_2]^-$, A_1 = 41.61 x10^{-4} cm^{-1}, A_2 = 14.57 x10^{-4} cm^{-1}, and A_3 = 12.23 x10^{-4} cm^{-1} for $[MoO(L^{COOMe})_2]^-$, A_1 = 45.50 x10^{-4} cm^{-1}, A_2 = 15.72 x10^{-4} cm^{-1}, and A_3 = 13.73 x10^{-4} cm^{-1} for $[MoO(bdt)_2]^-$ respectively. These values are in good agreement with the experimental results therefore support a d_{xy} type ground state orbital.

3.5.3 The Nature of Mo/W(V) Redox Orbital and Orientation of ^{95,97}Mo Hyperfine Tensor and g-Tensor

Spin density calculations on model compounds reveal Mo total spin densities of 78% for $[MoO(bdt)_2]^-$, 68% for $[MoO(L^{H})_2]^-$, 66% for $[MoO(L^{O})_2]^-$, 67% for $[MoO(L^{COOMe})_2]^-$ and 80% for $[WO(L^{H})_2]^-$ (Table 3.6). Additionally, the calculations show negative spin density on oxygen and positive spin densities on all sulfur atoms as depicted in Figure 3.10. The negative spin density observed on the oxygen is due to a spin polarization mechanism that resulted from configuration interaction (CI) of excited states which involves promotion of a β electron localized on an oxo based orbital into unoccupied Mo-based β orbitals. [42]

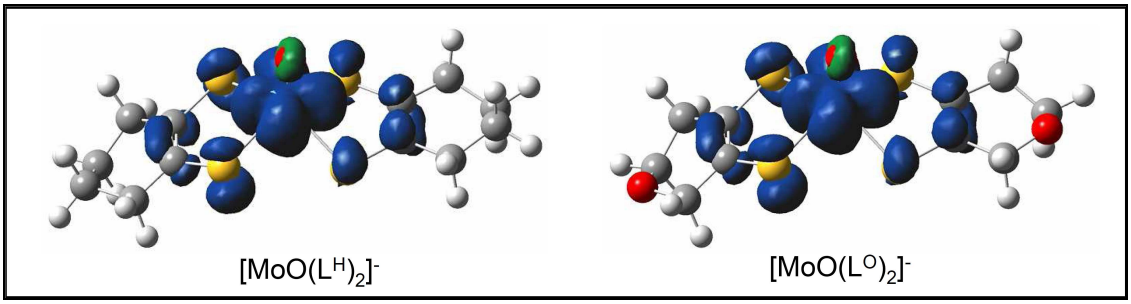

Figure 3.10: Contour plot of spin density distribution for $[MoO(L^{H})_2]^-$ and $[MoO(L^{O})_2]^-$.

Calculations on g- and A-tensors have been performed using fully optimized geometries with a Cartesian coordinate system defining the molecular frame. The vector along the Mo=O bond defines the z direction, while x and y axes lie along the plane perpendicular to the z axis with x axis bisecting the two dithiolene ligands. Figure 3.11 shows the orientation of Mo hyperfine tensor and g-tensor for $[MoO(L^{H})_2]^-$ as obtained from ORCA output orientation matrices. Analysis was done on other four compounds that reveal similar g-tensor and A-tensor orientations as seen in Figure 3.11, where one of principle g-tensor axis and hyperfine tensor axis are collinear, while the remaining two are rotated by ~30°. Compounds with C_2, C_s or C_{2h} point group symmetry must possess one of the principle g tensor components collinear with one of the principle component of the hyperfine tensor[103,106-108] which agrees well with our orientation results showing that the g_2 axis coincide with the A_3 axis.

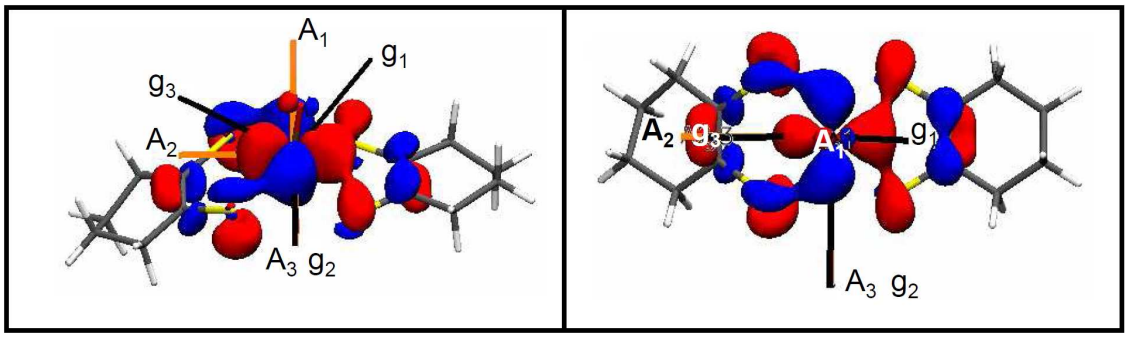

Figure 3.11: Schematic representation of the g-tensor and ^{95,97}Mo A-tensor for $[MoO(L^H)_2]^-$ overlayed on the β-LUMO as drawn from the orientation matrices in ORCA output files, side view (left) and top view (right).

Euler rotations obtained from ORCA output files were calculated using a zyz convention and yielded α = -0.40, β = 57.10 and γ = 1.40 for $[MoO(L^H)_2]^{2-}$. The theoretical β value is slightly higher compared to the α = -0.40, β = 30.02 and γ = 1.40 experimental values for $[MoO(L^H)_2]^-$. These values are in good agreement as they both possess large β-values which have dramatic effect on the spectral simulations. Table 3-3 shows the comparison between calculated and experimental Euler rotations of g-tensor relative to hyperfine tensor for all five compounds studied. Westmoreland and coworkers reported that an increase in covalency in the metal-ligand bonds along the equatorial plane leads to a rotation of the largest g value (g_1) away from the Mo≡O vector toward the equatorial plane.[101,109,110] This observation is consistent with our results showing that the g_1 tensor is rotated ~30° away from Mo≡O bond (Figure 3.11) in all Mo(V) compounds.

Table 3-3: Experimental vs. theoretical Euler angles.

Compound	$[MoO(L^H)_2]^-$	$[MoO(L^O)_2]^-$	$[MoO(L^{COOMe})_2]^-$	$[MoO(bdt)_2]^-$	$[WO(L^H)_2]^-$
			Experimental		
α	-0.40	1.00	-6.10	0.00	9.60
β	30.02	30.41	32.76	26.01	39.32
γ	1.40	-1.30	8.00	0.00	-45.40
			Theoretical		
α	-0.40	1.00	-6.10	0.00	9.60
β	57.10	55.6	56.70	28.60	79.10
γ	1.40	-1.30	8.00	0.00	-45.40

3.5.4 The Molecular Orbital Bonding Scheme

The nature of the frontier molecular orbital bonding scheme for $[MoO(L^H)_2]^-$, $[MoO(L^O)_2]^-$, $[MoO(L^{COOMe})_2]^-$, $[MoO(bdt)_2]^-$ and $[WO(L^H)_2]^-$ compounds have been determined by utilizing electronic structure calculations performed on computational models. Geometry optimizations for all five model compounds yield a pseudo square pyramidal geometry with one planer and one bent ene-dithiolene ligand attached to the metal center, and an oxo ligand at the apical position that agrees well with crystal structure geometries for these bis-dithiolene complexes.[65,94,111] EPR studies in all Mo and W compounds with d^1 system have revealed d_{xy} as redox orbital. This result agrees well with orbital splitting pattern according to $d_{z^2} > d_{x^2-y^2} > d_{xz}$, $d_{yz} > d_{xy}$ due to strong σ and π interaction of the metal with the apical oxo as observed in Figure 3.12.[68,112] This interaction leads to a strong destabilization of d_{z^2} and $d_{xz/yz}$ orbitals through σ and π interaction with apical oxo ligand while $d_{x^2-y^2}$ orbital is destabilized through σ interactions with the four equatorial ligands.

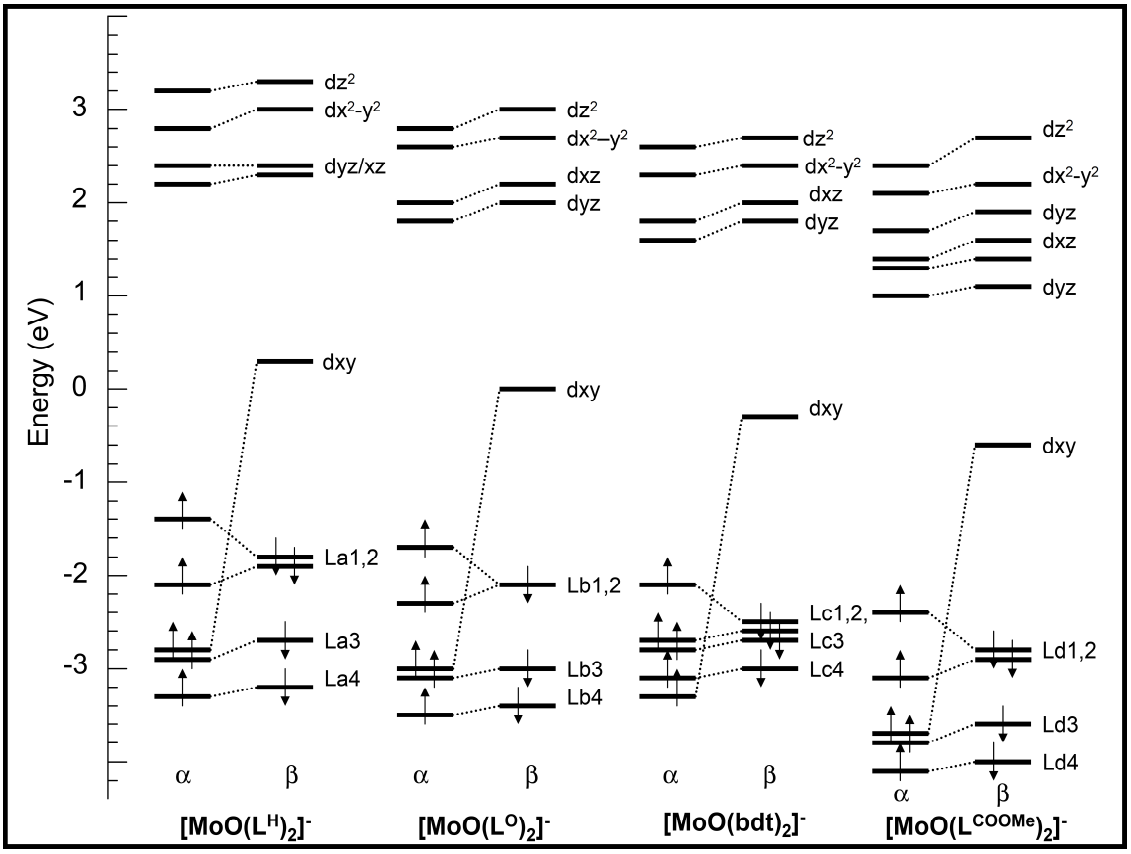

Figure 3.12: Molecular orbitals energy diagrams for $[MoO(L^{H})_2]^-$, $[MoO(L^{O})_2]^-$, $[MoO(bdt)_2]^-$ and $[MoO(L^{COOMe})_2]^-$ compounds obtained from spin unrestricted geometry optimized DFT calculations. Note the inverted bonding scheme.

Beneath the metal orbitals there are two sets of sulfur orbitals i) four out of plane sulfur orbitals (Figure 3.13), and ii) four inplane sulfur orbitals. These eight sulfur orbitals are the results of symmetry adapted linear combination of atomic orbitals from the two dithiolene ligands.[45] Electron density plots for the β HOMO -4 to HOMO for all four molybdenum compounds are shown in Figure 3.13.

For an idealized Cs symmetry the redox orbital is the Mo-dxy orbital where α component orbital has the unpaired electron and the β orbital is empty. Our results on all molybdenum compounds show an inverted bonding scheme (Figure 3.12) where the α Mo-d_{xy} orbital is more stabilized than its β counterpart. Spin unrestricted calculations show the unpaired electron in the α HOMO-2 (Mo-d_{xy}) orbital for $[MoO(L^{H})_2]^-$, $[MoO(L^{O})_2]^-$ and $[MoO(L^{COOMe})_2]^-$ compounds and in the α HOMO-4 orbital for $[MoO(bdt)_2]^-$.

For $[MoO(L^{H})_2]^-$ the α HOMO-2 has 68% Mo-d_{xy} character, 17% sulfur character and less that 1% apical oxo ligand character, whereas the β LUMO has 56% Mo-d_{xy} character, 28% sulfur character and 1% apical oxo ligand character. The presence of sulfur out of plane character in the unoccupied β orbital indicates a strong interaction between metal and ligand, and favors low energy ligand to metal charge transfers. The low energy charge transfer transition from β-HOMO orbital having sulfur out of plane ligand character to the β-LUMO possessing metal character has been assigned in all molybdenum and tungsten compounds and agree well with previously reported assignments.[96,113]

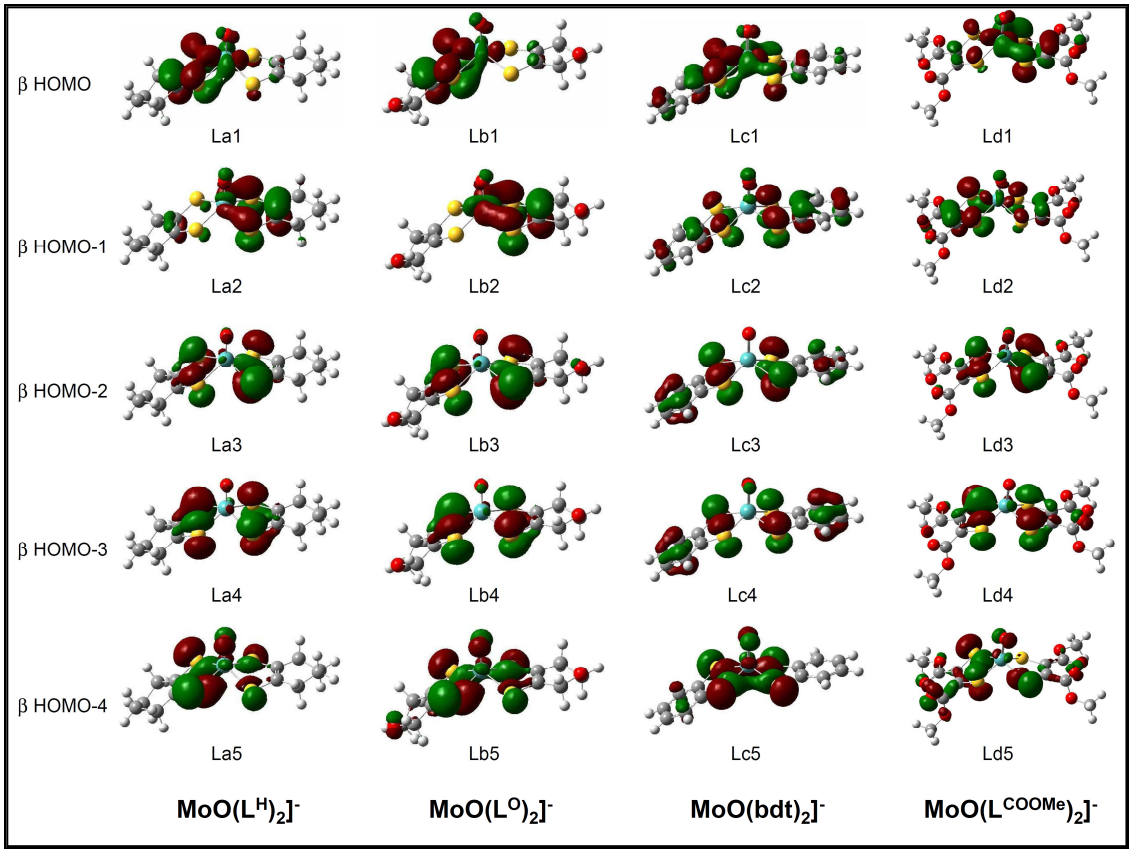

Figure 3.13: Kohn-Sham β molecular orbitals for $[MoO(L^{H})_2]^-$, $[MoO(L^{O})_2]^-$, $[MoO(bdt)_2]^-$ and $[MoO(L^{COOMe})_2]^-$ compounds obtained from unrestricted geometry optimized DFT calculation.

Kohn-Shan molecular orbitals and energy diagram for $[MoO(L^{H})_2]^-$ is shown in Figure 3.14. The α LUMO has 57% Mo-d_{yz} with 16% sulfur character and 21% apical oxo ligand characters, whereas its β spin counterpart LUMO+1 has 58% Mo-d_{yz}, 16% sulfur character and 19% apical oxo ligand character. The α LUMO +1 orbital has 59% Mo-d_{xz}, 20% sulfur character and 19% apical oxo ligand character whereas its counterpart spin orbital β LUMO+2 has 61% Mo-d_{xz}, 19 % sulfur character and 18% apical oxo ligand character. Since α LUMO, LUMO+1

and its counterpart β LUMO+1 and LUMO+2 have appreciable amount of apical oxo ligand character we anticipate a strong distortion along z- axis in the rRaman excitation profile, this is what has been reported in $[MoO(bdt)^{2}]^{-}$ compound by McNaughton et al.[114] The Mo-d_{z2} and Mo-d_{x2-y2} characters are mainly found in α LUMO+2 and LUMO+3 or β LUMO+3 and LUMO+4 orbital, therefore, only higher energy transitions involves these orbitals.

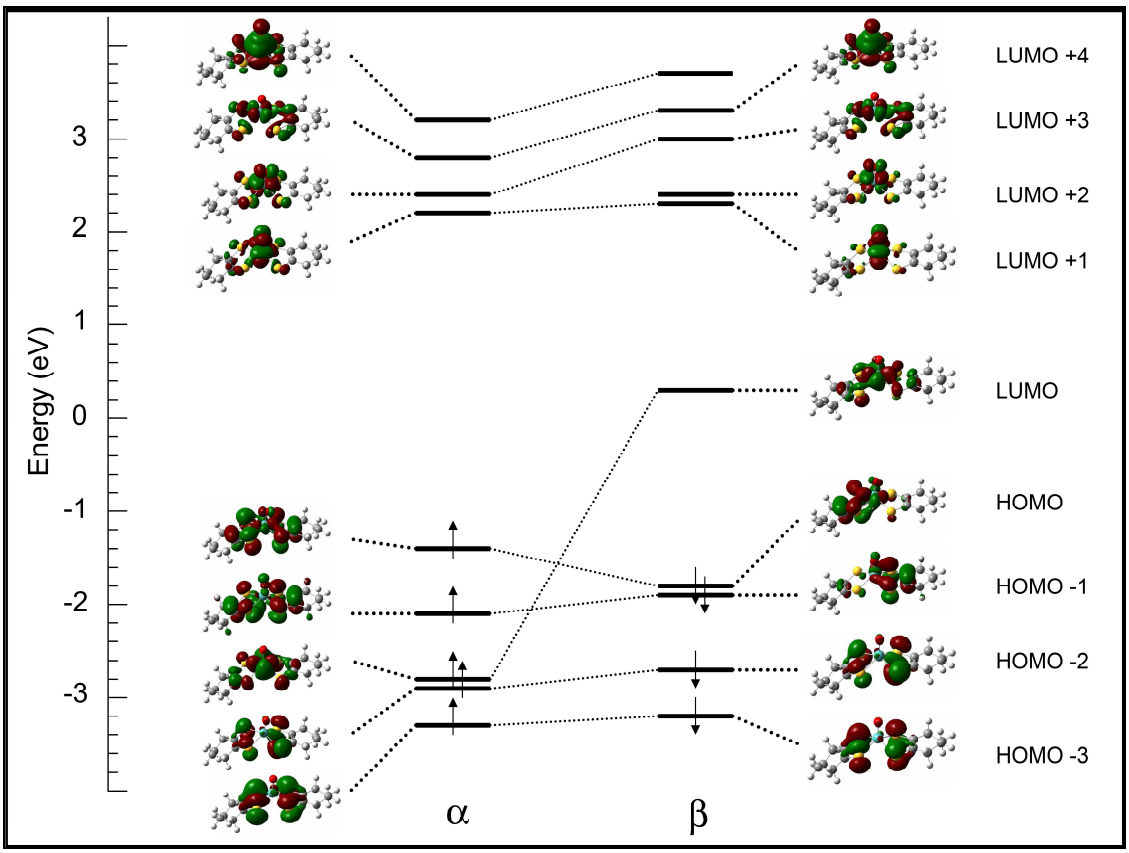

Figure 3.14: Kohn-Sham α and β molecular orbitals and energy diagram for $[MoO(L^{H})_2]^{-}$ compound obtained from unrestricted geometry optimized DFT calculation showing the inverted bonding scheme.

The α HOMO has 54% symmetrical sulfur out of plane with 28% bonding C=C ligand from both side of dithiolene ligands and 11% Mo-d_{xy} characters whereas, the β HOMO has 38% symmetrical sulfur out of plane with 29% bonding C=C ligand character mostly from unbent dithiolene, and 27% Mo-d_{xy} character. The HOMO-1 orbital has 44% symmetrical sulfur out of plane with 40% bonding C=C ligand character from both dithiolene ligands and 7% Mo-d_{xy} characters from α spin whereas, the β spin counterpart possesses 43% symmetrical sulfur out of plane with 39% bonding C=C ligand character mainly from bent dithiolene, and 9% Mo-d_{xy} character. The β HOMO has large percentages of Mo-d_{xy} character which decrease appreciably in the HOMO-1 orbital, indicative of strong communication between the ligand and metal orbitals therefore, favor the low energy ligand to metal charge transfer (LMCT) transitions.

3.5.5 Band Assignments

Combinations of electronic absorption spectroscopy, MCD spectroscopy and intensive bonding calculation performed on model compounds have been utilized to study the nature of charge transfers and its assignments. All electronic absorption spectra were Gaussian resolved and their energies matched with MCD spectra for accuracy. Time dependent DFT calculation as a useful probe of ground and excited state transitions has been performed on optimized geometry for Mo(V) and W(V) models. Therefore combinations of band intensities, energy position and computational methods have been used in bands assignments. For compounds with low symmetry (C_s) such as $[MoO(L^H)_2]^-$, $[MoO(L^O)_2]^-$,

$[MoO(L^{COOMe})_2]^-$, $[MoO(bdt)_2]^-$ and $[WO(L^H)_2]^-$ all transitions to the unoccupied d-orbitals are dipole allowed.[111]

$[MoO(L^H)_2]^-$ and $[MoO(L^O)_2]^-$ compounds

Experimental and theoretical electronic absorption band energy maxima, experimental MCD band maxima, oscillator strength and assignment for $[MoO(L^H)_2]^-$ and $[MoO(L^O)_2]^-$ compounds are presented in Table 3-4.

Band 1: This band occurs as a weak negative C-term in the MCD spectrum and assigned as β HOMO → LUMO transition in the $[MoO(L^H)_2]^-$ while for $[MoO(L^O)_2]^-$ compound is assigned as a combination of β HOMO-1 → LUMO and β HOMO → LUMO transitions. For $[MoO(L^H)_2]^-$ compound β HOMO consists of 27% Mo-d_{xy} character and 38% symmetrical Sop with 29% C=C ligands character mainly from unbent dithiolene, whereas LUMO contains 56% Mo-d_{xy} character and 28% symmetrical sulfur out of plane (Sop') ligand character. However for $[MoO(L^O)_2]^-$ compound HOMO-1 orbital consists of 29% Mo-d_{xy} and 38% symmetrical Sop with 28% C=C ligand characters dominantly from unbent dithiolene, HOMO orbital possesses 9% Mo-d_{xy}, 43% symmetrical Sop with 39% C=C bonding characters mostly from bent dithiolene, while LUMO consist of 55% Mo-d_{xy} and ~30% asymmetrical Sop ligand characters. In the $[MoO(L^O)_2]^-$ this band is dominated with β HOMO-1 → LUMO transition that involve combinations of ligand field and charge transfer transitions, supported with a weak intensity of this band that agrees well with a small experimental and theoretical oscillator strength.

Band 2: The first strong absorption band in the electronic absorption spectrum correspond to a strong positive C-term in the MCD spectra of both $[MoO(L^{H})_2]^-$ and $[MoO(L^{O})_2]^-$ compounds. This band is assigned as β HOMO-1 → LUMO transition in $[MoO(L^{H})_2]^-$ compound and as a combination of one electron promotion from β HOMO → LUMO and β HOMO-1 → LUMO transitions for $[MoO(L^{O})_2]^-$ compound. In $[MoO(L^{H})_2]^-$ compound the β HOMO-1 possesses 9% Mo-d_{xy}, 43% symmetrical Sop with 38% bonding C=C ligand characters mainly from unbent dithiolene, while β LUMO composition have been described above. This band is dominated by β HOMO → LUMO transition as evidently in the electron density different map (EDDM) in Figure 3.15. The strong intensity of this band is supported with strong experimental oscillator strength that agrees well with theoretical oscillator strength (Table 3-4) in both compounds. Our assignment for this band differ with assignments made by McNaughton et al.,[4] and MacMaster et al.[96] as Sip (Sσ) → Mo-d_{xy} transition in $[MoO(bdt)_2]^-$ and $[MoO(edt)_2]^-$ compounds. On the other hand our assignment is in good agreement with Hernandez-Marin et al.,[115] for $[MoO(edt)_2]^-$ and Waters et al.,[116] in previously assignment for $[MoO(bdt)_2]^-$ as Sop → Mo-d_{xy} transition.

Table 3-4: Band energy maxima, oscillator strength and assignments for $[MoO(L^H)_2]^-$ and $[MoO(L^O)_2]^-$ compounds.

$[MoO(L^H)_2]^-$						
Band #	UV-vis (cm^{-1})	MCD (cm^{-1})	Theory (UV-vis)	F (expt)	F (calc)	Assignment
1	8,770	8,730	8,156	0.0022	0.0015	β Sop' + dxy → dxy + Sop'
2	12,230	11,680; 12,875	10,645	0.0250	0.0484	β Sop' → dxy + Sop'
3	17,500	17,030	16,177	0.0208	0.0069	β Sop" → dxy + Sop'
4	21,730	18,290 21,670	17,910 19,220 19,255	0.0197	0.0002 0.0006 0.0013	α Sop' + dxy → dyz + Oπ* α Sop' + dxy → dxz + Oπ* β Sop" → dxy + Sop'
5	24,200	24,055	23,000 23,400	0.0140	0.0006 0.0011	β Sip' → dxy + Sop' β Sop' + dxy → dxz + Oπ*
6	26,460	25,980	25,640	0.0262	0.0016	α Sop' → dxz + Oπ*
7	29,260	29,090	27,260 27,700	0.0540	0.0242 0.0187	α Sop' + dxy → dz^2 + Oσ* α dxy → dxz + Oπ*
8	32,750	32,920	32,540	0.0726	0.0273	β Sop" → dyz + Op*
9	34,470	34,390	33,520	0.1084	0.0052	β Sop" → dxz + Oπ*

$[MoO(L^O)_2]^-$						
Band #	UV-vis (cm^{-1})	MCD (cm^{-1})	Theory (UV-vis)	f (Exp)	f (Theory)	Assignment
1	9,030	8,800	8,220	0.0038	0.0014	β Sop' → dxy + Sop' β Sop' + dxy → dxy + Sop'
2	11,920; 13,580	11,800; 13,220	10,490	0.0257	0.0467	β Sop' + dxy → dxy + Sop' β Sop' → dxy + Sop'
3	17,730	17,450	16,410	0.0198	0.0072	β Sop" → dxy + Sop'
4	20,610	19,540 21,180	17,620 18,970 19,475	0.0108	0.0001 0.0006 0.0014	α Sop' + dxy → dyz + Oπ* α Sop' + dxy → dxz + Oπ* β Sop" → dxy + Sop'
5	23,470	22,690 23,680	22,850 23,190	0.0248	0.0005 0.0015	β Sip' → dxy + Sop' β Sop' + dxy → dxz + Oπ*
6	26,110	26,260	25,310	0.0265	0.0009	α Sop' → dxz + Oπ*
7	28,890	28,820	27,060 27,680	0.0631	0.0228 0.0167	α Sop' + dxy → dz^2 + Oσ* α dxy → dxz + Oπ*
8	32,805	32,750	32,490	0.1145	0.0249	β Sop" → dyz + Oπ*
9	34,580	34,830	33,560	0.1192	0.0061	β Sop" → dxz + Oπ*

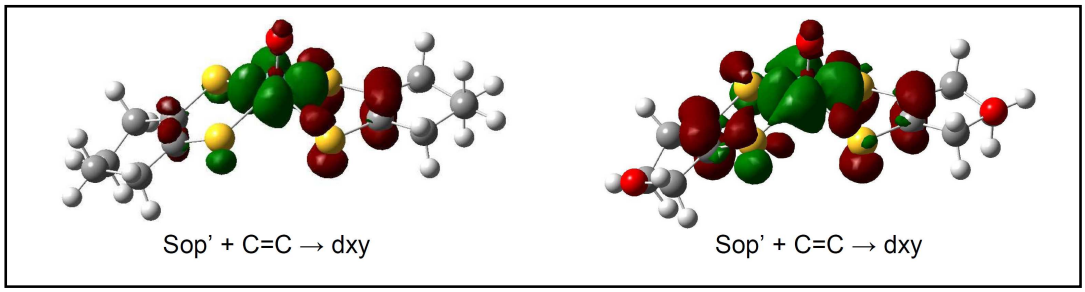

Figure 3.15: Electron density difference map (EDDM) for $[MoO(L^{H})_2]^-$ and $[MoO(L^{O})_2]^-$ compounds showing the ligand to metal charge transfer for band 2.

Band 3: This is the second intense band in the electronic absorption spectrum and corresponds to the second positive C-term peak in the MCD spectrum (Figure 3.16 and 3.17), where β HOMO-2 → LUMO transition is assigned for this band in both $[MoO(L^{H})_2]^-$ and $[MoO(L^{O})_2]^-$ compounds. The β HOMO-2 possesses asymmetrical sulfur out of plane (Sop") character while LUMO has Mo-d_{xy} and asymmetrical sulfur out of plane (Sop") ligand character. In contrast this band has been assigned previously as $b_2\sigma$ (Sip') → Mo-d_{xy} transition in $[MoO(edt)_2]^-$ compound by Hernandez-Marin et al.[115] From symmetry adapted linear combination of atomic orbitals sulfur in-plane orbitals are highly stabilized than sulfur out of plane, therefore we do expect to see the first four low energy charge transfer transitions to be from Sop orbital to the metal, which agrees well with this assignment.

Band 4: A weak positive-negative C-term (negative pseudo A-term) in the MCD spectrum corresponds to band 4 in the electronic absorption. This band contain transitions from α HOMO → LUMO, α HOMO → LUMO+1 and β HOMO-3 →

LUMO in both $[MoO(L^{H})_2]^-$ and $[MoO(L^{O})_2]^-$ compounds. In both compounds α HOMO possesses symmetrical Sop with C=C bonding characters from the two dithiolene side and Mo-d_{xy} characters, β HOMO-3 has asymmetrical Sop character whereas α LUMO and LUMO+1 possess Mo-d_{yz} with Oπ^* and Mo-d_{xz} with Oπ^* characters and β LUMO has Mo-d_{xy} + symmetrical Sop characters respectively. In the MCD spectra an energy gap of 1,640 and 3,230 cm^{-1} has been obtained between the two peaks forming the pseudo A-term in $[MoO(L^{O})_2]^-$ and $[MoO(L^{H})_2]^-$ compounds. These values are in good agreement with 1,350 and 1,310 cm^{-1} calculated energy gap between α HOMO $\rightarrow$ LUMO and α HOMO $\rightarrow$ LUMO+1 transitions. However in $[MoO(L^{H})_2]^-$ compound the energy gap has been underestimated. The assignment for this band is similar to b1,2(π) $\rightarrow$ b1,2-($d_{xz,yz}$) LMCT transitions assigned by McMaster et al. in $[MoO(edt)_2]^-$ compound.[96]

Band 5: A weak positive MCD band that corresponds to band 5 in the electronic absorption spectrum is assigned as a combination of β HOMO-5 $\rightarrow$ LUMO and β HOMO $\rightarrow$ LUMO+2 transitions in both $[MoO(L^{H})_2]^-$ and $[MoO(L^{O})_2]^-$ compounds. The HOMO-5 orbital possesses symmetrical S_{ip} whereas β HOMO, LUMO and LUMO+2 orbitals compositions have been discussed above.

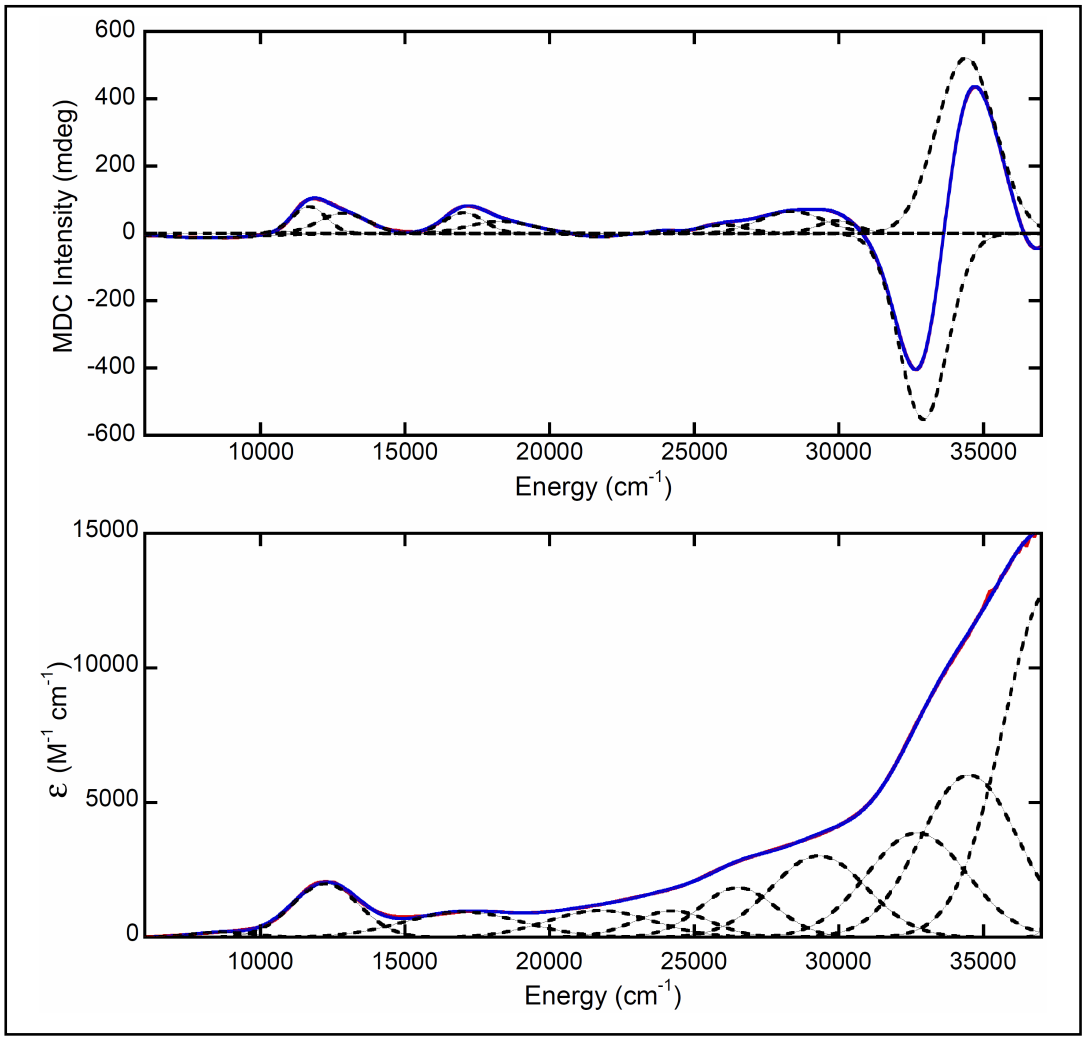

Figure 3.16: Gaussian resolved 5K, 7T MCD (top) and room temperature electronic absorption (bottom) spectrum for $[MoO(L^{H})_2]^-$ compound.

Band 6: Band 6 in the electronic absorption corresponds to a positive C-term band in the MCD spectrum and is assigned as α HOMO-1 $\rightarrow$ LUMO+1 transition in both $[MoO(L^{H})_2]^-$ and $[MoO(L^{O})_2]^-$ compounds. The α HOMO-1 has symmetrical Sop with bonding C=C ligand characters while LUMO+1 has Mo-d_{xz} with Oπ^* ligand characters. The weak intensity of bands 5 and 6 in the MCD spectra is

consistent to the weak calculated oscillator strength, therefore support their assignments.

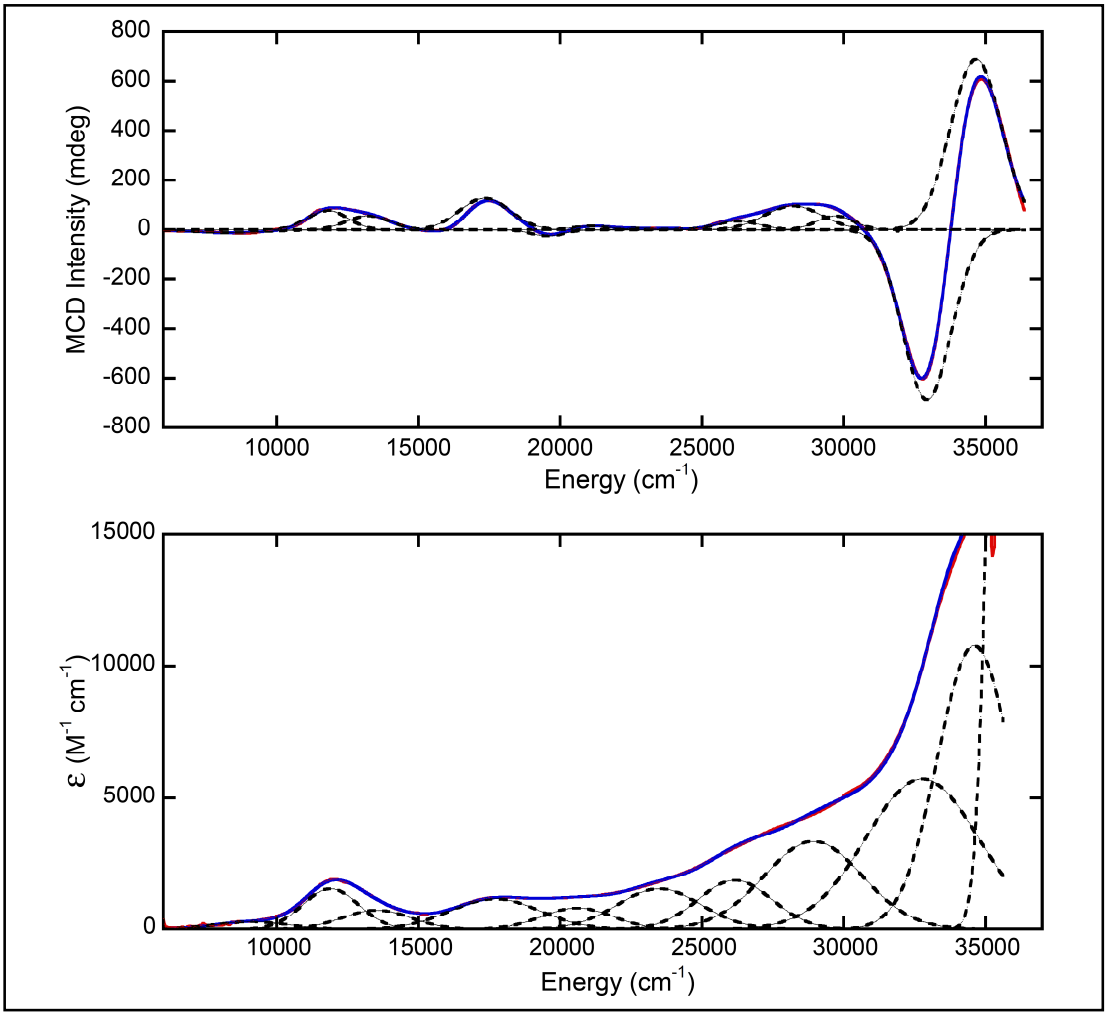

Figure 3.17: Gaussian resolved MCD (top) and electronic absorption (bottom) spectra for $[MoO(L^{O})_2]^-$ compound.

Band 7: A combination of α HOMO → LUMO+3 and α HOMO-2 → LUMO+1 transitions are assigned for this band in both $[MoO(L^{H})_2]^-$ and $[MoO(L^{O})_2]^-$ compounds. HOMO, HOMO-2 and LUMO+1 orbitals compositions have been

described above, while LUMO+3 possesses Mo-d_{z2} with Oσ* ligand character. This assignment is supported with a strong calculated oscillator strength (f = 0.0540 for $[MoO(L^H)_2]^-$ and f = 0.0631 for $[MoO(L^O)_2]^-$) which is in good agreement with the experimental oscillator strength (f = 0.0242 for $[MoO(L^H)_2]^-$ and f = 0.0228 for $[MoO(L^O)_2]^-$) (Table 3-4).

Band 8 and 9: An intense positive-negative MCD C-terms peaks (positive pseudo A-term) observed at higher energy region correspond to bands 8 and 9 in the electronic absorption spectrum (Figure 3.16 and 3.17). These bands are assigned as β HOMO-2 → LUMO+1 and β HOMO-2 → LUMO+2 transitions in both $[MoO(L^H)_2]^-$ and $[MoO(L^O)_2]^-$ compounds. The β HOMO-2 possesses asymmetrical Sop whereas LUMO+1 and LUMO+2 possess Mo-d_{xz} + Oπ* and Mo-d_{yz} + Oπ* characters as shown in the electron density difference map (EDDM) in Figure 3.18. MCD spectrum shows a separation of 1,830 cm^{-1} and 2,080 cm^{-1} for $[MoO(L^H)_2]^-$ and $[MoO(L^O)_2]^-$ compounds obtained between a negative and positive MCD C-terms. This gap is in a reasonable agreement with 980 cm^{-1} and 1,070 cm^{-1} theoretical separation gap between β HOMO-2 → LUMO+1 and β HOMO-2 → LUMO+2 transitions in $[MoO(L^H)_2]^-$ and $[MoO(L^O)_2]^-$ compounds, even though the calculated energy gap is half of the experimental energy gap. This assignment is consistent with Sop (π) → d_{xz}, d_{yz} transitions assigned for a pseudo A-term in $[MoO(edt)_2]^-$ compound by McMaster et al., [96] and Hernandez-Marin et al.[115]

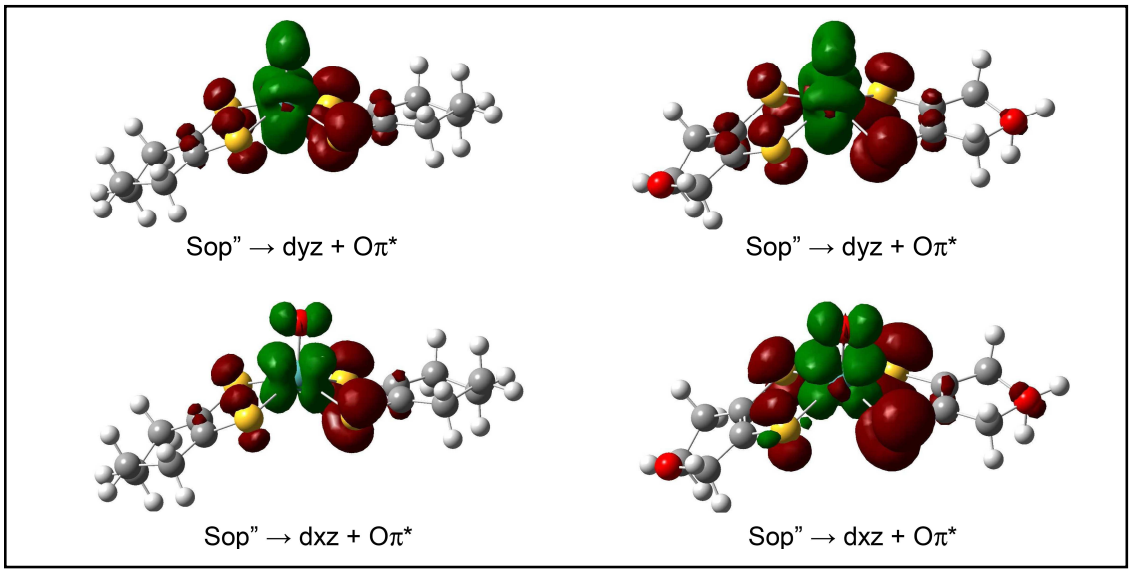

Figure 3.18: Electron density difference map (EDDM) for $[MoO(L^{H})_2]^-$ and $[MoO(L^{O})_2]^-$ compounds showing the ligand to metal charge transfer for band 8 (top) and band 9 (bottom).

$[MoO(L^{COOMe})_2]^-$ and $[MoO(bdt)_2]^-$ Compounds

Gaussian resolved MCD and electronic absorption spectra for $[MoO(L^{COOMe})_2]^-$ and $[MoO(bdt)_2]^-$ compounds are displayed in Figure 3.20 and 3.21.

Band 1: A weak negative C-term peak in the MCD spectrum correspond to a weak band in the electronic absorption spectrum, and is assigned as HOMO → LUMO transition. HOMO has symmetrical Sop with some Mo-d_{xy} character and LUMO possesses Mo-d_{xy} with some symmetrical S_{op} characters in both $[MoO(L^{COOMe})_2]^-$ and $[MoO(bdt)_2]^-$ compound. Combination of ligand field and ligand to metal charge transfer (LMCT) transitions assigned for this band is supported by a weak calculated oscillator strength (f = 0.0012 for $[MoO(L^{H})_2]^-$ and f = 0.0013 for $[MoO(L^{O})_2]^-$) which agrees well with the experimental oscillator

strength (f = 0.0013 for $[MoO(L^{H})_2]^-$ and f = 0.0054 for $[MoO(L^{O})_2]^-$) (Table 3-5). Additionally this assignment is consistent with band 1 assignment in $[MoO(L^{H})_2]^-$ and $[MoO(L^{O})_2]^-$ compounds.

Band 2: The β HOMO-1 → LUMO transition is assigned for a first intense band in the electronic absorption of $[MoO(L^{COOMe})_2]^-$ while for $[MoO(bdt)_2]^-$ compound a combination of β HOMO-1 → LUMO and β HOMO-2 → LUMO transitions are assigned for this band. The HOMO-1 orbital possesses symmetrical S_{op} character, HOMO-2 has asymmetrical Sop character while Mo-d_{xy} with some symmetrical Sop characters are present in the LUMO orbital. The HOMO-1 → LUMO transition is manifested in the electron density difference map (EDDM) in Figure 3.19. The intensity of this band is consistent with large experimental oscillator strength that is in good agreement with the theoretical oscillator strength (Table 3-5). The assignment of this band is consistent with $[MoO(L^{H})_2]^-$ and $[MoO(L^{O})_2]^-$ compound assignment for the same band.

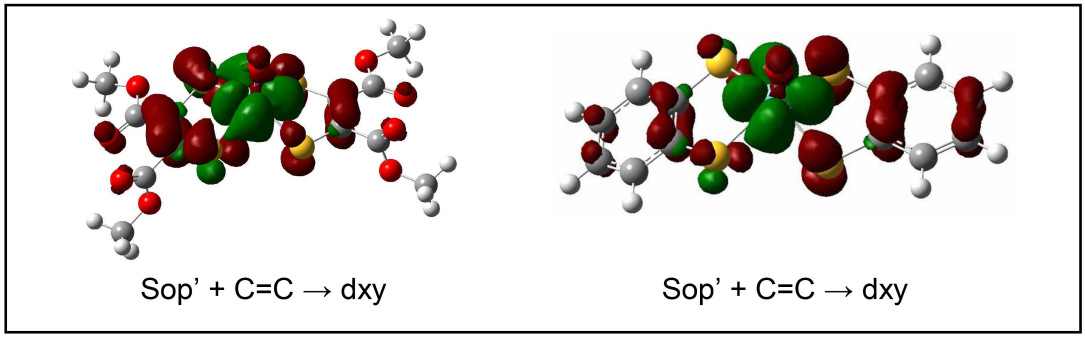

Figure 3.19: Electron density difference map (EDDM) for $[MoO(L^{COOMe})_2]^-$ and $[MoO(bdt)_2]^-$ compounds showing the ligand to metal charge transfer for band 2.

Table 3-5: Band energy maxima, oscillator strength and assignments for $[MoO(L^{COOMe})_2]^-$ and $[MoO(bdt)_2]^-$ compounds.

$[MoO(L^{COOMe})_2]^-$						
Band #	UV-vis (cm^{-1})	MCD (cm^{-1})	Theory (UV-vis)	F (expt)	F (calc)	Assignment
1	9,975	10,015	8,815	0.0013	0.0012	β Sop' + dxy → dxy + Sop'
2	13,265	13,220; 14,010	11,410	0.0224	0.0444	β Sop' + C=C → dxy + Sop'
3	17,830	17,850	16,550	0.0114	0.0042	β Sop" → dxy + Sop'
4	20,930	20,030 21,870	17,690 19,830 20,210	0.0089	0.0007 0.0008 0.0016	α Sop' + dxy → dyz + Oπ* α Sop' + dxy → dxz + Oπ* + α Sop' + dxy → dxz + Oπ*
5	23,400	23,480	21,455 21,710	0.0096	0.0013 0.0010	β Sip" → dxy + Sop' β Sip" → dxy + Sop'
6	26,200	26,840	25,180 25,765	0.0377	0.0038 0.0034	β Sop' + dxy → dxz + Oπ* β Sop' → dyz + Oπ* + C=Cπ*
7	28,370	29,350	27,830 28,430	0.0562	0.0061 0.0068	β Sop' → dxz + C=C* β Sop' → dxz + Oπ*
8	30,470	30,620	29,520 31,940	0.0799	0.0045 0.0197	β Sop" → dyz + Oπ* + C=Cπ*
9	32,930	33,100	32,470 34,270	0.0946	0.0019 0.0034	β Sop" → dxz + Oπ* + C=Cπ*
10	35,780	-	-	0.358	-	-

$[MoO(bdt)_2]^-$						
Band #	UV-vis (cm^{-1})	MCD (cm^{-1})	Theory (UV-vis)	f (Exp)	f (Theory)	Assignment
1	10,470	11,485	9,400	0.0054	0.0013	β Sop' + dxy → dxy + Sop'
2	13,740	13,350	12,080 12,930	0.0239	0.0498 0.0052	β Sop' → dxy + Sop' β Sop" → dxy + Sop'
3	15,335	16,420	15,300	0.0114	0.0007	β Sop" → dxy + Sop'
4	19,380	19,530 21,250	18,900 19,340 20,400	0.0089	0.0020 0.0004 0.0009	β Sip' → dxy + Sop' α Sop' + dxy → dyz + Oπ* α Sop' + dxy → dxz + Oπ*
5	23,305	23,280	22,465 24,575	0.0057	0.0018 0.0006	β Sip' → dxy + Sop' β Sip" → dxy + Sop'
6	26,665	26,415	25,090 26,705	0.0245	0.0005 0.0072	β Sop' + dxy → dxz + Oπ* α Sop' → dxz + Oπ*
7	-	-	-	-	-	-
8	29,420	29,480	29,580	0.0445	0.1137	β Sop" → dyz + Oσ*
9	31,385	31,380	30,380 30,535	0.0976	0.0021 0.0051	β Sop" → dxz + Oπ*
10	34,785	35,070	-	0.2631	-	-

Band 3: This band appears as a small positive C-term in the MCD spectrum for $[MoO(bdt)_2]^-$ compound while in $[MoO(L^{COOMe})_2]^-$ compound appears as a strong positive C-term peak. This band is assigned as β HOMO-2 → LUMO transition in $[MoO(L^{COOMe})_2]^-$ compound whereas in $[MoO(bdt)_2]^-$ compound is assigned as β HOMO-3 → LUMO transition. In the $[MoO(L^{COOMe})_2]^-$ compound β HOMO-2 possesses asymmetrical Sop character while LUMO has Mo-d_{xy} with symmetrical S_{op} ligand characters. The weak intensity of this band in $[MoO(bdt)_2]^-$ compound agrees well with a weak calculated oscillator strength for this transition, while for $[MoO(L^{COOMe)}{}_2]^-$ the strong intensity for this band is proportional to the calculated oscillator strength as observed in Table 3-5.

Band 4: A weak positive-negative patterns (negative pseudo A-term) in the MCD spectra correspond to band 5 in the electronic absorption (Figure 3.20 and 3.21). This band is assigned as a combination of β HOMO-4 → LUMO, α HOMO → LUMO, α HOMO → LUMO+1 transitions for $[MoO(bdt)_2]^-$ compound whereas α HOMO → LUMO, α HOMO → LUMO+1 and α HOMO → LUMO+2 transitions are assigned for $[MoO(L^{COOMe})_2]^-$ compound. The β HOMO-4 possesses asymmetrical S_{ip} character and Mo-d_{xy} with symmetrical S_{op} characters are present in β LUMO orbital while α LUMO possesses Mo-d_{xz} with Oπ* character, LUMO+1 and LUMO+2 orbitals have Mo-d_{yz} + Oπ* characters. The energy gap of 1,800 cm^{-1} obtained between a positive and negative C-terms peaks in the MCD spectrum of $[MoO(L^{COOMe})_2]^-$ compound which is close to 2,140 cm^{-1} theoretical energy gap between α HOMO → LUMO and α HOMO → LUMO+1 transitions

assigned for this band. This assignment is consistent with the assignment for band 4 in $[MoO(L^{H})_2]^-$ and $[MoO(L^{O})_2]^-$ compounds.

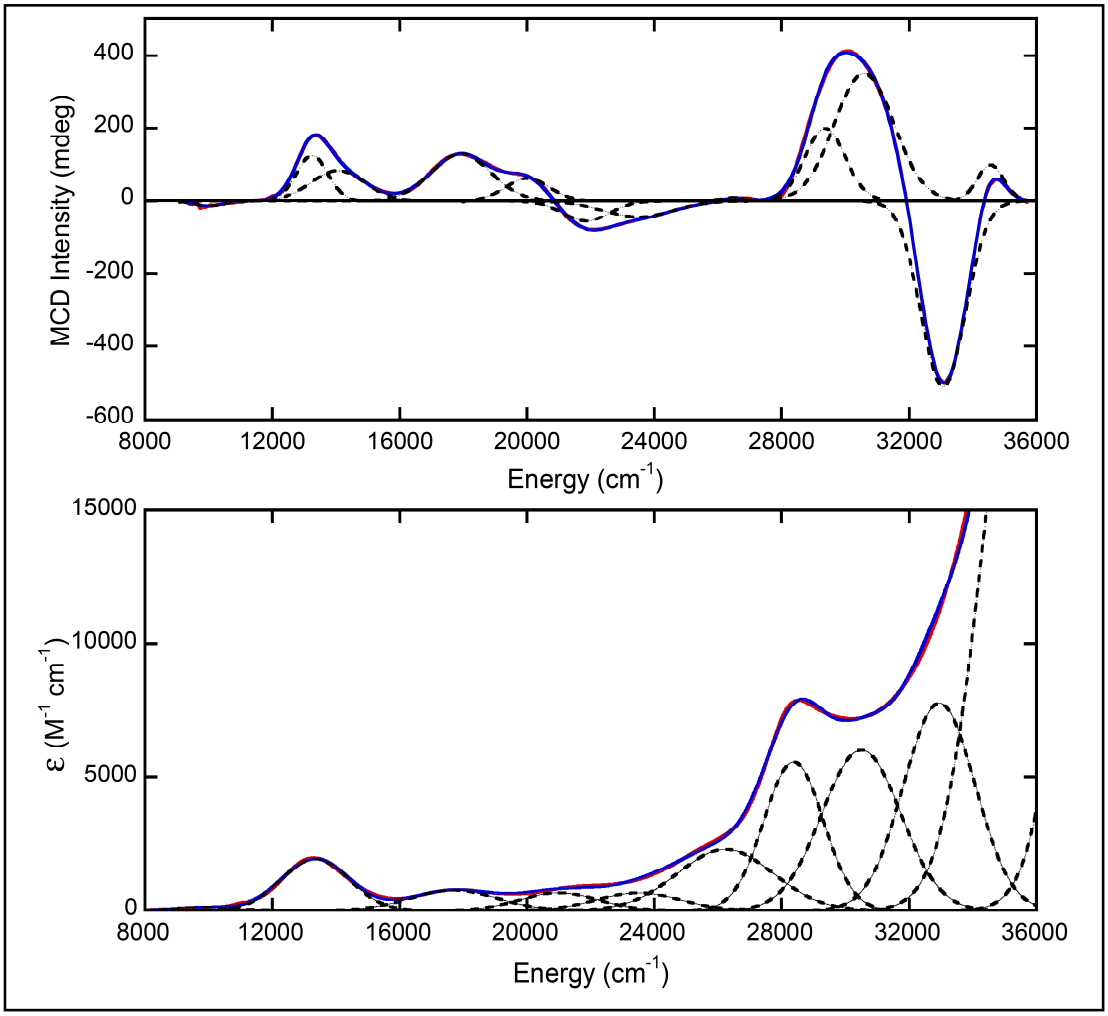

Figure 3.20: Gaussian resolved MCD (top) and electronic absorption (bottom) spectra for $[MoO(L^{COOMe})_2]^-$ compound.

Band 5: The third negative C-term peak in the MCD spectrum correspond to band 5 in the electronic absorption, and is assigned as β HOMO-5 → LUMO and β HOMO-6 → LUMO transitions in $[MoO(bdt)_2]^-$ however for $[MoO(L^{COOMe})_2]^-$ this

band is assigned as β HOMO-4 → LUMO and β HOMO-5 → LUMO transitions respectively. β HOMO-4 from $[MoO(L^{COOMe})_2]^-$ and β HOMO-5 from $[MoO(bdt)_2]^-$ possess symmetrical S_{ip} while β HOMO-5 from $[MoO(L^{COOMe})_2]^-$ and β HOMO-6 from $[MoO(bdt)_2]^-$ both possess asymmetrical S_{ip} ligand character.

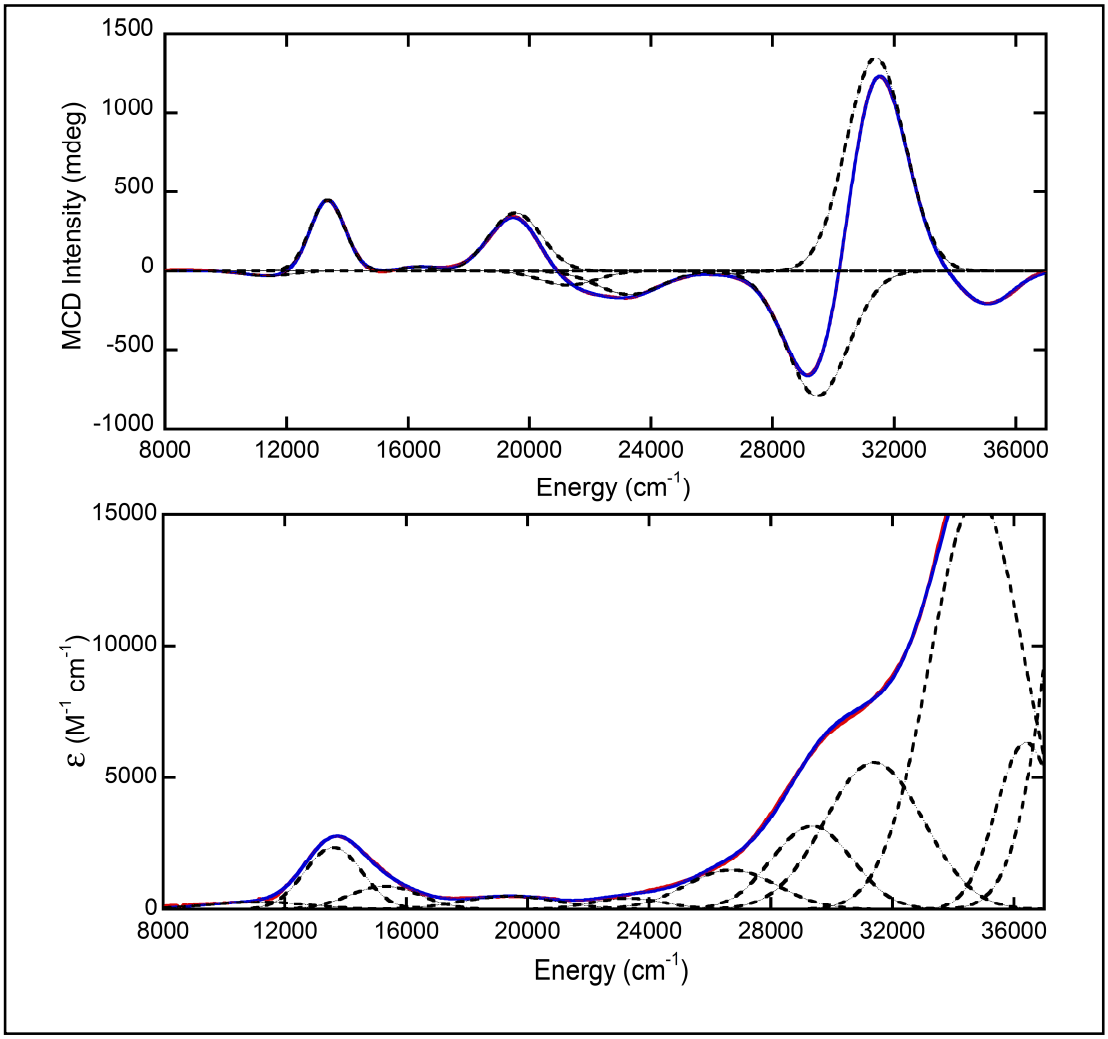

Figure 3.21: Gaussian resolved MCD (top) and electronic absorption (bottom) spectra for $[MoO(bdt)_2]^-$ compound.

Band 6: A combination of β HOMO-1 → LUMO+1 and β HOMO → LUMO+3 transitions are assigned for band 6 in $[MoO(L^{COOMe})_2]^-$ whereas β HOMO → LUMO+2 and α HOMO-1 → LUMO+1 transitions are assigned for $[MoO(bdt)_2]^-$ compound. The weak intensity of this band in the MCD spectrum is supported with a weak oscillator strength calculated for this band, and therefore supports the assignment.

Band 7: This band is only present in $[MoO(L^{COOMe})_2]^-$ compound and is assigned as β HOMO-1 → LUMO+2 and β HOMO-1 → LUMO+3 transitions. β HOMO-1 orbital has symmetrical S_{op} with bonding C=C character, β LUMO+3 possesses Mo-d_{xz} with Oπ* characters and LUMO+2 has Mo-d_{yz} + Oπ* characters.

Band 8 and 9: An intense pseudo A-term in the higher energy region of the MCD spectrum correspond to an intense bands 8 and 9 in the electronic absorption (Figure 3.20 and 3.21). These bands are assigned as β transitions from HOMO-2 → LUMO+1 and HOMO-2 → LUMO+2, whereas HOMO-2 possesses asymmetrical S_{op}, LUMO+1 and LUMO+2 possess Mo-d_{xz} with Oπ* and d_{yz} with Oπ* characters. These transitions are manifested in the electron density difference map (EDDM) in Figure 3.22. The energy gap of 2,480 cm^{-1} and 1,900 cm^{-1} between a negative and positive or positive and negative C-terms peaks in the MCD spectra for $[MoO(L^{COOMe})_2]^-$ and $[MoO(bdt)_2]^-$ compounds, is consistent with 2,330 and 955 cm^{-1} energy gap obtained between β HOMO-1 → LUMO+1 and HOMO-1 → LUMO+2 transitions in the theoretical calculations. The

assignment of these bands are similar to assignment made in $[MoO(L^{H})_2]^-$ and $[MoO(L^{O})_2]^-$ compounds for bands 8 and 9.

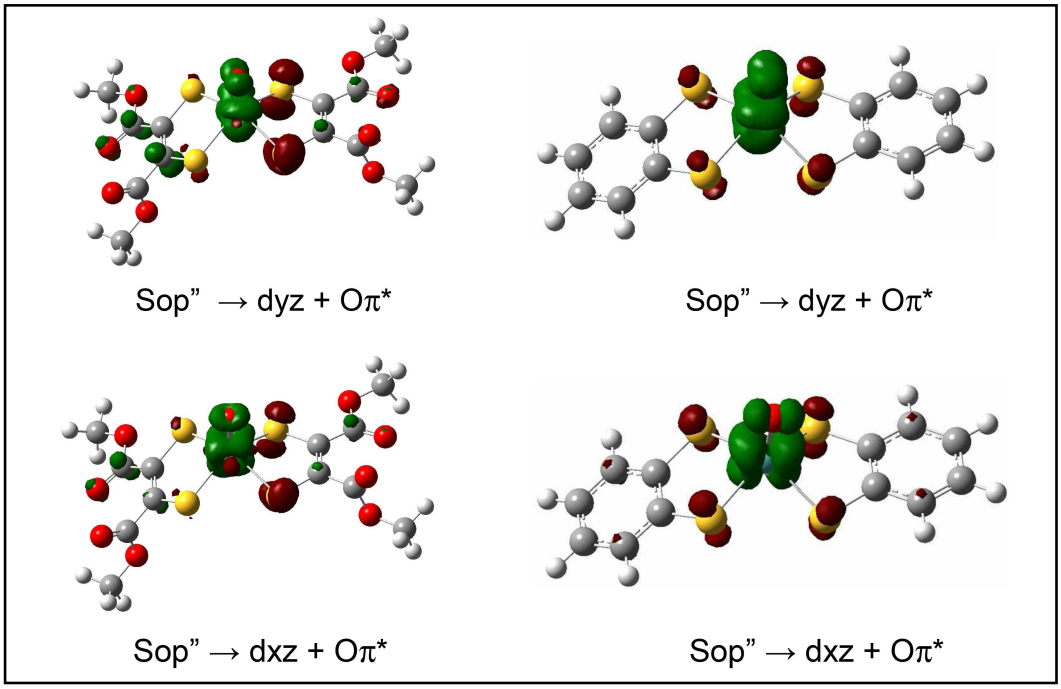

Figure 3.22: Electron density difference map for $[MoO(L^{COOMe})_2]^-$ and $[MoO(bdt)_2]^-$ compounds displaying the ligand to metal charge transfer (LMCT) transitions for bands 8 (top) and 9 (bottom).

3.6 Discussion

3.6.1 The Influence of Substituents Attached to Ene-dithiolene Ligands

The electronic absorption spectra for all molybdenum (V) compounds possess a weak band followed by an intense band in the low energy region. A blue shift is observed in bands 1 and 2 in the electronic absorption and MCD spectra of the $[MoO(L^{COOMe})_2]^-$ and $[MoO(bdt)_2]^-$ compounds (Figure 3.20 and 3.21), and this is

due to the electron withdrawing nature of the L^{COOMe} ligand in $[MoO(L^{COOMe})_2]^-$ and a delocalization effect in the bdt ligands of $[MoO(bdt)_2]^-$.[71] The L^{COOMe} ligand withdraws electron from the sulfur donor atoms. Resonance effects in the benzene ring of the bdt ligand pull electron density toward the rings. These effects weaken the donating ability of the bdt and L^{COOMe} sulfurs and consequently strengthen Mo≡O bond. The strong Mo≡O interactions due to poor donating character of L^{COOMe} and bdt ligands leads to stronger ligand field effect therefore support the higher energy charge transfer bands observed in $[MoO(L^{COOMe})_2]^-$ and $[MoO(bdt)_2]^-$. The blue shift phenomenon is also found in DFT calculation results shown in Figure 3.23. The Sop' → Mo-d_{xy} transition to occurs at higher energy (~27,000 and ~22,000 cm^{-1}) in $[MoO(L^{COOMe})_2]^-$ and $[MoO(bdt)_2]^-$ compounds, and at low energy (~17,000 cm^{-1}) in $[MoO(L^H)_2]^-$ and $[MoO(L^O)_2]^-$ compounds.

The effects of substituents on dithiolene ligands have been observed in the spin calculated populations of the dithiolene sulfurs. Total positive spin density of 22%, 24%, 26% and 17% for $S_{dithiolene}$ have been observed in $[MoO(L^H)_2]^-$ $[MoO(L^O)_2]^-$ $[MoO(^{LCOOMe})_2]^-$ and $[MoO(bdt)_2]^-$ compounds, (Table 3-7) respectively. A higher percentage of $S_{dithiolene}$ positive spin density is observed in $[MoO(L^H)_2]^-$ and $[MoO(L^O)_2]^-$ and this indicates a higher M-S covalent character with the L^H and L^O ligands, and supports the presence of the low energy charge transfer transitions that are observed in their electronic absorption and MCD spectra (Figure 3.16 and 3.17). The lower spin density on the sulfur donors of

$[MoO(bdt)_2]^-$ indicate a less covalent Mo-S bonds compared to the L^H/L^O ligands, and this support the occurrence of higher energy charge transfer bands as observed in the electronic and MCD spectra (Figure 3.21) of $[MoO(bdt)_2]^-$. However, a large positive spin density on sulfur observed in $[MoO(L^{COOMe})_2]^-$ compound, suggests a strong covalency and low energy charge transfer bands. This result is contrary to the electronic absorption and MCD spectra for $[MoO(L^{COOMe})_2]^-$ compound, which possess low energy charge transfer bands at slightly higher energies compared to $[MoO(bdt)_2]^-$.

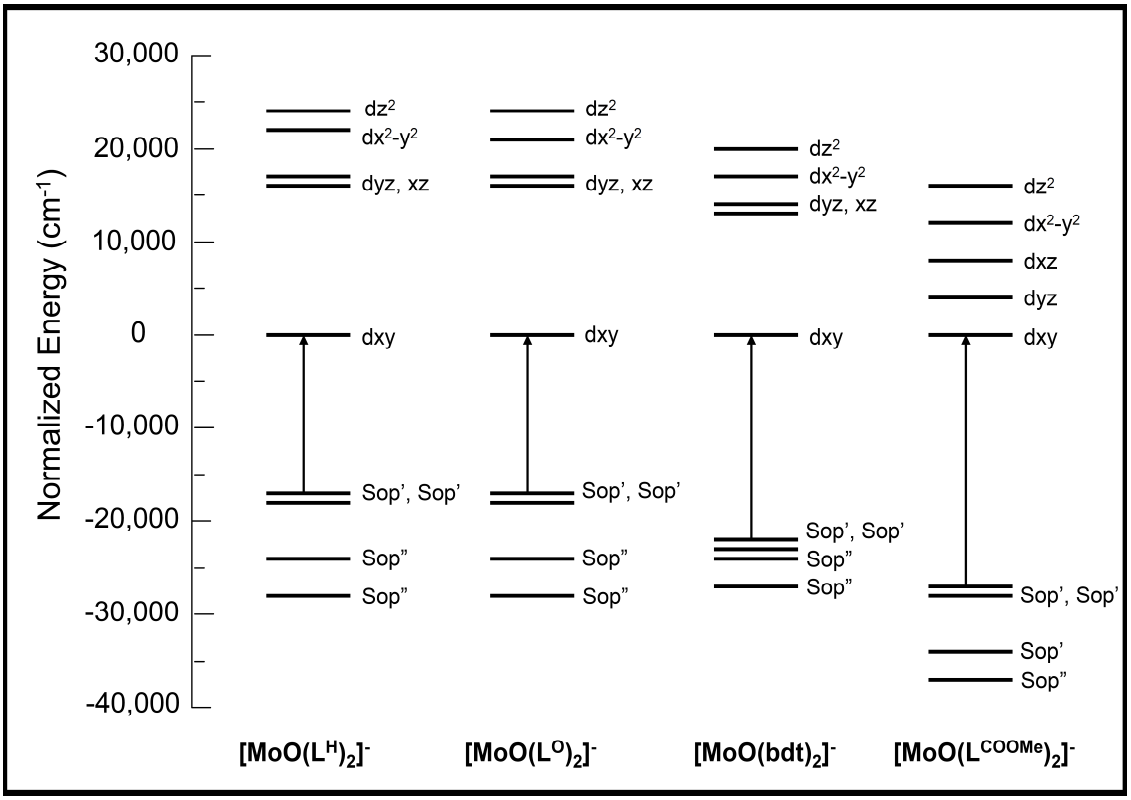

Figure 3.23: Calculated β-Spin orbitals for $[MoO(L^H)_2]^-$, $[MoO(L^O)_2]^-$, $[MoO(bdt)_2]^-$ and $[MoO(L^{COOMe})_2]^-$ compounds showing the lowest energy LMCT transition. The energies have been normalized to the dxy orbital in each compound.

3.6.2 Electron Transfer Pathways

Spin density results have been obtained from single point calculation performed on fully geometry optimized computational models for $[MoO(L^{H})_2]^-$, $[MoO(L^{O})_2]^-$, $[MoO(L^{COOMe})_2]^-$, $[MoO(bdt)_2]^-$ and $[WO(L^{H})_2]^-$. Table 3-7 shows the spin density composition for all five compounds. Our results show large composition of positive sulfur spin density of 16% in $[MoO(L^{H})_2]^-$, 17% in $[MoO(L^{O})_2]^-$, 20% in $[MoO(L^{COOMe})_2]^-$, 13% in $[MoO(bdt)_2]^-$ and 7% in $[WO(L^{H})_2]^-$) that mainly arise from the planer ene-dithiolene ligand while the bent ene-dithiolene ligand possess less percentage of positive sulfur spin density (7% for $[MoO(L^{H})_2]^-$, 7% for $[MoO(L^{O})_2]^-$, 6% for $[MoO(L^{COOMe})_2]^-$, 3% for $[MoO(bdt)_2]^-$ and 3% for $[WO(L^{H})_2]^-$) (Table 3-6). Therefore these results indicate strong ligand metal covalency in the planer dithiolene ligand. The large composition of sulfur positive spin density in the planer ene-dithiolene ligand may result in efficient electron transfer pathway in the catalytic cycle of enzymes that possess a square pyramidal Mo(V) intermediate.

Table 3-6: Spin density composition for $[MoO(L^{H})_2]^-$, $[MoO(L^{O})_2]^-$, $[MoO(L^{COOMe})_2]^-$, $[MoO(bdt)_2]^-$ and $[WO(L^{H})_2]^-$ compounds.

Compound	% Mo	%Oxo	$\%S_{dithiolene}$ (bent)	$\%S_{dithiolene}$ (unbent)	$\%S_{dithiolene}$ (total)
$[MoO(L^{H})_2]^-$	68.29	-2.78	6.64	15.48	22.12
$[MoO(L^{O})_2]^-$	66.12	-2.42	6.70	17.33	24.03
$[MoO(L^{COOMe})_2]^-$	66.87	-1.94	5.72	20.21	25.93
$MoO(bdt)_2]^-$	76.61	-2.95	3.42	13.20	16.62
$[WO(L^{H})_2]^-$	80.38	-2.79	3.16	7.35	10.51

3.6.3 Spin Hamiltonian Parameters for Oxo-molybdenum (V) Bis-dithiolene Compounds

EPR spectra of all compounds exhibit a rhombic g with $g_1 \neq g_2 \neq g_3$ consistent with C_s symmetry for the compounds. All five compounds possess larger g_1 value than g_e, this can be due to i) large metal to ligand covalency and ii) the presence of low energy charge transfer states for the molybdenum compounds. A larger spin orbit coupling constant makes additional contributions to the tungsten compounds. The ligands covalent nature in these compounds has been probed by spin density calculations showing that positive total $S_{dithiolene}$ spin populations of 22% for $[MoO(L^{H})_2]^-$, 24% for $[MoO(L^{O})_2]^-$, 26% for $[MoO(L^{COOMe})_2]^-$ and 17% for $[MoO(bdt)_2]^-$ respectively. This result suggests larger g_1 values according to a $[MoO(L^{COOMe})_2]^- > [MoO(L^{O})_2]^- > [MoO(L^{H})_2]^- > [MoO(bdt)_2]^-$ series. Interestingly, experimental EPR results do not show a clear trend in g_1 values increasing with respect to the substitutions on the dithiolene ligands as expected. This result is contrary to the trend observed in electronic absorption, MCD and calculated g-tensor results. Lack of clear trends in experimental g_1 values may be due to the presence of the same square pyramidal geometry in all compounds, similar result was reported by Davis and coworkers[71] in bis-dithiolene compounds.

The rhombic nature of EPR spectra (g values) obtained is consistent with other reported low symmetry molybdenum,[19,71,87,90,96,103] and tungsten[97] compounds. Our EPR results obtained from spectral simulation for all compounds exhibit axial ^{95,97}Mo hyperfine splitting pattern with $A_1 \neq A_2 \approx A_3$ values (Note: the presence of

one large and two small ^{95,97}Mo hyperfine components), with incorporation of Euler angle as reported in Table 3.5.1. The axial ^{95,97}Mo hyperfine tensor with two small and one large components has also been reported by McMaster and coworker[96] on $[MoO(edt)_2]^-$ compound which agrees well with our results. Dhawan et al. reported an axial ^{95,97}Mo hyperfine tensor with two large and one small components obtained from LMoO(bdt), LMoO(edt) and LMoO{$S(CH_2)_4S$} compounds,[103] this result disagree with our. Additionally Davis and coworkers reported a rhombic ^{95,97}Mo hyperfine tensor for $[MoO(4\text{-pedt})_2]^-$ compound (where 4-pedt = 1-(4-pyridine)-1,2-ethylene-dithiolate),[71] which also disagree with our axial ^{95,97}Mo hyperfine results. The axial ^{95,97}Mo hyperfine tensor with two large and one small components is expected for a perfect d_{z^2} ground state redox orbital with $A_S^{Mo} = [-2A_S^{Mo}, +A_S^{Mo}, +A_S^{Mo}]$, whereas a rhombic hyperfine splitting is expected for a distorted d_{xy}, $d_{x^2-y^2}$ or d_{z^2} redox orbitals with $A_S^{Mo} = [+A_S^{Mo}, 0, -A_S^{Mo}]$. Another alternative where a rhombic or axial ^{95,97}Mo hyperfine splitting with two large and one small component can be obtained is when spectral simulation is achieved without incorporation of Euler angles.

3.6.4 Implications to the DMSO Reductase Enzyme Family

The crystal structures of DMSO reductase enzyme family have been reported revealing a distorted trigonal prismatic geometry in the oxidized form[5,6,18,8,37] and square pyramid geometry in the reduced form.[34] Several spectroscopic and computational studies have been done on the oxidized Mo(VI), Mo(V) intermediate and Mo(IV) reduced forms of DMSO reductase enzyme family

detailing their electronic structure. However so far no crystal structure of Mo(V) intermediate in this enzyme family have been isolated which could be a useful probe, however, electronic absorption, MCD and EPR spectroscopies,[88,117] and computational studies[113] have been utilized and reveal the distorted trigonal prismatic geometry in Mo(V) intermediate of DMSO reductase enzyme. However these spectroscopic techniques can not be applied in arsenite oxidase, formate dehydrogenase and nitrate reductase enzymes due to the presence of iron sulfur clusters of which its absorption overlaps with enzyme active site absorption.

Crystal structure of both reduced and oxidized arsenite oxidase and formate dehydrogenase enzyme have two pyranopterin rings attached to the molybdenum center with apical oxygen, sulfur or selenium in the reduced form. EPR, rRaman studies on DMSO reductase Mo(V) intermediate supported the presence of two pyranopterin rings, oxygen from serine and hydroxyl coordinated to the molybdenum atom. EPR studies of nitrate reductase[29,23] formate dehydrogenase[10,40,93] and DMSO reductase,[19,88,92] enzymes Mo(V) intermediate exhibit a rhombic g tensors splitting pattern which is similar to our Mo(V) models EPR results. Our EPR results show that all model compounds have larger g_1 value than free electron g value, which is consistent with formate dehydrogenate enzyme EPR results (g_1 = 2.012, g_2 = 1.996 and g_3 = 1.985) that is proposed to have a square pyramidal geometry in Mo(V) state as model compounds.[40] In contrary g_1 value is weak in DMSOR enzyme (g_1 = 1.9988, g_2 = 1.9885, and g_3 = 1.9722) due to molybdenum sulfur non covalency nature present in Mo(V)

species[117] as the result of distorted trigonal prismatic geometry. Additionally all model compounds show axial ^{95,97}Mo hyperfine splitting pattern which is not consistent with rhombic ^{95,97}Mo hyperfine splitting observed in DMSO reductase enzyme Mo(V) intermediate.[117] This is due to geometric differences between distorted trigonal prismatic geometry present in DMSOR enzyme and square pyramid geometry for model compounds. Comparison of ^{95,97}Mo hyperfine between model compounds and formate dehydrogenase enzyme failed due to only one reported ^{95,97}Mo hyperfine.

Room temperature electronic absorption spectrum for Mo(V) intermediate DMSO reductase enzyme,[14,117] possesses three low energy bands at 12,250, 15,050 and 18,080 cm^{-1}, that occur at higher energy compared to the same bands observed in $[MoO(L^{H})_2]^-$, $[MoO(L^{O})_2]^-$, $[MoO(L^{COOMe})_2]^-$ and $[MoO(bdt)_2]^-$ compounds. The MCD spectra for all model compounds revealed negative-positive-positive pattern in the low energy spectral region, which is contrary to the enzyme MCD spectrum with negative-negative-positive pattern. Recently band 1 in DMSOR has been assigned as ligand field transition while band 2 and 3 are assigned as LMCT transitions,[113,117] however for our model compounds the first three bands have been assigned as LMCT transitions, and no ligand field transition has been observed at low energy region.

Comparison of arsenite oxidase enzyme putative Mo(V) intermediate with the Mo(V) model compounds is difficult due to lack of any spectroscopic information

on the intermediate. Therefore Mo(V) intermediate for formate dehydrogenase and DMSOR enzymes were compared with the Mo(V) model compounds. The model compounds under this study mimic the Mo(V) intermediate active site for arsenite oxidase and formate dehydrogenase, based on the active site geometry similarity in the reduced form between the enzymes and models compounds.

3.7 Conclusion

A combination of electronic absorption, MCD, EPR spectroscopies and intensive bonding calculation were used to study the electronic structure of Mo(V) bis-dithiolene compounds model for a putative Mo(V) intermediate of arsenite oxidase. Spectral simulation of EPR data collected in all model compounds possess rhombic g-tensor with axial ^{95,97}Mo hyperfine tensor consistent with pseudo Cs symmetry and a Mo-d_{xy} ground state orbital. Thus, the geometry of a Mo(V) intermediate for arsenite oxidase is suggestive of having a square pyramidal geometry and the absence of this intermediate in the catalytic mechanism is attributed to the abnormally higher reduction potentials of the iron sulfur clusters. The geometry is such that one part of the dithiolenes is bent and facile electron transfer to other prosthetic groups is suggested to be through the unbent side. Spin density calculation has revealed that the unbent side has more electron density than the bent side.

The low energy bands shift to higher energy are observed in $[MoO(L^{COOMe})_2]^-$ and $[MoO(bdt)_2]^-$ compounds and not in $[MoO(L^{H})_2]^-$ and $[MoO(L^{O})_2]^-$ compounds.

This shift is consistent with the electron withdrawing nature of COOMe ligand for $[MoO(L^{COOMe})_2]^-$ and resonance effect of benzene 1,2-dithiols ligand for $[MoO(bdt)_2]^-$. In general all charge transfer bands have been assigned by utilizing electronic absorption and MCD spectroscopies combined with TDDFT calculation and have been shown to be mainly LMCT transitions.

CHAPTER 4

The Electronic Structure of Mo(V) Intermediate of DMSO Reductase Enzyme

4.1 Introduction

Dimethyl sulfoxide reductase (DMSOR) is a pyranopterin molybdenum enzyme and a member of the dimethyl sulfoxide reductase family. It has been isolated from several bacterial species such as *Rhodobacter capsulatus, Rhodobacter sphaeroides* and *Escherichia coli*. The *E. coli* DMSOR enzyme possesses the molybdenum cofactor and four [4Fe-4S] clusters,[75,118,119] whereas *R. sphaeroides and R. capsulatus* enzymes posses only the molybdenum cofactor as its redox active center.[5,16,18] Consequently, the enzyme isolated from *Rhodobacter* species has been the subject to extensive crystallographic and spectroscopic studies leading to an increased understanding of the novel electronic structure properties of the enzyme.

Crystal structure analysis has revealed a distorted trigonal prismatic geometry for the oxidized form, where the active site has molybdenum center coordinated with two pyranopterin dithiolenes in the equatorial plane, a serine amino acid, and hydroxyl ligand.[5,16,18,118] In the reduced form, the active site has a square pyramidal geometry with two pyranopterin dithiolenes in the equatorial position and a serinate oxygen at an axial position bound to the molybdenum center.[5,16,89,120] The basic coordination geometries are supported by rRaman studies that show two pyranopterin dithiolenes attached to the molybdenum

center.[19-21,121,122] So far the crystal structure of the Mo(V) intermediate has not been determined, and only rRaman,[75] electrochemistry,[123] kinetic,[14] electronic absorption,[14,91] magnetic circular dichroism (MCD),[91] electron spin resonance (EPR),[22,78,88,90,92] and DFT,[113] studies have been reported. In general, all these methods were utilized to determine the reactivity and geometry of Mo(V) intermediate.

DMSOR catalyzes the reduction of dimethyl sulfoxide (DMSO) or trimethylamine N-oxide (TMAO) substrates to dimethyl sulfide (DMS) or trimethylamine (TMA) as elaborated in Equation (i).

$$DMSO/TMAO + 2H^+ + 2e^- \rightarrow DMS/TMA + H_2O \quad \text{..... (i)}$$

Kinetic studies conducted on DMSOR with DMSO and TMAO as substrates showed that TMAO is a faster substrate than DMSO.[14] The catalytic reaction of the enzyme with TMAO also produced ~100% of Mo(V) intermediate whereas only 80% of the Mo(V) intermediate was produced using DMSO as substrate, and the remaining 20% being a Mo(IV) species.[14,91] Therefore, this study utilized TMAO as a substrate for the generation of the Mo(V) intermediate.

During catalysis, DMSOR cycles between the Mo(VI), Mo(V) and Mo(IV) oxidation states (Scheme 1.0).[14,19,22,75] Despite the various studies done on this enzyme the Mo(V) species, which is a crucial intermediate during catalysis, has not been fully characterized. Thus, this Chapter reports its full characterization

in terms of the ^{95,97}Mo hyperfine tensor, its orientation with respect to the g tensor, and the nature of the redox orbital (SOMO) that is involved. It also reports on the full spectral assignment of the Mo(V) electronic absorption and MCD spectra, and the role played by the pyranopterin dithiolenes in electron transfer during catalysis.

4.2 Statement of the Problem

Several spectroscopic and crystallographic studies have been performed on the active site of oxidized and reduced DMSOR, however for the Mo(V) intermediate active site

- The ^{95,97}Mo hyperfine tensor has not yet been determined.
- The nature of the SOMO and the geometry of Mo(V) intermediate of the DMSO Reductase is unknown.
- It is not know which pyranopterin dithiolene in DMSOR is actively involved in the electron transfer process.

4.3 Hypotheses

- The geometry of the Mo(V) intermediate lies between idealized octahedral and trigonal prismatic geometry in line with the rhombic ^{95,97}Mo hyperfine tensor.
- Electron transfer regeneration is through the Q-pterin and not the P-pterin.

4.4 Materials and Methods

General

All reactions were carried out in anaerobic environment. The oxidized DMSO reductase enzyme "golden ball" sample was dissolved in 50 mM KH_2PO_4, 0.6 mM EDTA pH 6 buffer at desired concentration and then flashed with nitrogen for 45 minutes. Then 150 mM Trimethylamine-N-oxide (TMAO) and sodium dithionate were each dissolved in 50 mM KH_2PO_4, 0.6 mM EDTA pH 10 buffer and bubbled with nitrogen for 45 – 60 minutes. The ethylene glycol cryoprotectant and glassing agent was freeze pump thawed five times. At this time, the DSMOR sample, TMAO substrate, dithionate, and ethylene glycol were ready to use.

DMSOR Reductase Mo(V) Intermediate Preparation

250 μM of DMSO reductase enzyme was added in a cryogenic vial sealed with a septum followed by addition of ethylene glycol and 150 mM TMAO. The mixture was reduced with excess sodium dithionite, and stirred until a pink color appeared indicating the formation of the Mo(V) intermediate.

Electronic Absorption

Samples for room temperature electronic absorption spectra for both Mo(IV) and Mo(V) DMSO reductase were prepared as described above and placed in an anaerobic 1cm cuvette sealed with Teflon cap. The electronic absorption spectrum was collected under anaerobic condition using a Hitachi U-3501 UV-Vis

spectrophotometer that is capable of scanning a 180-3000 nm wavelength. The spectral bands were resolved using the Grams/AI (7.02) software package.

Magnetic Circular Dichroism (MCD)

Low temperature MCD samples were prepared in the same way as described in the DMSO reductase Mo(V) intermediate preparation, except a 2:1 ethylene glycol to protein ratio was maintained to obtain an optically transparent glass required for low temperature MCD measurements. Low temperature MCD data were obtained using a JASCO J-810 spectropolarimeter that is interfaced to a computer and an Oxford Instrument Spectromag 4000-7 split-coil superconducting magnet system operating at 7 T applied magnetic field. Depolarization of the incident radiation by the sample was determined by comparing the intrinsic circular dichroism of a standard Ni (+)-tartrate solution positioned in front of and then in back of each sample. Samples which were <10% depolarized were considered suitable.

Electron Paramagnetic Resonance (EPR)

Samples for EPR characterization were prepared the same way as for the electronic absorption. The sample mixture was placed in an EPR tube and quickly frozen in liquid nitrogen. EPR measurements were obtained using a Bruker EMX EPR Spectrometer operating at ~9.5 GHz (X-band) with the following instrument settings: 100 kHz modulation frequency, 6 Gauss modulation amplitude, 500 Gauss sweep width and 0.2 milliwatts of microwave

power. Spectral simulations were performed using Bruker's XSophe and the EasySpin simulation program.

Computational Model ([Mo(OCH$_3$)(S$_2$C$_2$(CH$_3$)$_2$)$_2$(OH)]$^-$) for DMSOR Mo(V) Intermediate

A computational model for the DMSOR Mo(V) Intermediate was constructed based on the crystal structure of oxidized Mo(VI) DMSO reductase enzyme. The computation model ([Mo(OCH$_3$)(S$_2$C$_2$(CH$_3$)$_2$)$_2$(OH)]$^-$) has two 2,3-dithiol but-2-ene ligands attached to the molybdenum in place of pyranopterin dithiolene, and the serine amino acid was substituted with a methoxy group. This computational model was fully optimized to obtain a minimal energy geometry for the Mo(V) intermediate species.

Computational Details

All calculations on the [Mo(OCH$_3$)(S$_2$C$_2$(CH$_3$)$_2$)$_2$(OH)]$^-$ computational model were performed at the density functional level of theory using ORCA and Gaussian 03W software packages. When using the Gaussian 03W program, a hybrid B3LYP functional with a 6-31G* basis set was used for carbon, oxygen and sulfur, while LANL2DZ and LANL2 effective core potential basis sets were used for molybdenum. The geometry of the [Mo(OCH$_3$)(S$_2$C$_2$(CH$_3$)$_2$)$_2$(OH)]$^-$ computational model was optimized in the spin unrestricted mode (UB3LYP). The lowest energy electronic transitions for the computational model were

predicted using time dependent density functional theory (TD-DFT) as implemented by the Gaussian 03W program.

EPR spin Hamiltonian parameters were calculated at the DFT level using the ORCA 2.7.0 program while MCD spectra were calculated using both ADF2009.01 and a multi-reference configuration interaction (MRCI, ORCA 2.7.0) method for comparison. A triple-zeta basis set (TZP in the ADF basis set notation) and the PBE GGA density functionals were used in the ADF calculations. Relativistic corrections were incorporated self consistently in the ADF and ORCA calculations with the ZORA scalar relativistic Hamiltonian. MRCI calculations were performed with the spectroscopy oriented configuration interaction (SORCI) MRCI functionality in ORCA 2.7.0. MCD and electronic absorption spectra were also calculated using both DFT (ADF) and *ab initio* based configuration interaction methods. GaussView and ADF input interfaces were used to prepare Input files.

4.5 Results and Discussion

4.5.1 Determination of Spin Hamiltonian Parameters (g-tensor, ^{95,97}Molybdenum and Proton Hyperfine Tensors)

Figure 4.1 shows high quality EPR data for the Mo(V) intermediate collected at 29K with an ~9 GHz microwave frequency showing very intense and highly resolved spectrum. Spectral simulation of the Mo(V) intermediate (Figure 4.1) reveals a rhombic g-tensor with g_1 = 1.9988, g_2 = 1.9885 and g_3 = 1.9722, which

indicates the presence of a low symmetry coordination environment. The calculated g anisotropy ($g_{anisotropy}$ = 0.0266, where $g_{anisotropy} = g_1 - g_3$) is in good agreement with the g anisotropy of 0.0251 reported for the *R. capsulatus* Mo(V) intermediate using glycol as the glassing agent.[90] Spectral simulations also gave a ^1H hyperfine tensor with A_1 = 10.05, A_2 = 9.20 and A_3 = 12.70 x10^{-4} cm^{-1} respectively. The observed rhombic g-tensor and ^1H hyperfine tensor are similar to what have been reported previously in *R. sphaeroides* and *R. capsulatus* DMSO reductase for the Mo(V) intermediate.[22,90-92]

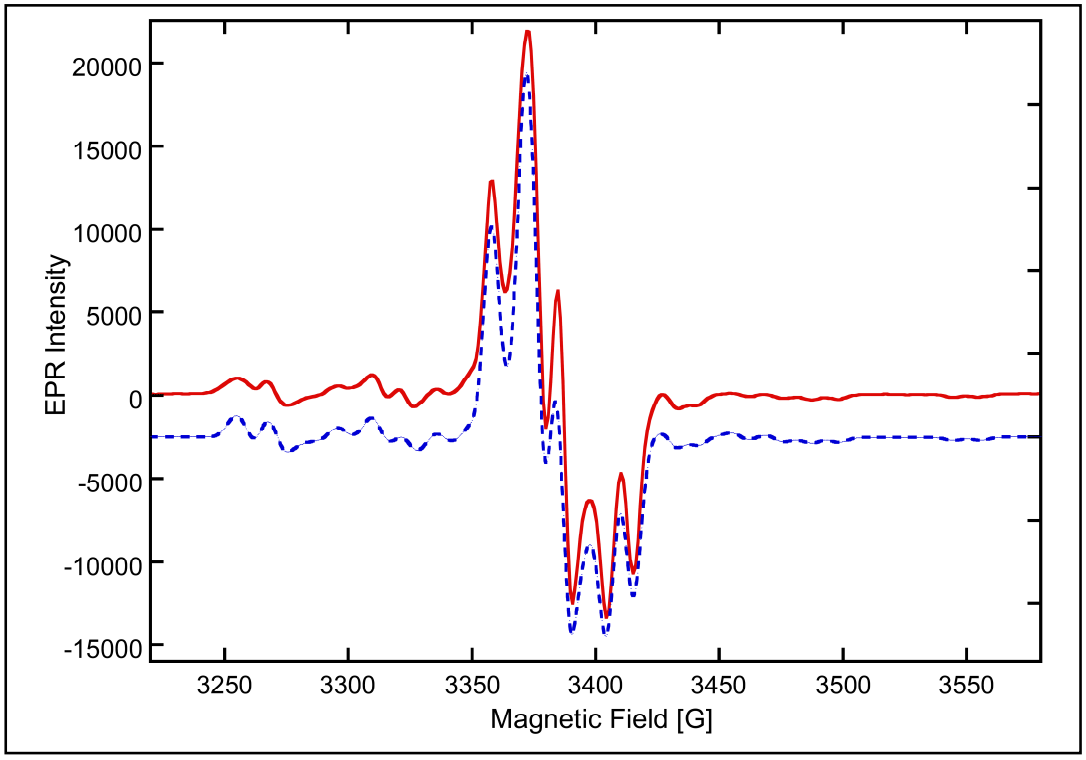

Figure 4.1: EPR spectra of DMSO reductase Mo(V) intermediate data (——) and simulation (– – –) showing the rhombic g-splitting pattern with molybdenum and proton hyperfine coupling.

For the first time a rhombic ^{95,97}Mo hyperfine tensor has been obtained from EPR spectral simulations of the DMSO reductase Mo(V) intermediate, with A_1 = 52.00, A_2 = 37.33 and A_3 = 13.33 x10^{-4} cm^{-1} and average hyperfine value (A_{ave}) of 34.22 x10^{-4} cm^{-1}. The ^{95,97}Mo hyperfine yielded a rhombic spin dipolar component of A_S^{Mo} = [-20.89, +3.11, +17.88] x 10^{-4} cm^{-1} which is unusual for Mo(V) enzymes and synthetic model compounds which commonly have axial dipolar components $A_S^{Mo} = \lfloor -2A_S^{Mo}, +A_S^{Mo}, +A_S^{Mo} \rfloor$ for dz^2 or $A_S^{Mo} = \lfloor +2A_S^{Mo}, -A_S^{Mo}, -A_S^{Mo} \rfloor$ for d_{xy} or $d_{x^2-y^2}$ orbitals. The rhombic nature of the dipolar contribution suggests a d_{z^2} – type ground state admixed with either a d_{xy} or $d_{x^2-y^2}$ orbital in the Mo(V) intermediate consistent with A_S^{Mo} =[$-2A_S^{Mo}$, 0, $+2A_S^{Mo}$] for a magnetic orbital observed in the rhombic limit.[42,52]

Table 4-1: DMSO reductase Mo(V) intermediate EPR spin Hamiltonian parameters.

DMSO reductase Mo(V) Intermediate														
This Work														
g-tensor				^{95,97}Mo A-tensor (x10^{-4} cm^{-1})				^{1}H A-tensor (x10^{-4} cm^{-1})			Euler Angle		
g_1	g_2	g_3	g_{ave}	A_1	A_2	A_3	A_{ave}	A_1	A_2	A_3	α	β	γ
1.9988	1.9885	1.9722	1.9865	52.00	37.33	13.33	34.22	10.05	9.20	12.70	-96.00	93.00	164.00
Reported													
g-tensor				^{95,97}Mo A-tensor (x10^{-4} cm^{-1})				^{1}H A-tensor (x10^{-4} cm^{-1})			References		
g_1	g_2	g_3	g_{ave}	A_1	A_2	A_3	A_{ave}	A_1	A_2	A_3			
1.9890	1.9770	1.9620	1.9760	-	-	-	-	9.80	10.55	9.15	92		
1.9937	1.9830	1.9686	1.9818	-	-	-	-	14.37	11.67	10.92	90		
1.9900	1.9800	1.9600	1.9767	-	-	-	-	-	-	-	91		
1.9924	1.9813	1.9645	1.9793	-	-	-	-	11.10	8.17	8.70	23		

The best spectral simulations are shown in Figure 4.1 and the spin Hamiltonian parameters are given in Table 4-1. These have been achieved with incorporation of Euler angles. Euler rotations of α = -96°, β = 93° and γ = 164° have been obtained from spectral simulations, where a minimum g value (g_3) is associated with the maximum hyperfine value (A_1), the middle g value (g_2) is associated with minimum hyperfine value (A_3) and maximum g value (g_1) is associated with middle hyperfine (A_2) respectively.

4.5.2 Correlation Between Experimental and Theoretical Spin Hamiltonian Parameters

Theoretical EPR spin Hamiltonian parameters have been calculated using a fully geometry optimized $[Mo(OCH_3)(S_2C_2(CH_3)_2)_2(OH)]^-$ computational model for the Mo(V) intermediate for comparison with experimental spin Hamiltonian parameters obtained from the DMSOR Mo(V) intermediate. ORCA calculation results gave a rhombic g-tensor with g_1 = 1.9815, g_2 = 1.9620 and g_3 = 1.9459 respectively. Although the ORCA calculation underestimated the g-tensor values for the Mo(V) intermediate, the rhombic nature of g-tensor agrees well with the experimental results (Table 4-2), and thus supports a low symmetry coordination environment.

Table 4-2: Experimental and theoretical EPR spin Hamiltonian parameters for DMSO reductase enzyme Mo(V) intermediate.

Experimental													
g-tensor				^{95,97}Mo A-tensor (x10^{-4} cm^{-1})				^{1}H A-tensor (x10^{-4} cm^{-1})			Euler Angle		
g_1	g_2	g_3	g_{ave}	A_1	A_2	A_3	A_{ave}	A_1	A_2	A_3	α	β	γ
1.9988	1.9885	1.9722	1.9865	52.00	37.33	13.33	34.22	10.05	9.20	12.70	-96.00	93.00	164.00
Theoretical													
1.9815	1.9620	1.9459	1.9631	53.09	34.04	14.52	33.88	10.33	6.37	5.77	-18.80	5.9	61.00

The rhombic ^{95,97}Mo hyperfine tensor obtained from the ORCA calculation yielded A_1 = 53.09, A_2 = 34.04, A_3 = 14.52 x10^{-4} cm^{-1} which averaged (A_{ave}) to 33.88 x10^{-4} cm^{-1}. The corresponding dipolar component is A_S^{Mo} = [-19.36, +0.16, +19.21] x 10^{-4} cm^{-1}. The ORCA calculated ^{95,97}Mo hyperfine couplings are in good agreement with experimental values (Table 4-2) and thus support d_{z^2} type ground state in the DMSOR Mo(V) intermediate.

Euler rotations of α = -19°, β = 6° and γ = 61° have been calculated from hyperfine orientation matrices obtained from the ORCA output file using a zxz rotation convention. Figure 4.2 shows the orientation of the g-tensor relative to the A-tensor as drawn from the orientation matrices in the ORCA output files, where the minimum g value (g_3) is associated with the maximum hyperfine value (A_1), similar to what was observed in the experimental results. In addition, the ORCA calculation results show that the middle g value (g_2) is associated with the middle hyperfine value (A_2) and the maximum g value (g_1) is associated with minimum hyperfine value (A_3) (Figure 4-2). The theoretical orientation of g_1

relative to A_3 and g_2 relative to A_2 do not agree with the experimental orientation. This may reflect a slight difference in the orientation of magnetic orbital along the x and y axes.

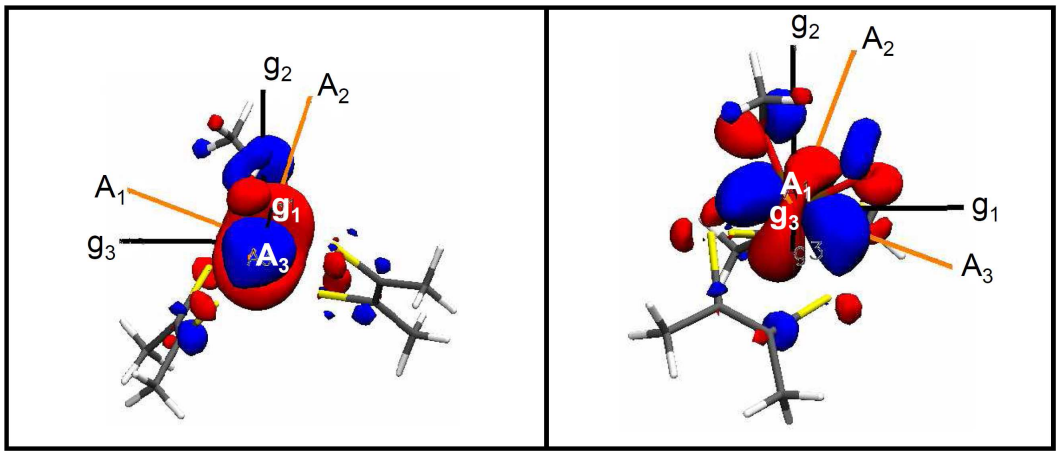

Figure 4.2: Schematic representation of the g-tensor and ^{95,97}Mo A-tensor for full optimized structure of DMSO reductase Mo(V) intermediate as drawn from the orientation matrices in ORCA output files, along z-axis (left) and along x-axis (right).

4.5.3 The Nature of SOMO and the Geometry of DMSO Reductase Mo(V) Intermediate

A full geometry optimization was performed on $[Mo(OCH_3)(S_2C_2(CH_3)_2)_2(OH)]^{1-}$, a computational model for DMSO reductase Mo(V) intermediate, in order to determine the low energy structure and the nature of the redox-active orbital (SOMO). This calculation result reveals a low symmetry geometry that lies in between idealized octahedral and trigonal prismatic geometries with the unpaired electron in a d_{z^2} type redox orbital. Figure 4.3 shows the d_{z^2} redox orbital for the

$[Mo(OCH_3)(S_2C_2(CH_3)_2)_2(OH)]^-$ model. The calculation showed that the unpaired electron resides in the α-HOMO (Figure 4.3) where its spin counterpart β-LUMO orbital is empty. The nature of the β-LUMO redox orbital is important in understanding the Mo(V)→Mo(IV) redox process, since this is the orbital that becomes occupied upon one electron reduction to form the Mo(IV) state. Therefore, the β-LUMO orbital possesses a dominant Mo character (~70%), with 0.02% OH, 9% OCH_3, 3.6 and 5.4% from P- and Q- pterin of $S_{dithiolene}$ ligands characters (Table 4-3).

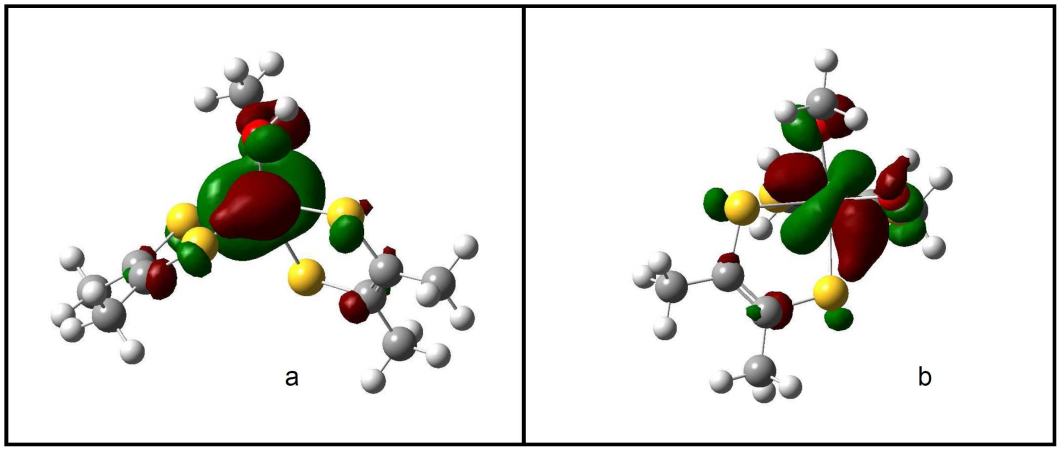

Figure 4.3: Electron density contour plot showing the SOMO orbital (a) along the z-axis and (b) along the x-axis for the $[Mo(OCH_3)(S_2C_2(CH_3)_2)_2(OH)]^-$ computational model of the DMSO reductase Mo(V) intermediate.

The spin density distribution was calculated using the $[Mo(OCH_3)(S_2C_2(CH_3)_2)_2(OH)]^-$ model in order to develop deep insight into the nature of the redox-active orbital and the nature of the atomic spin populations (Table 4-3). Figure 4.4 shows spin density distribution in the

$[Mo(OCH_3)(S_2C_2(CH_3)_2)_2(OH)]^-$ model. The calculation reveals that a very large positive spin population is associated with the molybdenum atom and ~10% positive spin is localized on the oxygen atom of the methoxy ligand. In addition the calculations also reveal a negative spin density (-13% total) on the dithiolene sulfurs. A negative spin population on the dithiolene sulfurs is the result of a spin polarization mechanism that results from configuration interaction (CI). Here, excited states involving promotion of an α electron localized on a dithiolene based orbital into unoccupied Mo-based α orbitals as ($S_{dithiolene} \rightarrow$ Mo) ligand-to-metal charge transfer (LMCT) states contribute to the negative spin population on sulfur.[42] Also the negative spin density signifies a reduced metal-ligand covalency in the $[Mo(OCH_3)(S_2C_2(CH_3)_2)_2(OH)]^-$ model and Mo(V) intermediate.

Table 4-3: β-LUMO Fragment composition (top) and spin densities (bottom) for $[Mo(OCH_3)(S_2C_2(CH_3)_2)_2(OH)]^-$ calculation model.

Fragment	% Mo	%OH	% OCH_3	%$S_{dithiolene}$ (P-Pterin)	%$S_{dithiolene}$ (Q-Pterin)	%$S_{dithiolene}$ (Total)
β-LUMO	69.63	0.02	8.96	3.56	5.41	8.97

Fragment	% Mo	%OH	% OCH_3	%$S_{dithiolene}$ (P-Pterin)	%$S_{dithiolene}$ (Q-Pterin)	%$S_{dithiolene}$ (Total)
Spin densities	97.03	3.11	9.81	-5.62	-7.56	-13.18

Occupation of the β-LUMO is important in the reduction of the Mo(V) intermediate to the Mo(IV) state. DFT calculations reveal a slightly higher percentage of $S_{dithiolene}$ (~5.4%) character from the Q-pterin and less (~3.6) from the P-pterin moiety in the β-LUMO of the Mo(V) intermediate model. The small

Mo-$S_{dithiolene}$ overlap in the SOMO would lead to poor pyranopterin dithiolene mediated electronic coupling of the active site with exogenous redox partners. In this regard, it is notable that for all DMSOR family enzymes that have been examined crystallographically and possess endogenous redox-active centers in addition to the molybdenum center, the nearest redox partner to the molybdenum lies to the Q- side of the center. Assuming the Q-pterin is indeed the physiological conduit for electron transfer regeneration in DMSOR, the LUMO orbital may play a significant role in the Mo(V)→Mo(IV) electron transfer process by contributing to an overall increase in electronic coupling between the Mo ion and the dithiolene component of the Q-pterin since this orbital possesses approximately three times the P-pterin dithiolene sulfur character as the SOMO orbital. Secondly, assuming the Q-pterin is the physiological conduit for electron transfer, the LUMO+1 orbital possesses approximately five times the Q-pterin dithiolene sulfur character as the SOMO orbital. We note that there would be an energetic penalty for utilizing the LUMO or LUMO+1 orbitals in the electron transfer regeneration step since they resides at higher energy than SOMO. However, this energy may be reduced due to the increased electron-electron repulsion that accompanies double occupation of the SOMO and associated electronic relaxation effects. Therefore, we propose that metal reduction might occur through either the Q- or P-pterin moiety in the Mo(V) to Mo(IV) reduction step. The Q-pterin electron transfer pathway is strongly supported by studies on $[Mo^{VI}O(OSiR3)(S_2C_2(COOMe)_2)_2]^-$, a synthetic model of the Mo(VI) from of the enzyme.[124]

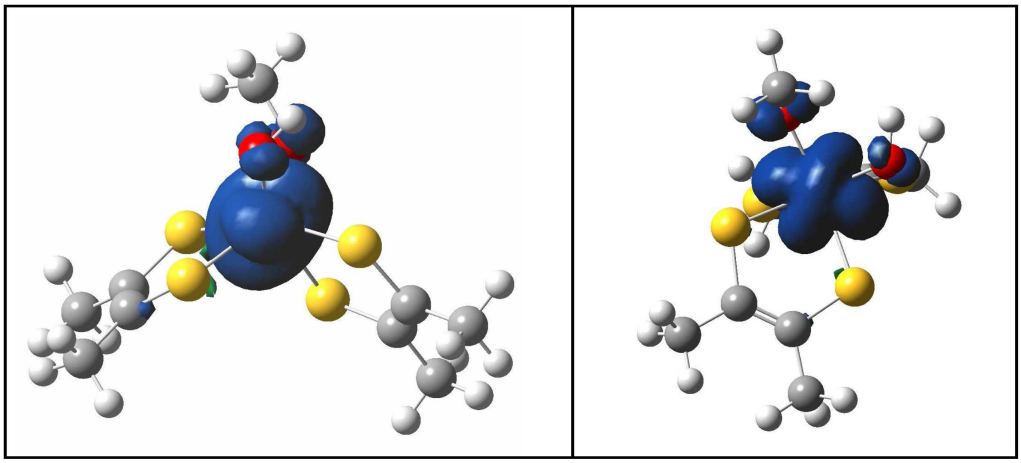

Figure 4.4: Calculated spin density on the d_{z2} orbital of the $[Mo(OCH_3)(S_2C_2(CH_3)_2)_2(OH)]^-$ computational model for the DMSO reductase Mo(V) intermediate.

4.5.4 Experimental MCD and Electronic Absorption Spectra

The DMSO reductase Mo(V) intermediate room temperature electronic absorption spectrum in the 9,500 - 28,000 cm^{-1} spectral region is displayed in Figure 4.5. The spectrum reveals a weak shoulder at 12,250 cm^{-1} (ε = 460 $M^{-1}cm^{-1}$), followed with two well-resolved bands at 15,070 cm^{-1} (ε = 1,705 $M^{-1}cm^{-1}$) and 18,050 cm^{-1} (ε = 2,430 $M^{-1}cm^{-1}$). The weak intensity of the first band signifies the ligand field transition, while the increased intensity of the second and third bands indicates that they are LMCT transitions. In addition, the electronic absorption spectrum also possesses a shoulder at 24,475 cm^{-1} (ε = 5,030 $M^{-1}cm^{-1}$). The room temperature electronic absorption spectrum for the DMSOR Mo(V) intermediate reported in this study is similar to the previously reported electronic absorption spectra of a glycerol inhibited DMSOR Mo(V) enzyme form,[91] with the

exception that bands 2 and 3 occur at higher energy (~400 cm^{-1}) in our spectrum compared to glycerol inhibited Mo(V) bands.

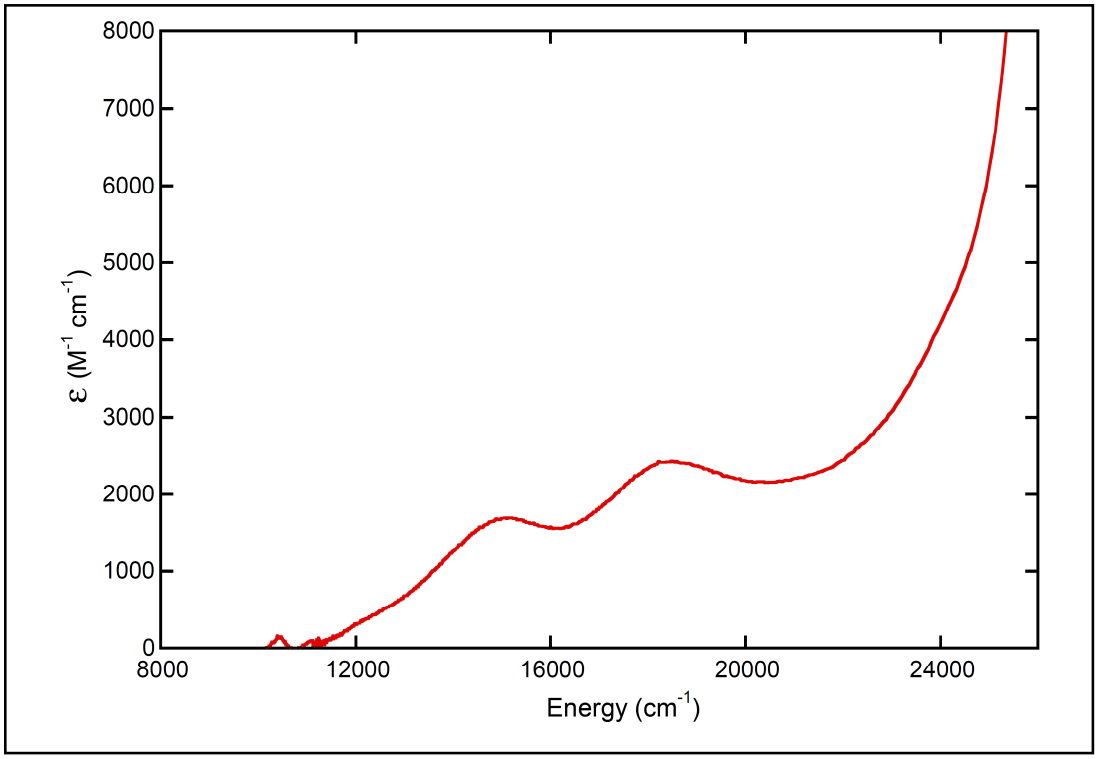

Figure 4.5: Room temperature electronic absorption spectra for DMSO reductase enzyme Mo(V) intermediate.

Variable temperature MCD spectroscopy is a higher resolution probe of the excited state electronic structure. Figure 4.6 shows the temperature difference MCD spectrum for the DMSOR Mo(V) intermediate from 9,500 – 28,000 cm^{-1}. The spectrum possesses seven temperature dependent C-term bands. The low temperature MCD spectrum reveals a weak negative C-term peak at 12,375 cm^{-1}, that was not shown in the MCD spectrum of the glycerol inhibited DMSOR

Mo(V) MCD spectrum but was reported to occur at 11,000 cm^{-1}.[91] Our MCD spectrum reveals two intense negative and positive MCD C-terms at 15,375 cm^{-1} and 17,660 cm^{-1}, followed by two weak negative-positive (+ve pseudo A) MCD C-terms at 18,920 cm^{-1} and 21,330 cm^{-1} respectively. At higher energy, the MCD spectrum reveals two intense positive-negative (-ve pseudo A-term) at 23,615 cm^{-1} and 25,895 cm^{-1} which are anticipated to arise from transitions that involve orbitally degenerate or nearly degenerate excited states possessing in-state spin-orbit coupling.[42]

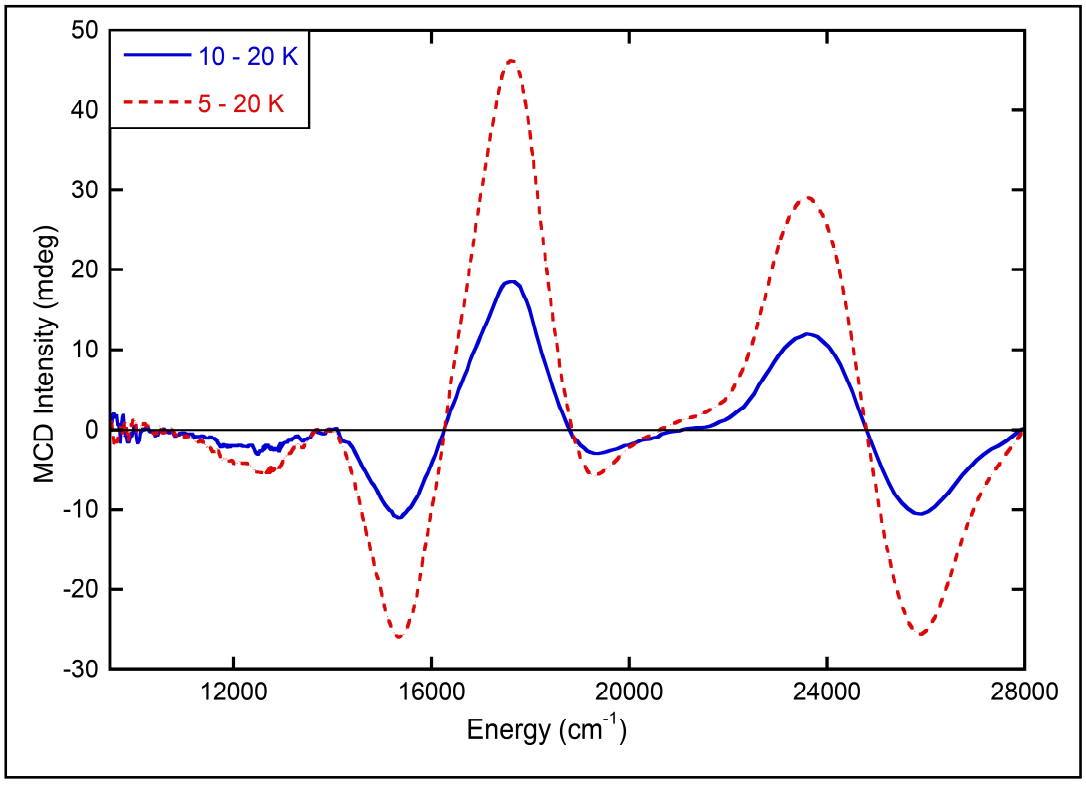

Figure 4.6: 5-20 K (·····) and 10-20 K (——) Temperature difference MCD spectra for the DMSO reductase enzyme Mo(V) intermediate showing temperature dependent C-terms.

4.5.5 Comparison Between Calculated and Experimental MCD Spectra

The magnetic circular magnetic (MCD) spectrum for the $[Mo(OCH_3)(S_2C_2(CH_3)_2)_2(OH)]^-$ computational model of the Mo(V) intermediate has been calculated using the spectroscopy oriented configuration interaction (SORCI) method for comparison with the experimental DMSOR Mo(V) intermediate MCD spectrum and to assist in making band assignments. Figure 4.7 displays the calculated MCD spectrum for the $[Mo(OCH_3)(S_2C_2(CH_3)_2)_2(OH)]^-$ model revealing temperature dependent C-term bands and individual calculated transitions (red sticks). It is clear that the MCD C-terms observed in the experimental spectrum of the Mo(V) intermediate have been accurately calculated without any scaling or energy shifts when using the SORCI method.

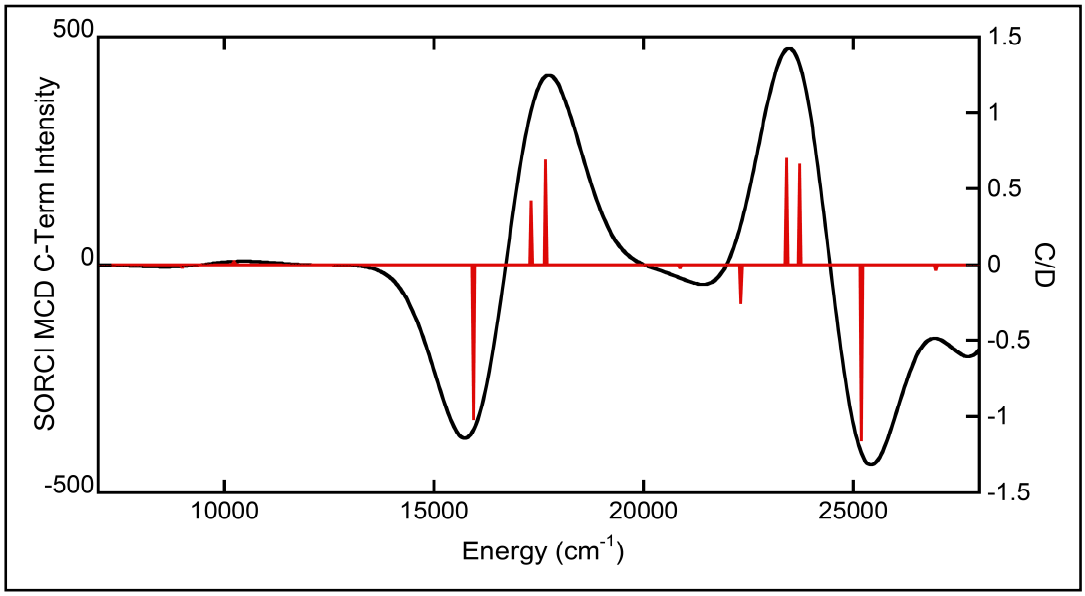

Figure 4.7: SORCI calculated MCD spectra for the $[Mo(OCH_3)(S_2C_2(CH_3)_2)_2(OH)]^-$ computational model of the DMSO reductase

enzyme Mo(V) intermediate showing temperature dependent C-terms with calculated transitions as red sticks.

Interestingly, the calculated MCD spectrum reveals a weak negative C-term followed by a positive MCD C-term at 8,555 cm^{-1} and 10,470 cm^{-1}. This band occurs as a weak negative MCD C-term in the experimental data. The negative C-term observed in experimental MCD spectrum might be due to the presence of additional spin-orbit or configuration interaction perturbations not accounted for in the calculations that affect the nature of the experimentally observed ligand field transitions in the MCD, or one of the ligand field bands is too weak to be observed. Figure 4.8 displays an experimental and calculated MCD spectra overlay showing temperature dependent C-term bands. Two intense negative and positive MCD C-term peaks at 15,735 cm^{-1} and 17,740 cm^{-1} are revealed in the calculated MCD spectrum, and the intensity and energy of these bands are similar to the same bands in the experimental spectrum. A weak negative C-term MCD peak at 21,410 cm^{-1} is observed in the calculated MCD spectrum and is similar to the negative MCD C-term peak revealed at lower energy (18,920 cm^{-1}) in the experimental MCD spectrum. A weak positive MCD C-term band observed in the experimental MCD spectrum is missing in the calculated MCD spectrum, and this may be the result of an overestimation of the transition energy for this band. In addition, the higher energy positive-negative (negative pseudo A-term) MCD C-term bands are revealed at 23,465 and 25,430 cm^{-1}, consistent with a negative pseudo A-term in the experimental spectrum. The intensity of

these bands is consistent with a LMCT transition with appreciable metal character.

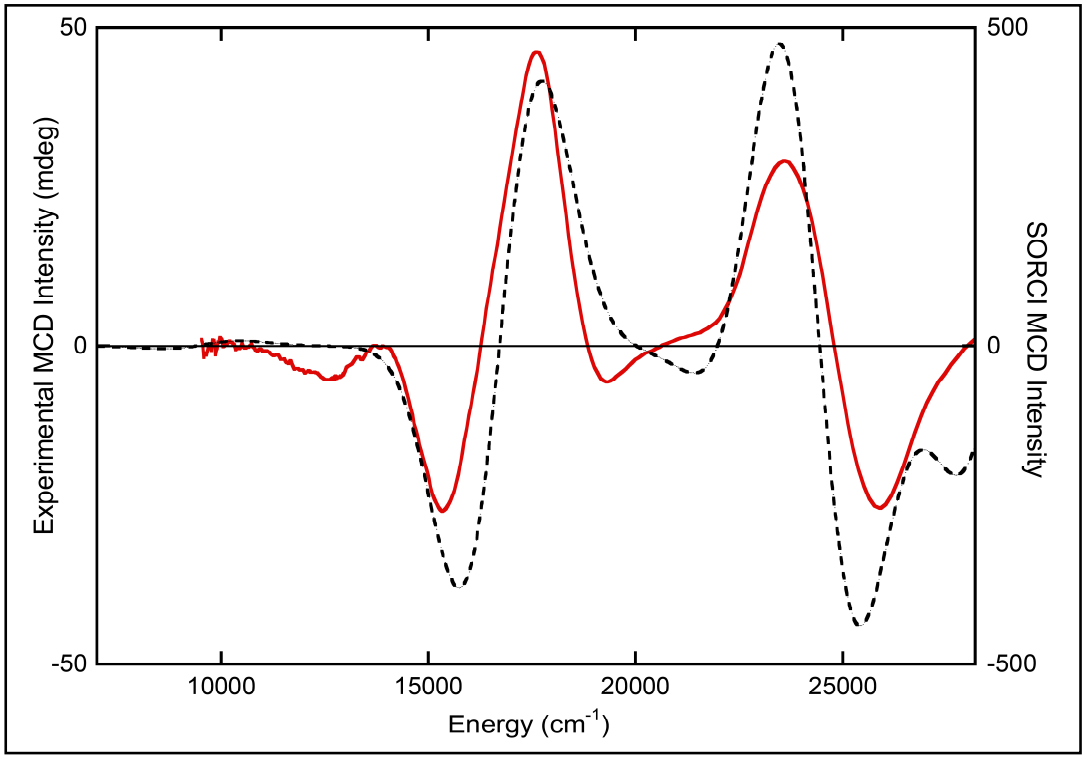

Figure 4.8: Experimental (·····) and SORCI calculated (——) MCD spectra for DMSO reductase enzyme Mo(V) intermediate showing MCD C-terms.

4.5.6 The Nature of the Frontier Molecular Orbitals and a Bonding Description for the $[Mo(OCH_3)(S_2C_2(CH_3)_2)_2(OH)]^-$ Computational Model of the DMSO Reductase Mo(V) Intermediate

Both ORCA and Gaussian 03W Density functional methods were used to calculate the electronic absorption and MCD spectra of the $[Mo(OCH_3)(S_2C_2(CH_3)_2)_2(OH)]^-$ computational model for comparison. A very high

quality MCD spectrum was obtained using the SORCI (ORCA) method with 12 calculated natural orbitals in the active space. Figure 4.9 displays 10 of these natural orbitals present in the active space of the SORCI calculation.

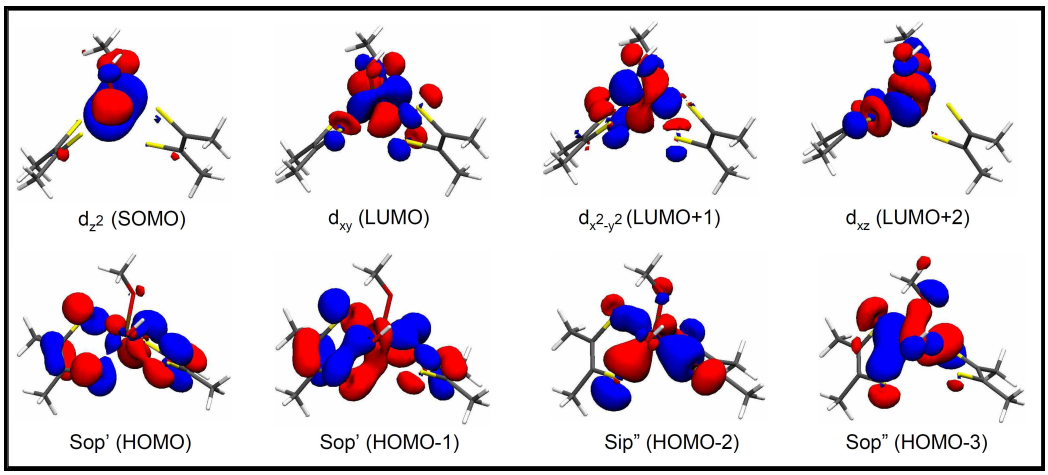

Figure 4.9: Frontier molecular orbitals obtained from the $[Mo(OCH_3)(S_2C_2(CH_3)_2)_2(OH)]^-$ computational model.

In bis-dithiolene compounds, the symmetry adapted linear combination of atomic orbitals from the two dithiolene ligands leads to formation of four out of plane and four in-plane sulfur ligand orbitals, where sulfur out of plane orbitals are more destabilized than the sulfur in-plane orbitals.[91] Results from our SORCI calculation (Table 4-4) reveal that the highest doubly occupied orbital (HOMO) has 12% Mo character with 34% and 25% S_{op} ($S_{dithiolene}$) character from the P-pterin and Q-pterin while the second unoccupied orbital (HOMO-1) has 23% Mo with 21% and 25% totally symmetrical S_{op} ($S_{dithiolene}$) character from the P- and Q-pterins. Therefore, the presence of a $S_{op}(p)$-C(p) π^* anti-bonding interaction

indicates the involvement of the pyranopterin dithiolene ligands in determining the energies of these orbitals.

The HOMO-2 orbital possesses 31% Mo character with 28% and 32% S_{ip} ($S_{dithiolene}$) character from the P- and Q-pterins. The absence of $S_{ip}(p)$-C(p) π^* anti-bonding interactions (Figure 4.9) reveals the non dependence of this orbital in the frontier molecular orbital scheme. Destabilization of S_{op} ($S_{dithiolene}$) and stabilization of S_{ip} ($S_{dithiolene}$) orbitals indicate the low valence ionization energy of the S_{op} ($S_{dithiolene}$) orbital, and we therefore anticipate low energy LMCT transitions in the Mo(V) intermediate to involve one-electron promotions from ligand-based orbitals with appreciable S_{op} ($S_{dithiolene}$) character to the lowest unoccupied Mo based orbitals.

Table 4-4: Molecular orbital percentage composition for the lowest unoccupied (LUMO) and the highest doubly occupied (HOMO) orbitals in the $[Mo(OCH_3)(S_2C_2(CH_3)_2)_2(OH)]^-$ computational model.

Fragment	% Mo	%OH	% OCH_3	%$S_{dithiolene}$ (P-pterin)	%$S_{dithiolene}$ (Q-pterin)	%Dithiolene (P-pterin)	%Dithiolene (Q-pterin)
LUMO+3	64	5	0	20	8	22	9
LUMO+2	66	5	8	2	16	2	18
LUMO+1	68	6	2	7	14	8	17
LUMO	70	2	7	11	7	13	8
SOMO	77	4	10	3	3	5	5
HOMO	12	1	1	34	25	51	36
HOMO-1	23	1	1	21	25	34	43
HOMO-2	31	2	3	28	32	30	34
HOMO-3	26	9	15	17	29	19	33
HOMO-4	23	5	23	29	16	32	17

For an idealized trigonal prismatic geometry, the orbital splitting pattern trend with increasing energy is $d_{z^2} > d_{xz,yz} > d_{xy},d_{x^2-y^2}$ respectively.[55] The d_{z^2} orbital is highly stabilized, while degenerate $d_{xz,yz}$ and $d_{xy},d_{x^2-y^2}$ orbital sets are destabilized. The SORCI calculation results (Table 4-4) reveal that the singly occupied molecular orbital (SOMO) possesses 77% molybdenum character, with 3% $S_{dithiolene}$ character from each Q and P-pterin dithiolene. The small contribution of $S_{dithiolene}$ character in the SOMO, which is supported by the negative spin populations on sulfur, supports the non covalent nature of the SOMO. All low energy unoccupied orbitals possess mainly Mo character with an appreciable amount of S_{op} and S_{ip} ($S_{dithiolene}$) character (Figure 4.9 and Table 4-4). The presence of sulfur character in the unoccupied orbitals indicates the covalent nature of these orbitals, and indicates low energy LMCT transitions are possible to these orbitals.

4.5.7 Band Assignments

Figure 4.10 displays the Gaussian resolved room temperature electronic absorption and low temperature MCD spectra for the DMSOR enzyme Mo(V) intermediate. Gaussian resolved temperature dependent MCD C-term peaks in the MCD spectrum agree very well with the Gaussian resolved electronic absorption bands and the calculated MCD spectrum (Figure 4.8). Therefore, room temperature electronic absorption and low temperature MCD spectra have been assigned based on transitions obtained from the calculated MCD spectrum and the use of small molecule analogues. Table 4-5 contains experimental

electronic absorption and MCD spectra band maxima, combined with experimental and theoretical oscillator strengths.

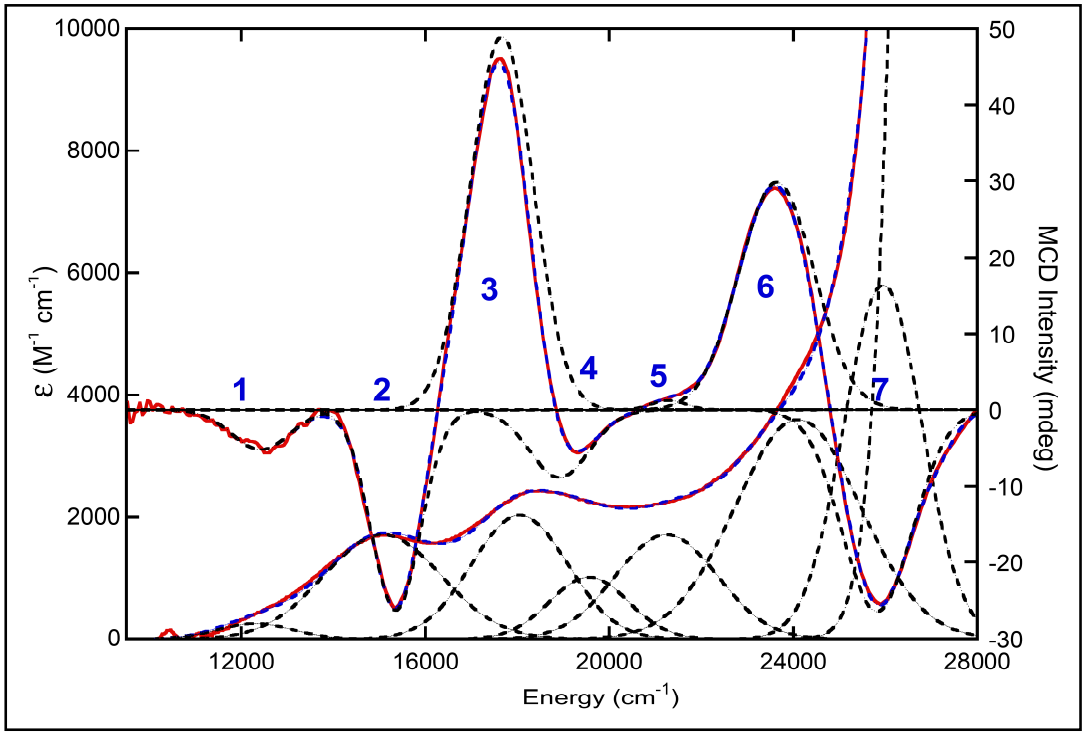

Figure 4.10: Overlay of the 5-20 K magnetic circular dichroism and 298K electronic absorption Gaussian resolved spectra for the DMSO reductase enzyme Mo(V) intermediate.

Band 1: This is a weak ligand field band (f = 0.002) in the electronic absorption which corresponds to a weak negative MCD C-term in the MCD spectrum and is assigned as the SOMO→LUMO/LUMO+1 transitions. The weak oscillator strength (f = 0.002) of this band is consistent with a weak calculated oscillator strength (f = 0.002), and therefore supports the ligand field assignment. This assignment is also consistent with the $d_{xy} \rightarrow d_{xz/dyz}$ ligand field transition

assignment for low energy bands in *des* oxo-molybdenum compounds examined by McNaughton et al.[61] In addition, this band was previously assigned as a $d_{xy} \rightarrow d_{xz/dyz}$ ligand field transition in the glycerol inhibited Mo(V) spectrum by Finnegan et al., although this assignment was made before the crystal structure of DMSOR was performed and only considered the presence of a single pyranopterin dithiolene.[91] Hernandez-Marin and coworkers assigned this band as $d_{yz} \rightarrow d_{xz}/d_{x^2-y^2}$ ligand field transition,[113] which is consistent with our assignment despite the differences in identification of the metal orbitals.

Table 4-5: Electronic absorption, MCD energy maxima, and theoretical and experimental oscillator strengths for the DMSO reductase enzyme Mo(V) intermediate.

	Energy (cm^{-1})		Oscillator Strength (f)	
Band #	UV-Vis	MCD	Experimental	Theoretical
1	12,300	12,375	0.002	0.002
2	15,070	15,375	0.024	0.010
3	18,050	17,660	0.023	0.061
4	19,560	18,920	0.009	0.001
5	21,240	21,330	0.020	0.017
6	24,100	23,615	0.053	0.100
7	25,950	25,895	0.053	0.020

Bands 2 and 3: These are two intense low energy charge transfer bands observed at 15,070 and 18,050 cm^{-1} in the electronic absorption and correspond to the intense negative and positive C-terms peaks at 15,375 and 17,660 cm^{-1} in the MCD spectrum. Bands 2 and 3 arise from strong spin-orbit mixing of excited

states that derive from HOMO→LUMO+1 and HOMO→LUMO one-electron promotions. The occurrence of HOMO→SOMO transition also contributes to the Band 3 bandshape. It's relatively high energy is expected due to the strong electron-electron repulsion when the SOMO orbital becomes doubly occupied as the result of the non-covalent (6% $S_{dithiolene}$ character) nature of the SOMO orbital. This assignment is supported by calculated oscillator strengths (f = 0.010 band 2, f = 0.061 band 3) that are in a reasonable agreement with experimental oscillator strength (f = 0.024 band 2 and f = 0.023 band 3). In contrast, band 2 was assigned as a HOMO→SOMO transition and band 3 as the HOMO-1→SOMO transition in DMSOR glycerol inhibited Mo(V).[91] Additionally, this assignment is consistent with the Hernandez-Marin et al. assignment for band 2, which is a combination of HOMO→LUMO (70%), and HOMO→LUMO+1 (68%) transitions, while band 3 was assigned as the HOMO→LUMO (72%) transition.[113]

Band 4: A weak band (f = 0.009) in the electronic absorption spectrum at 19,560 cm^{-1} corresponds to the weak C-term peak at 18,920 cm^{-1} in the MCD spectrum. This transition results from a combination of HOMO→ LUMO+1 (56%) and HOMO-1→ LUMO+1 (14%) one-electron promotions. In DMSOR glycerol inhibited Mo(V) intermediate this band was assigned as the HOMO→SOMO transition[91] which is contrary to our assignment, while Hernandez-Marin et al. assigned this transition as a combination of HOMO→LUMO+1 (47%) and HOMO-1→SOMO (66%) one electron promotions.[113]

Band 5: A positive C-term peak at 21,330 cm^{-1} in the MCD spectrum corresponds to band 5 at 21,240 cm^{-1} in the electronic absorption. This band is significantly intense in the DMSOR glycerol inhibited Mo(V) spectrum, but it was not assigned. Therefore, we have assigned this transition as resulting from a combination of HOMO-1→LUMO (51%) and HOMO→LUMO (21%) one-electron promotions which overlaps and is nearly cancelled by the positively signed C-term HOMO-1→SOMO transition. In addition, the experimental oscillator strength (f = 0.020) is in good agreement with combined calculated oscillator strength (f = 0.014), which provides further support for this assignment.

Table 4-6: Transition energies, MCD sign, assignments and oscillator strength obtained from SORCI calculation.

Band	Transition #	Transition Energy (cm^{-1})	Transition Type	MCD Sign	Oscillator Strength (f)
1	i ii	9,078 10,157	SOMO→LUMO+1 SOMO→LUMO	(–) (+)	0.0002 0.0009
2	iii	16,010	HOMO→LUMO+1 (57%) HOMO→LUMO (18%)	(–)	0.0060
3	iv v	17,396 17,496	HOMO→SOMO HOMO→LUMO (58%) HOMO→LUMO+1 (22%)	(+) (+)	0.0080 0.0200
4	vi	20,890	HOMO→LUMO+1 (56%) HOMO-1→LUMO+1 (14%)	(–)	0.0003
5	vii	22,316	HOMO-1→LUMO (51%) HOMO→LUMO (21%)	(–)	0.0050
6	viii ix	23,431 23,714	HOMO-1→SOMO HOMO-1→LUMO (38%) HOMO-1→LUMO+1 (20%)	(+) (+)	0.0090 0.0500
7	x	25,124	HOMO-1→LUMO+1 (52%) HOMO-1→LUMO (16%)	(–)	0.0100

Bands 6 and 7: This is the intense negative pseudo A-term at 23,615 and 25,895 cm^{-1} in the MCD spectrum, that correspond with intense bands 6 (f = 0.053) and 7 (f = 0.053) in the electronic absorption spectrum. Bands **6** and **7** are assigned as arising from transitions that are predominantly linear combinations of HOMO-1→LUMO and HOMO-1→LUMO+1 excitations. Our assignment does not agree with the HOMO-2→LUMO transition for band 7 in DMSOR glycerol inhibited Mo(V).[91] Hernandez-Marin et al, assigned band 6 as a combination of HOMO-1→LUMO (49%) and HOMO-1→LUMO+1 (47%) one-electron promotions, and, this is consistent with our assignment while band 7 was assigned as resulting from HOMO-1→LUMO (49%), HOMO-2→LUMO (56%) and SOMO→LUMO+2 excitations.[113]

4.5.8 The Electronic Structure Contribution to Mechanism

Several computational studies have been performed on DMSO Reductase at the crystal structure geometry in order to understand its electronic structure and oxygen atom transfer reactivity. During catalysis the enzyme is in the Mo(VI) state and is reduced to the Mo(IV)-H_2O state through a Mo(V) intermediate by two sequential coupled electron-proton transfers. It is believed that in the Mo(IV)-H_2O state water is lost through a dissociation mechanism to form a square pyramidal geometry in which the Mo(IV) state is oxidized back to Mo(VI) by introduction of substrate. Our geometry optimization of DMSOR Mo(IV)-H_2O at the Mo(V) intermediate geometry shows a loss of water to form $[Mo(OCH_3)(dithiolene)]^-$ (Mo(IV)) with an empty orbital (dz^2) lobe pointing towards

the substrate entrance channel (Figure 4.11). This result shows that the water loss can occur even when the geometry is not allowed to relax to its lowest energy geometry, which is a square pyramid geometry.

Transition state calculations were performed on the *des*-oxo-Mo(IV) square pyramidal geometry with TMAO as substrate in order to study the oxygen atom transfer reaction and for comparison with the Mo(V) $[Mo(OCH_3)(S_2C_2(CH_3)_2)_2(OH)]^-$ computational intermediate. Figure 4.12 shows the energy profile for the oxygen atom transfer reaction between [Mo(OCH_3)(dithiolene)] and the TMAO substrate. The energy profile starts with the reactant {[Mo(OCH_3)(dithiolene)]$^-$} (R) with a square pyramidal geometry (180° dihedral angle) at 0 kcal mol^{-1}, and the substrate (TMAO) at 4.00 Å distance. The transition state, {[Mo(OCH_3)(dithiolene)] + TMAO} (**TS**), lies ~15 kcal mol^{-1} above **R** and possesses a distorted trigonal prismatic geometry (132.5° dihedral angle). A further decrease in the Mo-$O_{substrate}$ distance to 2.15 Å {TMAO + [Mo(OCH_3)(dithiolene)]} results in a geometric change with 108.2° dithiolene dihedral angle. This is the point where the O-TMA bond breaks and a nascent Mo-oxo bond is formed (Figure 4.12). The formation of a stable distorted trigonal prismatic geometry six coordinated [Mo(VI)O(OCH_3)(dithiolene)] (**P**) product species with a 1.8 Å Mo-oxo bond lead to a sharp decrease in energy (~33 kcal mol^{-1}).

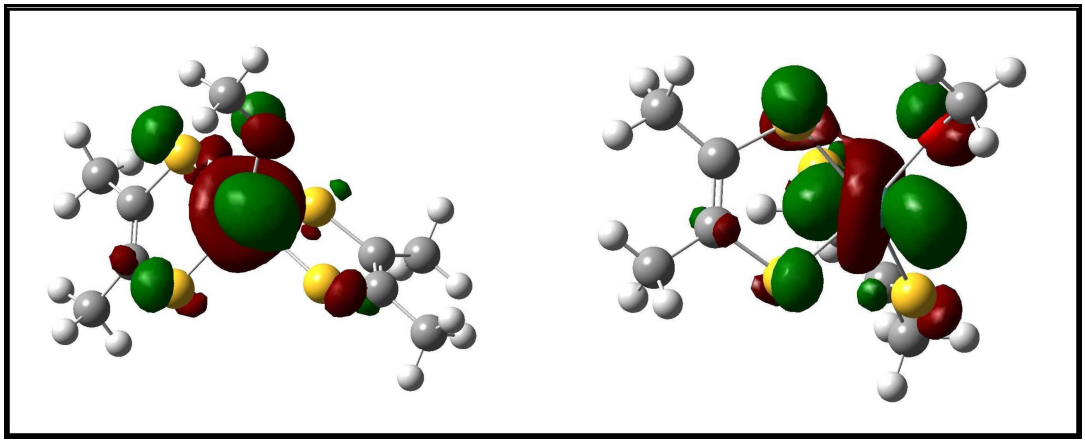

Figure 4.11: Reduced Mo(IV) $[Mo(OCH_3)(dithiolene)]^-$ at the Mo(V) geometry showing the d_{z2} orbital lobe pointing toward the substrate access channel. (left) view along z-axis and (right) view along x-axis.

Previously kinetic and computational studies on the oxygen atom transfer reaction with DMSO as substrate show the presence of two transition states and an intermediate,[125-130] whereby the oxygen atom transfer step is the rate limiting step.[14,131] In addition, computational studies on oxygen atom transfer reactions with mono-oxo $[MoO(mnt)_2]^-$ (where mnt = maleonitrile-1,2-dithiolate) using TMAO as substrate revealed the presence of two transition states at 17.1 kcal•mol^{-1} and 16.9 kcal•mol^{-1} with an intermediate at 15.5 kca•lmol^{-1}.[129] The presence of an intermediate in the oxygen atom transfer reaction suggested that TMAO is a slow substrate which is contrary to the kinetic studies of Cobb and coworkers[14] which showed TMAO to be a fast substrate. Our transition state calculations (Figure 4.12) using a des-oxo molybdenum model shows a single transition state at 15.2 kcal•mol^{-1} and a shoulder at low energy ~9.8 kcal•mol^{-1} with no intermediate observed. Therefore, the atom transfer step is barrierless

and indicative of a faster oxygen atom transfer reaction. This can be due to a lesser N-O bond enthalpy (-2 kcal•mol^{-1}) observed in TMAO compared to the -27 kcal•mol^{-1} S-O bond enthalpy in DMSO.[132] This result is consistent with the kinetic study by Cobb et al. on DMSOR using TMAO as substrate, where they reported a high rate constant (134.5 to 2300 s^{-1}) in the oxygen atom transfer step.[14]

EPR spin Hamiltonian parameters and MCD and electronic absorption transitions have been calculated using a low energy five coordinate $[Mo(OCH_3)(OH)(S_2C_2(CH_3)_2)_2]^-$ computation model for the Mo(V) DMSOR enzyme intermediate, and not the Mo(V) intermediate model with the Mo(VI) crystal structure geometry as reported previously.[113] Due to stability of our computation model the reduction of Mo(V) to Mo(IV) is expected to be energy demanding compared to destabilized Mo(V) models with a Mo(VI) crystal structure geometry. This result is supported by the kinetic study of Cobb et al. on DMSOR with TMAO as substrate that revealed the reduction of the DMSOR Mo(V) intermediate to the Mo(IV) state to be the rate limiting step with a 0.2 s^{-1} rate constant.[14] Furthermore, the low Mo-S covalency in the SOMO also supports the observation that reduction of Mo(V) to Mo(IV) is rate limiting.

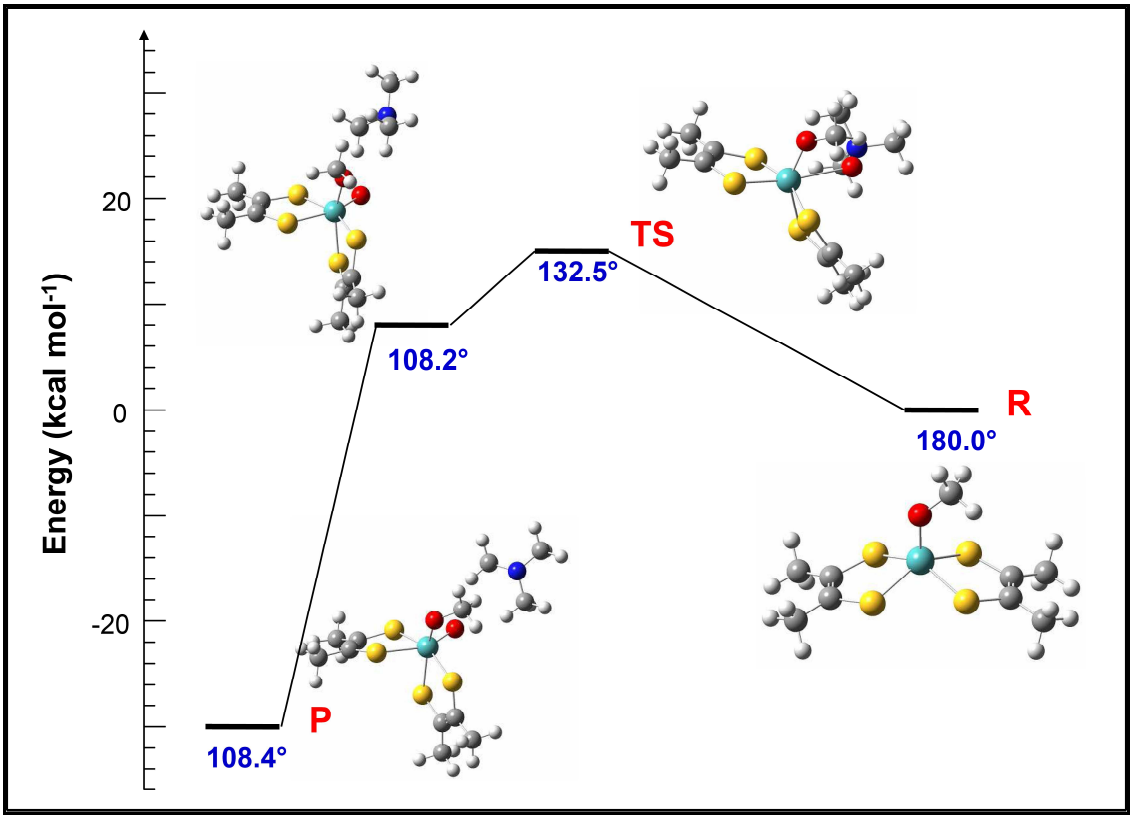

Figure 4.12: Energy profile for the oxygen atom transfer reaction between [Mo(OCH_3)(dithiolene)]$^-$ and TMAO substrate. Energies have been normalized to the reactant.

In addition, inspection of the [Mo(OCH_3)($S_2C_2(CH_3)_2)_2$(OH)]$^-$ computational model and the {[Mo(OCH_3)(dithiolene)] + TMAO} transition state (Figure 4.13) reveals a small geometric difference (0.19Å calculated root mean square deviation (RMSD)) between the two structures, with a dithiolene dihedral angle of 132.5° in the calculated transition state compared with 122° dihedral determined for [Mo(OCH_3)($S_2C_2(CH_3)_2)_2$(OH)]$^-$ computational model.

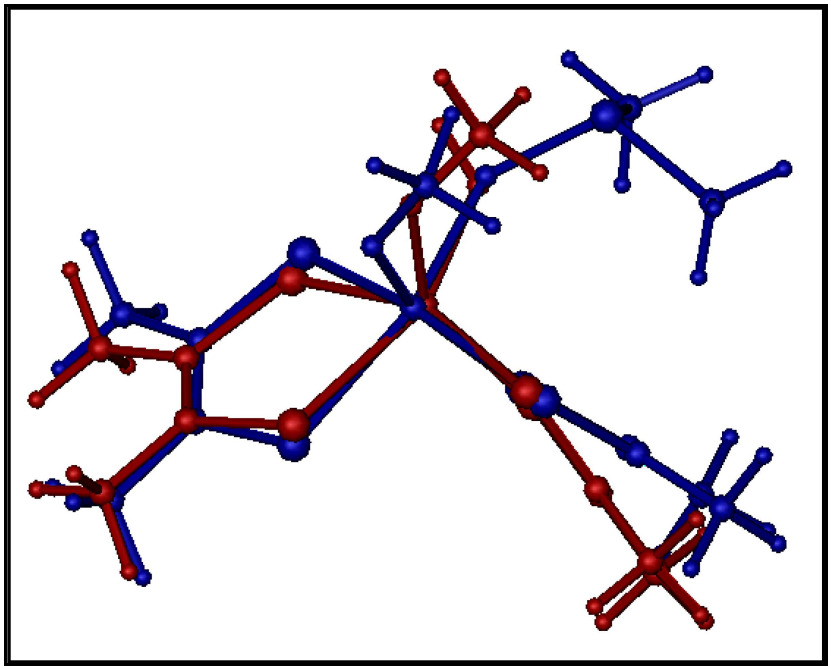

Figure 4.13: Overlay of the DMSOR transition state with TMAO and the fully geometry optimized $[Mo(OCH_3)(S_2C_2(CH_3)_2)_2(OH)]^-$ computational model for the DMSOR Mo(V) intermediate.

4.6 Conclusion

The DMSOR Mo(V) intermediate has been generated and spectroscopically and computationally characterized. An intense and well resolved EPR spectrum was obtained, and spectral simulation revealed a rhombic g-tensor and ^1H hyperfine tensor similar to what has been reported previously. The rhombic g-tensor is a clear indication of the low symmetry coordination environment for the Mo(V) intermediate. For the first time rhombic $^{95,97}Mo$ hyperfine tensors have been reported, and the rhombic dipolar contributions confirm the admixture of d_{z^2} ground state with other Mo d orbitals. Theoretical spin Hamiltonian parameters for a six coordinated Mo(V) intermediate computational model agree well with our

experimental results, and support a distorted geometry for the Mo(V) intermediate.

Calculated and experimental electronic absorption and MCD spectra for the Mo(V) intermediate are in good agreement and reveal seven bands. These bands occur at higher energy compared to previously reported spectra for glycol inhibited enzyme.[91] Theoretical MCD spectra have been calculated using the SORCI method and the results agree well with the experimental spectrum. Combinations of electronic absorption and MCD spectroscopies with theoretical MCD results have been utilized to make detailed band assignments. Band 1 is assigned as a ligand field transition, whereas LMCT transitions have been assigned for bands 2-7.

The low-covalent nature of the Mo-S interaction in the SOMO for the DMSOR Mo(V) intermediate is evident in the magnitude of the EPR g_1-value which is less than free electron value, negative spin densities on $S_{dithiolene}$, and low percentage composition of $S_{dithiolene}$ in the β-LUMO orbital. Additionally, SOMO possesses comparably small amount of sulfur character, compared to the amount in LUMO and LUMO+1 in P and Q pterin dithiolene respectively. We therefore propose electron transfer through these higher lying orbitals to form Mo(IV) active site in DMSO Reductase.

References

1. Hille R; The Mononuclear Molybdenum Enzymes. *Chemical Reviews* **1996,** *96*, 2757-2816.

2. Stiefel EI; Molybdenum Enzymes, Cofactors, and Chemistry. In Molybdenum Enzymes, Cofactors and Metal Systems. Washington, DC. American Chemical Society **1993**, 1-19.

3. Campbell WH; Nitrate Reductase Biochemistry Comes of Age. *Plant Physiology* **1996**,*111*, 355-361.

4. McNaughton RL, Helton ME, Rubie ND, Kirk ML; The Oxo-Gate Hypothesis and DMSO Reductase: Implications for a Psuedo-σ Bonding Interaction Involved in Enzymatic Electron Transfer. *Inorganic Chemistry* **2000**, *39*, 4386-4387.

5. Schindelin H, Kisker C, Hilton J, Rajagopalan KV, Rees DC; Crystal Structure of DMSO Reductase: Redox-Linked Changes in Molybdopterin Coordination. *Science* **1996**, *272*, 1615-1621.

6. Ellis PJ, Conrads T, Hille, Russ and Kuhn P; Crystal Structure of the 100 kDa Arsenite Oxidase from *Alcaligenes faecalis* in Two Crystal Forms at 164 Å and 2.03 Å. *Structure* **2001**, *9*, 125-132.

7. Conrads T, Hemann C, George GN, Pickering IJ, Prince RC, Hille R; The Active Site of Arsenite Oxidase from *Alcaligenes faecalis*. *Journal of the American Chemical Society, Communications* **2002**, *124*, 11276-11277.

8. Dias JM, Than ME, Humm A, Huber R, Bourenkov GP, Bartunik HD, Bursakov S, Calvete J, Caldeira JCCV, Moura I, Romão MJ; Crystal Structure of the First Dissimilatory Nitrate Reductase at 1.9 A Solved by MAD Methods. *Structure* **1999**, *7*, 65-79.

9. Moura JJG, Brondino CD, Trincão J, Romão MJ; Mo and W Bis-MGD Enzymes: Nitrate Reductases and Formate Dehydrogenases. *Journal of Biological Inorganic Chemistry* **2004**, *9*, 791-799.

10. Khangulov SV, Gladyshev VN, Dismukes GC, Stadtman TC; Selenium-Containing Formate Dehydrogenase H from Escherichia coli: A Molybdopterin Enzyme That Catalyzes Oxidation without Oxygen Transfer. *Biochemistry* **1998**, *37*, 3518-3528.

11. Andreae MO; Dimethylsulfoxide in Marine and Freshwaters; *Limnology and Oceanography* **1980**, *25*, 1054-1063.

12. Lovelock JE, Maggs RJ, Rasmussen RA; Atmospheric Dimethyl Sulphide and the Natural Sulphur Cycle. *Nature* **1972**, *237*, 452.

13. Chalson RJ, Lovelock JE, Andreae, Meinrat O. and Warren SG; Oceanic Phytoplankton, Atmospheric Sulfur, Cloud Albedo and Climate. *Nature* **1987**, *326*, 655-661.

14. Cobb N, Conrads T. Hille R; Mechanistic Studies of *Rhodobacter Sphaeroides* Me_2SO Reductase. *The Journal of Biological Chemistry* **2005**, *280*, 11007-110017.

15. Schneider F, Löwe J, Huber R, Schindelin H, Kisker C, Knäblein J; Crystal Structure of Dimethyl Sulfoxide Reductase from *Rhodobacter capsulatus* at 1.88 Å Resolution. *Journal of Molecular Biology* **1996**, 263, 53-69.

16. McAlpine AS, McEwan AG, Shaw AL, Bailey S; Molybdenum Active Centre of DMSO Reductase from *Rhodobacter capsulatus*: Crystal Structure of the Oxidised Enzyme at 1.82-Å Resolution and the Dithionite-Reduced Enzyme at 2.8-Å Resolution. *Journal of Biological Inorganic Chemistry* **1997**, *2*, 690-701.

17. McAlpine AS, McEwan AG, Bailey S; The High Resolution Crystal Structure of DMSO Reductase in Complex with DMSO. *Journal of Molecular Biology* **1998**, *275*, 613-623.

18. Li H-K, Temple C, Rajagopalan KV, Schindelin H; The 1.3 Å Crystal Structure of *Rhodobacter sphaeroides* Dimethyl Sulfoxide Reductase Reveals Two Distinct Molybdenum Coordination Environments. *Journal of the American Chemical Society* **2000**, *122*, 7673-7680.

19. Cobb N, Hemann C, Polsinelli GA, Ridge JP, McEwan, Alastair G. and Hille R; Spectroscopic and Kinetic Studies of Y114F and W116F Mutants of Me_2SO Reductase from *Rhodobacter capsulatus*. *The Journal of Biological Chemistry* **2007**, *282*, 35519-35529.

20. Garton SD, Temple CA, Dhawan IK, Barber MJ, Rajagopalan KV, Johnson MK; Resonance Raman Characterization of Biotin Sulfoxide Reductase Comparing Oxomolybdenum Enzyme in the Me_2SO Reductase Family. *Biochemistry* **2000**, *275*, 6798 -6805.

21. Johnson MK, Garton SD, Oku H; Resonance Raman as a Direct Probe for the Catalytic Mechanism of Molybdenum Oxotransferases. *Journal of Biological Inorganic Chemistry* **1997**, *2*, 797-803.

22. Garton SD, Hilton J, Oku H, Crouse BR, Rajagopalan KV, Johnson MK; Active Site Structures and Catalytic Mechanism of *Rhodobacter*

sphaeroides Dimethyl Sulfoxide Reductase as Revealed by Resonance Raman Spectroscopy. *Journal of the American Chemical Society* **1997**, *119*, 12906-12916.

23. George GN, Hilton J, Temple C, Prince RC, Rajagopalan KV; Structure of the Molybdenum Site of Dimethyl Sulfoxide Reductase. *Journal of the American Chemical Society* **1999**, *121*, 1256-1266.

24. González PJ, Rivas MG, Brondino CD, Bursakov SA, Moura I, Moura JJG; EPR and Redox Properties of Periplasmic Nitrate Reductase from *Desulfovibrio desulfuricans* ATCC 27774. *Journal of Biological Inorganic Chemistry* **2006**, *11*, 609-616.

25. Arnoux P, Sabaty M, Alric J, Frangioni B, Guigliarelli B, Adriano J-M, Pignol D; Structural and Redox Plasticity in the Heterodimeric Periplasmic Nitrate Reductase. *Nature Structural Biology* **2003**, *10*, 928-934.

26. Jepson BJN, Mohan S, Clarke TA, Gates AJ, Cole JA, Butler CS, Butt JN, Hemmings AM, Richardson DJ; Spectropotentiometric and Structural Analysis of the Periplasmic Nitrate Reductase from *Escherichia coli*. *The Journal of Biological Chemistry* **2007**, *282*, 6425-6437.

27. Bertero MG, Rothery RA, Palak M, Hou C, Lim D, Blasco F, Weiner JH, Strynadka NC; Insights into the Respiratory Electron Transfer Pathway from the Structure of Nitrate Reductase A. *Nature Structural Biology* **2003**, *10*, 681-687.

28. Jormakka M, Richardson D, Byrne B, Iwata S; Architecture of NarGH Reveals a Structural Classification of Mo-*bis*MGD Enzymes. *Structure* **2004**, *12*, 95-104.

29. Blasco F, Guigliarelli B, Magalon A, Asso M, Giordano, G and Rothery RA; The Coordination and Function of the Redox Centres of the Membrane-bound Nitrate Reductases. *Cellular and Molecular Life Sciences* **2001**, *58*, 179-193.

30. Vincent SP, Bray RC; Electron-Paramagnetic-Resonance Studies on Nitrate Reductase from *Escherichia coli* K12. *The Biochemical Journal* **1978**, *171*, 639-647.

31. Magalon A, Asso M, Guigliarelli B, Rothery RA, Bertrand P, Giordano G, Blasco F; Molybdenum Cofactor Properties and [Fe-S] Cluster Coordination in *Escherichia coli* Nitrate Reductase A: Investigation by Site-Directed Mutagenesis of the Conserved His-50 Residue in the NarG Subunit. *Biochemistry* **1998**, *37*, 7363-7370.

32. Anderson GL, Williams, Jeffrey and Hille R; The Purification and Characterization of Arsenite Oxidase from *Alcaligenes faecalis*, A Molybdenum-Containing Hydroxylase. *The Journal of Biological Chemistry* **1992**, *267*, 23674-23682.

33. Hoke KR, Cobb N, Armstrong FA, Hille R; Electrochemical Studies of Arsenite Oxidase: An Unusual Example of a Highly Cooperative Two-Electron Molybdenum Center. *Biochemistry* **2004**, *43*, 1667-1674.

34. George GN, Colangelo CM, Dong J, Scott RA, Khangulov SV, Gladyshev VN, Stadtman TC; X-ray Absorption Spectroscopy of the Molybdenum Site of *Escherichia coli* Formate Dehydrogenase. *Journal of the American Chemical Society* **1998**, *120*, 1267-1273.

35. Boyington JC, Gladyshev VN, Khangulov SV, Stadtman TC, Sun PD; Crystal Structure of Formate Dehydrogenase H: Catalysis Involving Mo, Molybdopterin, Selenocysteine, and an Fe_4S_4 Cluster. *Science* **1997**, *275*, 1305-1308.

36. Jormakka M, Törnroth S, Byrne B, Iwata S; Molecular Basis of Proton Motive Force Generation: Structure of Formate Dehydrogenase-N. *Science* **2002**, *295*, 1863-1868.

37. Almendra MJ, Brondino CD, Gavel O, Pereira AS, Tavares P, Bursakov S, Duarte R, Caldeira J, Moura JJG, Moura I; Purification and Characterization of a Tungsten-Containing Formate Dehydrogenase from *Desulfovibrio gigas*. *Biochemistry* **1999**, *38*, 16366-16372.

38. Raaijmakers H, Macieira S, Dias JM, Teixeira S, Bursakov S, Huber R, Moura JJG, Moura I, Roma MJ; Gene Sequence and the 1.8 A Crystal Structure of the Tungsten-Containing Formate Dehydrogenase from *Desulfovibrio gigas*. *Structure* **2002**, *10*, 1261-1272.

39. Raaijmakers H, Teixeira S, Dias JM, Almendra MJ, Brondino CD, Moura I, Moura JJG, Romão MJ; Tungsten-Containing Formate Dehydrogenase from *Desulfovibrio gigas*: Metal Identification and Preliminary Structural Data by Multi-Wavelength Crystallography. *Journal of Biological Inorganic Chemistry* **2001**, *6*, 398-404.

40. Raaijmakers HCA, Romão MJ; Formate-Reduced *E. coli* Formate Dehydrogenase H: The Reinterpretation of the Crystal Structure Suggests a New Reaction Mechanism. *Journal of Biological Inorganic Chemistry* **2006**, *11*, 849-854.

41. Rivas MG, González PJ, Brondino CD, Moura JJG, Moura I; EPR Characterization of the Molybdenum(V) Forms of Formate Dehydrogenase

from *Desulfovibrio desulfuricans* ATCC 27774 Upon Formate Reduction. *Journal of Inorganic Biochemistry* **2007**, *101*, 1617-1622.

42. Romão MJ; Molybdenum and Tungsten Enzymes: A Crystallographic and Mechanistic Overview. *Dalton Transaction* **2009**, 4041-4068.

43. Que L; *Physical Methods in Bioinorganic Chemistry Spectroscopy and Magnetism*. Sausalito, California: University Science Books; **2000**.

44. Solomon EI, Lever ABP eds; *Inorganic Electronic Structure and Spectroscopy*. Hoboken, New Jersey: John Wiley & Sons, Inc; **2006**.

45. Shriver DF, and Atkins PW; *Inorganic Chemistry*. Third Ed. Oxford, New York: Oxford University Press; **1999**.

46. Stiefel EI, Karlin KD eds. *Dithiolene Chemistry Synthesis, Properties, and Applications*. Progress in Inorganic Chemistry; Volume 52. Hoboken, New Jersey: John Wiley & Sons, Inc; **2004**.

47. Neese F, Solomon EI; MCD C-Term Signs, Saturation Behavior, and Determination of Band Polarizations in Randomly Oriented Systems with Spin S > 1/2. Applications to S = 1/2 and S = 5/2. *Inorganic Chemistry* **1999**, *38*, 1847-1865.

48. Hernandez-Marin E, Seth M, Ziegler T; A Theoretical Study of the Magnetic Circular Dichroism Spectrum for Sulfite Oxidase Based on Time-Dependent Density Functional Theory. *Inorganic Chemistry* **2009**, *48*, 2880-2886.

49. Kirk ML; Magnetic Circular Dichroism Spectroscopy of Pyranopterin Molybdenum Enzymes. In: Telser J, ed. *Paramagnetic Resonance of Metallobiomolecules*. Washington, DC: The American Chemical Society; **2003**, 340-357.

50. Weltner WJ; *Magnetics Atoms and Molecules*. New York: Dover Publication, Inc; **1983**.

51. Atherton NM; *Principles of Electron Spin Resonance*. Physical Chemistry Series. New York: Ellis Horwood PTR Prentice Hall; **1993**.

52. Cosper MM, Neese F, Astashkin AV, Carducci MD, Raitsimring, Arnold M. and Enemark JH; Determination of the g-Tensors and Their Orientations for *cis,trans*-(L-N_2S_2)$Mo^{V}OX$ (X = Cl, SCH_2Ph) by Single-Crystal EPR Spectroscopy and Molecular Orbital Calculations. *Inorganic Chemistry* **2005**, *44*, 1290-1301.

53. Drago RS; *Physical Methods for Chemists*. Second ed. Gainesville, Florida: Surfside Scientific Publishers; **1992**.

54. Ferraro JR, Nakamoto K, Brown CW; *Introductory Raman Spectroscopy*. Second ed. San Diego, California: Academic Press; **2003**.

55. Basu P, Stolz JF, and Smith MT; A Coordination Chemist's View of the Active Sites of Mononuclear Molybdenum Enzymes. *Current Science* **2003**, *84*, 1412-1418.

56. Nugent WA, Mayer JM; *Metal-Ligand Multiple Bonds*. A Wiley-Interscience Publication; **1988**.

57. Sugimoto H, Tano H, Suyama K, Kobayashi T, Miyake H, Itoh S, Mtei RP, Kirk ML; Chalcogenidobis(ene-1,2-dithiolate)molybdenum(IV) Complexes (chalcogenide E = O, S, Se): Probing Mo≡E and Ene-1,2-dithiolate Substituent Effects on Geometric and Electronic Structure. *Dalton Transactions* **2011**, *40*, 1119-1131.

58. Sugimoto H, Tsukube H; Chemical Analogues Relevant to Molybdenum and Tungsten Enzyme Reaction Centres Toward Structural Dynamics and Reaction Diversity. *Chemical Society Reviews* **2008**, *37*, 2609-1619.

59. Enemark JH, Cooney JJA, Wang J-J, Holm RH; Synthetic Analogues and Reaction Systems Relevant to the Molybdenum and Tungsten Oxotransferases. *Chemical Reviews* **2004**, *104*, 1175-200.

60. Goddard CA, Holm RH; Synthesis and Reactivity Aspects of the Bis(dithiolene) Chalcogenide Series. *Inorganic Chemistry* **1999**, *38*, 5389-5398.

61. Lim BS, Holm RH; Bis(dithiolene)molybdenum Analogues Relevant to the DMSO Reductase Enzyme Family: Synthesis, Structures, and Oxygen Atom Transfer Reactions and Kinetics. *Journal of the American Chemical Society* **2001**, *123*, 1920-1930.

62. McNaughton RL, Lim BS, Knottenbelt SZ, Holm RH, Kirk ML; Spectroscopic and Electronic Structure Studies of Symmetrized Models for Reduced Members of the Dimethylsulfoxide Reductase Enzyme Family. *Journal of the American Chemical Society* **2008**, *130*, 4628-4636.

63. Cotton FA, and Schmid G; Mononuclear Molybdenum(IV) Complexes with Two Multiply Bonded Chalcogen Ligands in Trans Configuration and Chelating Biphosphine Ligands. *Inorganic Chemistry* **1997**, *36*, 2267-2278.

64. Johnson AR, Davis WM, Cummins CC, Serron S, Nolan SP, Musaev DG, Morokuma K; Four-Coordinate Molybdenum Chalcogenide Complexes Relevant to Nitrous Oxide N–N Bond Cleavage by Three-Coordinate Molybdenum(III): Synthesis, Characterization, Reactivity, and Thermochemistry. *Journal of the American Chemical Society* **1998**, *120*, 2071-2085.

65. Sugimoto H, Sakurai T, Miyake H, Tanaka K, Tsukube H; Mononuclear Five-Coordinate Molybdenum(IV) and -(V) Monosulfide Complexes Coordinated with Dithiolene Ligands: Reversible Redox of Mo(V)/Mo(IV) and Irreversible Dimerization of $[Mo^{V}S]^{-}$ Cores to a Dinuclear $[Mo^{V}_{2}(\mu\text{-}S)_2]^{2-}$ Core. *Inorganic Chemistry* **2005**, *44*, 6927-6929.

66. Sugimoto H, Harihara M, Shiro M, Sugimoto K, Tanaka K, Miyake H, Tsukube H; Dioxo-Molybdenum(VI) and Mono-oxo-Molybdenum(IV) Complexes Supported by New Aliphatic Dithiolene Ligands: New Models with Weakened Mo=O Bond Characters for the Arsenite Oxidase Active Site. *Inorganic Chemistry* **2005**, *44*, 6386-6392.

67. Tano H, Tajima R, Miyake H, Itoh S, Sugimoto H. Selenidobis(dithiolene)metal(IV) Complexes (metal M = Mo, W) Potentially Related to the Nicotinic Acid Hydroxylase Reaction Center: Redox Aspects in Electrochemistry and Oxygen Atom Transfer from Me_3NO to M^{IV} Centers. *Inorganic Chemistry* **2008**, *47*, 7465-7467.

68. Coucouvanis D, Hadjikyriacou A, Toupadakis A, Koo SM, Ileperuma O, Draganjac M, Salifoglou A; Studies of the Reactivity of Binary Thio- and Tertiary Oxothiomolybdates toward Electrophiles. Reactions with Dicarbomethoxyacetylene and the Synthesis and Structures of the $[Et_4N_2[MoO(L)_2]$, *anti*-$[Et_4N]_2[Mo_2O_2S_2(L)_2]]$, *syn*-$[Ph_4P]_2[Mo_2O_2S_2(L)_2]$.2DMF, $[Ph_4P]_2[Mo(L)_3]$.DMF.C_6H_6, and $[Ph_4P]_2[Mo_2S_2(L)_4)$.2CH_2Cl_2 Complexes (L = 1,2-Dicarbomethoxy-1,2-ethylenedithiolate). *Inorganic Chemistry* **1991**, *30*, 754-767.

69. Mayer JM, Thorn DL, Tulip TH; Synthesis, Reactions, and Electronic Structure of Low-Valent Rhenium-Oxo Compounds. Crystal and Molecular Structure of $Re(O)I(MeC{\equiv}CMe)_2$. *Journal of the American Chemical Society* **1985**, *107*, 7454-7462.

70. Cotton, F. Albert and Feng X; Theoretical Study of Electronic Structures and Spectra of Chalcogenido Complexes of Molybdenum, *trans*-$Mo(Q)_2(PH_3)_4$ (Q = O, S, Se, Te). *Inorganic Chemistry* **1996**, *35*, 4921-4925.

71. Matz KG, Mtei RP, Leung B, Burgmayer SJN, Kirk ML; Noninnocent Dithiolene Ligands: A New Oxomolybdenum Complex Possessing a Donor-

Acceptor Dithiolene Ligand. *Journal of the American Chemical Society* **2010**, *132*, 7830-7831.

72. Davies ES, Beddoes RL, Collison D, Dinsmore A, Docrat A, Joule JA, Wilson CR, Garner CD; Synthesis of Oxomolybdenum Bis(dithiolene) Complexes Related to the Cofactor of the Oxomolybdoenzymes. *Journal of the Chemical Society, Dalton Transactions* **1997**, *2*, 3985-3996.

73. Donahue JP, Goldsmith CR, Nadiminti U, and Holm RH; Synthesis, Structures, and Reactivity of Bis(dithiolene)molybdenum(IV,VI) Complexes Related to the Active Sites of Molybdoenzymes. *Journal of the American Chemical Society* **1998**, *120*, 12869-12881.

74. Oku H, Ueyama N, Nakamura K; Thiolato-Activated Oxo-Metal Bond Features in Molybdenum and Tungsten Oxidoreductase Models As Revealed by Raman Spectroscopy. *Inorganic Chemistry* **1995**, *34*, 3667-3676.

75. Subramanian P, Burgmayer S, Richards S, Szalai V, Spiro TG; Resonance Raman Signatures of Oxomolybdenum Thiolate and Dithiolene Models of Molybdenum Proteins. *Inorganic Chemistry* **1990**, 29, 3849-3853.

76. Lim BS, Donahue JP, Holm RH; Synthesis and Structures of Bis(dithiolene)molybdenum Complexes Related to the Active Sites of the DMSO Reductase Enzyme Family. *Inorganic Chemistry* **2000**, *39*, 263-273.

77. Lorber C, Donahue JP, Goddard CA, Nordlander E, Holm RH; Synthesis, Structures, and Oxo Transfer Reactivity of Bis(dithiolene)tungsten(IV, VI) Complexes Related to the Active Sites of Tungstoenzymes. *Journal of the American Chemical Society* **1998**, *120*, 8102-8112.

78. Paradis JA, Wertz DW and Thorp HH; Electronic Structures of Tungsten-Chalcogen Multiple Bonds. *Journal of the American Chemical Society* **1993**, *115*, 5308-5309.

79. Das SK, Biswas D, Maiti, Rabindranath and Sarkar S; Modeling the Tungsten Sites of Inactive and Active Forms of Hyperthermophilic *Pyrococcus furiosus* Aldehyde Ferredoxin Oxidoreductase. *Journal of the American Chemical Society* **1996**, *118*, 1387-1397.

80. Musgrave KB, Donahue JP, Lorber C, Holm RH, Hedman B, Hodgson KO; An X-ray Spectroscopic Investigation of Bis(dithiolene) Molybdenum (IV, V, VI) and -Tungsten (IV, V, VI) Complexes: Symmetrized Structural Representations of the Active Sites of Molybdoenzymes in the DMSO Reductase Family and of Tungstoenzymes in the AOR and F(M)DH

Families. *Journal of the American Chemical Society* **1999**, *121*, 10297-10307.

81. Groysman S, Holm RH; Synthesis and Structures of Bis(dithiolene)tungsten(IV,VI) Thiolate and Selenolate Complexes: Approaches to the Active Sites of Molybdenum and Tungsten Formate Dehydrogenases. *Inorganic Chemistry* **2007**, *46*, 4090-4102.

82. Hine FJ, Taylor AJ, Garner CD; Dithiolene Complexes and the Nature of Molybdopterin. *Coordination Chemistry Reviews* **2010**, *254*, 1570-1579.

83. Novotny M, Lippard SJ, Foun- HD; Synthesis and Properties of Cationic Molybdenum(IV) Oxohaloisocyanide Complexes. *Inorganic Chemistry* **1974**, *13*, 828-831.

84. Oku H, Ueyama N, Kondo M, Nakamura A; Oxygen Atom Transfer Systems in Which the (μ-Oxo)dimolybdenum(V) Complex Formation Does Not Occur: Syntheses, Structures, and Reactivities of Monooxomolybdenum(IV) Benzenedithiolato Complexes as Models of Molybdenum Oxidoreductases. *Inorganic Chemistry* **1994**, *33*, 209-216.

85. Fourmond V, Burlat B, Dementin S, Arnoux P, Sabaty M, Boiry S, Guigliarelli B, Bertrand P, Pignol D, Léger C; Major Mo(V) EPR Signature of *Rhodobacter sphaeroides* Periplasmic Nitrate Reductase Arising from a Dead-End Species That Activates Upon Reduction. Relation to Other Molybdoenzymes from the DMSO Reductase Family. *The journal of Physical Chemistry. B*. **2008**, *112*, 15478-15486.

86. George GN, Turner NA, Bray RC, Morpeth FF, Boxer DH, Cramer SP; X-ray-Absorption and Electron-Paramagnetic-Resonance Spectroscopic Studies of the Environment of Molybdenum in High-pH and Low-pH forms of *Escherichia coli* Nitrate Reductase. *Biochemical Journal* **1989**, *259*, 693-700.

87. Bray RC, Vincent SP, Lowe DJ, Clegg, Roger A. and Garland PB; Electron-Paramagnetic-Resonance Studies on the Molybdenum of Nitrate Reductase from *Escherichia coli* K12. *The Biochemical Journal* **1976**, *155*, 201-203.

88. Raitsimring AM, Astashkin AV, Feng C, Enemark JH, Nelson KJ, Rajagopalan KV; Pulsed EPR Studies of the Exchangeable Proton at the Molybdenum Center of Dimethyl Sulfoxide Reductase. *Journal of Biological Inorganic Chemistry* **2003**, *8*, 95-104.

89. Bray RC, Adams B, Smith AT, Richards RL, Lowe DJ, Bailey S; Reactions of Dimethylsulfoxide Reductase in the Presence of Dimethyl Sulfide and the

Structure of the Dimethyl Sulfide-Modified Enzyme. *Biochemistry* **2001**, *40*, 9810-9820.

90. Bennet B, Benson N, McEwan, Alastair G. and Bray RC; Multiple States of the Molybdenum Centre of Dimethylsulphoxide Reductase from *Rhodobacter capsulatus* Revealed by EPR Spectroscopy. *European Journal of Biochemistry* **1994**, *225*, 321-331.

91. Finnegan MG, Hilton J, Rajagopalan KV and JMK; Optical Transitions of Molybdenum(V) in Glycerol-Inhibited DMSO Reductase from *Rhodobacter sphaeroides*. *Inorganic Chemistry Communications* **1993**, *32*, 2616-2617.

92. Bastian NR, Kay CJ, Barber, Michael J. and Rajagopalan KV; Spectroscopic Studies of the Molybdenum-containing Dimethyl Sulfoxide Reductase from *Rhodobacter sphaeroides* f. sp. *denitrificans*. *The Journal of Biological Chemistry* **1991**, *266*, 45-51.

93. Costa C, Teixeira M, Moura I, LeGall J, Moura JJG; Formate Dehydrogenase from *Desulfovibrio desulfuricans* ATCC 27774: Isolation and Spectroscopic Characterization of the Active Sites (heme, iron-sulfur centers and molybdenum). *Journal of Biological Inorganic Chemistry* **1997**, *2*, 198-208.

94. Boyde S, Ellis RS, Garner, Dadid and Clegg W; Structural Comparison of Oxobis(benzene-1,2-dithiolato)molybdenum –(V) and –(IV) Complexes. *Journal of Chemical Society, Chemical Communications* **1986**, 1541-1543.

95. Ellis SR, Collison D, Garner, C David and Clegg W; Thiol Exchange for Mo^{3+} (M = Mo, W) Centres; Synthesis and Structure of $[PPh_4][MO(SCH_2CH_2)_2]$. *Journal of Chemical Society, Chemical Communications* **1986**, 1483-1485.

96. McMaster J, Carducci MD, Yang Y-S, Solomon EI, Enemark JH; Electronic Spectral Studies of Molybdenyl Complexes. 2. MCD Spectroscopy of $[MoOS_4]^-$ Centers. *Inorganic Chemistry* **2001**, *40*, 687-702.

97. Das SK, Chaudhury PK, Biswas D, and Sarkar S; Modeling for the Active Site of Sulfite Oxidase: Synthesis, Characterization, and Reactivity of $[Mo^{VI}O_2(mnt)_2]^{2-}$ (mnt^{2-} = 1,2-Dicyanoethylenedithiolate). *Journal of the American Chemical Society* **1994**, *116*, 9061-9070.

98. Ueyama N, Oku H, Nakamura A; cis-Dioxobis(benzenedithiolato) tungsten(VI) and the Related Monooxotungsten(V) and -(IV) Complexes. Models of Tungsten Oxidoreductases. *Journal of the American Chemical Society* **1992**, *114*, 7310-7311.

99. Sung K-M, Holm RH; Substitution and Oxidation Reactions of Bis(dithiolene)tungsten Complexes of Potential Relevance to Enzyme Sites. *Inorganic Chemistry* **2001**, *40*, 4518-4525.

100. Hanson GR, Brunette AA, McDonell AC, Murray KS, Wedd AG; Electronic Properties of Thiolate Compounds of Oxomolybdenum(V) and Their Tungsten and Selenium Analogues. Effects of ^{17}O, ^{98}Mo, and ^{95}Mo Isotope Substitution upon ESR Spectra and ^{95}Mo Isotope. *Journal of the American Chemical Society* **1981**, *103*, 1953-1959.

101. Balagopalakrishna C, Kimbrough, John T. and Westmoreland TD; Electronic Structural Contributions to g Values and Molybdenum Hyperfine Coupling Constants in Oxyhalide Anions of Molybdenum(V). *Inorganic Chemistry* **1996**, *35*, 7758-7768.

102. Peariso K, Chohan BS, Carrano CJ, Kirk ML; Synthesis and EPR Characterization of New Models for the One-Electron Reduced Molybdenum Site of Sulfite Oxidase. *Inorganic Chemistry* **2003**, *42*, 6194-203.

103. Dhawan, Ish K. and Enemark JH; EPR Studies of Oxo-Molybdenum(V) Complexes with Sulfur Donor Ligands: Implications for the Molybdenum Center of Sulfite Oxidase. *Inorganic Chemistry* **1996**, *35*, 4873-4882.

104. Johnson MK, Rees DC, Adams MWW; Tungstoenzymes. *Chemical Reviews* **1996**, *96*, 2817-2840.

105. Hanson GR, Wilson GL, Bailey TD, Pilbrow JR, Wedd AG; Multifrequency Electron Spin Resonance of Molybdenum(V) and Tungsten(V) Compounds. *Journal of the American Chemical Society*, **1987**, *109*, 2609-2616.

106. Collison D, Mabbs FE, Enemark, J. H and Cleland J; The EPR Spectra and Electronic Structure of Low Symmetry Oxo-Molybdenum(V) Complexes. *Polyhedron* **1986**, *5*, 423-425.

107. Collison D, Eardley DR, Mabbs FE, Rigby, Keith and Enemark JH; Electronic Spin Resonance Studies of Low Symmetry Oxo- Molybdenum(V) ions Dilute in the Pseudo-Isostructural Chlorotin(IV) Moiety. *Polyhedron* **1989**, *8*, 1833-1834.

108. Collison D, Eardley DR, Mabbs FE, Rigby K, Bruck MA, Enemark JH, Wexler PA; Crystal and Molecular Structure of [$SnLCl_3$]. The Single-crystal Electron Paramagnetic Resonance Spectra of [$MoE(L)Cl_2$] and [$MoO(L)(NCS)_2$] Diluted in [$SnLCl_3$] [E=O or S; L = Tris(3,5-dimethylpyrazolyl)hydroborate]. *Journal Chemical Society, Dalton Transactions* **1994**, 1003-1011.

109. Swann J, Westmoreland TD; Density Functional Calculations of g Values and Molybdenum Hyperfine Coupling Constants for a Series of Molybdenum(V) Oxyhalide Anions. *Inorganic Chemistry* **1997**, *36*, 5348-5357.

110. Nipales NS, Westmoreland TD; Correlation of EPR Parameters with Electronic Structure in the Homologous Series of Low-Symmetry Complexes Tp*$MoOX_2$ (Tp* = Hydrotris(3,5-dimethylpyrazol-1-yl)borate; X = F, Cl, Br). *Inorganic Chemistry* **1997**, *36*, 756-757.

111. Kapre R, Ray K, Sylvestre I, Weyhermüller T, George SD, Neese F, Wieghardt K; Molecular and Electronic Structures of Oxo-bis(benzene-1,2-dithiolato)chromate(V) Monoanions. A Combined Experimental and Density Functional Study. *Inorganic Chemistry* **2006**, *45*, 3499-3509.

112. Collison D, Mabbs FE, and Rigby K; The Electronic Structure of "Non-Axial" Mono-Oxo Complexes of the Early Transition Elements. *Polyhedron* **1989**, *8*, 1832-1832.

113. Hernandez-Marin E, Seth M, Ziegler T; Density Functional Theory Study of the Electron Paramagnetic Resonance Parameters and the Magnetic Circular Dichroism Spectrum for Model Compounds of Dimethyl Sulfoxide Reductase. *Inorganic Chemistry* **2010**, *49*, 1566-76.

114. McNaughton RL; Electronic Structure Studies of Molybdenum-Thiolate Complexes Related to Pyranopterin Molybdenum Enzyme. **2002**.

115. Hernandez-Marin E, Seth M, Ziegler T; Density Functional Theory Study of the Magnetic Circular Dichroism Spectra of Molybdenyl Complexes. *Inorganic Chemistry* **2010**, *49*, 6066-6076.

116. Waters T, Wang X-B, Yang X, Zhang L, O'Hair RAJ, Wang L-S, Wedd AG; Photoelectron Spectroscopy of the Doubly-Charged Anions $[M^{IV}O(mnt)_2]^{2-}$ (M = Mo, W; mnt = $S_2C_2(CN)_2^{2-}$): Access to the Ground and Excited States of the $[M^{V}O(mnt)_2]^{-}$ Anion. *Journal of the American Chemical Society* **2004**, *126*, 5119-29.

117. Mtei RP, Ganna L, Stein B, Rubie N, Hille R, and Kirk ML; Spectroscopic and Electronic Structure Studies of a DMSO Reductase Catalytic Intermediate: Implications for Electron and Atom Transfer Reactivity. *Submitted to American Chemical Society* **2011**.

118. George GN, Doonan CJ, Rothery RA, Boroumand N, Weiner JH; X-ray Absorption Spectroscopic Characterization of the Molybdenum Site of *Escherichia coli* Dimethyl Sulfoxide Reductase. *Inorganic Chemistry* **2007**, *46*, 2-4.

119. Rothery RA, Weiner JH; Topological Characterization of *Escherichia coli* DMSO Reductase by Electron Paramagnetic Resonance Spectroscopy of an Engineered [3Fe-4S] Cluster. *Biochemistry* **1993**, *32*, 5855-5861.

120. George GN, Nelson KJ, Harris HH, Doonan CJ, Rajagopalan KV; Interaction of Product Analogues with the Active Site of *Rhodobacter sphaeroides* Dimethyl Sulfoxide Reductase. *Inorganic Chemistry* **2007**, *46*, 3097-104.

121. Gruber S, Kilpatrick L, Bastian NR, Rajagopalan KV, Spiro TG; Dithiolene Coordination in the Molybdopterin Cofactor of DMSO Reductase: In Situ Evidence from Resonance Raman Spectroscopy. *Journal of the American Chemical Society* **1990**, *112*, 8179-8180.

122. Kilpatrick L, Rajagopalan KV, Hilton J, Bastian NR, Stiefel EI, Pilato RS, Spiro TG; Resonance Raman Spectroscopic Characterization of the Molybdenum Active Site of DMSO Reductase. *Biochemistry* **1995**, *34*, 3032-3039.

123. Kondo-François A-Z, Bernhardt PV, McEwan AG, Ridge JP; The First Non-turnover Voltammetric Response from a Molybdenum Enzyme: Direct Electrochemistry of Dimethylsulfoxide Reductase from *Rhodobacter capsulatus*. *Journal of Biological Inorganic Chemistry* **2002**, *7*, 879-883.

124. Sugimoto H, Tatemoto S, Suyama K, Miyake H, Mtei RP, Itoh S, Kirk ML; Monooxomolybdenum(VI) Complexes Possessing Olefinic Dithiolene Ligands: Probing Mo-S Covalency Contributions to Electron Transfer in Dimethyl Sulfoxide Reductase Family Molybdoenzymes. *Inorganic Chemistry* **2010**, *49*, 5368-5370.

125. Hernandez-Marin E, Ziegler T; A Kinetic Study of Dimethyl Sulfoxide Reductase Based on Density Functional Theory. *Canadian Journal of Chemistry* **2010**, *88*, 683-693.

126. Hofmann M; Electronic State of the Dimethyl Sulfoxide Reductase Active Site. *Inorganic Chemistry* **2008**, *47*, 5546-5548.

127. McNamara JP, Hillier IH, Bhachu TS, Garner CD; The Nature and Function of the Catalytic Centres of the DMSO Reductases. *Dalton Transactions* **2005**, 3572-3579.

128. Tenderholt AL, Wang J-J, Szilagyi RK, Holm RH, Hodgson KO, Hedman B, Solomon EI; Sulfur K-edge X-ray Absorption Spectroscopy and Density Functional Calculations on Mo(IV) and Mo(VI)=O Bis-dithiolenes: Insights into the Mechanism of Oxo Transfer in DMSO Reductase and Related

Functional Analogues. *Journal of the American Chemical Society* **2010**, *132*, 8359-8371.

129. Thapper A, Deeth RJ, Nordlander E; A Density Functional Study of Oxygen Atom Transfer Reactions between Biological Oxygen Atom Donors and Molybdenum(IV) Bis(dithiolene) Complexes. *Inorganic Chemistry* **2002**, *41*, 6695-6702.

130. Hofmann M; What is the Best Theoretical Method to Study Molybdenum Dithiolene Complexes? *Journal of Molecular Structure: THEOCHEM* **2006**, *773*, 59-70.

131. Adams B, Smith AT, Bailey S, McEwan AG, and Bray RC; Reactions of Dimethylsulfoxide Reductase from *Rhodobacter capsulatus* with Dimethyl Sulfide and with Dimethyl Sulfoxide: Complexities Revealed by Conventional and Stopped-Flow Spectrophotometry. *Biochemistry* **1999**, *38*, 8501-8511.

132. Lee SC, Holm RH; Toward an Expanded Oxygen Atom Transfer Reactivity Scale: Computational Investigation of the Energetics of Oxo Transfer Reaction Couples. *Inorganica Chimica Acta* **2008**, *361*, 1166-1176.